

**INTERFACIAL STUDY OF DYE-
SENSITIZED SOLAR CELLS USING
PHOTOELECTRON AND ION
SCATTERING SPECTROSCOPY**

by

Altaf Abdullah Shamsaldeen

Thesis

Submitted to Flinders University

for the Degree of

Doctor of Philosophy

College of Science and Engineering

November 2020

*In the Name of Allah, the Most Gracious, the Most Merciful. Praise be
to Allah, the Cherisher and Sustainer of the worlds.*

In the loving memory of my beloved Dad

TABLE OF CONTENTS

TABLE OF CONTENTS.....	i
ABSTRACT.....	v
DECLARATION.....	vii
ACKNOWLEDGMENTS.....	viii
ABBREVIATIONS.....	x
List of Figures.....	xii
List of Tables.....	xvii
Chapter One.....	1
1 Background.....	1
1.1 Photovoltaics.....	2
1.1.1 Historical timeline.....	2
1.1.2 The Photovoltaic system.....	3
1.1.3 Photovoltaic generation.....	3
1.2 References.....	5
Chapter Two.....	6
2 Dye Sensitized Solar Cell.....	6
2.1 The anatomy of DSSC.....	6
2.2 Operating Principle.....	7
2.2.1 Excitation.....	7
2.2.2 Injection.....	7
2.2.3 Dye regeneration.....	8
2.2.4 Iodine reduction.....	8
2.2.5 Charge Recombination.....	8
2.3 Basic materials of DSSC.....	9
2.3.1 Substrate.....	9
2.3.2 Sensitizer.....	13
2.3.3 Electrolyte.....	17
2.3.4 Counter electrode.....	19
2.4 Cell stability.....	19
2.4.1 Stability tests.....	20
2.5 Research aims.....	22
2.6 Reference.....	24

Chapter Three.....	31
3 Experimental techniques	31
3.1 Photoelectron Spectroscopy	31
3.1.1 X-ray Photoelectron Spectroscopy (XPS).....	32
3.1.2 XPS Analysis	34
3.2 Ultraviolet Photoelectron Spectroscopy (UPS).....	35
3.3 Metastable Induced Electron Spectroscopy (MIES).....	36
3.3.1 The Singular Value Decomposition	37
3.4 Neutral Impact Collision Ion Scattering Spectroscopy (NICISS).....	38
3.4.1 NICISS analysis	40
3.5 Photovoltaic Characterization	40
3.6 Stability test	41
3.7 Materials and Sample Preparation	42
3.8 References.....	44
Chapter Four	46
4. Influence of TiO ₂ Surface Defects on the Adsorption of N719 Dye Molecules	46
4.1 Abstract.....	46
4.2 Introduction.....	47
4.3 Materials and Methods.....	48
4.3.1 Sample preparation	48
4.3.2 Methods.....	48
4.4 Results and Discussion.....	49
4.4.1 Study of Ru depth profile and dye adsorption	49
4.4.2 The Chemical state and component concentrations	51
4.4.3 Analysis of electronic properties with UP spectra	58
4.4.4 Analysis of MIE spectra.....	60
4.4.5 Singular Value Decomposition	61
4.4.6 Gaussian Fitting	62
4.5 Conclusions.....	64
4.6 References.....	65
Chapter Five.....	67
5 Ion Scattering and Electron Spectroscopic Investigation on DPA/dye/TiO ₂ interface of Dye Sensitized Solar Cells.....	67
5.1 Abstract.....	67

5.2	Introduction.....	68
5.3	Experimental	69
5.3.1	Sample preparation	69
5.3.2	Methods.....	69
5.3.2.1	J-V characteristics	69
5.3.2.2	NICISS, XPS and UPS.....	70
5.4	Results and Discussion.....	70
5.5	The influence of different concentrations of DPA on dye coverage and depth	73
5.6	Changes in the chemical state	75
5.7	Analysis of UP spectra.....	82
5.8	Singular Value Decomposition analysis (SVD).....	83
5.9	The adsorption configuration of the dye molecules on TiO ₂ surface and the cell performance .	84
5.10	Conclusion	85
5.11	Reference	86
Chapter Six		89
6	The effect of the carboxylic chenodeoxycholic as a co-adsorbent on the dye formation on dye/TiO ₂ interface.....	89
6.1	ABSTRACT:.....	89
6.2	Introduction:.....	90
6.3	Experimental	91
6.3.1	Sample preparation	91
6.4	Methods.....	92
6.4.1	J-V characteristics	92
6.4.2	NICISS, XPS, UPS and MIES	92
6.1	Results and Discussion.....	92
6.1.1	Photovoltaic performance	92
6.1.2	Restructuring the dye layers.....	94
6.1.3	Chemical characteristics	97
6.1.4	UPS analysis of TiO ₂ /dye interface with various CDCA concentrations	103
6.1.5	The observation from MIES	104
6.2	Conclusion	105
6.3	Reference	106
Chapter Seven		109
7.	Interfacial study of aged semiconductor/dye/electrolyte in Dye Sensitized Solar Cells.....	109

7.1	ABSTRACT:.....	109
7.2	Introduction:.....	110
7.3	Experimental	112
7.4	Results and Discussion.....	112
7.4.1	JV- Curve (Stability test)	112
7.4.2	Elemental depth profiles	117
7.4.3	XPS	119
7.4.3.1	Elements intensities as the cell ages	123
7.4.3.2	Intensity ratios as the cell ages.....	130
7.4.4	Analysis of MIE spectra.....	135
7.5	Light-set aging cells	137
7.5.1	Identifying the mechanisms behind changes in the cell performance.....	138
7.6	Heat and dark sets aging cells	140
7.7	Summary	146
7.8	Conclusion	146
7.9	References:.....	148
Chapter Eight		152
8.	Conclusion and future work.....	152

ABSTRACT

With the rapid increase in population, the world's energy demand also expected to increase. Solar energy is an ideal energy source and can be used all over the world, as it is readily available globally for presumably the entirety of human existence, which made it the most promising renewable energy source that will fulfil the world energy demand.

Dye-sensitized solar cells (DSSCs) are photoelectrochemical solar cells manufactured by using dyes and mimic photosynthesis in plants. Their efficiency reached up to 13% by optimizing material and structural properties. However, there are still some challenges that need to be improved before DSSCs successfully enters the photovoltaic market for application. The main two issues are low cell performance and long-term stability.

There are three main processes summarized the path of charges in DSSCs, charge generation, charge collection and charge recombination, which significantly affects the cell performance. Different components are used in manufacturing DSSC, and each one of them plays an essential role in influencing the interface. Studying the structure of the TiO_2/dye and $\text{TiO}_2/\text{dye}/\text{electrolyte}$ interfaces and understanding their effect on the charge transportation process will be the aim of this dissertation.

Using specific surface sensitive techniques, photoelectron spectroscopy (PES) including, X-ray photoelectron spectroscopy (XPS), ultra-violet photoelectron spectroscopy (UPS) and metastable induced electron spectroscopy (MIES) to observe the changes in the dye/ TiO_2 and $\text{TiO}_2/\text{dye}/\text{electrolyte}$ interface from both molecular and electronic perspective. While neutral impact collision ion scattering spectroscopy (NICISS) used to measure the molecular coverage and concentration depth profiling of the dye.

In chapter 4, two different processes were applied on the TiO_2 substrate, heating with four ascending temperatures and heating-sputtering with different doses using Argon projectiles (Ar^+) were used to investigate the dye adsorption and configuration on TiO_2 surface. The heating process was more effective in removing the surface contaminations, while in the heating-sputtering processes, contaminations were removed, and surface defects such as the oxygen vacancies (Ti^{3+}) were created on TiO_2 surface. An observation of an increase in the dye adsorption was obtained

using the heating process, while a decrease in the dye adsorption resulted from the heating-sputtering process. Furthermore, both processes show different dye configuration of TiO₂ substrate.

Two different functional groups were used during a study investigating the addition of co-adsorbents in repressing dye aggregation on TiO₂. In chapters 5 and 6, the phosphonic acid decylphosphonic acid (DPA) and the carboxylic acid chenodeoxycholic Acid (CDCA) were used, respectively. Different concentrations of these co-adsorbents were used. It was shown that both types of co-adsorbents suppressed the formation of dye thicker layers. However, they behave differently concerning the type of dye that has been used.

The results show that the incorporation of co-adsorbent within the dye solution affected the dye adsorption and configuration on the TiO₂ surface. When co-adsorbents are adsorbed on the TiO₂ surface, they work as a buffer layer and replacing the weakly interacting and undesirable dye molecules that not involved in charge generation.

In chapter 7, a 1000 h stability test was conducted in three different conditions to investigate the degradation mechanisms of DSSC performance using DPA as a co-adsorbent. Light exposed condition, heat condition, and dark condition. The changes of the dye and electrolyte components on the TiO₂/dye/electrolyte interface as cell ages were investigated using PES and NICISS for a better understanding of the process at the molecular level. The results show that the DSSCs containing co-adsorbent have more stabilized cell performance. Co-adsorbents remove the weakly dye molecule leading to better adsorbent of the electrolyte and additives, resulting in stabilizing the open-circuit voltage as the cell ages.

PES and NICISS are powerful surface sensitive techniques that have been used in this work to gain an insight into the DSSC interfaces at a molecular level as the cell ages.

DECLARATION

I certify this thesis does not incorporate without acknowledgement any material previously submitted for degree or diploma in any university; and that to the best of my knowledge and belief it does not contain any material previously published or written by another person except where due reference is made in the text.

Altaf Abdullah Shamsaldeen 2020

ACKNOWLEDGMENTS

This thesis, and a doctoral trip, would not have been possible without the support of Allah Almighty, who guided me in difficult and faltering circumstances, who gave me the will to complete this project. Furthermore, the blessings in the form of wonderful counsellors, colleagues, parents, friends and family, and the appropriate opportunities that brought them. Allah will not thank those who do not thank people. So, thank you very much, everyone, who supported my trip.

Firstly, I express my sincere thanks to my supervisor, Prof. Gunther Andersson, for his invaluable guidance throughout my PhD, without his technical and moral support I would not have been able to complete my work. Working in his group during the PhD period, I have become grateful for the opportunity to learn from such a dedicated professional, and to work closely with a good person. Thank you, Gunther, you are the most pedagogical person I have ever met,

I owe my deepest gratitude to Prof. Lars Kloo and his group at KTH in Sweden for their instructional and guidance in teaching me the principle of manufacturing DSSC.

My heartiest thanks to my colleagues (my second family) in Andersson's group for their guidance and assistance throughout my project. Dr. Benjamin Chambers, Dr. Yanting Yin, Dr. Herri Trilaksana, Jesse Daughtry, Liam Howard-Fabretto, Amira Ramadan Alghamdi, Abdulrahman Alotabi, Gowri Krishnan, Anahita Motamedisade, Anand Kumar, Ahlam Rayan M Alharbi and Sunita Gautam Adhikari. THANK YOU for providing me the opportunity to conduct my researches in a resilient atmosphere, especially during my pregnancy.

I also would like to thank the Electronics and Mechanical workshop members, Chris Price and Andrew Dunn, who were friendly, hardworking and for their immediate help.

I gratefully acknowledge the generous financial support of the Public Authority of Applied Education and Training in Kuwait.

I heard a lot about the mental illness during the PhD, we may sink completely under challenging situations if we do not achieve the desired balance that gives us the courage and ability to see things real size, and this is what friends and family do.

To all my friends, thank you for your constant encouragement. It has really meant a lot.

To all my family, each one of you played a different role in supporting me during my research by providing me with all the support and love that I need. (Thank you, Dallah!)

From the depth of my heart, I would like to thank my Mom whose her supplication was the secret of my success and (My father, May Allah have mercy on him) who raised me with love and continuously supported me in various capacities.

My three little musketeers Muhammad, Azzam and Rakan. Your birth during my study (Azzam and Rakan) added the joy and pleasure to our life, and I know that this period was also hard to all of you, especially while I was writing this dissertation combined with the world pandemic of COVID-19. May Allah protect all of you for a heart that lives from your heartbeat, and a mother who sees her present and her future in all of you.

Thank you for disturbing me all the time and waking up the HULK in me!

If you read this thesis and are not impressed, then I invite you to blame the Unknown Soldier who always supported me during my research, providing the invaluable support and even providing some necessary persuasion to assist me in completing my PhD journey. My loving husband, I appreciate your support and being patiently bearing with me and taking care of the kids in those stressful years during my PhD.

Love u you are my oxygen.♥☐

Please forgive me if I miss mentioning some of you; I have a poor memory.☺☐

ABBREVIATIONS

AD	Auger de-excitation
AN	Auger neutralization
CB	Conduction Band
CDCA	Chenodeoxycholic Acid
CE	Counter Electrode
CSP	concentrating solar power
DOS	Density of States
DSSC	Dye-Sensitized Solar Cell
E_{Binding}	Binding Energy
E_{kinetic}	Kinetic Energy
FF	Fill Factor
FTO	Fluorine-doped tin oxide
FWHM	full-width half maximum
HOMO	Highest Occupied Molecular Orbital
ITO	Indium Thin Oxide
IV	Current-Voltage
J_{sc}	Short-circuit current density
LUMO	Lowest Unoccupied Molecular Orbital
MIES	Metastable Induced Electron Spectroscopy
MPP	Maximum Power Point
N719	Di-tetrabutylammonium cis-bis (isothiocyanate) bis (2,2'-bipyridyl-4,4' dicarboxylate) ruthenium (II)
NICISS	Neutral Impact Collision Ion Scattering Spectroscopy
PES	Photoelectron Spectroscopy
P_{in}	Incident Sunlight Power
P_{max}	Maximum Power
PV	Photovoltaics
RI	Resonant Ionization
SVD	Singular Value Decomposition

4TBP	4-tert-butylpyridine
TCO	Transparent Conducting Oxide
TiO ₂	Titanium Dioxide
TOF	Time Of Flight
UHV	Ultra-High Vacuum
UPS	Ultraviolet Photoelectron Spectroscopy
UV	Ultraviolet
VB	Valence Band
V _{oc}	Open-circuit Voltage
WE	working electrode
WF	Work Function
XPS	X-ray Photoelectron Spectroscopy
Z907	Cis-Bis(isothiocyanato) (2,2'-bipyridyl-4,4'-dicarboxylato)(4,4'-dinonyl-2'-bipyridyl) ruthenium(II)

List of Figures

Figure 2-1: Schematic diagram of DSSC working principle	7
Figure 2-2: The electron transfer processes in DSSCs. Electron excited (1) then injected into the conduction band of TiO ₂ (2), then diffuse through the TiO ₂ /TCO (3). The redox couple regenerate the oxidized dye (4). Electrolyte reduced at the counter electrode (5). Electron loss by the recombination with the dye cation (6) or with the redox couple (7).....	9
Figure 2-3: The molecular structure of N719 and Z907 dyes [44].	14
Figure 2-4: Molecular structure of DPA and CDCA[48].....	17
Figure 3-1: The Inelastic Electron Mean Free Path for different solides plotted againes the kinetic energy [4].....	32
Figure 3-2: UP spectrum with labelled valence band (~3 eV) and secondary electron cut off to measure the work function (21.2 eV - 17.2 eV = 4 eV).....	36
Figure 3-3: Example of NISS row data spectrum of N719 dye on TiO ₂ (The signals in TOF spectra assigned to Ruthenium at 4 μs , Titanium at 4.5 μs, Oxygen at 6.4 μs and Carbon at 7.4 μs.	39
Figure 3-4: NISS result shows Ru depth profile in N719 with 20 mM CDCA, the relative concentration is via two axis-energy loss and depth scale.....	39
Figure 4-1: A) NISS spectra of TiO ₂ before and after immersion in N719 dye. The inset shows the peak at ~4 related to Ru. B) The concentration depth profile of N719 dye on a pre-heated 600 °C TiO ₂ surface and a pre-heated 200 °C then sputtered 18·10 ¹⁴ ions/cm ² TiO ₂ surface are shown in. C) Molecular coverage of Dye N719 as a function of temperature and D) as a function of sputtering doses.	50
Figure 4-2: Concentration depth profile of dye N719 on A) pre-heated TiO ₂ surface and B) pre-heated-sputtered TiO ₂ surface.....	51
Figure 4-3: A) High-resolution scan of Ti 2p spectrum showing Ti ⁴⁺ and the defect Ti ³⁺ at a sputtering dose of (18·10 ¹⁴ ions/cm ²). B) Defect concentrations are represented by the ratio of Ti ³⁺ to Ti peak as a function of sputtering doses (Red data represent 200 °C heated sample without sputtering). C) High-resolution scan of C1s and Ru 3d. C-C at 285 eV, C-O at 286.7 eV and COO at 289.3 eV and 281.7 eV correspond to Ru 3d _{5/2} (sample 200 °C Heating).....	54
Figure 4-4: High-resolution scan of N1s spectra heated-sputtered (6·10 ¹⁴) TiO ₂ . The increase of NTBA related to pre-sputtered TiO ₂ with low doses, B) High-resolution scan of N1s spectra pre-heated TiO ₂ at	

400 °C. C) High-resolution S2p spectra of Heated (600 °C) TiO₂ and D) High-resolution S2p spectra of Heated-sputtered ($6 \cdot 10^{14}$ ions/cm²) TiO₂ fitted with two spin S contributions. 55

Figure 4-5: A) Ratio Intensities of Ru to Ti as a function of heating temperature, B) as a function of sputtering doses. (Red data represent 200 °C heated sample without sputtering)..... 56

Figure 4-6: A) Ratio of XPS intensities between N_{pyd} / N_{NCS} , as a function of heating temperature. B) As a function of pre-heating- sputtering doses. (Red data represent 200 °C heated sample without sputtering) 57

Figure 4-7 Ratio intensity of S-A/Ru and S-B/Ru with different sputtering doses..... 58

Figure 4-8: UP spectra A) pre-heated TiO₂ surface as a function of heating temperatures (B) pre-heated-sputtered TiO₂ surface as a function of doses. The inset shows UP spectra of the emission of Ti³⁺ on sputtered TiO₂ surface with different doses. 59

Figure 4-9: UP spectra after dye adsorption for (A) pre-heated (B) pre-heated- sputtered TiO₂ surface and. The inset shows UP spectra showing the emission in the valance band region after dye adsorption 60

Figure 4-10: The work function (± 0.1 eV) of A) pre-heated and B) pre-heated-sputtered TiO₂ before and after dye adsorption..... 60

Figure 4-11: MIE spectra after dye adsorption for (A) pre-heated (B) pre-heated- sputtered TiO₂ surface and. The inset shows MIE spectra showing the emission in the valance band region after dye adsorption. 61

Figure 4-12: (A), (C) The decomposed MIES reference spectra using SVD and the comparison with the dyed and undyed TiO₂. (B) and (D) are the weighting factors of the individual reference spectra for fitting MIES spectra of pre-heated and pre-heated-sputtered dyed on TiO₂ surface. Where alfa represents the dye and beta represents pristine TiO₂ surface..... 62

Figure 4-13: Gaussian peak fitting for MIES reference spectra-2 in A) pre-heated, B) pre-heated-sputtered TiO₂ samples. The calculated DOS using DFT calculations are shown as vertical lines. 63

Figure 5-1: J-V characteristics for DSSCs fabricated with different concentration of DPA using two different dyes: N719 (A) and Z907 (B). 71

Figure 5-2: Efficiency, Jsc, Voc and FF for DSSCs based on different concentration of DPA using two different dyes:N719(A) and Z907(B). (The dashed line is used for guiding eyes)..... 72

Figure 5-3: NICISS Concentration depth profile of Ru with varying concentrations of DPA using N719 (A) and Z907 (B) as sensitizer..... 74

Figure 5-4: Molecular coverage of Ru with different concentration of DPA using N719 (A) and Z907 (B) as sensitizer. (The dashed line is used for guiding eyes)	74
Figure 5-5: short-circuit current, efficiency, open-circuit voltage and fill factor with the coverage of the dye N719 (left) and Z907 (right).	75
Figure 5-6: (A) Carbon 1s, (B) Oxygen 1s, (C) Nitrogen 1s, (D) Sulfur 2p , (E) Titanium 2p and (F) phosphors 2p spectra.	76
Figure 5-7: intensity ratio of Ru/Ti and P/Ti with different concentration of DPA using N719 (A) and Z907 (B) as sensitizer. (The dashed line is used for guiding eyes).	79
Figure 5-8: Intensity ratio of N_{Total}/Ru versus the molar ratio of DPA in the solution using N719 (A) and Z907 (B) as sensitizer. (The dashed line is used for guiding the eye).	80
Figure 5-9: The intensity ratio between N_{pyd} and NNCS with different concentration of DPA using N719 (A) and Z907 (B) as sensitizer. (The dashed line is used for guiding eyes).	80
Figure 5-10: Intensity ratio of the total S and S components with Ru versus the molar ratio of DPA in the solution using N719 (A) and Z907 (B) as sensitizer. (The dashed line is used for guiding eyes).	81
Figure 5-11: UP spectra comparison with different concentration of DPA using N719 (A) and Z907 (B) as sensitizer. (Inset shows the magnified region of the HOMO level).	82
Figure 5-12: SVD reference spectra A, reference spectra B compared with pristine N719, and their respective weighting factors for samples sensitized with N719.	84
Figure 5-13: SVD reference spectra A compared with pristine Z907, reference spectra B compared with pristine DPA and their respective weighting factors (right) for samples sensitized with Z907.	84
Figure 6-1: J-V measurements of DSSCs based on different concentration of CDCA using two different dyes: N719(A) and Z907(B).	94
Figure 6-2: NCISS Concentration depth profile of Ru with varying concentrations of CDCA using N719 (A) and Z907 (B) as sensitizer. The concentration is plotted via two axis, the energy loss represent the measurement and the depth scale which is approximation due to the shape of porous titania.	96
Figure 6-3: Molecular coverage of Ru with different concentration of DPA using N719 (A) and Z907(B) as sensitizer.	96
Figure 6-4: Short-circuit current and efficiency (left y-axis), open-circuit-voltage and fill factor (right y-axis) with the coverage of the dye N719(A) and Z907(B). The x-axis are different for better illustration of the data.	97

Figure 6-5: High resolution XP spectra;(A) Carbon 1s, (B) Titanium 2p, (C) Oxygen 1s, (D) Nitrogen 1s in N719 dye, (E) Nitrogen 1s in Z907 dye, and (F) Sulfur 2p.	98
Figure 6-6: intensity ratio of Ru/Ti with different concentration of CDCA using N719 (A) and Z907 (B) as sensitizer.	100
Figure 6-7: The intensity ratio between N_{pyd} and N_{NCS} with different concentration of CDCA using N719 (A) and Z907 (B) as sensitizer.	101
Figure 6-8: Intensity of S1/Ru and S2/Ru with different concentration of CDCA using N719 (left) and Z907 (B) as sensitizer.	102
Figure 6-9: UP spectra of samples sensitized using N719 (A) and Z907 (B) with different concentration of CDCA showing the valence band level.	103
Figure 6-10: MIE spectra of samples sensitized using N719 (A) and Z907 (B) with different concentration of CDCA.	104
Figure 7-1: Photovoltaic parameters of DSSCs sensitized with N719 and N719/DPA in three different conditions during the aging test.	114
Figure 7-2: Series and Shunt resistance of DSSCs sensitized with N719 and N719/DPA in three different conditions during the aging test.	116
Figure 7-3: Concentration depth profile of N719 (left) and N719/DPA (right) aged sample in three different conditions. (With respect to iodine depth scale).	118
Figure 7-4: Molecular coverage of N719 (A) and N719/DPA (B) aged sample in three different conditions.	119
Figure 7-5: A) High resolution scan of Titania and Ti intensity in three different conditions in B) N719 and C) N719/DPA samples.	123
Figure 7-6: High-resolution scan of A) Oxygen and B) Carbon.	124
Figure 7-7: Ru/Ti ratio intensity of N719 (A) and N719/DPA (B) aged samples in three different conditions.	125
Figure 7-8: A) High resolution scan of Nitrogen in A) Dye, B) 4TBP, C) BMII and D) electrolyte.	126
Figure 7-9: High resolution scan of S, S_{Total} intensity of N719 (B) and N719/DPA (C) aged samples in three different conditions.	127

Figure 7-10: A) High resolution scan of I, and the I_{Total} intensity of N719 (B) and N719/DPA (C) aged samples in three different conditions.	128
Figure 7-11: P intensity of N719/DPA aged samples in three different conditions.....	129
Figure 7-12: Intensity ratio of S_1/Ru representing (NCS) and S_2/Ru representing (oxidized sulfur) of N719 (left) and N719/DPA (right) aged samples in three different conditions.	133
Figure 7-13: Intensity ratio of I_1/I_{Total} representing (I_{3-}) and I_2/I_{Total} representing (I_{-}) of N719 (left) and N719/DPA (right) aged samples in three different conditions.....	134
Figure 7-14: MIES spectra of aged samples (showin the HOMO level).	136
Figure 7-15: MIE spectra of reference samples N719 and electrolyte.....	137
Figure 7-16: N719 and N719/DPA disassembled aged cell in the heat-set	141
Figure 7-17: J_{sc} and V_{oc} performance with XPS intensity ratio of $N1/\text{Ru}$, I_2/I_{Total} , and D) S_2/Ru of aged samples in the light-set.....	143
Figure 7-18: J_{sc} and V_{oc} performance with XPS intensity ratio of $N1/\text{Ru}$, I_2/I_{Total} , and D) S_2/Ru of aged samples in the heat-set.	144
Figure 7-19: J_{sc} and V_{oc} performance with XPS intensity ratio of A) I_1/I_{Total} , B) $N1/\text{Ru}$, C) N_2/Ru and D) S_2/Ru of aged samples in the dark-set.....	145
Figure 8-1: Modified DSSC.....	155

List of Tables

<i>Table 4.1: Peak positions (eV) with uncertainty of ± 0.2 and the relative peak intensities ± 0.3 for the ascending temperature pre-treated TiO₂ samples.</i>	52
<i>Table 4.2: Peak positions (eV) with uncertainty of ± 0.2 and the relative peak intensities ± 0.4 for the Ar+ sputtered at different doses pre-treated TiO₂ samples.</i>	53
<i>Table 5.1: The influence of various concentrations of DPA using the dye N719 on the cell performance. The N719: DPA ratio is shown in the first column and the respective DPA molar ratio in the second column.</i>	71
<i>Table 5.2: The influence of various concentrations of DPA using the dye N719 on the cell performance. The Z907: DPA ratio is shown in the first column and the respective DPA molar ratio in the second column.</i>	72
<i>Table 5.3: Peak positions (eV) with uncertainty of ± 0.2 and the relative peak intensities ± 0.3 for N719 based samples.</i>	77
<i>Table 5.4: Peak positions (eV) with uncertainty of ± 0.2 and the relative peak intensities ± 0.3 for Z907 based samples.</i>	78
<i>Table 5.5: Work Function ± 0.1 eV.....</i>	83
<i>Table 6.1: The influence of various concentrations of CDCA on the performance of the N719 cells.</i>	93
<i>Table 6.2: The influence of various concentrations of CDCA on the performance of the Z907 cells.</i>	93
<i>Table 6.3: Peak positions (eV) with uncertainty of ± 0.2. Small peaks have relative intensities errors of ± 0.4 for (Ru, N3, S1, and S2) and an uncertainty of ± 0.3 for the other components in N719 based samples.</i>	99
<i>Table 6.4: Peak positions (eV) with uncertainty of ± 0.2. Small peaks have relative intensities errors of ± 0.4 for (Ru, N3, S1, and S2) and an uncertainty of ± 0.3 for the other components in Z907 based samples.</i>	99
<i>Table 6.5: Work Function ± 0.1 (eV).....</i>	103
<i>Table 7.1: Photovoltaic parameters of N719 DSSCs during the three conditions of aging test.....</i>	113
<i>Table 7. 2: Photovoltaic parameters of N719/DPA DSSCs during the three conditions of aging test.</i>	113

Table 7.3: Peak positions (eV) ± 0.2 and the relative intensities with errors of ± 0.4 for (Ru, N3, S1, S2, I1 and I2) and ± 0.3 for the other components in N719 samples in the light-set. Remaining percentage is F and Sn. 120

Table 7.4: Peak positions (eV) ± 0.2 and the relative intensities with errors of ± 0.4 for (Ru, N3, S1, S2, I1 and I2) and ± 0.3 for the other components in N719/DPA samples in the light-set. Remaining percentage is F and Sn. 120

Table 7.5: Peak positions (eV) ± 0.2 and the relative intensities with errors of ± 0.4 for (Ru, N3, S1, S2, I1 and I2) and ± 0.3 for the other components in N719 samples in the heat-set. Remaining percentage is F and Sn. 121

Table 7.6: Peak positions (eV) ± 0.2 and the relative intensities with errors of ± 0.4 for (Ru, N3, S1, S2, I1 and I2) and ± 0.3 for the other components in N719/DPA samples in the heat-set. Remaining percentage is F and Sn. 121

Table 7.7: Peak positions (eV) ± 0.2 and the relative intensities with errors of ± 0.4 for (Ru, N3, S1, S2, I1 and I2) and ± 0.3 for the other components in N719 samples in the dark-set. Remaining percentage is F and Sn. 122

Table 7.8: Peak positions (eV) ± 0.2 and the relative intensities with errors of ± 0.4 for (Ru, N3, S1, S2, I1 and I2) and ± 0.3 for the other components in N719/DPA samples in the dark-set. Remaining percentage is F and Sn. 122

Table 7.9: N1s intensity ratio in N719 sample..... 130

Table 7.10: N1s intensity ratio in N719/DPA sample..... 131

Chapter One

1 Background

The 2019 world population statistics estimate that there are 7.7 billion individuals and projection estimates show an increase to ~9.8 billion by the year 2050 [1]. The world energy consumption in 2018 was estimated to be ~14,000 megatons (Mt) of oil, and with projected increases in population, energy demand is also expected to increase. Currently, the world depends majorly on fossil fuels as an energy resource. However, fossil fuels are limited and exhaustible. Projections show that world production and consumption of fossil fuels will significantly be reduced as resources diminish, and a shift to sustainable renewable energy sources is expected. Renewable energy sources include all sources of energy that are harnessed from natural processes such as; solar, water, wind and geothermal heat. The bulk (48 %) of renewable energy production is projected to be from solar energy by the year 2050, according to the U.S. Energy Information Administration [2]. Solar energy has several advantages to other energy sources as it is relatively limitless, has minimal pollution impact, and negligible health and environmental risks, and solar energy harnessing equipment require low maintenance [3]. However, it is not without disadvantages such as high initial costs for material and installation, the requirement for space, geographical limitation for installation, and the need for large battery banks to compensate for night time and cloudy days. Nevertheless, the rapid developments in increased efficiency of solar energy capturing technologies and the long-term environmental benefits make solar energy a cost-effective energy alternative on the long-term surpassing other renewable sources of energy.

Solar energy is an ideal energy source and can be used all over the world, as it is readily available globally for presumably the entirety of human existence. The sun supplies the earth approximately 3×10^{24} joule/year of energy which is 10^4 times more than world's energy consumption, and collecting just 0.1 % of that will provide the earth with its energy demands. This theoretical potential of solar energy striking the earth's surface in one and a half hours is 480 exajoules (EJ) which exceeds worldwide energy consumption in the year 2001 from all energy sources combined 430 EJ [4]. Currently, there are primarily three technologies that have been developed to capture solar energy for multiple purposes. These technologies are; photovoltaics (PV) that captures and stores sunlight energy to convert it to electricity, concentrating solar power (CSP) that captures

heat from the sun (thermal energy) to drive large electric turbines, and solar heating and cooling systems that collect solar thermal energy to heat water and air or conditioning. Photovoltaics is currently one of the few renewable, low-carbon energy resources that could be scaled up to meet worldwide electricity demand and achieve energy sustainability [5].

1.1 Photovoltaics

1.1.1 Historical timeline

Photovoltaic is defined as utilizing the generation of a voltage when radiant energy falls on the boundary between different substances (photo = light, voltaic = electrical potential). The *-voltaic* part of *photovoltaic* comes from the name of Italian physicist Alessandro Volta, the inventor of the electric battery in 1799. The phenomenon of light or radiant energy conversion to electricity was later described in 1839 by French scientist Edmond Becquerel who coined the term “Photovoltaic effect”. Thirty-four years later, the English electrical engineer Willoughby Smith discovered that selenium has the property of becoming electrically conductive when it absorbs light in 1873 [6]. In 1876, Richard Evans Day and his student William Grylls Adams elaborated that selenium could produce electricity from light without heating or requirement of moving parts and thus was easy to maintain. In 1883, American inventor Charles Fritts invented the first selenium cell using gold-coated selenium surface that had a 1-2 % conversion efficiency, whereas in 1888 Russian scientist Aleksandr Stoletov was credited with the building and full description of the photovoltaic effect of the first solar cell. The process of photovoltaic effect was still poorly understood until 1905 when German-born theoretical physicist Albert Einstein explained the photoelectric process, accomplishment for which he was awarded the Nobel Prize in Physics in 1921. Later, in the 1940s a physicist at Bell Laboratories in the USA named Russell Shoemaker Ohl discovered that silicon is more efficient than selenium by accidentally using cracked silicon that had positively (p) charged impurities on one side and negatively (n) charged silicon on the other (p-n junction). When he allowed light to the silicon, he noted that a stronger electrical current was achieved when connected to a circuit than selenium. Thirteen years later (1956), Bell laboratories produced the first practical silicon solar cell of 6 % efficiency [7]. Since then, the conventional photovoltaic silicon-based solar cells labelled the first generation solar cells; have populated the market during the last 60 years and manufacturers have enhanced their conversion

efficiency to ~ 25-29 % [8]. Today, while silicon solar cells are still popular, they have some manufacturing and financial limitations. For example, the need for highly pure silicon with no defects, which imposes high manufacturing costs. In addition, the manufacturing of silicon solar cells requires a vacuum to maintain purity. Moreover, higher conversion efficiencies are required if solar cells are to be used to supply and maintain energy demands of industrial and large scale. Therefore, new alternatives for silicon cells are pursued that are cheaper to produce and are made of accessible and affordable materials.

1.1.2 The Photovoltaic system

The basic principle and design of a photovoltaic or a solar cell system involve two absorber layers of opposing charges (p and n) creating a p-n junction in between them. The two absorber layers are sandwiched between two electrodes to allow harnessing the electrical current flow. Absorber layers are made from materials that are efficient in absorbing radiation at visible light wavelengths; such materials belong to a class of substances known as semiconductors. Examples of semiconductor materials used include crystalline silicon, gallium arsenide (GaAs), indium phosphide (InP), and copper indium selenide (CuInGaSe) [9]. As sunlight photons are absorbed in the p-n layer, energy from the photons is transferred to an electron within the n layer, causing it to jump to a higher energy state. Once the excitation energy of induced photons is sufficient for the electron to overcome the band gap, thus such electrons are capable of achieving the conduction band minimum. These excited electrons create a hole (positive charge) as they jump to the conduction band. A proportion of the excited electrons and holes move towards the positive electrode at the p-n junction due to the electron mean free path. Because of the effect of built-in electric field at the p-n junction, such electrons can cross the p-n junction, while holes are separated. Where at the p-n junction the electrons in the n-type diffuse the junction and combined with the holes in the p-type. As electrons flow through the electric load, the process produces an electrical current.

1.1.3 Photovoltaic generation

The photovoltaic cell is classified into three generations based on the material used in each generation. The first-generation solar cell systems are based on a single crystal or multi-crystalline silicon wafers. However, to avoid recombination of electrons and holes in the solar cell, a highly

pure semiconductor with no defect must be used, which imposes high manufacturing and energy costs [10]. Second-generation solar cells are based on thin-film technology such as Cadmium Telluride (CdTe) and Copper Indium Gallium Selenide (CuInGaSe). These are more flexible, lighter materials and have reduced production costs as they can be manufactured at lower temperatures and have short fabrication processes. However, they have lower conversion efficiencies, and the materials needed are hard to find and contaminates the environment. Therefore, these types of solar cells do not offer an advantage to the first-generation solar cell system, and alternatives are still being pursued. The third-generation solar cells focus on finding highly efficient solar cells of low cost that employ different technologies and is not limited by the Shockley Queisser limit. Where the Shockley Queisser is calculated by examining the amount of the electrical energy that is extracted per incident photon. This generation employs a variety of different technologies such as quantum dot, organic polymer, dye-sensitized and perovskite solar cells [11, 12].

In the past three decades, dye-sensitized solar cells have attracted the attention of scientists because of their reasonable conversion efficiency, low production cost, and simple fabrication processes compared to silicon solar cells and can be made without limited resources or toxic materials. The dye-sensitized solar cell (DSSC) is the focus of this dissertation, and an elaborate literature review will be presented from hereafter in the next chapter

1.2 References

1. *World Population Prospects 2019*; United Nations: Department of Economics and Social Affairs Population Division, 2019.
2. *Annual Energy Outlook 2019*; The U.S. Energy Information Administration 2019, p 1-83.
3. Tsao, J.; Lewis, N.; Crabtree, G., Solar Faqs. U.S. Department of Energy: Office of Basic Energy Science, 2006; pp 1-24.
4. Mahmud, M. A. P.; Huda, N.; Farjana, S. H.; Lang, C., Environmental Impacts of Solar-Photovoltaic and Solar-Thermal Systems with Life-Cycle Assessment. *Energies* **2018**, *11*, 2346.
5. Ballestrín, J.; Burgess, G.; Cumpston, J., Heat Flux and Temperature Measurement Technologies for Concentrating Solar Power (Csp). In *Concentrating Solar Power Technology*, Elsevier: 2012; pp 577-e4.
6. Petrova-Koch, V.; Hezel, R.; Goetzberger, A., High-Efficient Low-Cost Photovoltaics Recent Developments, Springer Series in Optical Sciences; Vol. 140.
7. Green, M. A., Silicon Photovoltaic Modules: A Brief History of the First 50 Years. *Progress in Photovoltaics* **2005**, *13*, 447-455.
8. Blakers, A.; Zin, N.; McIntosh, K. R.; Fong, K., High Efficiency Silicon Solar Cells. *Pv Asia Pacific Conference 2012* **2013**, *33*, 1-10.
9. Sundaram, S.; Benson, D.; Mallick, T. K., Potential Environmental Impacts from Solar Energy Technologies. In *Solar Photovoltaic Technology Production*, Sundaram, S.; Benson, D.; Mallick, T. K., Eds. Academic Press: 2016; pp 23-45.
10. Mann, S. A.; de Wild-Scholten, M. J.; Fthenakis, V. M.; van Sark, W. G. J. H. M.; Sinke, W. C., The Energy Payback Time of Advanced Crystalline Silicon Pv Modules in 2020: A Prospective Study. *Progress in Photovoltaics* **2014**, *22*, 1180-1194.
11. Sharma, S.; Jain, K. K.; Sharma, A., Solar Cells: In Research and Applications—a Review. *Materials Sciences and Applications* **2015**, *6*, 1145-1155.
12. Yun, S. N.; Qin, Y.; Uhl, A. R.; Vlachopoulos, N.; Yin, M.; Li, D. D.; Han, X. G.; Hagfeldt, A., New-Generation Integrated Devices Based on Dye-Sensitized and Perovskite Solar Cells. *Energy & Environmental Science* **2018**, *11*, 476-526.

Chapter Two

2 Dye Sensitized Solar Cell

The nano-crystalline dye-sensitized solar cell (DSSC) is one of the most promising solar cell technologies that employ a photo-electrochemical system in which a dye-coated semiconductor is formed between a photo-sensitized anode and an electrolyte solution. DSSC is also called the Grätzel cell named after Michael Grätzel, the Swiss chemist who developed the cell in 1991 with his co-workers recording efficiencies up to 7 % [1]. Since then, these cells have been attracting the attention of scientists because of their reasonable conversion efficiency, low production cost, and simple fabrication processes compared to silicon solar cells. Unlike traditional solar cells, the DSSCs have an attractive advantage as they can work effectively in low light conditions and shade which makes them suitable to be used for buildings and indoor applications [2, 3]. DSSCs are less susceptible to energy loss by heat generation where the efficiency is nearly temperature independent in a range of 25 °C - 65 °C while in the same range the efficiency of a silicon solar cell declines. Another advantage of DSSC is that the materials used are biocompatible and commonly available [4, 5].

2.1 The anatomy of DSSC

The structure of a typical DSSC consists of two transparent substrates coated with a thin conductive material such as fluorine or indium doped tin oxide. The working electrode (WE) is further coated with a thick layer (approximately 10 μm) of TiO₂ nanoparticles forming a mesoporous structure to provide a high surface area for sufficient dye adsorption thus improving light harvesting. After heating, the WE is immersed in a sensitized dye solution. The counter electrode (CE) is coated with a thin layer of catalytic material, usually platinum as the conductive substrate. Both electrodes are sealed by heat press using a thermal plastic Surlyn gasket sealant. The Surlyn gasket also acts as a spacer that provides a space between the two electrodes allowing electrolytes to fill this gap. Usually, the electrolyte solution contains iodide/triiodide (I^-/I_3^-) redox mediators that have direct contact with the dye and could penetrate through to the mesoporous TiO₂. Figure 2-1 shows a typical DSSC.

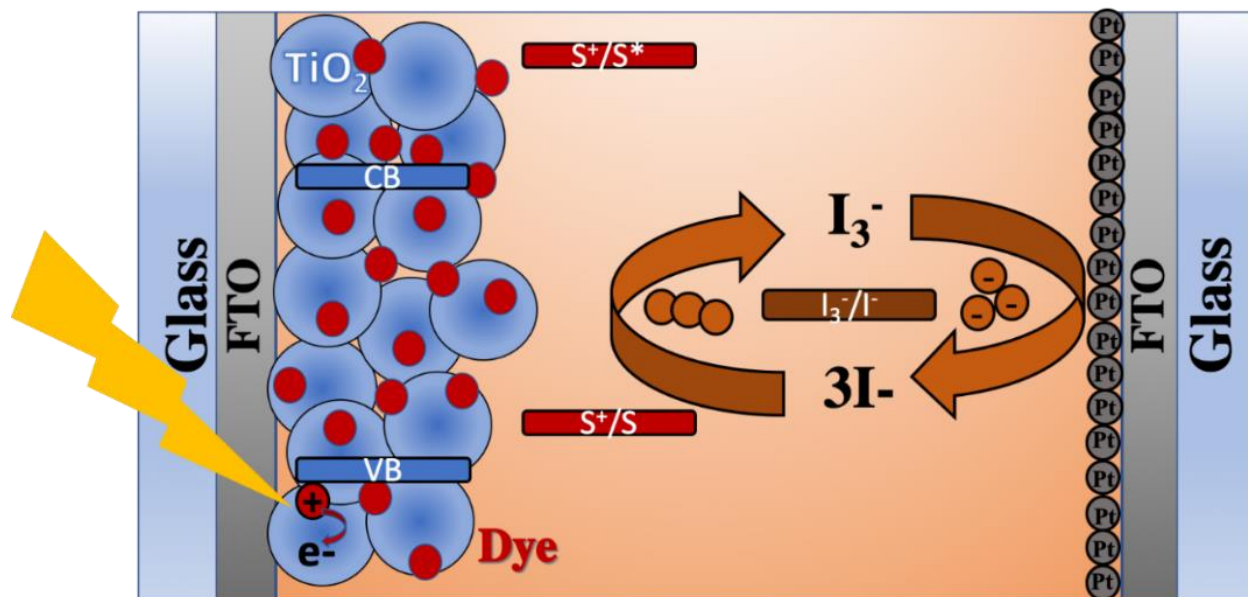


Figure 2-1: Schematic diagram of DSSC working principle

2.2 Operating Principle

2.2.1 Excitation

When the cell is irradiated by light, the dye will be promoted to its excited state (S^*) upon a photon ($h\nu$) absorption. The photoexcitation of the dye results in electrons jumping from the highest occupied molecular orbital (HOMO) to the lowest unoccupied molecular orbital (LUMO) of the dye molecule Figure 2-2 (route 1) followed by injection into the conduction band of the TiO_2 Figure 2-2 (route 2). The released electron will leave the dye in an oxidized state (S^+), changing from the ground state (S) to the excited state (S^*). The process as following.



2.2.2 Injection

The excited electron injected into the conduction band of the TiO_2 substrate passing through the external circuit to reach the CE so that the energy can be utilized in performing the electrical work Figure 2-2 (route 3). The injection generally occurs from the π^* -orbital of the anchoring group in the dye to the TiO_2 conduction band. Efficient electron injection is further enhanced by strong

electronic interactions that form when the dye binds to the TiO₂ through a carboxyl group and the energetic location of the TiO₂ conducting band. This process takes 10 femtoseconds (fs) to 100 picoseconds (ps) timescales to occur [6].

2.2.3 Dye regeneration

For the current generation to continue; the dye must be reduced back to its ground state (*S*). The oxidized dye is regenerated in the range of microsecond (μ s), by obtaining an electron from the redox-coupled in the electrolyte solution that fills the space between the WE and CE Figure 2-2 (route 4). When the electrons reach the CE from the external circuit, they will react with the electrolyte. The iodide/triiodide is the most commonly used electrolyte solution that gives the best cell efficiencies when combined with TiO₂. The oxidized dye is reduced back to its original state by electron transfer from iodide ions (I^-) forming tri-iodide ions (I_3^-), the process shows as following:



2.2.4 Iodine reduction

Iodide ions are regenerated in the electrolyte solution by reduction of triiodide at the CE Figure 2-2 (route 5). The electron transfer from I^- ions to the oxidized dye and regeneration of I^- ions from I_3^- ions at the CE link the two transport processes, and the circuit is completed through the external load as the following [7].



2.2.5 Charge Recombination

In addition, there are some possibilities for recombination reactions that compete with the forward reaction that impede DSSC performance. Recombination reactions occurs due to nearness between the electrons and holes, and the lack of potential barrier at the TiO₂/dye/electrolyte interface. After an electron is injected, they tend to recombine with either the oxidized dye Figure 2-2 (route 6) or with the triiodide in the electrolyte Figure 2-2 (route 7). Electron recombination is considered to be one of the major reasons in lowering cell efficiency.

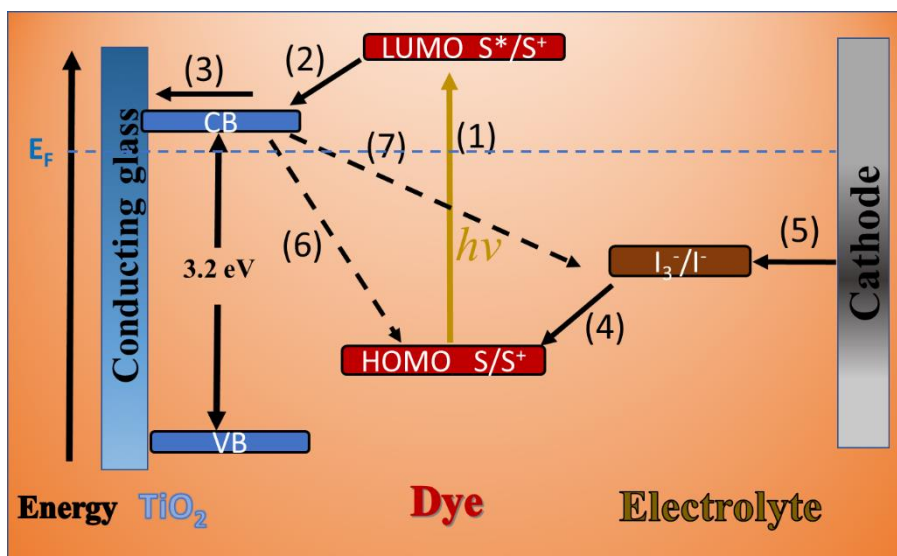


Figure 2-2: The electron transfer processes in DSSCs. Electron excited (1) then injected into the conduction band of TiO_2 (2), then diffuse through the TiO_2/TCO (3). The redox couple regenerate the oxidized dye (4). Electrolyte reduced at the counter electrode (5). Electron loss by the recombination with the dye cation (6) or with the redox couple (7).

2.3 Basic materials of DSSC

2.3.1 Substrate

The best results for DSSC were obtained using transparent glass substrates with high optical transparency, low cost, and tolerance of temperatures as high as $450\text{ }^\circ\text{C}$ - $500\text{ }^\circ\text{C}$ prevents impurities such as water and oxygen from entering the cell. However, it has some disadvantages like fragility, rigidity, and heavyweight. Alternative substrate materials are plastic foils that overcome most of the glass disadvantages. They are lightweight and flexible, with few disadvantages including low-temperature tolerance with maximum tolerance at $150\text{ }^\circ\text{C}$ - $160\text{ }^\circ\text{C}$

The substrate is coated with Transparent conducting oxide (TCO) on one side, allowing low electric resistance. Fluorine doped tin oxide (FTO) and Indium doped tin oxides (ITO) are the most common TCO used in coating the substrates of DSSC [8, 9].

A study done by Siam et al. comparing the influence of FTO and ITO on the performance of DSSC shows that the sheet resistance of FTO remain constant, while the ITO resistance can go up from $18\ \Omega/\text{sq}$ to $52\ \Omega/\text{sq}$ after thermal annealing at $450\text{ }^\circ\text{C}$ for 2 h [10]. Since TiO_2 requires high

annealing temperature, FTO is more suitable than ITO [11]. Thus, FTO is mostly recommended in DSSC as a substrate because of its low resistance and temperature-stable sheet resistance.

2.3.1.1 Mesoporous Semiconductor

The photoanode (working electrode) consists of a mesoporous semiconductor structure having a high surface area enabling more dye adsorption and significantly increase the light absorption [12]. A wide bandgap and its conduction band are located slightly below the LUMO level of the dye for efficient electron injection. Many studies were conducted in this field testing electrode materials such as titanium dioxide (TiO_2), Zinc oxide (ZnO) [13], Tin oxide (SnO_2) [14], Strontium titanate (SrTiO_3) [15], and Tungsten trioxide (WO_3) [16]. The non-toxicity and low cost made TiO_2 the common semiconductor used in DSSC. Thus, TiO_2 was used in this thesis to make our cells.

2.3.1.2 Titanium dioxide (TiO_2)

TiO_2 is a semiconductor material that has a good chemical stability under visible irradiation in solution. TiO_2 is widely used because of its flexible manufacturing process; it is cheap, non-toxic, and is used in the production of pigments, paints, cosmetics, and food products. Furthermore, it is of great industrial interest due to its potential applications as sensors, photocatalysts, and optical coatings due to the high refractive index and good optical transmission. TiO_2 exists in three crystalline forms, the anatase, rutile, and brookite. The anatase is more favorable than rutile for DSSC manufacture because of the high-band gap of 3.2 eV with more surface area and more chemically stable compared to rutile with a bandgap of 3 eV [17, 18].

The studies around the semiconductor were often focused on structure changes on the semiconductor or using insulating layers or by surface treatments. Structure changes, to control the semiconductor configuration, by fabricating different morphologies of the semiconductors such as, nanorods [19], nanowires [20], nanosheets [21], nanotubes [22], and nanoparticles [23]. Another approach is by depositing an insulating layer like ZnO or Al_2O_3 on the semiconductor [24], working as an energy barrier slowing down the charge recombination. TiCl_4 treatment of the TiO_2 substrate is known to improve the short circuit current in DSSC by increasing the surface roughness and forming about 1 nm shell of ultrapure TiO_2 [25], in addition, increasing the dye adsorption and the electron lifetime. A recent study conducted by our group investigating the effect of TiCl_4 treatment on DSSC performance. The results revealed that upon TiCl_4 treatments, an

upward shift of TiO₂ conduction band, measured using Inverse photoemission spectroscopy (IPES) and UV-photoelectron spectroscopy (UPS). Furthermore, an increase in the dye coverage observed by using neutral impact collision ion scattering spectroscopy (NICISS) [26].

To increase the surface area, acid treatments of TiO₂ substrate, by HNO₃ [27], and HCl [28] increased the dye adsorption and enhanced the DSSC performance. However, some studies reported that some type of acid treatment decreases cell efficiency such as HNO₃, H₃PO₄ and H₂SO₄ [28]. The discrepancies of these findings investigated by Park et al. [29]. Acid treatment increases the surface area and porosity of TiO₂. In addition, increase Ti³⁺ (oxygen vacancy) in TiO₂ led to an increase in the amount of dye adsorbed on the TiO₂ substrate by the HNO₃ treatment, improving the overall conversion efficiency of DSSC [29].

Introducing defects (Ti³⁺) in the form of oxygen vacancies is another approach to control the electronic structure of the TiO₂ surface (which is the focus of chapter 4).

2.3.1.3 Defects on metal oxide

The modification of TiO₂ surface plays a significant role in cell performance. Several studies were involved in this field to enhance the surface activity, charge transport, and the electronic structure of TiO₂. Introducing defects such as Ti³⁺ (oxygen vacancies) sites play an essential role in improving the charge transfer and conductivity, enhancing the dispersion and the strong bonding with metals, in addition, influencing the surface catalytic activity. A study by Krishnan et al. where they use Ar⁺ sputtering to introduce Ti³⁺ defect on atomic layer deposition (ALD) TiO₂ substrate to deposit and reduce the agglomeration of the gold cluster [30]. Furthermore, introducing defects on metal oxides enhance the catalytic performance of Li-ion batteries [31]. Another study done by Guillemot et al. They investigated the ability of defects produced on titanium to interact with surrounding proteins and cells. Their findings indicated that the treated titanium has a great influence on the interaction with the surrounding tissues [32].

Many studies attempted to enhance DSSC performance. Some of these studies focused on creating defects in the counter electrode, where improvement in DSSC performance obtained by doping urea on WO₃ creating oxygen vacancies where, WO₃ used as a counter electrode in DSSC,

introducing oxygen vacancies into WO_3 improved its catalytic performance to facilitate electron transfer from the counter electrode to the electrolyte [16].

Other studies were performed by introducing defect sites on the semiconductor layer in the form of oxygen vacancies that create active sites for interacting with dye ligands, namely oxygen atoms of carboxylic acid side chains in the dye. Such reports have used a wide variety of approaches to create oxygen vacancies or Ti^{3+} defects. Heating under vacuum by Yu et al. where they create oxygen vacancies during the fabrication of using a flat thin film of TiO_2 with the thickness of 300 nm was prepared at 500 °C. Defects were created by post-annealing at various temperatures 400 °C, 450 °C, and 500 °C in an ultra-high vacuum for 10 minutes. The surface morphology was characterized by atomic force microscopy with a surface roughness of 0.72 nm allowing only monolayer dye attachment to the surface and avoiding dye aggregation. Their results showed a linear decrease in DSSC performance as the concentration of Ti^{3+} sites increased. They concluded that the oxygen vacancy site served as electron recombination centres [33]. However, in another study, introducing Ti^{3+} defect sites on the TiO_2 microsphere enhances the transient photocurrent density from 1.78 $\mu\text{A cm}^{-2}$ to 53.78 $\mu\text{A cm}^{-2}$ [34].

Ellis-Gibbins et al. did a study, determined the adsorption isotherm for Ru-N719 on two different TiO_2 surfaces, flat surface and, mesoporous surface. Their study shows the maximum dye coverage was $(2.2 \pm 0.3) \times 10^{-10}$ mol/ cm^2 on the porous TiO_2 substrate, and $(1.2 \pm 0.1) \times 10^{-10}$ mol/ cm^2 on the flat TiO_2 for the same calculated area. They explained the difference in coverage by the existence of defect sites on the porous substrate, which are preferred sites for dye adsorption [35].

Many studies conducted showed that introducing defect effects on changing the surface properties. Furthermore, different methods used to introduce defects such as ultraviolet (UV) radiation, plasma [36], high energy particle bombardment, and thermal annealing to high temperatures [37]. In chapter 4 controlled amount of Ti^{3+} created on TiO_2 substrate by Ar^+ bombarding in an Ultra-high vacuum (UHV) chamber. The addition of defects on the sample and how it will influence the adsorption configuration of the dye molecule are investigated using a combination of neutral impact collision ion scattering spectroscopy (NICISS), X-ray photoelectron spectroscopy (XPS), UPS, and metastable induced electron spectroscopy (MIES).

2.3.2 Sensitizer

The sensitized dye is one of the essential components in DSSC, converting the absorbed incident photon to an electron. This electron is then transferred into the conduction band of the semiconductor. The level of dye adsorption to the semiconductor surface affects the performance of a DSSC, which usually takes place via special anchoring groups attached to the dye molecule. The exact nature of the binding involves a mixture of coordination modes. Chemisorption is preferred over physisorption. The physisorption is a weak bond where the adsorbent is attached to the surface by van der Waals forces, while the chemisorption is stronger [38]. The carboxylate and phosphonate group in the dye is attached by chemisorption to the oxide substrate through chemical bonding to the atoms in the oxide surface by covalent or ionic bonds sharing and exchange of electrons. The carboxylic acid (-COOH) considered as the standard anchoring group in the dye. Achieving good performance in DSSC efficiency, the sensitizer must have several properties [39]. First, the absorption spectrum of the sensitizer should cover as much as possible the whole visible region (400 nm - 700 nm) and even part of the near-infrared region of light to maximize the light absorption. Second, the sensitizer should be strongly adsorbed on the semiconductor surface, enabling high electron injection and more stabilized cells over long periods. Third, the sensitizer should have suitable energy levels to ensure electron injection and dye regeneration where the LUMO or the excited state should be higher in energy than the conduction band of the semiconductor to minimize the losses during electron transfer reactions and for efficient electron transfer between the dye and the semiconductor. In order to regenerate the oxidized dye, the oxidized level of the dye should be more positive than the redox potential in the electrolyte. In addition, the sensitizer must be photostable for long-term use to stand about 20 years of exposure to natural light before it degraded [40]. Moreover, the dye aggregation on the TiO₂ surface is an undesirable phenomenon affecting the electron injection, where the addition of the co-adsorbents can avoid this aggregation. (Further details will be discussed in the co-adsorbent section)

Different photosensitizers, including metal complexes such as ruthenium (Ru) complex chlorophyll derivatives, porphyrins, phthalocyanines, platinum complexes, fluorescent dyes, and polymeric films have all been designed and tested for their sensitization properties. The highest efficiency was recorded of 13 % using the porphyrin dye in 2014 [41], a year later a new record efficiency of 14.3 % was achieved by a cell using an organic dye with an electron donor- π -bridge-

electron acceptor (D- π -A) structure [42]. Ru-dyes applied mostly in the fabrication of DSSC, and this is due to their photophysical and electrochemical properties that include the broad absorption spectrum, suitable charge separation at the metal to side chains where the excited state LUMO level at the bipyridyl (Ru-bpy), and the ground state HOMO level at the thiocyanide (SCN-Ru) side chain, absorption group in the visible region, in addition, the long lifetime in the excited state and the stability. The reduction of the oxidized dye through the thiocyanate ligand, where these ligands play an essential role in reduction the oxidized dye, pointing in the direction of the electrolyte [43].

The most widely used Ru sensitizers are N3, the black dye N769, N719 and Z907, the common dyes N719 and Z907 used in this thesis.

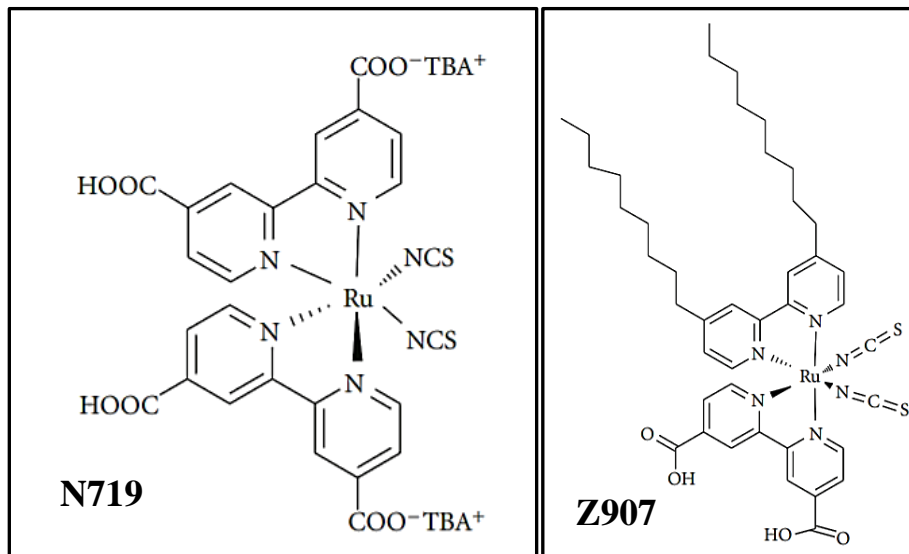


Figure 2-3: The molecular structure of N719 and Z907 dyes [44].

2.3.2.1 N719

Figure 2-3 shows the structure of the Ru-based dye N719, made of two bipyridyl groups with carboxylic acid groups and tetra-butyl-ammonium (TBA⁺) group attached on each of them and two thiocyanate ligands all coordinated to Ru ion in the central. Containing the two TBA⁺ groups made the N719 more successful dye improving the performance of DSSC, where the carbocyclic acid group bind strongly with the TiO₂, thus allowing fast electron injection to the conduction band of TiO₂ [45]. Furthermore, the position of the dye LUMO is higher in energy than the position of

the conduction band of TiO₂, allowing efficient electron injection. In addition, the energy of the HOMO level of N719 is more positive than the redox potential of the electrolyte for efficient dye regeneration. With the above properties of N719 make it a practical candidate for DSSC, it has shown reproducibly efficiencies exceeding 10 %.

2.3.2.2 Z907

Figure 2-3 shows the structure of the Ru-based dye Z907 containing long alkyl chain attached to each of the bipyridyl groups. Increasing the hydrophobicity of the dye and the stability of the cell if the water is used in the electrolyte or access into the cell over time [46]. This structure led to the extraordinary stability of the cell passing a 1000 h at 80 °C, with a reasonable conversion efficiency of 7.3 % [47].

2.3.2.3 Co-adsorbent

In the process of fabricating DSSCs, the coated substrate with semiconductor immersed in the dye solution in order the dye molecules to be adsorbed on the mesoporous structure of the semiconductor. In this step, the dye molecules may form multilayers or pack very tightly due to the hydrogen bonding. Therefore dye molecules will agglomerate causes π -stacking aggregation of the dye, which in turn hinders the electronic propagation Dye aggregation is an unwanted process for long-term stability device, where the aggregation causes a change of the dye adsorption mode. Furthermore, the amount of adsorbed dye and their molecular spatial structure on the substrate have a great influence on the cell performance, where the energy level of the high dye loading can be shifted resulting in different electronic properties of the excited and ground state of the dye [48-50]. In addition, the dark current in DSSC resulted from electrons injected into the conduction band of TiO₂ tend to recombine with the oxidized dye or the oxidized redox couple from the electrolyte causes a decrease in the cell performance. Therefore, to alleviate these drawbacks, the employment of small molecules such as co-adsorbents used to be adsorbed simultaneously with the dye to decrease and prevent the dye aggregation without interacting with other species in the electrolyte [51, 52]. Co-adsorbent containing either carboxylic or phosphonic groups on one end and long hydrophobic alkyl groups on the other end. The co-adsorbent attached on the TiO₂ surface by its carboxylic or phosphonic groups. While the alkyl group act as a buffer between TiO₂ and the electrolyte, preventing charge recombination [48, 53]. Adding co-adsorbent

simultaneously with the dye solution affords to prevent dye aggregation by occupying the uncovered sites on the TiO₂ surface and preventing the close approach of the dye molecules; also they are known to compete with the dye on TiO₂ surface and suppress the charge recombination by acting as physical layer [54, 55], and improving the cell efficiency by reducing the charge recombination [54, 56]. Understanding the influence of co-adsorbents on the binding configuration of dye molecules on the TiO₂ substrate is the aim of chapters 5 and 6.

To improve the cell performance, several types of co-adsorbents have been studied and adsorbed onto the TiO₂ as well as the dye. For example, Zakeerudin and co-workers reported in 2003 for the first time stabilized of the open circuit voltage and improvement in the cell efficiency, when the co-adsorbent decylphosphonic acid (DPA) used with the ruthenium-based dye Z907, achieving overall efficiency of 7.3 %, due to the long aliphatic chain in DPA preventing water from the interface [55]. In 2004, Wang and co-workers used the co-adsorbent 3-phe-nylprpoionic acid (PPA) in DSSC based on ionic liquid electrolyte, they observe 15 % decrease of the dye loading with an increase in the short-circuit current cussed by the co-grafting of PPA with the dye Z907 on TiO₂ surface. Where the co-grafting of PPA with Z907 increase the mobility of electron transport thus improving the efficiency [57]. Furthermore, Liu and co-workers fabricate DSSC using Z907 as sensitizer and employing [Co(bpy)3]^{3+/2-} as redox couple and compare the cell performance using two different phosphonic co-adsorbents DPA and octadecylphosphonic acid (OPA). The overall efficiency of 8.7 % achieved by using OPA as co-adsorbent. The improvement in efficiency attributed to a decrease in the electron recombination, where OPA was shown to reduce the π -stacking aggregation of the dye, which in turn hinders the electronic propagation [58]. Another study by Hou et al. found that using co-adsorbents based on acetyl acetone and its derivatives in DSSCs had the best photovoltaic performance. Their UV-Vis absorption results showed that the amount of dye loading was decreased after adsorbing co-absorbents. Further analysis of the dye loading using X-ray photoelectron spectroscopy to investigate the presence and the concentration of the dye revealed the atomic concentration of Ru is slightly lower on TiO₂ with adsorption of co-absorbents. They also investigated the effect of the co-adsorbent on the photovoltaic performance of the cell showing increases in efficiency from 7.73 % to 8.07 % with and without co-adsorbents [59]. Another study by Lee et al. studied the addition of deoxycholic acid (DCA) co-adsorbents on the performance Of DSSCs based on organic dyes. They found that DCA improves the photocurrent and photovoltage of DSSC [60]. Several kinds of phosphate-based

co-adsorbents were investigated by Shen et al. Their XPS data revealed a higher peak of phosphonate when increasing the proton number in the co-adsorbents, which is consistent with their abilities to bind with oxide, in turn reducing the dye loading on the TiO₂ surface. The photocurrent-voltage (I-V) characteristics of the cells revealed that co-adsorbents with fewer protons are more favourable and co-adsorbents with no protons improve the photovoltaic performance of the cell [61].

The employment of the co-adsorbent in the dye solution forms more complex molecular layers affecting in the interphase of dye /TiO₂, the steadiness of this interface has a crucial effect on the cell performance and is important for the long-term stability of DSSC. In chapters 5 and 6, DPA and CDCA Figure 2-4, were used as co-adsorbents to investigate their mechanisms in reducing the dye aggregation.

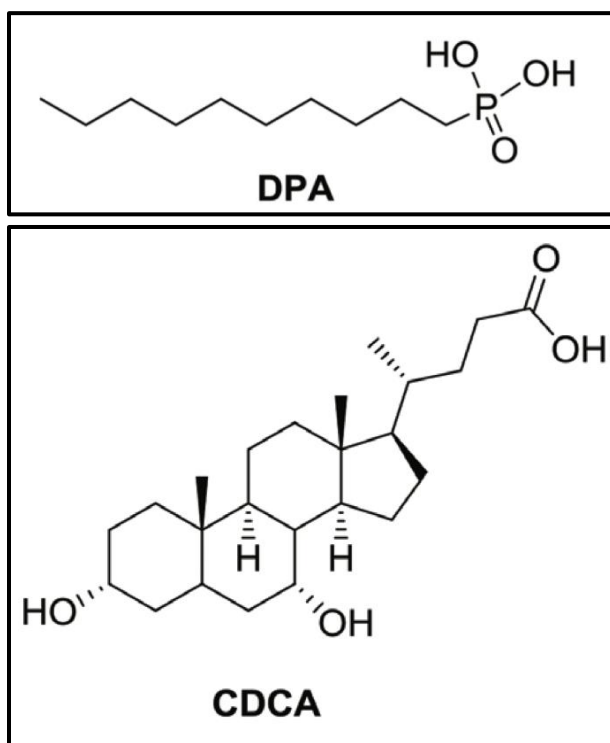


Figure 2-4: Molecular structure of DPA and CDCA[48]

2.3.3 Electrolyte

The Electrolyte is one of the most crucial components in DSSC. It works equivalent to hole conductor as an electron transferee and in regenerating the sensitized dye from the oxidized state.

It must meet some requirements to be used in DSSC. A good chemical and long-term thermal stability to prevent dye degradation. Good contact with the photo-electrode and counter electrode to ensure fast diffusion of charge carriers with low viscosity to minimize the transport problems and a suitable solvent for the additives without causing dissolution of the adsorbed dye [62]. Electrolytes are divided based on their state, liquid electrolytes, quasi-solid electrolytes and solid electrolytes. Liquid electrolytes have the advantage of its low viscosity, the ease in preparation and high conductivity. However, using liquid electrolytes causes some problems such as electrolytes leakage, volatilization of the solvent and corrosion of the counter electrode. The quasi-solid state is a state where the substance is between solid and liquid state, and the main problem with this state still having solvent which is unstable for long-time storage. These issues have been solved by developing different materials to replace the liquid and quasi-solid electrolytes with solid-state electrolytes. In the solid electrolytes are based on molecular or polymeric hole conductors where the liquid is replaced by solid-state hole transporting material. The major difference between the liquid-based DSS and solid-based DSS is that the charge transfer in liquid DSS occurs through ionic diffusion of the redox couple while in solid DSS charge transfer through hole-transporting. So far, the standard redox system I^-/I_3^- used in the Grätzel cell is the most commonly used in DSSCs. Showing effective and fast oxidized dye regenerating [62-64]. In this field, different strategies used either by improving or designing different electrolytes alternatives to the standard redox system I^-/I_3^- . Notably SCN^-/SCN_2 [41], Br_2/Br^- , ferrocene/ferrocenium and $Co(III)/Co(II)$ [65]

2.3.3.1 Additives

The stability of the electrolyte is a big concern for long-term stability DSSC. Liquid electrolyte is one of the main causes of low long-term stability, so in order to improve the DSSC, a suitable electrolyte composition is needed. Additives have been introduced to liquid electrolyte, where they play an essential role in improving the photovoltaic parameters of DSSC. These additives are interacting with the TiO_2 /electrolyte, affecting on the band edge movement of the TiO_2 surface [66]. There are two main types of additives used in the electrolyte. One is alkyl or guanidium cations, and they induce a positive shift to the conduction band of the TiO_2 away from the vacuum increasing the electron injection and enhancing the short circuit photocurrent (J_{sc}) [67, 68]. Another type is the heterocyclic nitrogen compound such as, 4-tert-butylpyridine (4TBP), which

expected to de-protonate the N719 dye, thus resulting in blue-shifted absorption spectrum. Where another explanation of the blue-shift was due to the negative shift in the conduction band energy of the TiO₂ [69, 70] This increasing of Voc was attributed to either the negative shift to the conduction band of TiO₂ or to the elimination of electron recombination in the TiO₂/electrolyte interface. The negative shift of TiO₂ conduction band edge could be assigned to 4TBP due to the surface adsorption [71]. The degradation of N719 dye was investigated by Hassing and coworkers using Raman and Fluorescent Emission to investigate the using of polarized resonance Raman Spectroscopy in DSSC. However, their results show that the Raman spectra of N719 and its 4TBP substituted products are almost identical, therefore difficult to observe N719 dye degradation by using the conventional Raman spectroscopy [72]. Nguyen and coworkers investigated the accelerated lifetime test by using a thermal test for 100 °C. They found that the addition of 4TBP to the electrolyte without Li⁺ ions enhance the N719 dye lifetime at high temperatures. When the 4TBP was removed from the electrolyte, the degradation rate of N719 was increased, and the electrolyte composition highly affected the degradation process of the Ru dye N719 [70].

2.3.4 Counter electrode

The reduction of the oxidized electrolyte is the main requirement of the counter electrode, where this reaction occurs at its interface. ITO and FTO glass coated with platinum are the most commonly used, offering a more stable electrode with more electron transfer [1, 73]. However, the high cost of platinum led to different alternative materials that have been investigated, such as, carbon nanostructure [74], metal sulfides [75], and nitrides. [76]

2.4 Cell stability

The performance of the cells has been monitored during the aging test. Several types of tests were used to evaluate the stability of DSSCs. The tests can be divided to indoor test, outdoor test and accelerated test, where the accelerated stability test is the most commonly used to evaluate the outdoor durability in controlled condition with different stress factors (temperature, humidity, light intensity and UV) within a short period of time.

Furthermore, there are several factors that effects on the cell stability, factors that may be external such as UV-light, temperature, light intensity, humidity, water and oxygen penetration into the

cell, and the major extrinsic issue is DSSCs sealing. An internal factor triggered by the chemical degradation of the cell's materials, namely the dye desorption from the TiO₂ substrate or dye degradation, corrosions of the counter electrode and the dye/electrolyte reaction. In addition, the choice of cell's components, cell's manufacturing and the synthesis methods all can play a role in influencing the stability of the cell.

2.4.1 Stability tests

In terms of the stability tests, several studies were conducted to study the stability of DSSCs. Grätzel and co-workers performed an accelerated test, reported a minor degradation of Ru-based DSSCs sensitized with the dyes K-19 [77] and Z907 [78] were tested endure 1000 h of aging at 1.5 AM illumination of visible light at 60 °C, and at 80 °C in the dark. In an outdoor condition, a stability test was studied on a large area module of DSSCs were designed by Dai et al. [79]. DSSCs sensitized with the dye N719, had a significant decrease in the cell performance was reported Sommeling et al. When they studied a cyclic test of thermal stress in dark 85 °C alternated by full sun illumination [80]. More stability tests can be found in literature [81-84].

From the previous stability studies, it appeared that exposing the cells to the temperature is one of the most affecting factors on cell performance. Despite the decrease in cell performance in silicon solar cell at a temperature in the range of 50 °C – 60 °C, DSSCs performance rises with that temperature [85-87]. An outdoor comparison study between a polycrystalline Si solar and DSSC sensitized with the dye N719 was conducted by Asgher et al. in Abu Dhabi. They found that the output power of DSSCs increased parabolically, while a linear decrease in the output power of Si- based cells as the temperature increased high up to 60 °C in the summer months. Furthermore, combined to the temperature the irradiance was also changing during their measurement, an exceptional performance was obtained from DSSCs than from Si cells when compared with the I-V curves obtained from each of them. A 20-30 % increase in the energy was yield in DSSCs performance [87].

Another factor that causes DSSC degradation is the presence of water in the cell. Source of water in DSSCs can be from the electrolyte solvent contains residual water, or the poor sealing of the cell will allow water infiltration. The intrusion of water in DSSCs led to desorption the dye from TiO₂ surface and degraded the electrolyte by forming of the iodate (IO₃⁻) instead of the triiodide

[88, 89]. Using the hydrophobic dye Z907 efficiency [90] and carbazole dye and MK2 can solve this issue. However, degradation of the counter electrode by the iodine redox electrolyte was observed at 80 °C [89].

The stability of DSSCs using Ru-based dyes has been studied by different research groups using different techniques such as incident-photon-to-current conversion efficiency (IPCE) technique [91], electrochemical impedance spectroscopy (EIS) [92], Fourier transform infrared (FTIR) spectroscopy [93], and scanning electron microscopy (SEM) [94].

Agrell et al. study the degradation mechanisms of DSSCs using UV-VIS and IR spectroscopy techniques. Their results revealed a decrease in the UV-VIS absorption band of the thiocyanate ion ligand at around 2100 cm^{-1} with a reduction in the CN intensity in the IR spectra. They concluded that thiocyanate ligand in the dye is the most sensitive part of the dye [95]. Lohrasbi et al. conducted a degradation study under ambient condition combining EIS and FTIR spectroscopy, they reported that the degradation of the DSSC performance is due to the detachment of the dye from the TiO_2 surface. They observed an increase in the band between $3000\text{--}3600\text{ cm}^{-1}$, which is related to the water permeation into the cell and adsorbed on the TiO_2 surface. The decrease observed the detachment of the dye at the band 2100 cm^{-1} assigned to the SCN combined with a decrease in the bands at 2974 cm^{-1} , 2929 cm^{-1} and 2872 cm^{-1} assigned to TBA^+ [93].

DSSCs are a chemical complex system that consists of different components, and each component plays an essential role in cell performance. As Hagfeldt pointed that “The TiO_2 film, on its own, does not conduct electrical current, the dye, on its own, cannot be exposed to sunlight and the electrolyte is corrosive” [84]. However, combining all together with the right ratio, we will obtain a stabilized and active solar cell.

In chapter 7. A study of understanding the cause's in DSSC instability and how the electrochemical changes happening as the cell ages, a 1000 h stability test was conducted, mainly to investigate the TiO_2 /dye/electrolyte interface. In this study, DSSCs were disassembled for analysis after each period. To the best of our knowledge, disassembling DSSC during intervals time of the aging test has never been studied yet, and we anticipate that this study with ion and electron spectroscopy techniques can spotlight on the degradation mechanisms in DSSC.

2.5 Research aims

Although the literature covers a wide variety of research on DSSCs, this dissertation will focus on three major themes by investigating the influence of several factors using surface sensitive techniques. In chapter 4, producing defects on TiO₂ surface by using two different methods (Sputtering, Heating). By sputtering with different doses of Argon bombardment and heat treatments on the TiO₂ samples, we will gain more information whether the presence of defect sites will be more favourable to dye adsorption or not, and how the number of defects created influences the dye organization and adsorption on TiO₂ surface

In chapter 5 and 6, using different types of co-adsorbents, phosphonate co-adsorbent (in chapter 5) and chenodeoxycholic acid (in chapter 6) to investigate how does the type and concentrations of co-adsorbents affect the layer structure of the dye. Using surface sensitive techniques, and by using ion spectroscopy technique to observe the formation of the sensitized dye on the TiO₂ surface. With the knowledge of the co-adsorbents adsorption at different concentrations, we will be able to design a DSSC of better performance. In this chapter, the N719 and Z907 ruthenium-based dyes were used for fabricating DSSCs.

The interface is defined as the region where various materials are in contact with each other. In DSSCs the TiO₂/dye/electrolyte interface where the charge transport and most of the degradation issues occurred at that interface. Therefore, the TiO₂/dye/electrolyte interface is the region of the highest interest in DSSCs and was studied.

There are some degradation studies in DSSC. However, electron and ion spectroscopic techniques needed for further investigation. In chapter 7, investigates a 1000-hour stability test of DSSC. Three different conditions selected to deeply explore the degradation mechanisms of DSSC performance with and without the use of the co-adsorbent. Light exposed condition, heat condition, and dark condition. The changes of the dye and electrolyte components on the interface of TiO₂ as cell ages was investigated using electron and ion spectroscopic techniques leading for better understanding of the process in the molecular level. Our research will provide a broader view with a better understanding of the mechanism happening within the interface in DSSC and investigating the degradation mechanism at the TiO₂/dye/electrolyte interface as the cell ages can provide a

better way in selecting and controlling the cell components, where the charge transport occurs at that interface.

2.6 Reference

1. O'Regan, B.; Grätzel, M., A Low-Cost, High-Efficiency Solar Cell Based on Dye-Sensitized Colloidal TiO₂ Films. *Nature* **1991**, *353*, 737–740.
2. Grätzel, M., Solar Energy Conversion by Dye-Sensitized Photovoltaic Cells. *Inorganic Chemistry* **2005**, *44*, 6841-6851.
3. Fakharuddin, A.; Jose, R.; Brown, T. M.; Fabregat-Santiago, F.; Bisquert, J., A Perspective on the Production of Dye-Sensitized Solar Modules. *Energy & Environmental Science* **2014**, *7*, 3952-3981.
4. Hamed, N.; Ahmad, M.; Urus, N.; Mohamad, F.; Nafarizal, N.; Ahmad, N.; Soon, C.; Ameruddin, A.; Faridah, A.; Shimomura, M. In *Performance Comparison between Silicon Solar Panel and Dye-Sensitized Solar Panel in Malaysia*, AIP Conference Proceedings, AIP Publishing LLC: 2017; p 020029.
5. Meneses-Rodriguez, D.; Horley, P. P.; Gonzalez-Hernandez, J.; Vorobiev, Y. V.; Gorley, P. N., Photovoltaic Solar Cells Performance at Elevated Temperatures. *Solar Energy* **2005**, *78*, 243-250.
6. Boschloo, G.; Hagfeldt, A., Characteristics of the Iodide/Triiodide Redox Mediator in Dye-Sensitized Solar Cells. *Acc Chem Res* **2009**, *42*, 1819-26.
7. Shalini, S.; Prabhu, R. B.; Prasanna, S.; Mallick, T. K.; Senthilarasu, S., Review on Natural Dye Sensitized Solar Cells: Operation, Materials and Methods. *Renewable & Sustainable Energy Reviews* **2015**, *51*, 1306-1325.
8. Jasim, K. E., Dye Sensitized Solar Cells-Working Principles, Challenges and Opportunities. *Solar Cells-Dye-Sensitized Devices* **2011**, *8*, 172–210.
9. Toivola, M.; Halme, J.; Miettunen, K.; Aitola, K.; Lund, P. D., Nanostructured Dye Solar Cells on Flexible Substrates-Review. *International Journal of Energy Research* **2009**, *33*, 1145-1160.
10. Sima, C.; Grigoriu, C.; Antohe, S., Comparison of the Dye-Sensitized Solar Cells Performances Based on Transparent Conductive ITO and FTO. *Thin Solid Films* **2010**, *519*, 595-597.
11. Steim, R.; Kogler, F. R.; Brabec, C. J., Interface Materials for Organic Solar Cells. *Journal of Materials Chemistry* **2010**, *20*, 2499-2512.
12. O'Regan, B.; Grätzel, M., A Low-Cost, High-Efficiency Solar Cell Based on Dye-Sensitized Colloidal TiO₂ Films. *Nature* **1991**, *353*, 737-740.
13. He, Y.; Hu, J.; Xie, Y., High-Efficiency Dye-Sensitized Solar Cells of up to 8.03% by Air Plasma Treatment of ZnO Nanostructures. *Chem Commun (Camb)* **2015**, *51*, 16229-32.
14. Birkel, A.; Lee, Y.-G.; Koll, D.; Meerbeek, X. V.; Frank, S.; Choi, M. J.; Kang, Y. S.; Char, K.; Tremel, W., Highly Efficient and Stable Dye-Sensitized Solar Cells Based on SnO₂ Nanocrystals Prepared by Microwave-Assisted Synthesis. *Energy Environ. Sci.* **2012**, *5*, 5392-5400.
15. Yang, S. M.; Kou, H. Z.; Wang, J. C.; Xue, H. B.; Han, H. L., Tunability of the Band Energetics of Nanostructured SrTiO₃ Electrodes for Dye-Sensitized Solar Cells. *Journal of Physical Chemistry C* **2010**, *114*, 4245-4249.

16. Elbohy, H.; Reza, K. M.; Abdulkarim, S.; Qiao, Q., Creation of Oxygen Vacancies to Activate WO_3 for Higher Efficiency Dye-Sensitized Solar Cells. *Sustainable Energy & Fuels* **2018**, *2*, 403-412.
17. Grätzel, M., Dye-Sensitized Solar Cells. *Journal of photochemistry and photobiology C: Photochemistry Reviews* **2003**, *4*, 145-153.
18. Narayan, M. R., Review: Dye Sensitized Solar Cells Based on Natural Photosensitizers. *Renewable & Sustainable Energy Reviews* **2012**, *16*, 208-215.
19. Liu, B.; Aydil, E. S., Growth of Oriented Single-Crystalline Rutile TiO_2 Nanorods on Transparent Conducting Substrates for Dye-Sensitized Solar Cells. *J Am Chem Soc* **2009**, *131*, 3985-90.
20. Wang, X. Y., et al., Synthesis of Long TiO_2 Nanowire Arrays with High Surface Areas Via Synergistic Assembly Route for Highly Efficient Dye-Sensitized Solar Cells. *Journal of Materials Chemistry* **2012**, *22*, 17531-17538.
21. Mahmood, K.; Park, S. B., Highly Efficient Dye-Sensitized Solar Cell with an Electrostatic Spray Deposited Upright-Standing Boron-Doped ZnO (BZO) Nanoporous Nanosheet-Based Photoanode. *Journal of Materials Chemistry A* **2013**, *1*, 4826-4835.
22. Jung, Y.; Li, X.; Rajan, N. K.; Taylor, A. D.; Reed, M. A., Record High Efficiency Single-Walled Carbon Nanotube/Silicon P-N Junction Solar Cells. *Nano Lett* **2013**, *13*, 95-9.
23. Song, M. Y.; Kim, D. K.; Ihn, K. J.; Jo, S. M.; Kim, D. Y., Electrospun TiO_2 Electrodes for Dye-Sensitized Solar Cells. *Nanotechnology* **2004**, *15*, 1861-1865.
24. Zhang, X. T.; Sutanto, I.; Taguchi, T.; Meng, Q. B.; Rao, T. N.; Fujishima, A.; Watanabe, H.; Nakamori, T.; Uragami, M., Al_2O_3 -Coated Nanoporous TiO_2 Electrode for Solid-State Dye-Sensitized Solar Cell. *Solar Energy Materials and Solar Cells* **2003**, *80*, 315-326.
25. Barbe, C. J.; Arendse, F.; Comte, P.; Jirousek, M.; Lenzmann, F.; Shklover, V.; Grätzel, M., Nanocrystalline Titanium Oxide Electrodes for Photovoltaic Applications. *Journal of the American Ceramic Society* **1997**, *80*, 3157-3171.
26. Adhikari, S. G.; Shamsaldeen, A.; Andersson, G. G., The Effect of TiCl_4 Treatment on the Performance of Dye-Sensitized Solar Cells. *J Chem Phys* **2019**, *151*, 164704.
27. Lin, Q.-B.; Wang, L.-W.; Huang, S.-H., Effects of Different Treatment of TiO_2 Electrodes on Photovoltaic Characteristics of Dye-Sensitized Solar Cells. *Surface Engineering and Applied Electrochemistry* **2015**, *51*, 394-400.
28. Hao, S. C.; Wu, J. H.; Fan, L. Q.; Huang, Y. F.; Lin, H. M.; Wei, Y. L., The Influence of Acid Treatment of TiO_2 Porous Film Electrode on Photoelectric Performance of Dye-Sensitized Solar Cell. *Solar Energy* **2004**, *76*, 745-750.
29. Park, K. H.; Jin, E. M.; Gu, H. B.; Shim, S. E.; Hong, C. K., Effects of HNO_3 Treatment of TiO_2 Nanoparticles on the Photovoltaic Properties of Dye-Sensitized Solar Cells. *Materials Letters* **2009**, *63*, 2208-2211.

30. Krishnan, G.; Al Qahtani, H. S.; Li, J. D.; Yin, Y. T.; Eom, N.; Golovko, V. B.; Metha, G. F.; Andersson, G. G., Investigation of Ligand-Stabilized Gold Clusters on Defect-Rich Titania. *Journal of Physical Chemistry C* **2017**, *121*, 28007-28016.
31. Song, H.; Luo, M.; Wang, A., High Rate and Stable Li-Ion Insertion in Oxygen-Deficient Li₃O₈ Nanosheets as a Cathode Material for Lithium-Ion Battery. *ACS Appl Mater Interfaces* **2017**, *9*, 2875-2882.
32. Guillemot, F.; Porte, M. C.; Labrugere, C.; Baquey, C., Ti⁴⁺ to Ti³⁺ Conversion of TiO₂ Uppermost Layer by Low-Temperature Vacuum Annealing: Interest for Titanium Biomedical Applications. *J Colloid Interface Sci* **2002**, *255*, 75-8.
33. Yu, Y.; Wu, K. J.; Wang, D. L., Dye-Sensitized Solar Cells with Modified TiO₂ Surface Chemical States: The Role of Ti³⁺. *Applied Physics Letters* **2011**, *99*, 192104.
34. Xu, Y.; Wu, S.; Wan, P.; Sun, J.; Hood, Z. D., Introducing Ti³⁺ Defects Based on Lattice Distortion for Enhanced Visible Light Photoreactivity in TiO₂ Microspheres. *RSC advances* **2017**, *7*, 32461-32467.
35. Ellis-Gibbins, L.; Johansson, V.; Walsh, R. B.; Kloo, L.; Quinton, J. S.; Andersson, G. G., Formation of N719 Dye Multilayers on Dye Sensitized Solar Cell Photoelectrode Surfaces Investigated by Direct Determination of Element Concentration Depth Profiles. *Langmuir* **2012**, *28*, 9431-9.
36. Rajmohan, G. D.; Dai, X. J.; Tsuzuki, T.; Lamb, P. R.; du Plessis, J.; Huang, F. Z.; Cheng, Y. B., Modifying TiO₂ Surface Architecture by Oxygen Plasma to Increase Dye Sensitized Solar Cell Efficiency. *Thin Solid Films* **2013**, *545*, 521-526.
37. Xiong, L.-B.; Li, J.-L.; Yang, B.; Yu, Y., Ti³⁺ in the Surface of Titanium Dioxide: Generation, Properties and Photocatalytic Application. *Journal of Nanomaterials* **2012**, *2012*.
38. Hirose, F.; Kuribayashi, K.; Shikaku, M.; Narita, Y.; Takahashi, Y.; Kimura, Y.; Niwano, M., Adsorption Density Control of N719 on TiO₂ Electrodes for Highly Efficient Dye-Sensitized Solar Cells. *Journal of the Electrochemical Society* **2009**, *156*, B987-B990.
39. Nguyen, T.-D.; Lin, C.-H.; Mai, C.-L.; Wu, C.-G., Function of Tetrabutylammonium on High-Efficiency Ruthenium Sensitizers for Both Outdoor and Indoor DSC Application. *ACS omega* **2019**, *4*, 11414-11423.
40. Aghazada, S.; Nazeeruddin, M. K., Ruthenium Complexes as Sensitizers in Dye-Sensitized Solar Cells. *Inorganics* **2018**, *6*, 52.
41. Mathew, S.; Yella, A.; Gao, P.; Humphry-Baker, R.; Curchod, B. F.; Ashari-Astani, N.; Tavernelli, I.; Rothlisberger, U.; Nazeeruddin, M. K.; Grätzel, M., Dye-Sensitized Solar Cells with 13% Efficiency Achieved through the Molecular Engineering of Porphyrin Sensitizers. *Nature chemistry* **2014**, *6*, 242-247.
42. Kakiage, K.; Aoyama, Y.; Yano, T.; Oya, K.; Fujisawa, J.; Hanaya, M., Highly-Efficient Dye-Sensitized Solar Cells with Collaborative Sensitization by Silyl-Anchor and Carboxy-Anchor Dyes. *Chem Commun (Camb)* **2015**, *51*, 15894-7.
43. Agrell, H. G.; Lindgren, J.; Hagfeldt, A., Coordinative Interactions in a Dye-Sensitized Solar Cell. *J Photoch Photobio A* **2004**, *164*, 23-27.

44. Qin, Y. C.; Peng, Q., Ruthenium Sensitizers and Their Applications in Dye-Sensitized Solar Cells. *International Journal of Photoenergy* **2012**, 2012.
45. Johansson, E. M.; Hedlund, M.; Siegbahn, H.; Rensmo, H., Electronic and Molecular Surface Structure of Ru(Tcterpy)(Ncs)₃ and Ru(Dcbpy)₂(Ncs)₂ Adsorbed from Solution onto Nanostructured Tio₂: A Photoelectron Spectroscopy Study. *J Phys Chem B* **2005**, 109, 22256-63.
46. Park, J.; Lee, P.; Ko, M. J., Design and Fabrication of Long-Term Stable Dye-Sensitized Solar Cells: Effect of Water Contents in Electrolytes on the Performance. *International Journal of Precision Engineering and Manufacturing-Green Technology* **2019**, 6, 125-131.
47. Wang, P.; Zakeeruddin, S. M.; Comte, P.; Charvet, R.; Humphry-Baker, R.; Grätzel, M., Enhance the Performance of Dye-Sensitized Solar Cells by Co-Grafting Amphiphilic Sensitizer and Hexadecylmalonic Acid on Tio₂ Nanocrystals. *Journal of Physical Chemistry B* **2003**, 107, 14336-14341.
48. Manthou, V. S.; Pefkianakis, E. K.; Falaras, P.; Vougioukalakis, G. C., Co-Adsorbents: A Key Component in Efficient and Robust Dye-Sensitized Solar Cells. *ChemSusChem* **2015**, 8, 588-99.
49. Liu, W. Q.; Jiang, H. Y.; Shi, J.; Lu, B. J.; Cai, H. F.; Mao, Z. M.; Kong, F. T., In Situ Evaluation of Kinetics and Interaction Mechanism between Chenodeoxycholic Acid and N719 on Dye-Sensitized Nanofilm Surface. *ACS Applied Energy Materials* **2020**, 3, 3310-3317.
50. Shalini, S.; Balasundaraprabhu, R.; Kumar, T. S.; Prabavathy, N.; Senthilarasu, S.; Prasanna, S., Status and Outlook of Sensitizers/Dyes Used in Dye Sensitized Solar Cells (Dssc): A Review. *International Journal of Energy Research* **2016**, 40, 1303-1320.
51. Yum, J. H.; Jang, S. R.; Humphry-Baker, R.; Grätzel, M.; Cid, J. J.; Torres, T.; Nazeeruddin, M. K., Effect of Coadsorbent on the Photovoltaic Performance of Zinc Pthalocyanine-Sensitized Solar Cells. *Langmuir* **2008**, 24, 5636-40.
52. Neale, N. R.; Kopidakis, N.; Van De Lagemaat, J.; Grätzel, M.; Frank, A. J., Effect of a Coadsorbent on the Performance of Dye-Sensitized Tio₂ Solar Cells: Shielding Versus Band-Edge Movement. *The Journal of Physical Chemistry B* **2005**, 109, 23183-23189.
53. Chandiran, A. K.; Zakeeruddin, S. M.; Humphry-Baker, R.; Nazeeruddin, M. K.; Grätzel, M.; Sauvage, F., Investigation on the Interface Modification of Tio₂ Surfaces by Functional Co-Adsorbents for High-Efficiency Dye-Sensitized Solar Cells. *Chemphyschem* **2017**, 18, 2724-2731.
54. Najm, A. S.; Ludin, N. A.; Abdullah, M. F.; Almessiere, M. A.; Ahmed, N. M.; Al-Alwani, M. A. M., Areca Catechu Extracted Natural New Sensitizer for Dye-Sensitized Solar Cell: Performance Evaluation. *Journal of Materials Science-Materials in Electronics* **2020**, 31, 3564-3575.
55. Wang, P.; Zakeeruddin, S. M.; Humphry-Baker, R.; Moser, J. E.; Grätzel, M., Molecular-Scale Interface Engineering of Tio₂ Nanocrystals: Improve the Efficiency and Stability of Dye-Sensitized Solar Cells. *Advanced Materials* **2003**, 15, 2101-2104.
56. Li, J.; Wu, W. J.; Yang, J. B.; Tang, J.; Long, Y. T.; Hua, J. L., Effect of Chenodeoxycholic Acid (Cdca) Additive on Phenothiazine Dyes Sensitized Photovoltaic Performance. *Science China-Chemistry* **2011**, 54, 699-706.

57. Wang, P.; Zakeeruddin, S. M.; Humphry-Baker, R.; Grätzel, M., A Binary Ionic Liquid Electrolyte to Achieve $\geq 7\%$ Power Conversion Efficiencies in Dye-Sensitized Solar Cells. *Chemistry of Materials* **2004**, *16*, 2694-2696.
58. Liu, Y.; Jennings, J. R.; Wang, X.; Wang, Q., Significant Performance Improvement in Dye-Sensitized Solar Cells Employing Cobalt(III/II) Tris-Bipyridyl Redox Mediators by Co-Grafting Alkyl Phosphonic Acids with a Ruthenium Sensitizer. *Phys Chem Chem Phys* **2013**, *15*, 6170-4.
59. Hou, R. E.; Yuan, S.; Ren, X.; Zhao, Y.; Wang, Z. Y.; Zhang, M. H.; Li, D. D.; Shi, L. Y., Effects of Acetyl Acetone-Typed Co-Adsorbents on the Interface Charge Recombination in Dye-Sensitized Solar Cell Photoanodes. *Electrochimica Acta* **2015**, *154*, 190-196.
60. Lee, K. M.; Suryanarayanan, V.; Ho, K. C.; Thomas, K. R. J.; Lin, J. T., Effects of Co-Adsorbate and Additive on the Performance of Dye-Sensitized Solar Cells: A Photophysical Study. *Solar Energy Materials and Solar Cells* **2007**, *91*, 1426-1431.
61. Shen, H. P.; Li, X.; Li, J. B.; Wang, W. L.; Lin, H., Effect of Proton Numbers of Phosphate-Based Co-Adsorbents on the Photovoltaic Performance of Dye-Sensitized Solar Cells. *Electrochimica Acta* **2013**, *97*, 160-166.
62. Gao, J., et al., Light-Induced Interfacial Dynamics Dramatically Improve the Photocurrent in Dye-Sensitized Solar Cells: An Electrolyte Effect. *ACS Appl Mater Interfaces* **2018**, *10*, 26241-26247.
63. Yu, Z.; Vlachopoulos, N.; Gorlov, M.; Kloo, L., Liquid Electrolytes for Dye-Sensitized Solar Cells. *Dalton Trans* **2011**, *40*, 10289-303.
64. Pradhan, S. C.; Hagfeldt, A.; Soman, S., Resurgence of DSCs with Copper Electrolyte: A Detailed Investigation of Interfacial Charge Dynamics with Cobalt and Iodine Based Electrolytes. *Journal of Materials Chemistry A* **2018**, *6*, 22204-22214.
65. Mathew, S.; Yella, A.; Gao, P.; Humphry-Baker, R.; Curchod, B. F. E.; Ashari-Astani, N.; Tavernelli, I.; Rothlisberger, U.; Nazeeruddin, M. K.; Grätzel, M., Dye-Sensitized Solar Cells with 13% Efficiency Achieved through the Molecular Engineering of Porphyrin Sensitizers. *Nature Chemistry* **2014**, *6*, 242-247.
66. Gao, J. J.; Achari, M. B.; Kloo, L., Long-Term Stability for Cobalt-Based Dye-Sensitized Solar Cells Obtained by Electrolyte Optimization. *Chemical Communications* **2014**, *50*, 6249-6251.
67. Bai, Y.; Cao, Y.; Zhang, J.; Wang, M.; Li, R.; Wang, P.; Zakeeruddin, S. M.; Grätzel, M., High-Performance Dye-Sensitized Solar Cells Based on Solvent-Free Electrolytes Produced from Eutectic Melts. *Nat Mater* **2008**, *7*, 626-30.
68. Li, D.; Wang, M.; Wu, J.; Zhang, Q.; Luo, Y.; Yu, Z.; Meng, Q.; Wu, Z., Application of a New Cyclic Guanidinium Ionic Liquid on Dye-Sensitized Solar Cells (DSCs). *Langmuir* **2009**, *25*, 4808-14.
69. Bella, F.; Sacco, A.; Pugliese, D.; Laurenti, M.; Bianco, S., Additives and Salts for Dye-Sensitized Solar Cells Electrolytes: What Is the Best Choice? *Journal of Power Sources* **2014**, *264*, 333-343.
70. Stergiopoulos, T.; Rozi, E.; Karagianni, C. S.; Falaras, P., Influence of Electrolyte Co-Additives on the Performance of Dye-Sensitized Solar Cells. *Nanoscale Res Lett* **2011**, *6*, 307.

71. Nguyen, P. T.; Hansen, P. E.; Lund, T., The Effect of 4-Tert-Butylpyridine and Li⁺ on the Thermal Degradation of TiO₂-Bound Ruthenium Dye N719. *Solar Energy* **2013**, *88*, 23-30.
72. Wang, Y. Q.; Lu, J.; Yin, J.; Lu, G.; Cui, Y. M.; Wang, S. S.; Deng, S. Y.; Shan, D.; Tao, H. L.; Sun, Y. M., Influence of 4-Tert-Butylpyridine/Guanidinium Thiocyanate Co-Additives on Band Edge Shift and Recombination of Dye-Sensitized Solar Cells: Experimental and Theoretical Aspects. *Electrochimica Acta* **2015**, *185*, 69-75.
73. Hassing, S.; Jernshøj, K. D.; Nguyen, P. T.; Lund, T., In Vitro Polarized Resonance Raman Study of N719 and N719-Tbp in Dye Sensitized Solar Cells. *Journal of Technology Innovations in Renewable Energy* **2016**, *5*, 21-32.
74. Ito, S.; Zakeeruddin, S. M.; Comte, P.; Liska, P.; Kuang, D. B.; Grätzel, M., Bifacial Dye-Sensitized Solar Cells Based on an Ionic Liquid Electrolyte. *Nature Photonics* **2008**, *2*, 693-698.
75. Nam, J. G.; Park, Y. J.; Kim, B. S.; Lee, J. S., Enhancement of the Efficiency of Dye-Sensitized Solar Cell by Utilizing Carbon Nanotube Counter Electrode. *Scripta Materialia* **2010**, *62*, 148-150.
76. Wang, M. K.; Anghel, A. M.; Marsan, B.; Ha, N. L. C.; Pootrakulchote, N.; Zakeeruddin, S. M.; Grätzel, M., Cos Supersedes Pt as Efficient Electrocatalyst for Triiodide Reduction in Dye-Sensitized Solar Cells. *Journal of the American Chemical Society* **2009**, *131*, 15976-+.
77. Jiang, Q.; Li, G.; Gao, X., Highly Ordered Tin Nanotube Arrays as Counter Electrodes for Dye-Sensitized Solar Cells. *Chemical communications* **2009**, 6720-6722.
78. Wang, P.; Klein, C.; Humphry-Baker, R.; Zakeeruddin, S. M.; Grätzel, M., A High Molar Extinction Coefficient Sensitizer for Stable Dye-Sensitized Solar Cells. *J Am Chem Soc* **2005**, *127*, 808-9.
79. Wang, P.; Zakeeruddin, S. M.; Moser, J. E.; Nazeeruddin, M. K.; Sekiguchi, T.; Grätzel, M., A Stable Quasi-Solid-State Dye-Sensitized Solar Cell with an Amphiphilic Ruthenium Sensitizer and Polymer Gel Electrolyte. *Nat Mater* **2003**, *2*, 402-7.
80. Dai, S. Y., et al., The Design and Outdoor Application of Dye-Sensitized Solar Cells. *Inorganica Chimica Acta* **2008**, *361*, 786-791.
81. Sommeling, P. M.; Spath, M.; Smit, H. J. P.; Bakker, N. J.; Kroon, J. M., Long-Term Stability Testing of Dye-Sensitized Solar Cells. *J Photoch Photobio A* **2004**, *164*, 137-144.
82. Mastroianni, S.; Lanuti, A.; Penna, S.; Reale, A.; Brown, T. M.; Di Carlo, A.; Decker, F., Physical and Electrochemical Analysis of an Indoor-Outdoor Ageing Test of Large-Area Dye Solar Cell Devices. *ChemPhysChem* **2012**, *13*, 2925-2936.
83. Asghar, A.; Emziane, M.; Pak, H.; Oh, S., Outdoor Testing and Degradation of Dye-Sensitized Solar Cells in Abu Dhabi. *Solar energy materials and solar cells* **2014**, *128*, 335-342.
84. Asghar, M. I.; Miettunen, K.; Halme, J.; Vahermaa, P.; Toivola, M.; Aitola, K.; Lund, P., Review of Stability for Advanced Dye Solar Cells. *Energy & Environmental Science* **2010**, *3*, 418-426.
85. Harikisun, R.; Desilvestro, H., Long-Term Stability of Dye Solar Cells. *Solar Energy* **2011**, *85*, 1179-1188.

86. Lepikko, S.; Miettunen, K.; Poskela, A.; Tiihonen, A.; Lund, P. D., Testing Dye-Sensitized Solar Cells in Harsh Northern Outdoor Conditions. *Energy Science & Engineering* **2018**, *6*, 187-200.
87. Raga, S. R.; Fabregat-Santiago, F., Temperature Effects in Dye-Sensitized Solar Cells. *Phys Chem Chem Phys* **2013**, *15*, 2328-36.
88. Asghar, A.; Emziane, M.; Pak, H. K.; Oh, S. Y., Outdoor Testing and Degradation of Dye-Sensitized Solar Cells in Abu Dhabi. *Solar Energy Materials and Solar Cells* **2014**, *128*, 335-342.
89. Kato, N.; Takeda, Y.; Higuchi, K.; Takeichi, A.; Sudo, E.; Tanaka, H.; Motohiro, T.; Sano, T.; Toyoda, T., Degradation Analysis of Dye-Sensitized Solar Cell Module after Long-Term Stability Test under Outdoor Working Condition. *Solar Energy Materials and Solar Cells* **2009**, *93*, 893-897.
90. Hara, K.; Wang, Z.-S.; Cui, Y.; Furube, A.; Koumura, N., Long-Term Stability of Organic-Dye-Sensitized Solar Cells Based on an Alkyl-Functionalized Carbazole Dye. *Energy & Environmental Science* **2009**, *2*, 1109-1114.
91. Wang, P.; Yang, L.; Wu, H.; Cao, Y. M.; Zhang, J.; Xu, N. S.; Chen, S.; Decoppet, J. D.; Zakeeruddin, S. M.; Grätzel, M., Stable and Efficient Organic Dye-Sensitized Solar Cell Based on Ionic Liquid Electrolyte. *Joule* **2018**, *2*, 2145-2153.
92. Heo, N.; Jun, Y.; Park, J. H., Dye Molecules in Electrolytes: New Approach for Suppression of Dye-Desorption in Dye-Sensitized Solar Cells. *Scientific reports* **2013**, *3*, 1-6.
93. Sonai, G. G.; Tiihonen, A.; Miettunen, K.; Lund, P. D.; Nogueira, A. F., Long-Term Stability of Dye-Sensitized Solar Cells Assembled with Cobalt Polymer Gel Electrolyte. *Journal of Physical Chemistry C* **2017**, *121*, 17577-17585.
94. Lohrasbi, M.; Pattanapanishawat, P.; Isenberg, M.; Chuang, S. S. In *Degradation Study of Dye-Sensitized Solar Cells by Electrochemical Impedance and Ftir Spectroscopy*, 2013 IEEE Energytech, IEEE: 2013; pp 1-4.
95. Jang, Y. J.; Thogiti, S.; Lee, K. Y.; Kim, J. H., Long-Term Stable Solid-State Dye-Sensitized Solar Cells Assembled with Solid-State Polymerized Hole-Transporting Material. *Crystals* **2019**, *9*, 452.
96. Agrell, H. G.; Lindgren, J.; Hagfeldt, A., Degradation Mechanisms in a Dye-Sensitized Solar Cell Studied by Uv-Vis and Ir Spectroscopy. *Solar Energy* **2003**, *75*, 169-180.

Chapter Three

3 Experimental techniques

3.1 Photoelectron Spectroscopy

The photoelectron spectroscopy (PES) is a surface analysis technique that provides a comprehensive elemental and electronic analysis of a sample's surface; by using either X-rays or ultraviolet (UV) light as an excitation source for electron emission. It works via the photoelectric effect, which was observed first by Heinrich Hertz in 1887, and Albert Einstein explained it in 1905. The photoelectric effect can be described as the emission of an electron (photoelectron) from the sample upon absorbance of incident photons with energy ($h\nu$) higher than the binding energy (E_{Binding}) of that electron [1].

The difference between these energies presents as the kinetic energy (E_{kinetic}) of the emitted photoelectrons and is measured by electron spectroscopy with a hemispherical analyser. Einstein's photoelectric equation describes the relationship between photon energy and the kinetic energy of the emitted photoelectron.

$$E_{\text{Kinetic}} = h\nu - \Phi_{\text{Spec}} - E_{\text{Binding}} \quad \text{Equation 3.1}$$

Where Φ_{Spec} is the work function of the spectrometer and is obtained by measuring a highly conductive metal sample such as Au or Ag where they have well-defined features.

PES is a surface-sensitive technique and the information obtained from different orbitals within the sample where the photons can penetrate the sample and measure the outermost layer, and into some depth of the sample surface.

The surface-sensitive of this technique is due to the electron mean free path (λ), where the electrons can travel before interacting with the surrounding atoms or electrons [2, 3]. Figure 3-1 shows the electron mean free path.

Knowing the electron energy loss, the intensity of electron attenuation can be measured by

$$I(E, \alpha, d) = I_o \exp\left(-\frac{d}{\cos(\theta) \cdot \lambda(E)}\right) \quad \text{Equation 3.2}$$

I = measured intensity

I_0 = initial intensity at the outermost layer

d = depth from which electrons emitted

θ = angle between the detector and surface normal

$\lambda(E)$ = electron mean free path

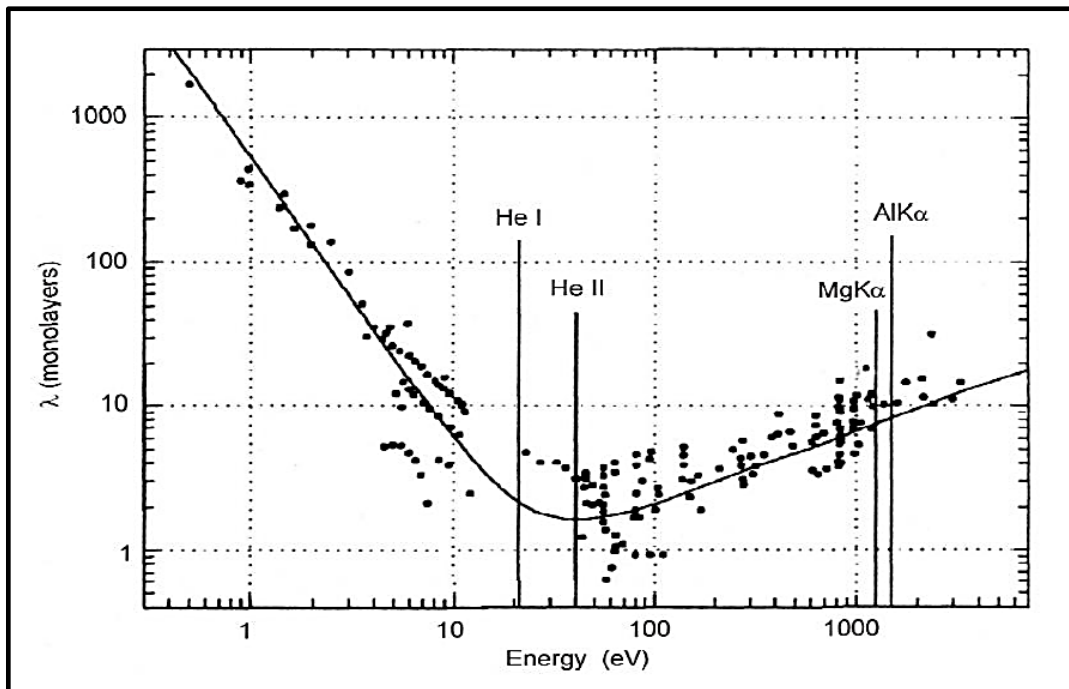


Figure 3-1: The Inelastic Electron Mean Free Path for different solids plotted against the kinetic energy [4]

Based on the origin of photoelectrons, PES is classified into two categories: photoelectrons from core orbitals into some depth of the sample and photoelectrons from valence orbitals in the outermost layer. The photoemission process occurs for discrete energies defined by quantum mechanics. The core electrons are strongly bound and require high photon energy to overcome the attractive forces and release electrons (emitted by X-ray photoelectron spectroscopy), while the valence electrons require lower energy and have delocalized molecular characteristic (emitted by ultraviolet photoelectron spectroscopy).

3.1.1 X-ray Photoelectron Spectroscopy (XPS)

X-ray photoelectron spectroscopy (XPS) is used to obtain the chemical information, such as the

elemental composition and element valence state of a sample surface.

Surface analysis by XPS involves irradiating the sample with X-rays. XPS sends massive amounts of photons to interact with atoms and transfer their energy to excite electrons by striking them, usually from Al $K\alpha$ and Mg $K\alpha$, providing photons with energy of 1486.6 eV and 1254.6 eV, respectively. The electrons get excited to an unoccupied state (energy level) and become photoelectrons [2, 3, 5]. The intense photons of the X-ray will be able to penetrate $\sim 1 \mu\text{m}$ into the sample, but only electrons from a depth between 1-10 nm will escape from the sample surface without losing their energy due to collisions through the sample [6]. The core electrons emitted at different binding energies then enter into the hemispherical analyser through a detector to measure their kinetic energy. From equation 3.1, we can calculate the binding energy of the emitted electrons, which is correspondent to the element from which the electrons emitted from and the core orbitals of where electrons ejected [7].

In this study, X-rays from Mg $K\alpha$ source with a photon energy of 1253.6 eV used to obtain the information depth of 3~5 nm of the sample with medium magnification lens mode used to analyse an area of 7 mm in diameter.

When the photoelectron emitted from the sample, it will result in a hole in the core of the atom, leaving the atom in an excited state. There are two processes for the relaxation of the atom. Firstly, via the electronic transition from higher energy level filling that hole and release of excess energy by the emission of X-ray photon. Secondly, by Auger electrons, in this process, the relaxation occurs when the excess energy leftover from transition is then passed to another higher-level electron and liberated [8, 9].

To enable the transmission of photoelectrons to the analyser and to minimise the re-contamination rate of a freshly cleaned sample, the sample must be placed in an Ultra-high vacuum (UHV) chamber for analysing. This is an essential step because using the UHV chamber can remove the adsorbed gases from the sample, eliminate adsorption of contaminants keeping the sample clean for a sufficiently long time, prevent arcing and high voltage breakdown, and increases the mean free path for electrons, ions, and photons.

The peak position, the full-width half maximum (FWHM), and the peak intensity are the primary information obtained from an XPS spectrum. Changes in the peak position of an individual element

indicate a change in its chemical states, such as oxidation or reduction.

Binding energy can be observed as the energy difference between the initial and final state after the photoelectron leaves the atom. Because each element has a unique set of binding energies, XPS can also be used to identify and determine the concentration of elements in the surface by observing the recorded electron intensity correlated to certain element [5].

XPS instruments consist of an X-ray source, a hemispherical analyser, and an electron detector. Operated in a UHV apparatus built by SPECS (SPECS, Berlin, Germany), at a base pressure of a few 10^{-10} mbar with SPECS PHOIBOS-HSA3500 analyzer and spectra recorded at pass energy of 10 eV. The X-ray source used is $MgK\alpha$ radiation and operated at 200 W, 12 kV and with excitation energy of 1253.6 eV. A survey scan was recorded with a pass energy of 40 eV while high-resolution scans were recorded at pass energy of 10 eV. The high-resolution spectra were fitted by Shirley background to eliminate the electron scattering background, and Gaussian-Lorentzian functions to fit the peaks [8, 10].

3.1.2 XPS Analysis

The peaks of each element in the sample in the XPS spectrum were fitted using a Shirley background. Shirley background was used to create a non-linear background to incorporate the changes in the data.

The cross-section of each element is different, thus for accurate measurements for the intensity of each element, the sensitivity factor should be considered. The sensitivity factor of each element was used in this work from Jolm Moulder as illustrated in reference [5].

The intensity of the peak is measured as follows:

$$\text{Specific intensity} = \frac{\text{peak area of element}}{\text{Atomic Sensitivity factor of element}} \quad \text{Equation 3.3}$$

By summing all of the element intensities to measure the percentage composition representing each element in the sample.

$$\text{Percentage composition} = \frac{\text{Specific intensity of element}}{\text{Total (Specific intensity) elements}} \times 100 \quad \text{Equation 3.4}$$

The uncertainty of the peak intensity was measured by applying small variations within a probable fitting of the area under the peak of each element. Then by applying equation 3.6, to measure the

error between the element ratio.

$$r = \frac{I_1}{I_2} \quad \text{Equation 3.5}$$

$$\Delta r = \sqrt{\left(\frac{\partial r}{\partial I_1}\right)^2 \delta I_1^2 + \left(\frac{\partial r}{\partial I_2}\right)^2 \delta I_2^2} \quad \text{Equation 3.6}$$

Where, I_1 and I_2 represent the specific intensity of each element in the sample, and δI represent the variation in fitting the area underneath the peak of each element divided by the elements' sensitivity factor.

3.2 Ultraviolet Photoelectron Spectroscopy (UPS)

In ultraviolet photoelectron spectroscopy (UPS) a helium discharge lamp was used to create UV radiation with excitation energy of 21.2 eV (He I) to excite the electrons. UPS is a very surface-sensitive technique, with this energy UPS probes the valence band (VB) and ejects electrons from the sample surface from depths up to ~ 3 nm and provide information about the density of occupied valance states and orbitals, and secondary electrons. The distribution of secondary electrons can be extrapolated to determine work-function (WF) of a sample. where the WF is defined as the minimum energy required to remove an electron from the sample surface [11]. Figure 3-2 shows the UP spectrum, where both the valance band and the work function can be measured by plotting a line of best fit to the regions across the x-axis. The work-function is calculated by taking the onset cut-off of the secondary electron cascade via kinetic energy scale (converted via excitation energy minus binding energy) [12].

The ejected electrons will travel in a UHV chamber, and to ensure that all secondary electrons are emitted an additional bias of -10 eV to the kinetic energy of the emitted electrons is used to accelerate them into the hemispherical analyser. The following equation can calculate the binding energy of the electrons in UPS method:

$$E_{Binding} = 21.2 \text{ eV} - (E_{Kinetic} + 10 \text{ eV}) - \Phi_{Spec} \quad \text{Equation 3.7}$$

The definition of units in the equation is same as Equation 3.1.

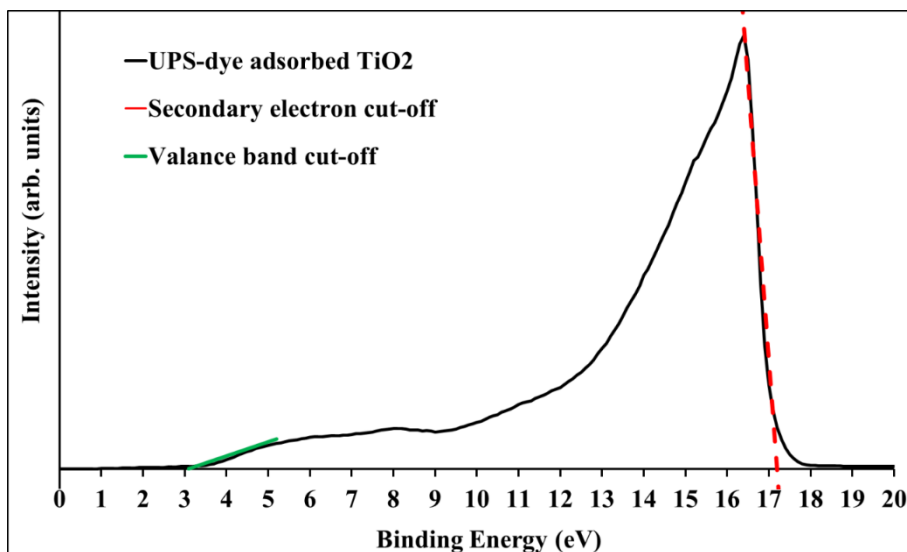


Figure 3-2: UP spectrum with labelled valance band (~ 3 eV) and secondary electron cut off to measure the work function (21.2 eV - 17.2 eV = 4 eV).

3.3 Metastable Induced Electron Spectroscopy (MIES)

In the previous techniques, the information collected by photons penetrating the sample surface in order of a few nanometres. The electronic structures at surfaces are relevant studies where changes occur in the outermost layer involving the charge transfer and chemical bonding changes that are happening at that interface.

In MIES, metastable helium atoms used to bombard the sample surface where the helium atoms are excited to a metastable state ($\text{He}^* 2s1s$) with excitation energy of 19.8 eV to obtain the information from the VB for the outermost layer of the sample.

Two primary mechanisms are employed when He^* atoms approach the sample surface, and these are resonant ionization (RI) followed by Auger neutralization (AN) and Auger de-excitation (AD).

The first mechanism, RI, and AN applies to metal surfaces. RI happens when the sample surface has an unoccupied state then electrons of $2s$ orbital in He^* will transmit their energy to the sample surface leading to excitation and emission of electrons, [13] which can be measured by

$$E_{kinetic} = E'_i - 2(\Phi + \varepsilon) \quad \text{Equation 3.8}$$

Where Φ is the work function of the surface, ε is the average binding energy of electrons involved in the Auger process that results in He^+ ions while an electron is emitted and E'_i is the ionisation

potential of the He. In AN, the He^+ will be neutralised when an electron from the sample surface loses its energy to fill the vacant orbital. The second mechanism, AD, takes place in samples having a low bandgap, which is not applicable in this work.

UPS and MIES are conducted in UHV. A two-stage cathode discharge from MFS (Clausthal-Zellerfeld, Germany) is used to generate UV light (21.2 eV) and metastable helium atoms He^* ($^3\text{S}_1$, 19.8 eV) simultaneously. A chopper with a frequency of 2 kHz is used to separate the signal obtained from the UV photons and He^* .

In UPS and MIES spectrum, the density of states (DOS) appears as peaks related to the occupation of the energy state of available electrons as a function of binding energy. These peaks can be fitted with Gaussian curves and compared with the theoretical calculations. The theoretical calculation of the DOS and assigning to molecular functional groups were done in the collaboration from the group of Lars Kloo at the KTH in Sweden.

3.3.1 The Singular Value Decomposition

For analysing a series of UPS and MIES spectra, the Singular Value Decomposition (SVD) algorithm is applied. When a series of spectra are measured for a series of an experiment such as sputtering the samples with different doses or heating with at various temperature intervals, SVD procedure is applied to obtain the spectrum that contributes to the series. The details of the procedure can be found in the literature [14-16]. A summary of the method is given here. The SVD algorithm is applied in two steps. First, the number of base spectra determined, which is required to reconstruct the set of measured spectra. These base spectra are the result of a mathematical procedure and do not necessarily have a physical meaning. As an example, the base can have negative intensities, which is physically meaningless. Linear combinations resulting from SVD should have meaningful physical spectra. By following the procedure of Morgner et al. [16], the matrix formed by the base spectra multiplied by $(n \times n)$ matrix, where n is the number of base spectra. The elements of the $(n \times n)$ matrix are designed with two criteria, where all reference spectra are positive, and the measured spectra must fit with a linear combination of the reference spectra.

$$S_i = \sum_n a_n S_n^r \quad \text{Equation 3.9}$$

Where S_i are the measured spectra, S_n^r are the reference spectra and a_n are the weighting

coefficients. The sum of all weighting coefficients should add up to unity ($\sum_n a_n \approx 1$) within an error bar of 0.1, approximately.

3.4 Neutral Impact Collision Ion Scattering Spectroscopy (NICISS)

NICISS is a technique that can obtain concentration and depth profiles of elements on soft matter surfaces. NICISS apparatus consists of an ion source of an inert gas where helium ions are mostly used as projectiles, a vacuum chamber, and a detector to measure the time of flight (TOF) of the backscattered ions, and electrostatic deflection units used to pulse the ion beam. NICISS can determine the amount of elements present in a sample and the average thickness with a probing depth of about 20 nm at a resolution of few angstroms (Å) [17, 18]. In this technique, the sample placed in a high vacuum chamber where it bombarded by a pulsed beam of helium ions with kinetic energy in the range of 1-5 keV (3 keV used in this work measuring an area of 1 mm in diameter) [19]. The helium projectiles are backscattered from the atoms as neutralised ions and lose energy in the backscattering process. The backscattered projectiles have the velocity decreased because of the kinetic energy loss. While such a difference in velocity can be determined by the time of flight (TOF) detector, which records the time of a projectile backscattered to the detector. The TOF can be used to determine the velocity of the projectile and thus the energy loss from the target to the detector can be extracted. Such energy loss is different and correlated to the atom mass the He ion hits. By knowing the TOF of the backscattered helium, the mass of the target atoms where He ion collided can be studied. In addition, there are two types of energy loss processes. Initially, the projectiles lose energy in the backscattering process. This energy loss used to identify the mass of the atom from which the projectile backscattered. Secondly, the projectiles lose energy on their trajectory through the bulk by low angle scattering and electronic excitations (stopping power) [20]. The second type of energy loss here is used to determine the depth from which the projectile backscattered. Their TOF determines the energy of the backscattered projectile from the target to the detector. The instrument's TOF path length is 1.24 m, with a scattering angle of 12°. Combinations of these two ways of energy loss are used to determine the concentration depth profile of the elements. NICISS results are in the form of a spectrum consisting of individual peaks and steps that identify different atoms that represented in the sample and is recorded as intensity vs. TOF which is shown in Figure 3-3. Helium ions cannot be backscattered from hydrogen, because hydrogen is lighter than helium, therefore no energy loss of hydrogen [18]. In this work,

the concentration depth profile of Ru was plotted as a function of both the depth and energy loss as in Figure 3-4.

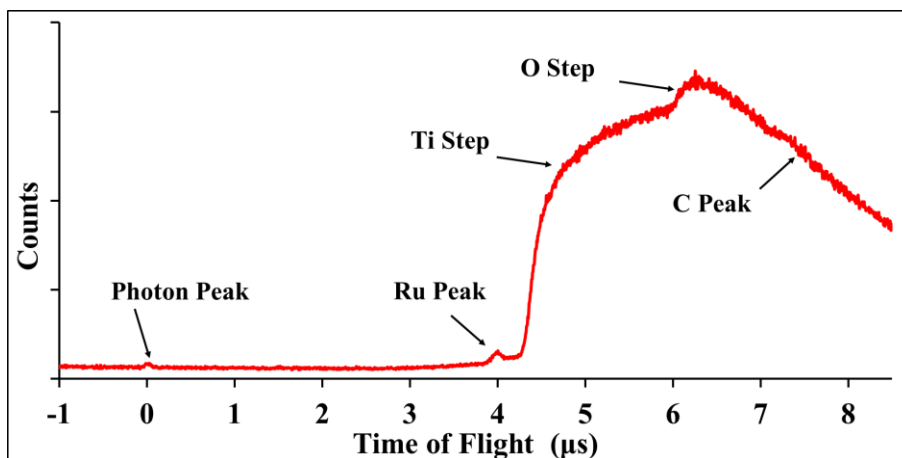


Figure 3-3: Example of NICISS row data spectrum of N719 dye on TiO₂ (The signals in TOF spectra assigned to Ruthenium at 4 μs, Titanium at 4.5 μs, Oxygen at 6.4 μs and Carbon at 7.4 μs).

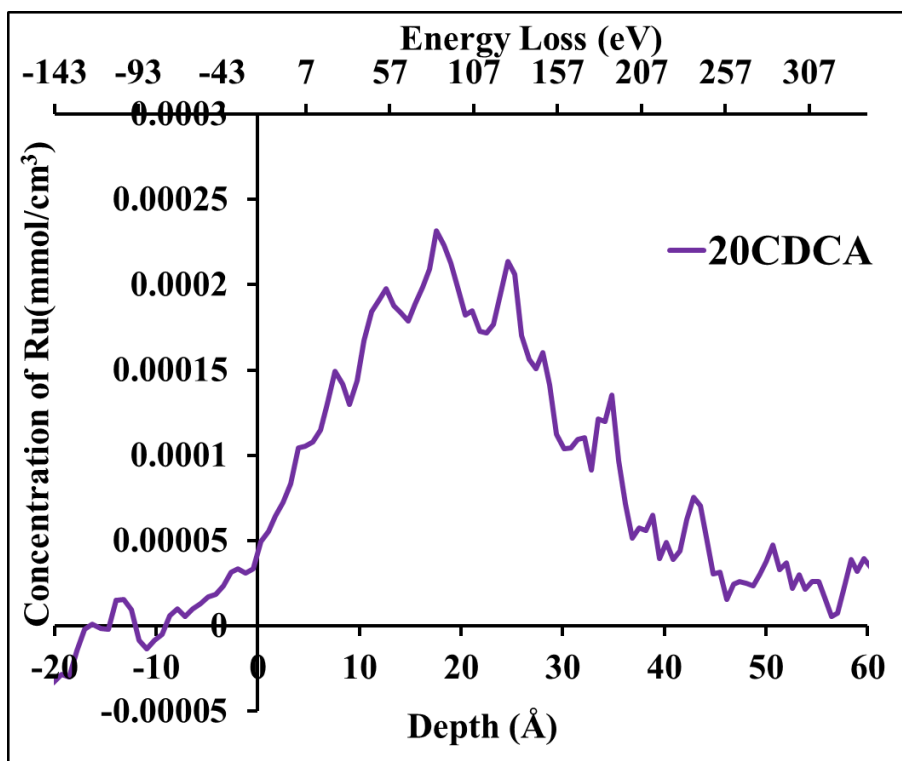


Figure 3-4: NICISS result shows Ru depth profile in N719 with 20 mM CDCA, the relative concentration is via two axis-energy loss and depth scale

The conversion from TOF spectrum to energy spectrum by using the following equation:

$$I(E) = I(t) \frac{dt}{dE} \frac{1}{d\sigma/d\Omega(E)} \frac{1}{\det(E)} \quad \text{Equation 3.10}$$

Where $I(E)$ is the energy loss spectrum, $I(t)$ is the contribution of element in TOF spectrum, $d\sigma/d\Omega(E)$ is the differential cross section, $\det(E)$ is the detector sensitivity and the factor dt/dE has to be considered for the non-linear relation between the TOF and the energy. The energy loss spectrum is converted to concentration depth profile by using the following equation.

$$I(d) = I(E) \frac{dE}{dz} f \quad \text{Equation 3.11}$$

Where z is the depth of the element, and f is a factor converting the backscattered projectiles to concentration of the target element.

3.4.1 NICISS analysis

To measure the concentration of Ru presents on different NICISS spectra of different samples a calibration was applied by measuring the spectrum in parallel of dyed titania surface and a polymer samples Poly (3-hexylthiophene) (P3HT), and the latter one is for normalisation reference. By measuring both of the samples under the same conditions and measuring the step height of the sulfur in the polymer, then dividing the molar density by the measured step height of the sulfur, a conversion factor will be obtained and used to calibrate the dyed sample to measure the Ru concentration. The error involved in NICISS was determined by measuring the variations of fitting the backgrounds.

3.5 Photovoltaic Characterization

The cell efficiency can evaluate the performance of DSSC, and it can be defined as the capability of the cell to convert the input energy (sunlight) to an output of electrical energy. The power conversion efficacy (η) of the cell is the ratio between the powers generated by the cell (P_{output}) to the power of the incident light on the cell (P_{input}) and is expressed as a percentage.

$$\eta = \frac{P_{\text{output}}}{P_{\text{input}}} \quad \text{Equation 3.12}$$

P_{input} is a function of the solar spectrum, and the solar spectrum that reaches the earth is different at different times of the day and locations. To make solar cells' testing consistent, the cells are

tested using a universally accepted reference solar spectrum with air mass coefficient (AM) of 1.5G. where the AM 1.5G is the spectral distribution of the global solar radiation at sea level after passing the atmosphere 1.5 times with a radiation intensity of 100 mW/cm² [21].

P_{output} of the cell can be experimentally measured from the current-voltage (I-V) characterization. Parameters such as the short-circuit current (I_{sc}), the open-circuit voltage (V_{oc}), and the fill factor can be determined from the I-V characteristics. The short-circuit current (I_{sc}) is the maximum current output of the cell when no voltage is applied, and the open-circuit voltage (V_{oc}) is the maximum voltage of the cell when there is no current flow through the external circuit. When the current and voltage are at maximum power point I_{max} and V_{max} , P_{output} of the cell can be calculated using equation 3.13

$$P_{output} = I_{max} V_{max} \quad \text{Equation 3.13}$$

The Fill Factor is defined as the ratio between the P_{output} to the product of V_{oc} and I_{sc} , and can be measured using the following equation:

$$FF = \frac{P_{output}}{I_{sc}V_{oc}} \quad \text{Equation 3.14}$$

And the overall performance of the cell can be evaluated by its efficiency and can be calculated using the following equation.

$$\eta = \frac{I_{sc}V_{oc} FF}{P_{input}} \times 100 \quad \text{Equation 3.15}$$

The generated photocurrent is often expressed as current per unit area and thus J-V interchangeably used for I-V characteristics of device, when (J) current density is expressed.

The cells were tested using Oriel solar simulator fitted with a 1000 W Xe lamp filtered to give an output of 100 mW/cm² at AM 1.5, and the lamp was calibrated using Si cell. The efficiencies were measured using Keithley 2400 source meter operated by Labview software.

3.6 Stability test

The acceleration stability test carried out in ATLAS- Suntest CPS+. DSSCs were exposed to intense light and temperature of ~60 °C continuous for a period of 1000 h and were taken out at certain times for characterization. The stability tests were categorised into three different

conditions. 1) light-condition DSSCs placed in (ATLAS- Suntest CPS+) exposing to the light and heat. 2) heat-condition DSSCs covered and placed in (ATLAS- Suntest CPS+). 3) dark-condition DSSCs kept in dark as reference cells.

3.7 Gaussian Materials and Sample Preparation

Working-electrodes

DSSCs were fabricated following the standard protocol. Fluorine-doped Tin Oxide (FTO) coated substrate (Dyesol -TEC15) were cleaned in an ultrasonic bath for 30 mins in deionized water with detergent, then rinsed with deionized water continued by a second ultrasonic bath for 30 mins with ethanol and finally dried using dry nitrogen. FTO substrate were pre-treated by immersing into 40 mM aqueous TiCl_4 solution (Sigma-Aldrich) at 70 °C for 30 min, after which they were rinsed with water and ethanol and further heated at 300 °C for 3 h. TiO_2 paste (GreatCell-18NR-AO) with anatase with an average particle size 20 nm and scatter particles sized ≤ 450 nm, were screen-printed on the pre-treated FTO substrates with an active area of 0.36 cm². The 450 nm sized nanoparticles provided higher efficiency caused by the light scattering effect based on its diameter. The screen-printed TiO_2 electrodes were gradually heated at 120 °C for 5 min, 325 °C and 375 °C each for 10 min and 500 °C for 30 min. The sintered electrode received a second TiCl_4 treatment as described above, and a second final sintering at 400 °C for 30 min. After cooling to 80 °C, the electrodes were immersed into the dye solutions for 24 h.

In chapter 5, The TiO_2 -electrodes were soaked in the dye solutions of (0.3 mM) N719 and (0.3 mM) Z907 (purchased from Greatcell), respectively for assembling the reference cells for comparison purpose. Decylphosphonic acid (DPA) (Sigma-Aldrich) with a range of concentration were added as co-adsorbent to the dye solution. For each sample a fresh solution of dye/DPA was used in 1:1 volume ratio with the respective variation in the DPA concentration. Seven working electrodes were prepared for reference samples and co-adsorbed samples with different concentration.

In chapter 6, The TiO_2 -electrodes were soaked in the dye solutions of (0.3 mM) N719 and (0.3 mM) Z907, respectively for assembling the reference cells for comparison purpose. Chenodeoxycholic acid (CDCA) (Chem-Supply) with a range of concentration (5 mM, 10 mM,

15 mM and 20 mM) were used as co-adsorbent in the dye solution. For each sample a fresh solution of dye/CDCA was used by adding equal volumes of dye and CDCA solutions with a 1:1 volume ratio to form solutions with the concentrations described above. Seven working electrodes were prepared for reference samples and co-adsorbed samples with different CDCA concentrations.

In chapter 7, The TiO₂-electrodes were soaked in the dye solutions of N719/DPA with molar ratio of 0.2 obtained from the best cell performance in chapter 5.

Counter-electrodes

FTO-coated substrate (Dyesol -TEC7) pre-drilled for electrolyte injection and cleaned as described above were used. 4.8 mM H₂PtCl₆ (Sigma-Aldrich) were drop-casted onto the cleaned FTO then sintered at 400 °C for 30 min.

Cell assembly

The TiO₂ electrode and the platinized counter electrode were assembled using a 60 μm thick thermoplastic Surlyn frame (Solaronix). Subsequently the electrolyte was introduced under vacuum through the drilled hole. The electrolyte used had a composition of 0.5 M 4-tert butylpyridine (4TBP), 0.03 M I₂ and 0.6 M BMII (Chem-Supply) dissolved in acetonitrile. The holes were sealed with a Surlyn sheet and covered subsequently with a glass sheet.

3.8 References

1. Reinert, F.; Hüfner, S., Photoemission Spectroscopy—from Early Days to Recent Applications. *New Journal of Physics* **2005**, *7*, 97-97.
2. Kovalev, A.; Wainstein, D., Surface Analysis Techniques for Investigations of Modified Surfaces, Nanocomposites, Chemical, and Structure Transformations. In *Self-Organization During Friction*, 2006; pp 81-120.
3. Tougaard, S., Surface Analysis | X-Ray Photoelectron Spectroscopy. In *Reference Module in Chemistry, Molecular Sciences and Chemical Engineering*, 2013.
4. Seah, M. P.; Dench, W., Quantitative Electron Spectroscopy of Surfaces: A Standard Data Base for Electron Inelastic Mean Free Paths in Solids. *Surface and interface analysis* **1979**, *1*, 2-11.
5. Jolm F. Moulder, W. F. S., Peter E.'Sobol, Kennetlf D. Bomben, Handbook of X-Ray Photoelectron Spectroscopy. **1995**.
6. Moulder, J. F.; Chastain, J., *Handbook of X-Ray Photoelectron Spectroscopy: A Reference Book of Standard Spectra for Identification and Interpretation of Xps Data*; Physical Electronics, 1995.
7. Hofmann, S., Auger- and X-Ray Photoelectron Spectroscopy in Materials Science. *springer series in surface sciences* **49** **2013**.
8. Oswald, S., X-Ray Photoelectron Spectroscopy in Analysis of Surfaces. In *Encyclopedia of Analytical Chemistry*, 2013.
9. D.J. O'Connor, B. A. S., R.St.C. Smart, Book Surface Analysis Methods in Materials Science. **2003**.
10. Hüfner, S., *Photoelectron Spectroscopy: Principles and Applications*; Springer Science & Business Media, 2013.
11. Hofft, O.; Bahr, S.; Himmerlich, M.; Krischok, S.; Schaefer, J. A.; Kempter, V., Electronic Structure of the Surface of the Ionic Liquid [Emim][Tf(2)N] Studied by Metastable Impact Electron Spectroscopy (Mies), Ups, and Xps. *Langmuir* **2006**, *22*, 7120-3.
12. Chambers, B. A.; Neumann, C.; Turchanin, A.; Gibson, C. T.; Andersson, G. G., The Direct Measurement of the Electronic Density of States of Graphene Using Metastable Induced Electron Spectroscopy. *2d Materials* **2017**, *4*.
13. Morgner, H., The Quantitative Characterization of Liquid and Solid Surfaces with Metastable Helium Atoms. In *AIP Conference Proceedings*, 2000; pp 687-698.
14. Berlich, A.; Liu, Y. C.; Morgner, H., Evaporation of Ni and Carbon Containing Species onto Nio/Ni as Case Study for Metal Support Catalysts Investigated by Metastable Induced Electron Spectroscopy (Mies). *Radiation Physics and Chemistry* **2005**, *74*, 201-209.
15. Oberbrodthage, J., Determination of a Solute Electron Energy Spectrum Not Accessible Experimentally by Means of Singular Value Decomposition. *Journal of Electron Spectroscopy and Related Phenomena* **2000**, *107*, 231-238.

16. Morgner, H., The Characterisation of Liquid and Solid Surfaces with Metastable Helium Atoms. *Advances in Atomic, Molecular and Optical Physics* **2000**, 42, 387-488.
17. Andersson, G.; Morgner, H., Investigations on Solutions of Tetrabutylonium Salts in Formamide with Niciss and Iciss: Concentration Depth Profiles and Composition of the Outermost Layer. *Surface Science* **2000**, 445, 89-99.
18. Andersson, G.; Morgner, H., Impact Collision Ion Scattering Spectroscopy (Iciss) and Neutral Impact Collision Ion Scattering Spectroscopy (Niciss) at Surfaces of Organic Liquids. *Surface Science* **1998**, 405, 138-151.
19. Andersson, G.; Morgner, H.; Pohl, H., Energy-Loss Straggling of Helium Projectiles at Low Kinetic Energies: Deconvolution of Concentration Depth Profiles of Inorganic Salt Solutes in Aqueous Solutions. *Physical Review A* **2008**, 78.
20. Andersson, G.; Morgner, H., Determining the Stopping Power of Low Energy Helium in Alkanethiolates with Neutral Impact Collision Ion Scattering Spectroscopy (Niciss). *Nuclear Instruments & Methods in Physics Research Section B-Beam Interactions with Materials and Atoms* **1999**, 155, 357-368.
21. Gueymard, C. A.; Myers, D.; Emery, K., Proposed Reference Irradiance Spectra for Solar Energy Systems Testing. *Solar Energy* **2002**, 73, 443-467.

Chapter Four**4. Influence of TiO₂ Surface Defects on the Adsorption of N719 Dye Molecules****4.1 Abstract**

Surface defects influence the dye adsorption on titanium dioxide (TiO₂) used as substrate in dye-sensitized solar cells (DSSCs). In this study, we used different Ar⁺ sputtering doses to create a controllable amount of defects on a TiO₂ surface with different pre-heating temperatures to analyse the influence of defects on the N719 dye adsorption. TiO₂ was pre-treated with two different treatments: i) heating to 200 °C then sputtering with different doses, and ii) heating at 4 ascending temperatures starting at 200 °C. After pre-treatments, the TiO₂ samples were immersed in N719 dye solution for 24 hours at room temperature. Creation of Ti³⁺ surface defects and their influence on dye adsorption on the TiO₂ surface were determined by X-ray photoelectron spectroscopy (XPS), ultraviolet photoelectron spectroscopy (UPS) and metastable induced electron spectroscopy (MIES). Neutral impact collision ion scattering spectroscopy (NICISS) was used to determine the dye coverage on the TiO₂ surface.

It was found that Ti³⁺ surface defects were formed by Ar⁺ sputtering but not by pre-treatment through heating only. MIES analysis of the outer-most layer and density of states calculations showed the thiocyanate ligand of N719 dye was forced upward away from the TiO₂ surface. Both XPS and NICISS results indicate that the amount of adsorbed N719 dye decreased with increasing number of Ti³⁺ surface defects. Thus, generating surface defects reduces the ability of the dye to adsorb onto the TiO₂ surface. Heating as pre-treatment of the TiO₂ increases dye adsorption, without causing defects on TiO₂ surface.

4.2 Introduction

Dye sensitized solar cells (DSSCs) have attracted scientific and industrial attention due to their excellent performance, in particular under diffuse light conditions, low production cost, simple fabrication, low energy consumption of the fabrication process compared to silicon solar cells and being environment-friendly [1]. The basic structure of a DSSC has a sandwich configuration which consists of two conducting glass electrodes sandwiching a thin film made of a wide band gap semiconductor coated with a thin film of a photosensitiser dye, and a redox couple electrolyte solution, commonly the iodide-triiodide complex [2]. The best photoelectron conversion efficiency has been reported for cells based on titanium dioxide (TiO_2) [3]. TiO_2 has become the preferred material as wide band gap semiconductor in DSSCs because of its unique properties, such as the conduction band edge being positioned at a lower energy level than the excited state energy levels of many dyes allowing an efficient electron injection of dye electrons to the semiconductor. In addition, the usage of TiO_2 is widespread because it allows for a flexible manufacturing process, and nontoxicity as it is used in the production of pigments, paints, cosmetics, food products, and it is of low cost [4, 5].

In order to maximize and enhance the dye adsorption on TiO_2 surface, many studies focused on controlling and modifying the electronic properties of TiO_2 [6, 7]. In addition, many studies reported the effects of defects on the TiO_2 surface on the DSSC performance [8, 9]. Defects can act as important active sites for the adsorption of dyes molecules on the TiO_2 surface and can influence the photocatalytic properties of TiO_2 [10]. Creating surface defects on TiO_2 leads to the formation of unpaired electrons or Ti^{3+} forming a donor level in the electron structure of TiO_2 [11]. Various methods have been used to create surface defects, such as plasma treatment [12], UV irradiation [13], heating under vacuum, and high energy particles bombardment including electron, Ar^+ and γ -ray [14]. It is important to note that heating can influence the TiO_2 surface in two ways: removal of species adsorbed to the TiO_2 surface and generation of defects.

In the present work, we applied two different techniques for generating defects on the TiO_2 surface. The first method was heating the TiO_2 samples under controlled vacuum conditions. The second method involved sputtering of the TiO_2 surface with Ar^+ ions. The overall aim of the present work is to analyse the influence of the surface density of defects on the dye adsorption onto the TiO_2 surface.

4.3 Materials and Methods

4.3.1 Sample preparation

The samples were prepared by spreading a portion of the TiO₂ paste on the substrate using the doctor blade method [15]. Adhesive tape was used to cover about 2 mm in parallel on either side of the substrate. The thickness of the TiO₂ layer can be controlled with the thickness of the adhesive tape. The TiO₂ paste was flattened on the substrate using a razor blade. The TiO₂ samples were prepared from DSL 18NR-T paste from Dyesol (GreatCell Solar, Australia) containing 19.4 % TiO₂ with particle size averaging at 20 nm and are mostly of anatase structure [16]. The TiO₂ samples were heated to 450 °C for 30 minutes. Sintering TiO₂ samples removes the organic components from the TiO₂ paste and ensures good adhesion between TiO₂ particles on the substrate.

TiO₂ was pre-treated in UHV for generating defects prior to its immersion into the N719 solution following two different procedures. First, TiO₂ samples were heated to 200 °C to remove surface contaminations then sputtered with different Ar⁺ doses. Second, TiO₂ samples were heated at 4 temperature points: 200 °C, 400 °C, 500 °C and 600 °C. After applying the pre-treatments of the TiO₂ samples were immersed in dye solution for 24 hours at room temperature. Samples were then rinsed with ethanol to remove excess dye and blow dried with dry nitrogen.

4.3.2 Methods

Experimental details for neutral impact collision ion scattering spectroscopy (NICISS), X-ray photoelectron spectroscopy (XPS), ultraviolet photoelectron spectroscopy (UPS), and metastable induced electron spectroscopy (MIES) can be found in chapter 3. Singular value decomposition (SVD) was used to analyse a series of MIE spectra. The SVD procedure results in reference spectra which are used to reproduce the MIE spectra as a linear combination representing the sample surface with specific composition and electronic structure. A summary is provided in chapter 3 and more details of the procedure can be found in references [17, 18].

In order to identify the contributions of electron emission from specific functional groups to the reference spectra, the reference spectra were fitted with Gaussian curves where each Gaussian curve represents a range of electronic states of the functional groups forming the molecules on the surface. For this purpose, the UP and MIE reference spectra are fitted with a minimum number of Gaussian curves [19]. Each peak was assigned to a specific functional

group in the N719 dye. The density functional theory calculations (DFT) of N719 dye molecules were determined using the program package Gaussian 09 Revision-B.01-SMP. The DOS were extracted from the calculation files utilising Gauss View. The peak positions and full width at half maximum (FWHM) were fitting parameters that were kept the same for the UP and MIE spectra. The purpose of the fitting procedure is to determine to which degree a specific electron orbital is present in the electron spectra and it's the same in UP and MIE spectra. The peak intensities were allowed to be different for the UP and MIE spectra. This procedure was applied to both pre-heated sputtered and pre-heated only TiO₂ surfaces after dye adsorption.

4.4 Results and Discussion

4.4.1 Study of Ru depth profile and dye adsorption

NICISS was applied for determining concentration depth profile of N719 deposited onto TiO₂ sample. Figure 4-1A shows the concentration depth profile of undyed and dyed TiO₂, the signals in time of flight (TOF) spectra can be assigned to titanium (4.5 μ s), oxygen (6.4 μ s), and carbon (7.4 μ s). After TiO₂ sample was immersed in N719 dye a very broad and intense signal appeared at \sim 4 μ s and is attributed to Ru adsorbed on the sample. NICISS was then applied to measure the concentration depth profiles of pre-heated, and pre-heated and sputtered TiO₂ substrates immersed in N719 dye. The total amount of adsorbed dye was determined by integrating the concentration depth profiles generated by NICISS which has been shown to be a direct and accurate method for determining the amount of adsorbed dye [20]. The results show that the Ru concentration depth profiles have variations in the width as well as in the depth of the profiles at which the maximum occurs Figure 4-1B. The coverage of the TiO₂ surface with N719 is shown in Figure 4-1C and Figure 4-1D, for the pre-heated, and pre-heated and sputtered TiO₂, respectively. For the pre-heated samples, a clear increase in dye coverage on TiO₂ can be seen, while for the pre-heated-sputtered TiO₂ samples the highest coverage is at low sputtering doses with a monotonic decrease with increasing sputter dose. Figure 4-2A and B shows the ruthenium (Ru) concentration depth profiles of the pre-heated and pre-heated-sputtered samples after dye immersion.

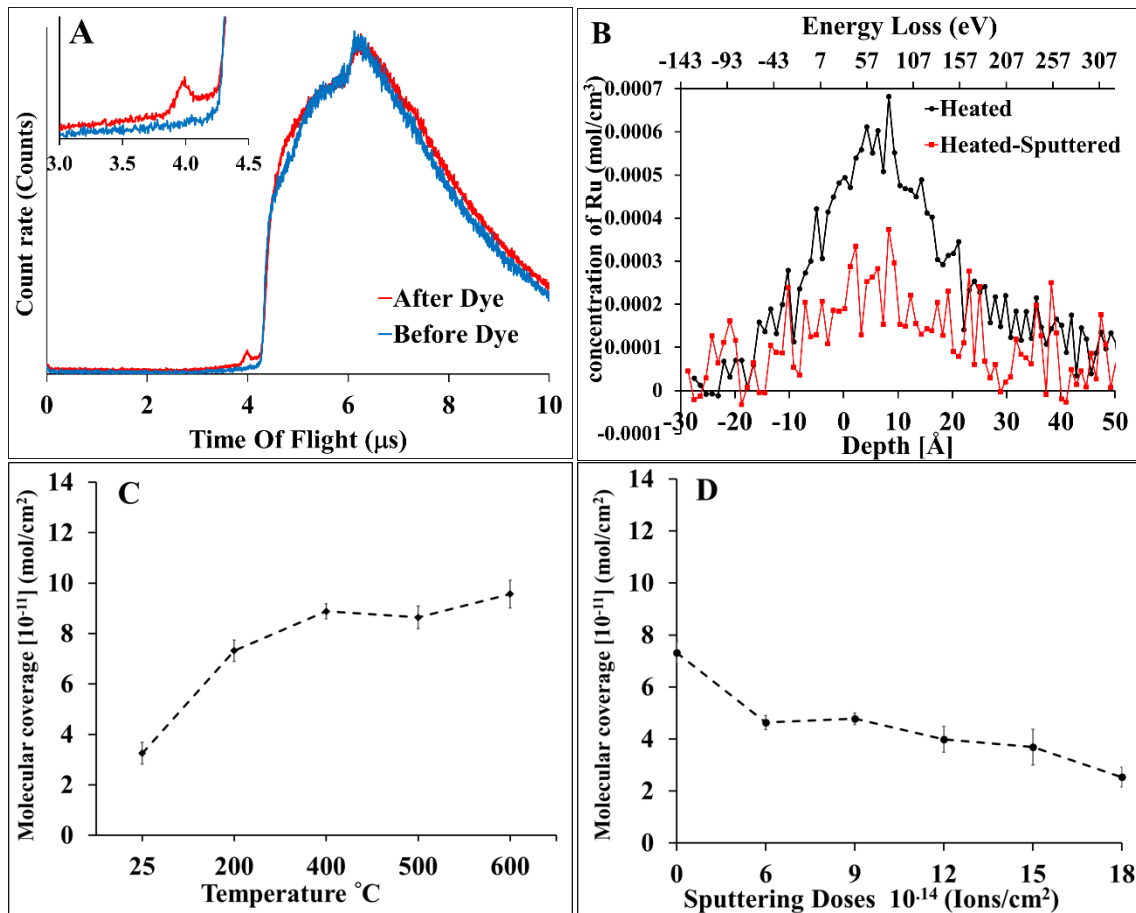


Figure 4-1: A) NICISS spectra of TiO_2 before and after immersion in N719 dye. The inset shows the peak at ~ 4 related to Ru. B) The concentration depth profile of N719 dye on a pre-heated 600 $^{\circ}\text{C}$ TiO_2 surface and a pre-heated 200 $^{\circ}\text{C}$ then sputtered $18 \cdot 10^{14}$ ions/cm^2 TiO_2 surface are shown in. C) Molecular coverage of Dye N719 as a function of temperature and D) as a function of sputtering doses.

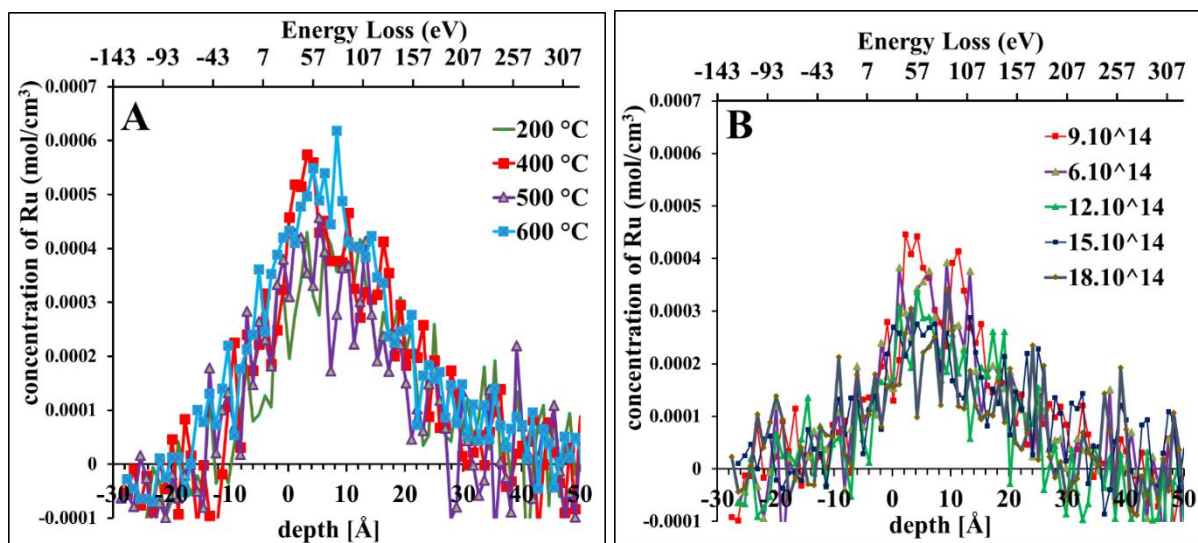


Figure 4-2: Concentration depth profile of dye N719 on A) pre-heated TiO₂ surface and B) pre-heated-sputtered TiO₂ surface.

4.4.2 The Chemical state and component concentrations

XPS was performed on all samples, and high-resolution XP spectra for the pre-treated TiO₂ samples were recorded. The peak positions and the relative peak intensities for the pre-treated samples after dye adsorption are listed in Table 4.1 and Table 4.2. All samples were calibrated with the C-C bond at 285.0 eV.

Table 4.1: Peak positions (eV) with uncertainty of ± 0.2 and the relative peak intensities ± 0.3 for the ascending temperature pre-treated TiO_2 samples.

Element/Temperature		Untreated	200°C	400 °C	500°C	600°C
<i>C1</i>	Position	285.0	285.0	285.0	285.0	285.0
	intensity%	8.7	5.6	11.3	12.2	12.4
<i>C2</i>	Position	286.1	285.9	286.1	286.2	286.2
	intensity %	7.4	9.7	4.6	4.6	5.8
<i>C3</i>	Position	288.8	289.1	288.6	288.9	288.9
	intensity %	2.2	1.4	2.8	2.2	1.9
<i>O1</i>	Position	530.3	530.4	530.1	530.2	530.2
	intensity %	42.0	48.4	48.2	43.4	48.2
<i>O2</i>	Position	530.9	531.1	530.9	530.9	531.1
	intensity %	13.3	7.4	6.3	11.0	6.0
<i>O3</i>	Position	532.1	532.2	531.8	532.0	532.1
	intensity %	4.9	4.8	4.2	3.8	3.5
<i>Ti (Ti⁴⁺)</i>	Position	459.2	459.2	458.9	459.0	459.0
	intensity %	19.2	19.5	18.4	18.7	18.6
<i>Ru</i>	Position	281.3	281.3	281.1	281.0	281.1
	intensity %	0.16	0.26	0.3	0.30	0.29
<i>N_{pyd}</i>	Position	400.4	400.4	400.2	400.2	400.2
	intensity %	1.6	1.6	2.3	1.9	1.9
<i>N_{NCS}</i>	Position	398.6	398.4	398.0	397.9	398.1
	intensity %	0.5	0.8	0.9	0.9	0.8
<i>N_{TBA}</i>	Position	0.0	401.6	0.0	402.3	402.3
	intensity %	0.0	0.0	0.0	0.2	0.2
<i>S</i>	Position	0.0	161.7	162.1	162.2	162.0
	intensity %	0.0	0.4	0.7	0.8	0.4

Table 4.2: Peak positions (eV) with uncertainty of ± 0.2 and the relative peak intensities ± 0.4 for the Ar⁺ sputtered at different doses pre-treated TiO₂ samples.

Element/Dose [ions/cm ²]		6·10 ¹⁴	9·10 ¹⁴	12·10 ¹⁴	15·10 ¹⁴	18·10 ¹⁴
C1	Position	285.0	285.0	285.0	285.0	285.0
	intensity %	9.2	8.2	7.7	6.7	5.3
C2	Position	286.1	286.1	286.2	286.3	286.2
	intensity %	6.1	6.6	3.6	3.1	5.1
C3	Position	289.0	289.0	289.0	289.1	289.4
	intensity %	1.3	1.3	1.4	0.9	0.9
O1	Position	530.3	530.3	530.3	530.3	530.6
	intensity %	52.5	47.2	51.0	52.9	54.2
O2	Position	531.3	531.2	531.2	530.9	531.5
	intensity %	5.7	9.7	9.7	7.3	7.9
O3	Position	532.0	532.4	532.3	531.7	532.4
	intensity %	2.7	4.1	3.6	5.9	4.0
Ti (Ti ⁴⁺)	Position	459.1	459.1	459.1	459.0	459.3
	intensity %	19.6	19.8	20.7	21.5	21.0
Ti (Ti ³⁺) after sputtering	Position	457.5	457.4	457.4	457.6	457.7
	intensity %	1.6	2.2	2.3	2.7	3.2
Ru	Position	281.1	281.1	281.1	281.2	281.5
	intensity %	0.2	0.22	0.18	0.1	0.12
N _{pyd}	Position	400.3	400.3	400.3	400.3	400.7
	intensity %	1.4	1.6	1.2	0.9	1.0
N _{NCS}	Position	398.1	398.1	398.1	398.0	398.2
	intensity %	0.6	0.7	0.5	0.3	0.3
N _{TBA}	Position	402.3	402.2	401.9	0.0	-0.2
	intensity %	0.3	0.2	0.1	0.0	0.0
S1	Position	162.0	162.0	162.1	162.1	162.4
	intensity %	0.3	0.3	0.3	0.1	0.1
S2	Position	162.8	162.6	163.0	162.7	163.0
	intensity %	0.2	0.2	0.1	0.2	0.1

Heating the samples did not affect the Ti oxidation state, indicating that the heat treatment under vacuum conditions does not affect measurably induced Ti^{3+} defects. In contrast, the heated and then sputtered samples have an additional Ti component at 457.5 ± 0.1 eV; attributed to Ti^{3+} defect states [21]. A high-resolution scan of the Ti 2p spectra is shown in Figure 4-3A. As the sputtering doses increased, the intensity of Ti^{3+} defect states increased as shown in Figure 4-3B.

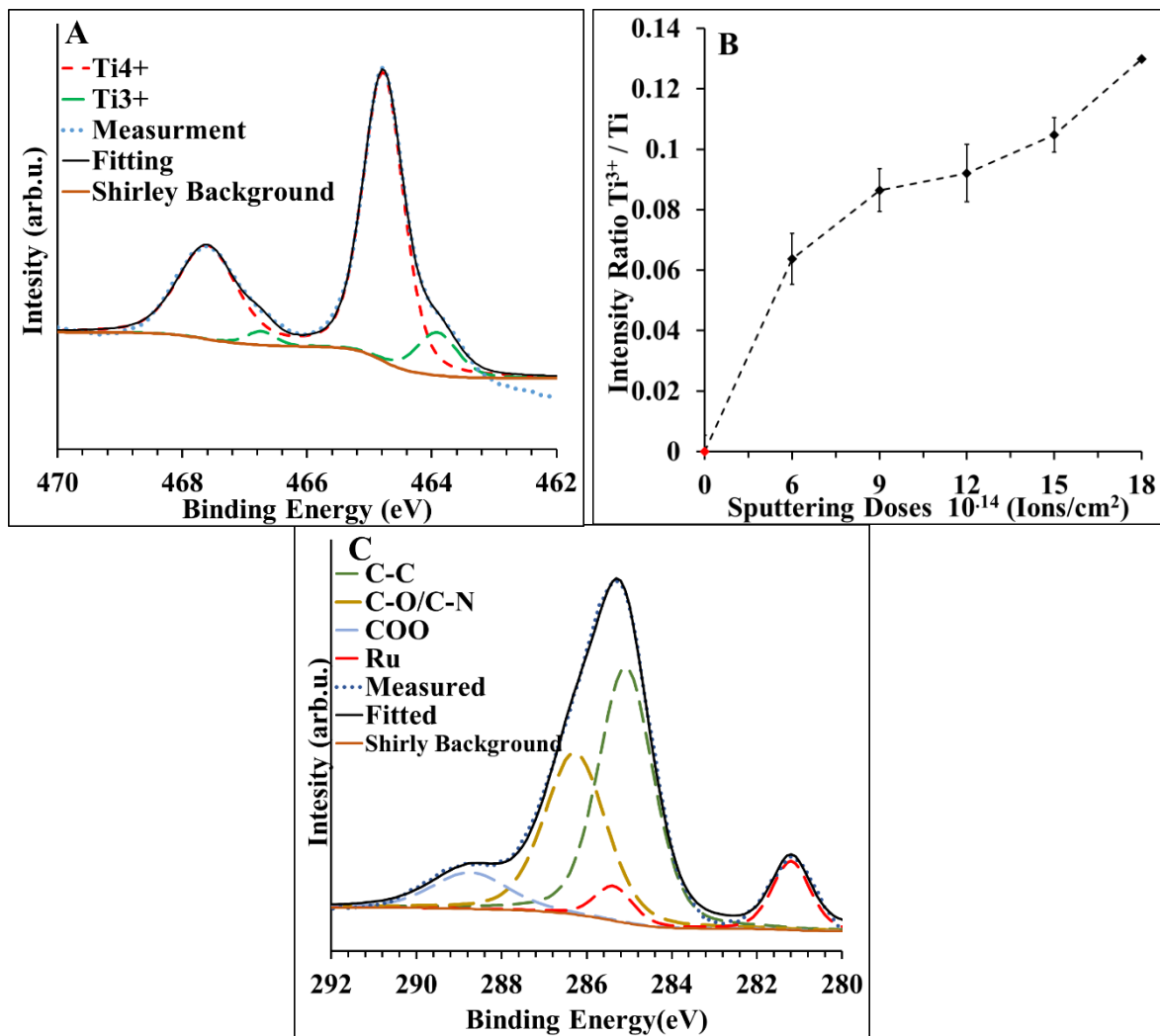


Figure 4-3: A) High-resolution scan of Ti 2p spectrum showing Ti^{4+} and the defect Ti^{3+} at a sputtering dose of ($18 \cdot 10^{14}$ ions/cm²). B) Defect concentrations are represented by the ratio of Ti^{3+} to Ti peak as a function of sputtering doses (Red data represent 200 °C heated sample without sputtering). C) High-resolution scan of C1s and Ru 3d. C-C at 285 eV, C-O at 286.7 eV and COO at 289.3 eV and 281.7 eV correspond to Ru 3d_{5/2} (sample 200 °C Heating).

Following the immersion of the TiO₂ substrates into the dye solution, XP spectra were acquired. Peaks arising from the dye layer corresponding to ruthenium (Ru 3d) at $281.7[22] \pm 0.2$ eV as shown in Figure 4-3C, nitrogen (N 1s) at 402.6 ± 0.2 eV, 400.5 ± 0.2 eV and 398.4 ± 0.2 eV as can be seen in Figure 4-4A and B, and sulphur (S 2p) at 162.1 ± 0.2 eV [22] as in Figure 4-4C and D, are indicative of successful dye adsorption. The high resolution C1s and Ru 3d spectrum was fitted with 5 peaks. The Ru 3d_{5/2} located at 281.2 ± 0.2 eV and Ru 3d_{3/2} at 285.3 ± 0.2 eV with the latter overlapping with the carbon C1s contribution in the spectrum. Fitting the C1s spectra resulted in three peaks, the main C peak located at 285.0 eV is attributed to C-C bonds, the peak at 286.7 ± 0.2 eV corresponds to C-O, and peak at 289.3 ± 0.2 eV corresponds to COObonds [23].

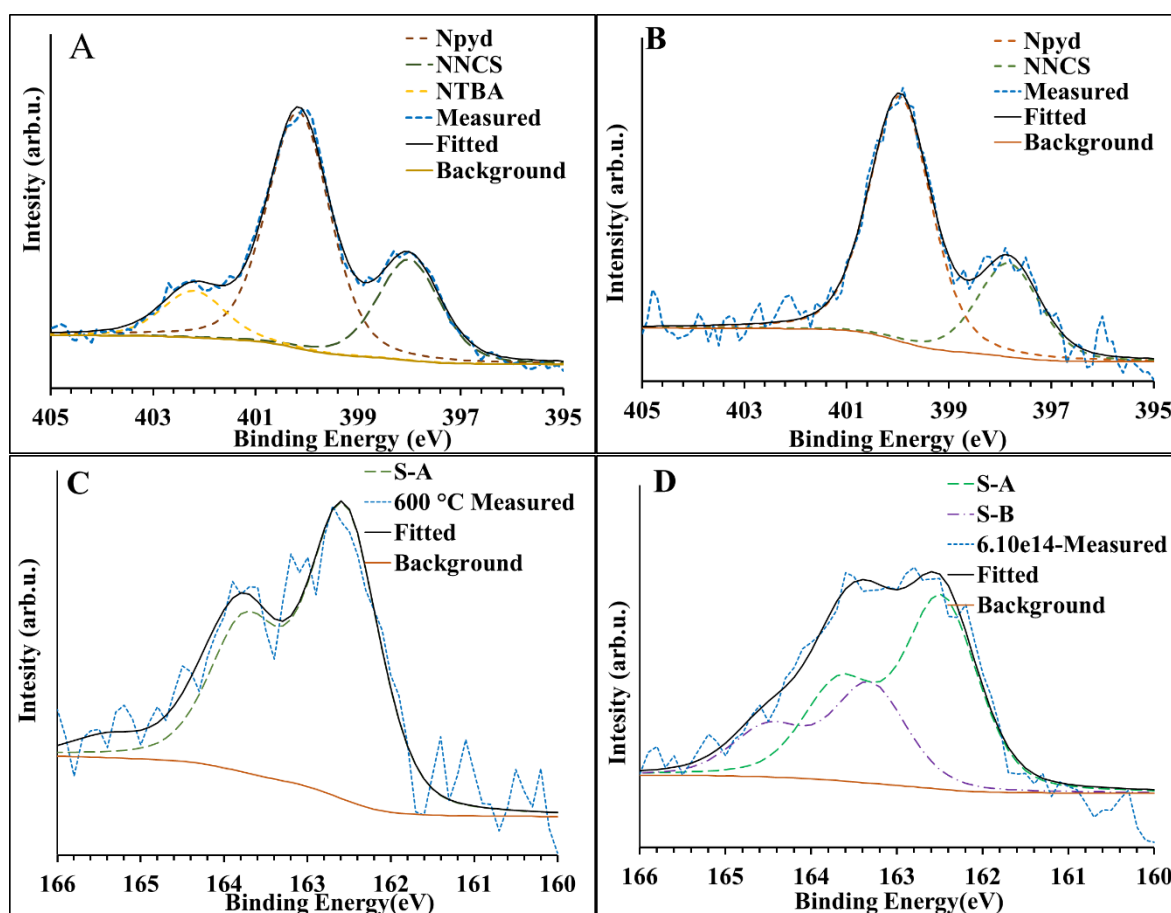


Figure 4-4: High-resolution scan of N1s spectra heated-sputtered ($6 \cdot 10^{14}$) TiO₂. The increase of NTBA related to pre-sputtered TiO₂ with low doses, B) High-resolution scan of N1s spectra pre-heated TiO₂ at 400 °C. C) High-resolution S2p spectra of Heated (600 °C) TiO₂ and D) High-resolution S2p spectra of Heated-sputtered ($6 \cdot 10^{14}$ ions/cm²) TiO₂ fitted with two spin S contributions.

Changes in the amount of dye adsorption configuration induced by the treatments

Ruthenium

The influence of the two treatments on the amount of dye adsorbed on the TiO₂ surface was measured by comparing the intensity ratio between Ru/Ti for all samples. For the pre-heated TiO₂ samples, the Ru/Ti ratio is increasing with an increase in temperature, which means that the dye adsorption is increasing when the heating temperature is increased, as shown in Figure 4-5A. During heating, surface contaminations like moisture and hydrocarbons are removed, which allows for more dye molecules' adsorption to the TiO₂ surface. The heated-sputtered TiO₂ samples show a decreasing Ru/Ti ratio with increasing sputtering doses, as shown in Figure 4-5B. This decrease is occurring even though sputtering decreases surface contaminations more than the heating treatment only. However, sputtering also induces defects due to the preferential removal of oxygen and the formation of Ti³⁺ defects. Introducing oxygen vacancies on a TiO₂ surface will reduce the Ti⁴⁺ oxidation state and affect the electrostatic interactions of the -COO⁻ groups of the N719 dye with the TiO₂. The interactions between the Ti⁴⁺ oxidation state and the -COO⁻ are stronger than those with the Ti³⁺ oxidation state [24].

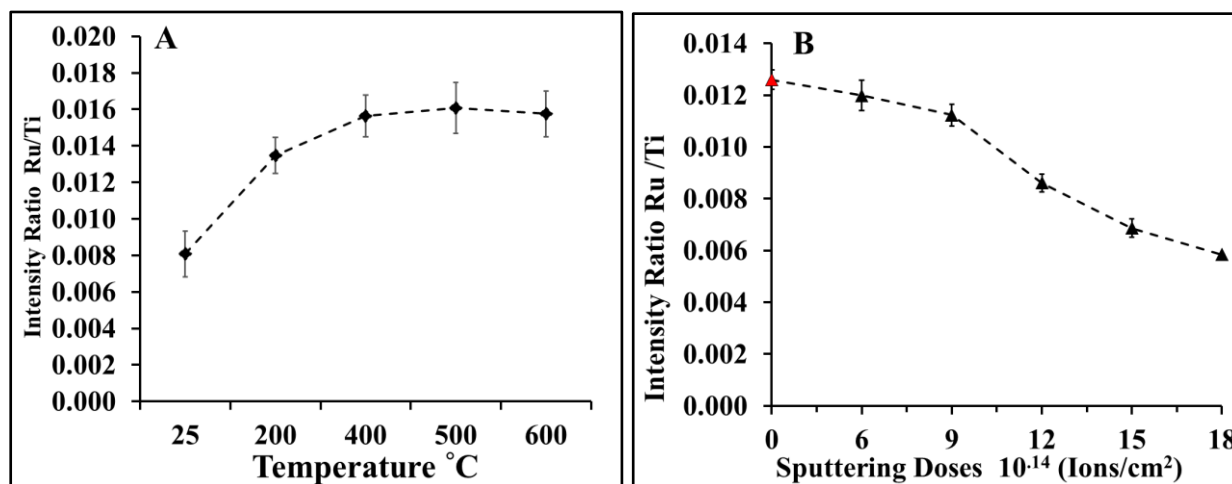


Figure 4-5: A) Ratio Intensities of Ru to Ti as a function of heating temperature, B) as a function of sputtering doses. (Red data represent 200 °C heated sample without sputtering)

Nitrogen

There are six nitrogen atoms surrounding the Ru atom in the N719 dye. In order to characterize the dye coverage on the TiO₂ sample, a high-resolution scan of the N1s peaks was measured and is shown in Figure 4-4A. The peak located at 400.5 ± 0.2 eV represents N from the pyridine

ligands in the dye (N_{pyd}). The second peak located at 398.4 ± 0.2 eV was assigned to N in the thiocyanate groups (N_{NCS}). An increase in the peak located at 402.6 ± 0.2 eV appeared only with samples pre-heated at (500 °C and 600 °C) and with samples pre-heated-sputtered with doses ($6 \cdot 10^{14}$ ions/cm², $9 \cdot 10^{14}$ ions/cm² and $12 \cdot 10^{14}$ ions/cm²) and was assigned to nitrogen atoms in N_{TBA} as its illustrate in Figure 4-4B. This small intensity peak could indicate that a small amount of TBA ions are present, or they are located deeper in the molecular surface layers. In addition, it may also be under the detection limit of XPS.

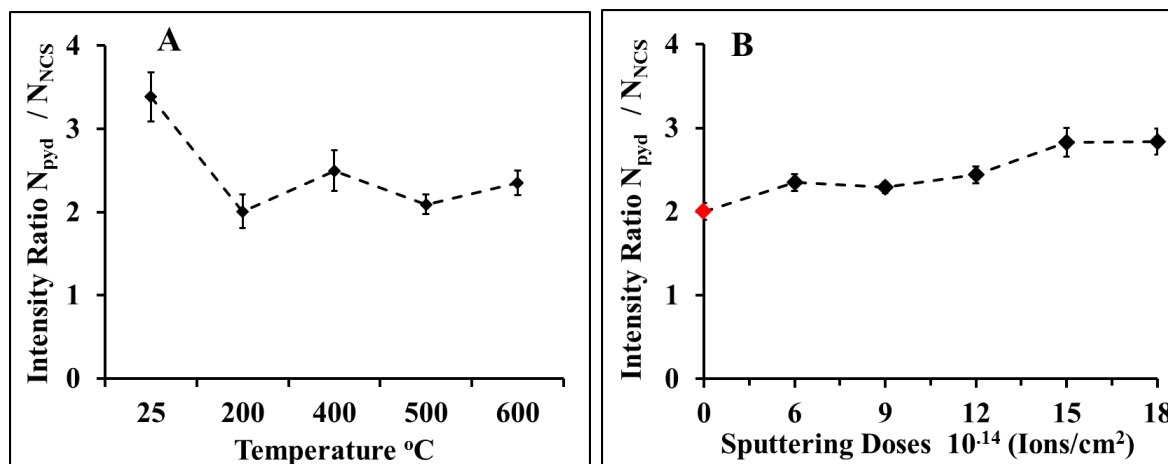


Figure 4-6: A) Ratio of XPS intensities between $N_{\text{pyd}}/ N_{\text{NCS}}$, as a function of heating temperature. B) As a function of pre-heating- sputtering doses. (Red data represent 200 °C heated sample without sputtering)

The $N_{\text{pyd}}: N_{\text{NCS}}$ (2:1) ratio for the pre-heated samples is close to the ratio of the groups in the dye molecules apart from the non-heated sample (25 °C) which had a larger ratio as can be seen in Figure 4-6A. This indicates a stable orientation of the dye molecules when they adsorb on a pre-heated TiO_2 surface. In contrast, for the pre-heated-sputtered TiO_2 samples the same ratio increased with increasing sputter doses as in Figure 4-6B. This suggests that increasing the number of defects on the TiO_2 surface results in a rearrangement of the dye molecules with the N_{NCS} orienting more toward the TiO_2 surface with increasing number of defects.

Sulphur

The effect of the pre-treatments methods on S can be seen in Figure 4-4C and Figure 4-4D. The S 2p spectra of the pre-heated TiO_2 samples were fitted with a single S contribution which is related to the NCS ligands. For the pre-heated-sputtered TiO_2 samples fitted with two S doublet contributions had to be used for fitting the S peak in XP spectra. The larger S 2p doublet has a similar binding energy to the one in pre-heated samples (S-A) and is found at 162.2 ± 0.2 eV. The second doublet is shifted by approximately 0.75 eV toward higher binding and is found

at 162.9 ± 0.2 eV. This contribution is assigned to S in the NCS group of the dye interacting with the TiO_2 surface (S-B) [25]. Figure 4-7 shows the ratio intensity of S-A/Ru and S-B/Ru with different sputtering doses. The intensity ratio of S-A/Ru decreases, while the intensity ratio S-B/Ru increases with increasing Ti^{3+} defect states, where the more TiO_2 defects created allows for more oxidation species to be adsorbed like S.

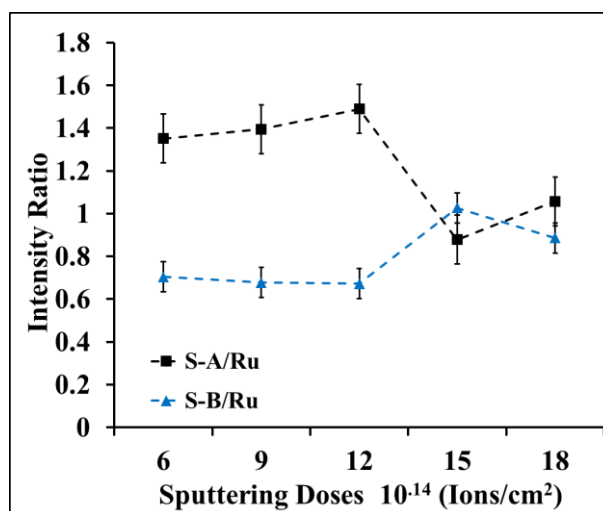


Figure 4-7 Ratio intensity of S-A/Ru and S-B/Ru with different sputtering doses.

From the previous results, the recording of the second S-B peak and the increase in the S-B/Ru ratio together with the increase in the $N_{\text{pyd}}: N_{\text{NCS}}$ ratio indicate that NCS group is forced toward the TiO_2 surface. This suggests reduced dye adsorption and altered orientation of the dye at the TiO_2 surface more in the presence of Ti^{3+} oxidation state. It has been shown previously that thiocyanate ligands might interact with TiO_2 surface, and it is plausible that this is occurring in our samples as well [26]. XPS also shows that the bonds were formed between NCS groups and the TiO_2 surface in the pre-heated sputtered TiO_2 .

A similar conclusion to NICISS can be drawn from XPS analysis, where for the pre-heated samples, an increase in the dye adsorption occurs, and the adsorption decreases with an increase in the sputtering doses in the pre-heated-sputtered TiO_2 surface. Therefore, the change in nitrogen and sulphur intensities measured by XPS is showing how the dye reorients and has different types of bonding based on the different pre-treated TiO_2 surfaces.

We can conclude that the dye interacts with TiO_2 substrate through NCS group and this interaction increases as the surface defects Ti^{3+} increased.

4.4.3 Analysis of electronic properties with UP spectra

UPS measurements were recorded for untreated and treated TiO_2 surfaces. Figure 4-8 shows

the UP spectra of pre-heated and pre-heated-sputtered TiO₂ samples. Both sets of spectra show similar features with a double peak structure corresponding to O 2p with binding energy at 5.3 eV and 7.8 eV, assigned to oxygen planes [27]. Heating the samples did not create any surface defects as no peak related to Ti³⁺ could be found. The Ti³⁺ occurs around 1.1 eV. For the heated-sputtered TiO₂ samples, an additional peak appeared around 1.1 eV which can be attributed to Ti³⁺ in Figure 4-8B [24, 27, 28]. The intensity of this peak increases with increasing sputter doses which also corresponds to the appearance of the Ti³⁺ peak in the XP spectra. After dye adsorption a new peak at 2.1 eV appeared in all UP spectra which are related to the dye adsorption on TiO₂ surface as shown in Figure 4-9.

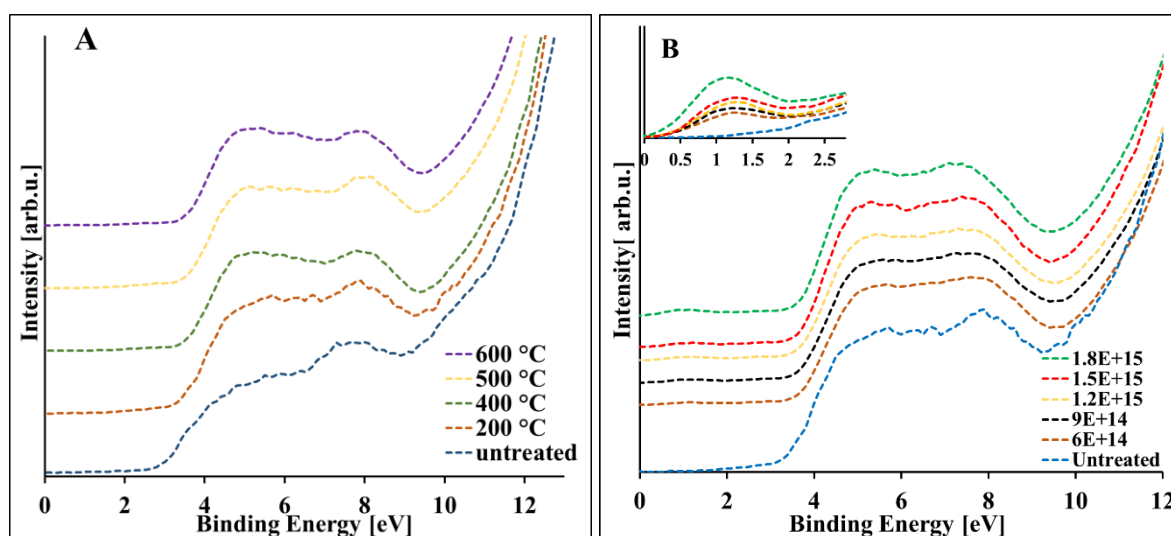


Figure 4-8: UP spectra A) pre-heated TiO₂ surface as a function of heating temperatures (B) pre-heated- sputtered TiO₂ surface as a function of doses. The inset shows UP spectra of the emission of Ti³⁺ on sputtered TiO₂ surface with different doses.

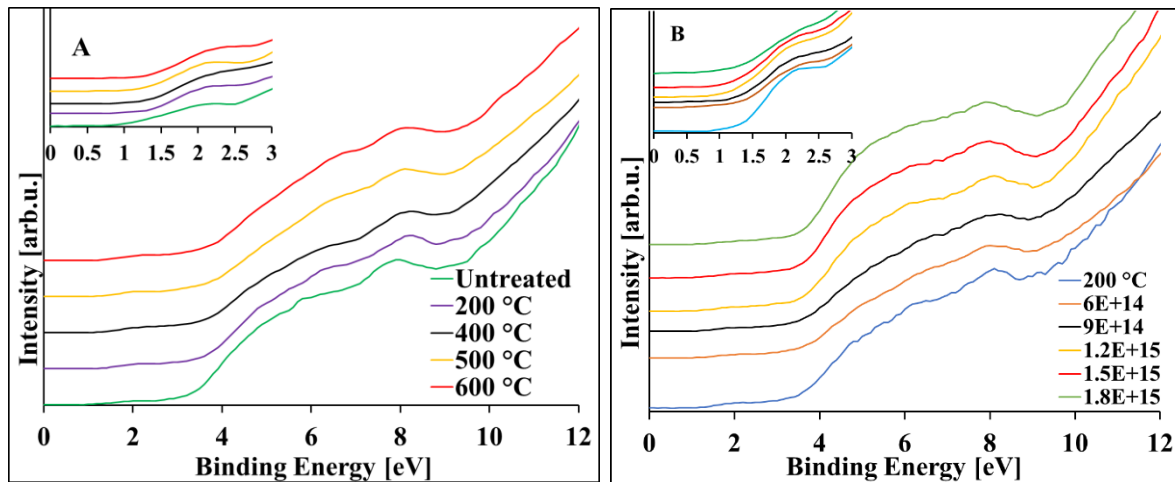


Figure 4-9: UP spectra after dye adsorption for (A) pre-heated (B) pre-heated- sputtered TiO_2 surface and. The inset shows UP spectra showing the emission in the valance band region after dye adsorption

The work function for both treatments was measured and provided in Figure 4-10. In both treatments, there is a similar change in work function, where after the treatments, the work function stable at 4.5 ± 0.1 eV, and after dye adsorption, the work function decreased to $\sim 4.1 \pm 0.1$ eV.

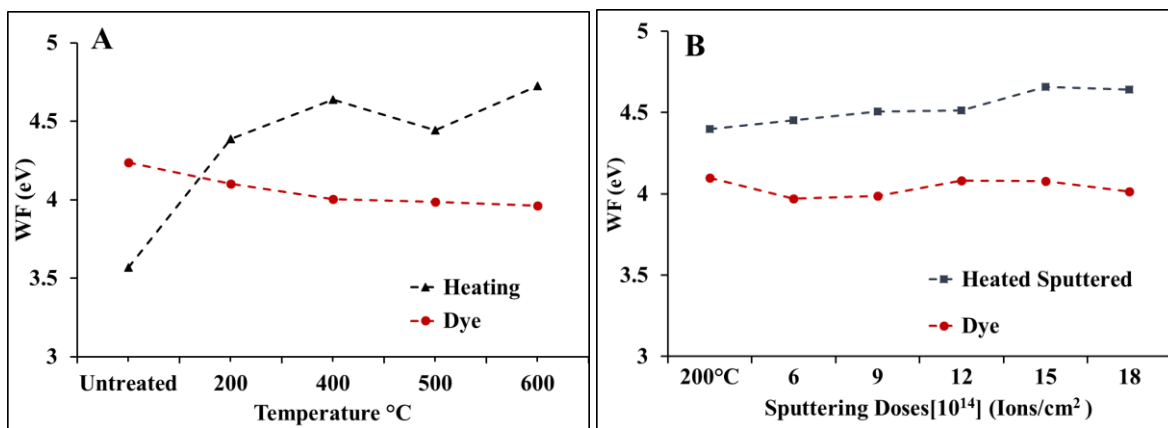


Figure 4-10: The work function (± 0.1 eV) of A) pre-heated and B) pre-heated-sputtered TiO_2 before and after dye adsorption.

4.4.4 Analysis of MIE spectra

Valence spectra of MIES have been measured for both treatments after dye adsorption Figure 4-11. As the temperature increases, the features become more prominent at ~ 2.4 eV and ~ 3.8 eV, as shown in Figure 4-11A, while in the pre-heated sputtered samples, the spectra had the smoothest spectrum at highest sputtering doses at ~ 2.4 eV and ~ 3.8 eV Figure 4-11B. Those peaks are an indication of dye adsorption on TiO_2 . The SVD was further used to analyze the

MIE spectra for both treatments.

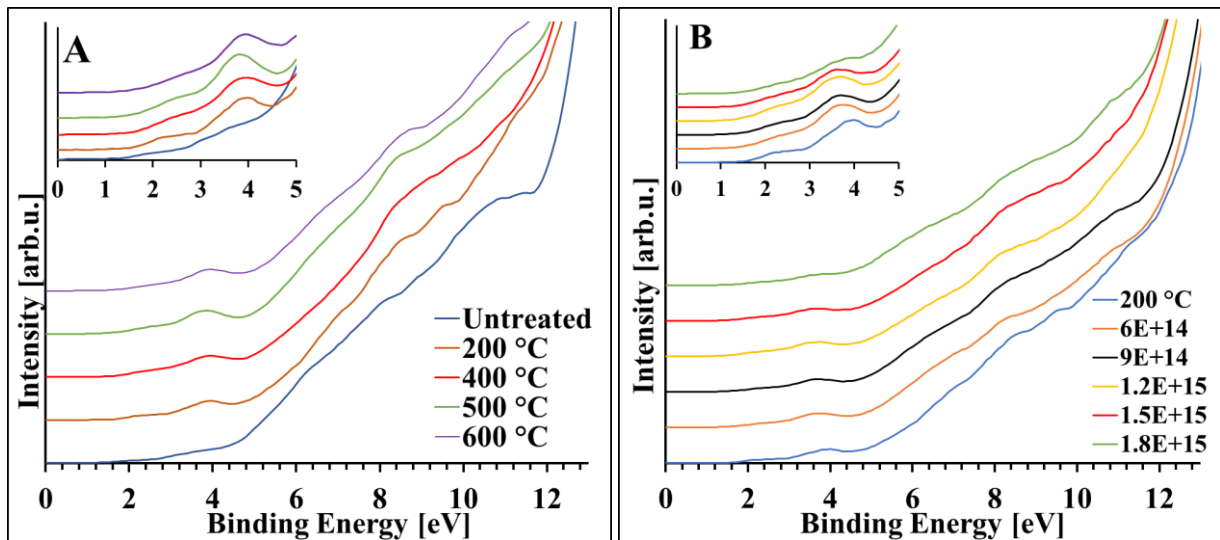


Figure 4-11: MIE spectra after dye adsorption for (A) pre-heated (B) pre-heated- sputtered TiO_2 surface and. The inset shows MIE spectra showing the emission in the valance band region after dye adsorption.

4.4.5 Singular Value Decomposition

SVD was applied to evaluate the components quantitatively in the MIE spectra for both treatments after dye adsorption. In MIE spectra, the SVD analysis of both sets of treatments can be described with two reference spectra; each is shown in Figure 4-12A and Figure 4-12C. Reference spectra 1 in pre-heated and pre-heated sputtered dyed samples are similar to the MIE spectra of untreated-dyed TiO_2 samples, thus they represent the dye adsorbed on the sample.

In addition, Reference spectra 2 in both pre-heated and pre-heated-sputtered dyed samples are similar to the MIE spectra of the pre-heated pristine TiO_2 sample. Thus, they can be identified as representing the TiO_2 substrate.

SVD reveals the surface coverage of the dye via weighting factors for each base spectrum as shown in Figure 4-12B and Figure 4-12D.

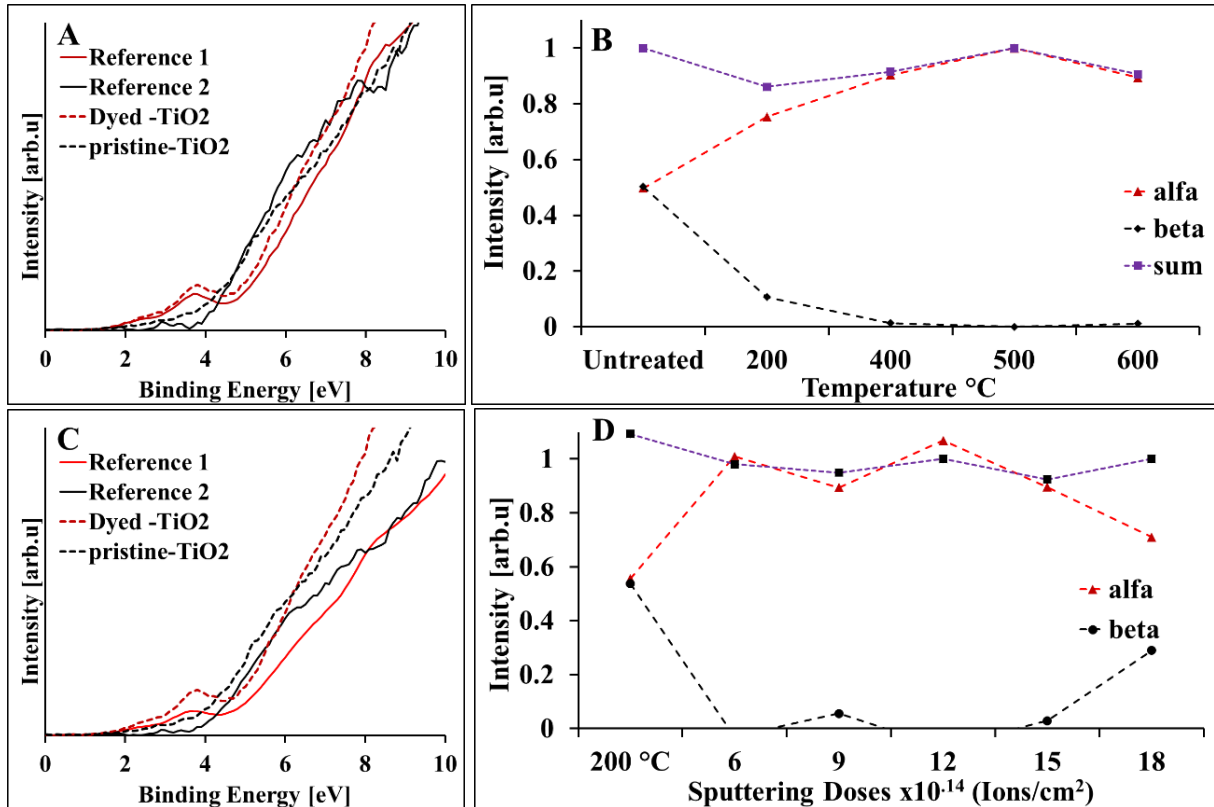


Figure 4-12: (A), (C) The decomposed MIES reference spectra using SVD and the comparison with the dyed and undyed TiO₂. (B) and (D) are the weighting factors of the individual reference spectra for fitting MIES spectra of pre-heated and pre-heated-sputtered dyed on TiO₂ surface. Where alfa represents the dye and beta represents pristine TiO₂ surface.

The related weighting factors for the SVD of MIE spectra reveal the composition ratio of the functional groups in the outermost surface layer. In pre-heated TiO₂ samples the dye coverage was increasing, and a complete dye surface coverage was found at pre-treatment with heating at 500 °C, then there was a slight decrease to 90 % at 600 °C. While in the pre-heated-sputtered TiO₂ samples the weighting factors for the SVD reveal that the maximum coverage of the dye was at doses $6 \cdot 10^{14}$ to $12 \cdot 10^{14}$. The weighting factors of both treatments revealed that the dye adsorption increases with increasing temperature, while the adsorption decreases with increasing sputtering doses. It is also important to note that the MIE reference spectra are the same for both cases. This means that the structure of the outermost part of the dye layer on the TiO₂ surface is the same for both surface treatments.

4.4.6 Gaussian Fitting

To analyze the dye orientation, both SVD reference spectra were fitted with minimum numbers of Gaussian curves to fit into a spectrum following the procedure described in [19]. The fitted

peaks were assigned to the functional groups in the N719 dye by comparing the peak position with the theoretically calculated DOS. The peak positions and FWHM were kept constant between UPS and MIES, and only the intensity was used as a fitting parameter.

The reference spectra were fitted with Gaussian curves. The peaks' binding energy was compared with theoretically calculated DOS to relate each peak to its respective functional group in dye N719 Figure 4-13. The DOS calculations are shown as vertical lines. The dominant peaks are located at 2 eV and ~ 3.7 eV correspond to Ru with NCS groups, and peaks between 6 eV to ~ 9 eV correspond to pyridine ring and carboxyl groups in N719. We can conclude from the Gaussian fitting and the weighting factors for each treatment that all the dye N719 functional groups were observed on the outermost layer. The HOMO level is found in the NCS ligands of Ru based dyes where the reduction of the oxidized dye through these ligands is favored in solar cells and hence, it is preferred for the NCS group to be projected away from the TiO₂ surface towards the electrolyte [29].

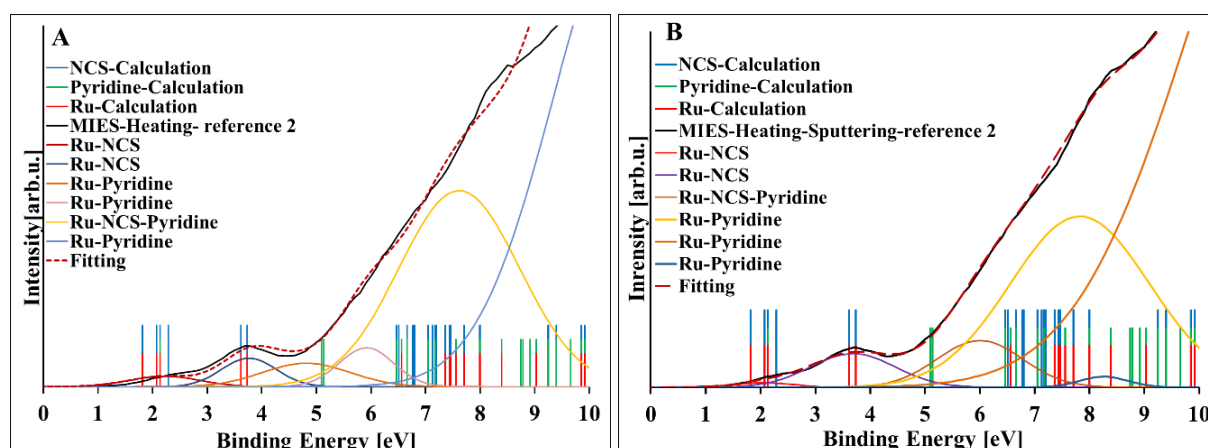


Figure 4-13: Gaussian peak fitting for MIES reference spectra-2 in A) pre-heated, B) pre-heated-sputtered TiO₂ samples. The calculated DOS using DFT calculations are shown as vertical lines.

The dye adsorption increased in the pre-heated TiO₂ samples, while the adsorption decreased as the defects increased in pre-heated-sputtered TiO₂. The main indication is through determining the amount of adsorbed dye via the Ru intensity in XPS and NISS. The findings are also supported by the XPS results of N, C, O, and S. The second S peak observed at higher binding energy in the pre-heated-sputtered TiO₂ samples indicating that S atoms in NCS groups interact strongly with TiO₂ surface. Furthermore, the intensity ratio of N_{pyd}/N_{NCS} drops when heated but stays constant for all heating temperatures. This means that the orientation of the dye molecules on the heated titania surface does not change once water and adventitious

hydrocarbons have been removed through mild heating at 200 °C. For the sputtered surfaces $N_{\text{pyd}}/N_{\text{NCS}}$ ratio increased with increasing sputter doses, indicating a preferential orientation of the dye molecules where NCS ligand are oriented toward TiO_2 surface and N_{pyd} away from the surface with increasing sputter dose.

All the dye ligands were observed in MIES. The MIE spectra are the same for both titania treatments. The spectra indicate that the composition of the outermost part of the dye layer is the same and that any preferred orientation of the dyes is just occurring within the dye layer and does not influence the outermost part of the dye layer.

The obtained results show that the dye N719 adsorbed on TiO_2 in different configuration depending on pre-treatment method

4.5 Conclusions

Both NICISS and XPS indicate that pre-heating treatment of TiO_2 surface resulted in increased dye adsorption with little alteration of the TiO_2 surface. However, dye adsorption on the heated and sputtered TiO_2 surface decreases with increasing sputter dose and has a strong inverse correlation with the concentration of Ti^{3+} surface defects created by Ar^+ sputtering. The noted change in NCS orientation suggests that introducing Ti^{3+} surface defects on TiO_2 samples results in an altered orientation of the NCS ligands toward the TiO_2 surface thus, reducing the dye adsorption. The MIE spectra are the same for both titania treatments. This shows that the composition of the outermost part of the dye layer is the same and that any preferred orientation of the dyes is occurring only within the dye layer and does not influence the outermost part of the dye layer.

In summary, heating of TiO_2 surface results in the removal of hydrocarbons leading to better dye adsorption on TiO_2 surface. Whereas, heating and Ar^+ sputtering results in creation of surface defects that lead to reduced dye adsorption on TiO_2 surface. Therefore, our data suggests that heating pre-treatment of TiO_2 surfaces prior to dye adsorption might result in a more efficient DSSC production.

4.6 References

1. Ghann, W.; Kang, H.; Sheikh, T.; Yadav, S.; Chavez-Gil, T.; Nesbitt, F.; Uddin, J., Fabrication, Optimization and Characterization of Natural Dye Sensitized Solar Cell. *Sci Rep* **2017**, *7*, 41470.
2. Grätzel, M., Conversion of Sunlight to Electric Power by Nanocrystalline Dye-Sensitized Solar Cells. *Journal of Photochemistry and Photobiology A: Chemistry* **2004**, 3–14.
3. Subramanian, A.; Wang, H.-W., Effect of Hydroxyl Group Attachment on Tio₂ Films for Dye-Sensitized Solar Cells. *Applied Surface Science* **2012**, *258*, 7833-7838.
4. Zhang, Q.; Dandeneau, C. S.; Zhou, X.; Cao, G., Zno Nanostructures for Dye-Sensitized Solar Cells. *Advanced Materials* **2009**, *21*, 4087-4108.
5. Mehmood, U.; Rahman, S.; Harrabi, K.; Hussein, I. A.; Reddy, B. V. S., Recent Advances in Dye Sensitized Solar Cells. *Advances in Materials Science and Engineering* **2014**, 1-12.
6. Kohtani, S.; Kawashima, A.; Masuda, F.; Sumi, M.; Kitagawa, Y.; Yoshioka, E.; Hasegawa, Y.; Miyabe, H., Chiral Alpha-Hydroxy Acid-Coadsorbed Tio₂ Photocatalysts for Asymmetric Induction in Hydrogenation of Aromatic Ketones. *Chemical communications* **2018**, *54*, 12610-12613.
7. Kohtani, S.; Kawashima, A.; Miyabe, H., Reactivity of Trapped and Accumulated Electrons in Titanium Dioxide Photocatalysis. *Catalysts* **2017**, *7*, 1-16.
8. Zhao, H.; Pan, F.; Li, Y., A Review on the Effects of Tio₂ Surface Point Defects on Co₂ Photoreduction with H₂O. *Journal of Materiomics* **2017**, *3*, 17-32.
9. Moma, J.; Baloyi, J., Modified Titanium Dioxide for Photocatalytic Applications. In *Photocatalysts - Applications and Attributes*, Khan, S. B.; Akhtar, K., Eds. IntechOpen: 2018.
10. Yu, Y.; Wu, K.; Wang, D., Dye-Sensitized Solar Cells with Modified Tio₂ Surface Chemical States: The Role of Ti³⁺. *Applied Physics Letters* **2011**, *99*, 1-4.
11. Pan, X.; Yang, M. Q.; Fu, X.; Zhang, N.; Xu, Y. J., Defective Tio₂ with Oxygen Vacancies: Synthesis, Properties and Photocatalytic Applications. *Nanoscale* **2013**, *5*, 3601-14.
12. Nakamura, I.; Negishi, N.; Kutsuna, S.; Ihara, T.; Sugihara, S.; Takeuchi, K., Role of Oxygen Vacancy in the Plasma-Treated Tio₂ Photocatalyst with Visible Light Activity for No Removal. *Molecular Catalysis* **2000**, *161*, 205-212.
13. Mezheny, S.; Maksymovych, P.; Thompson, T. L.; Diwald, O.; Stahl, D.; Walck, S. D.; Yates, J. T., Stm Studies of Defect Production on the -(1×1) and -(1×2) Surfaces Induced by Uv Irradiation. *Chemical Physics Letters* **2003**, *369*, 152-158.
14. Xiong, L.; Li, J.; Yang, B.; Yu, Y., Ti³⁺ in the Surface of Titanium Dioxide: Generation, Properties and Photocatalytic Application. *Journal of Nanomaterials* **2012**, 1-13.
15. Berni A., M. M., Schmidt H., Doctor Blade. In: Aegerter M.A., Mennig M. (Eds) Sol-Gel Technologies for Glass Producers and Users. Springer, Boston, Ma. **2004**.
16. Wang, H.; Liu, M.; Yan, C.; Bell, J., Reduced Electron Recombination of Dye-Sensitized Solar Cells Based on Tio(2) Spheres Consisting of Ultrathin Nanosheets with [001] Facet Exposed. *Beilstein J Nanotechnol* **2012**, *3*, 378-87.

17. Oberbrodthage, J., Determination of a Solute Electron Energy Spectrum Not Accessible Experimentally by Means of Singular Value Decomposition. *Electron Spectrosc. Relat. Phenom* **2000**, *107*, 231-238.
18. Schmerl, N. M.; Quinton, J. S.; Andersson, G. G., On the Growth of Evaporated Lif on P3ht and Pcbm. *The Journal of Physical Chemistry C* **2018**, *122*, 23420-23431.
19. Acres, R. G.; Ellis, A. V.; Alvino, J.; Lenahan, C. E.; Khodakov, D. A.; Metha, G. F.; Andersson, G. G., Molecular Structure of 3-Aminopropyltriethoxysilane Layers Formed on Silanol-Terminated Silicon Surfaces. *The Journal of Physical Chemistry C* **2012**, *116*, 6289-6297.
20. Ellis-Gibbins, L.; Johansson, V.; Walsh, R. B.; Kloo, L.; Quinton, J. S.; Andersson, G. G., Formation of N719 Dye Multilayers on Dye Sensitized Solar Cell Photoelectrode Surfaces Investigated by Direct Determination of Element Concentration Depth Profiles. *Langmuir* **2012**, *28*, 9431-9439.
21. Bharti, B.; Kumar, S.; Lee, H.-N.; Kumar, R., Formation of Oxygen Vacancies and Ti 3+ State in Tio 2 Thin Film and Enhanced Optical Properties by Air Plasma Treatment. *Scientific reports* **2016**, *6*, 32355.
22. Hahlin, M.; Johansson, E. M. J.; Scholin, R.; Siegbahn, H.; Rensmo, H., Influence of Water on the Electronic and Molecular Surface Structures of Ru-Dyes at Nanostructured Tio2. *Journal of Physical Chemistry C* **2011**, *115*, 11996-12004.
23. Singh, J.; Gusain, A.; Saxena, V.; Chauhan, A.; Veerender, P.; Koiry, S.; Jha, P.; Jain, A.; Aswal, D.; Gupta, S., Xps, Uv-Vis, Ftir, and Exafs Studies to Investigate the Binding Mechanism of N719 Dye onto Oxalic Acid Treated Tio2 and Its Implication on Photovoltaic Properties. *The Journal of Physical Chemistry C* **2013**, *117*, 21096-21104.
24. Johansson, E. M. J.; Hedlund, M.; Siegbahn, H.; Rensmo, H., Electronic and Molecular Surface Structure of Ru(Tcterpy)(Ncs)3 and Ru(Dcbpy)2(Ncs)2 Adsorbed from Solution onto Nanostructured Tio2: A Photoelectron Spectroscopy Study. *The Journal of Physical Chemistry B* **2005**, *109*, 22256-22263.
25. Oscarsson, J.; Hahlin, M.; Johansson, E. M. J.; Eriksson, S. K.; Lindblad, R.; Eriksson, A. I. K.; Zia, A.; Siegbahn, H.; Rensmo, H., Coadsorption of Dye Molecules at Tio2 Surfaces: A Photoelectron Spectroscopy Study. *Journal of Physical Chemistry C* **2016**, *120*, 12484-12494.
26. Lee, K. E.; Gomez, M. A.; Regier, T.; Hu, Y.; Demopoulos, G. P., Further Understanding of the Electronic Interactions between N719 Sensitizer and Anatase Tio2 Films: A Combined X-Ray Absorption and X-Ray Photoelectron Spectroscopic Study. *The Journal of Physical Chemistry C* **2011**, *115*, 5692-5707.
27. Krischok, S.; Günster, J.; Goodman, D. W.; Höfft, O.; Kempter, V., Mies and Ups(Hei) Studies on Reduced Tio2(110). *Surface and Interface Analysis* **2005**, *37*, 77-82.
28. Liu, G.; Jaegermann, W.; He, J.; Sundström, V.; Sun, L., Xps and Ups Characterization of the Tio2/Znpgly Heterointerface: Alignment of Energy Levels. *The Journal of Physical Chemistry B* **2002**, *106*, 5814-5819.
29. Schölin, R.; Quintana, M. a.; Johansson, E. M. J.; Hahlin, M.; Marinado, T.; Hagfeldt, A.; Rensmo, H. k., Preventing Dye Aggregation on Zno by Adding Water in the Dye-Sensitization Process. *The Journal of Physical Chemistry C* **2011**, *115*, 19274-19279.

Chapter Five**5 Ion Scattering and Electron Spectroscopic Investigation on DPA/dye/TiO₂ interface of Dye Sensitized Solar Cells****5.1 Abstract**

The influence of the phosphonic co-adsorbent decylphosphonic acid (DPA) on the adsorption of Ru based dyes onto TiO₂ surface in dye-sensitized solar cells was investigated using a combination of ion scattering and electron spectroscopic techniques. Neutral impact collision ion scattering spectroscopy (NICSS) was employed to quantify the adsorption of the dyes. X-ray photoelectron spectroscopy (XPS) was applied to determine the chemical composition of the sample. The valence electron structure was measured with ultraviolet photoelectron spectroscopy (UPS). Increasing the concentration of DPA in the dye solution used to sensitize the TiO₂ surface decreases the dye loading while maintaining cell performance.

5.2 Introduction

Dye-sensitized solar cell (DSSC) is a promising low-cost technology that can directly convert solar energy to electrical energy using a simple manufacturing process and abundant materials. DSSC comprises of dye-sensitized molecules which are absorbed on a mesoporous semiconductor for which usually TiO_2 is used. When the dye is photoexcited, electrons will be injected into the conduction band of TiO_2 [1]. The oxidized dye will be regenerated by a redox mediator (such as iodide/triiodide (I^-/I_3^-), $\text{SeCN}_3/\text{SeCN}^-$, Br_2/Br^- and Co(III)/Co(II)) in the electrolyte [2, 3]. Many efforts have been applied to improve the efficiencies of DSSCs. Currently, the maximum efficiency reported is 14 % [4]. There are several drawbacks that are limiting the improvement of DSSCs. Charge recombination, where electrons injected into the conduction band of TiO_2 recombine with cations formed by the dye and the electrolyte, are affecting the cell performance by decreasing the open-circuit voltage (V_{oc}) [5]. The dye/dye intermolecular interaction on the TiO_2 surface is one of the most important factors and can affect charge separation in DSSCs in two different ways [6]. High loading of the TiO_2 surface with dye increases the absorption of light, leading to an increase in the short-circuit current (J_{sc}). On the other side, the formation of dye multilayers causes the dye to aggregate on the TiO_2 surface, increasing the distance between the top dye molecules and the TiO_2 surface, leading to impeding the charge carriers transfer and also decrease the generation of dye molecules close to the TiO_2 surface which cannot be reached by the electrolyte. [7, 8]. Therefore, there have been many attempts to decrease and prevent the formation of aggregates and multilayers. The use of additives and co-adsorbents is one of the attempts to decrease and prevent dye aggregation and thus avoiding the formation of dye multilayers. Co-adsorbents are small molecules containing either carboxylic or phosphonic groups on one end of the molecule and long hydrophobic alkyl groups on the other end. Adding co-adsorbent simultaneously with the dye solution can lead to preventing dye aggregation by occupying the uncovered sites on the TiO_2 surface [9]. In addition, the use of co-adsorbents in the dye solution can influence to some extent the anchoring configuration of dye molecules on TiO_2 substrate [10, 11] and improve the cell performance [12, 13]. Thus, adding co-adsorbents to the dye solutions when forming the dye/ TiO_2 interface can be expected to improve the performance of DSSCs.

However, the formation of the dye/ TiO_2 interface in the presence of co-adsorbents is not fully understood and requires further analysis.

In the present work, decylphosphonic acid (DPA) was used in different concentration as co-adsorbent with two of the most commonly used dyes, N719 and Z907. Neutral impact collision ion scattering spectroscopy (NICISS) in conjunction with X-ray photoelectron spectroscopy (XPS) was employed to determine the structure of the dye layer by measuring concentration depth profiles of the elements of the co-adsorbent/dye formed on the TiO₂ surface. UV-photoelectron spectroscopy (UPS) was used to determine the valence electron structure of the co-adsorbent/dye layer. The results obtained from NICISS, XPS and UPS, were used to elucidate the performance of the respective DSSCs.

5.3 Experimental

5.3.1 Sample preparation

Details of DSSCs fabrication can be found in chapter 3. The working electrodes with various DPA concentrations as co-adsorbents were manufactured for both the N719 and the Z907 dyes and assembled into fully operating DSSCs. All cells were made identical with the same components and had the same compositions, apart from the difference in the dye used (N719 or Z907) and DPA concentrations. Any changes in the cell performance attributed to the concentration of DPA. Working electrodes of N719-based dye and Z907-based dye were fabricated for comparison purposes. (Six cells were fabricated to test the reproducibility and the average of best three cells used in this work).

5.3.2 Methods

5.3.2.1 J-V characteristics

All I-V measurements were conducted using an Oriel solar simulator system fitted with a 150 W Xenon lamp (Newport) filtered to give irradiation of 100 mW/cm², an equivalent of 1 sun at air mass (AM 1.5G). A Si reference cell was used to calibrate the light intensity prior to the I-V measurement. A Keithley 2400 source meter operated by LabVIEW software was used to obtain the open-circuit voltage (V_{oc}), short-circuit current density (J_{sc}), the fill factor (FF) and the over conversion efficiency (η) of the cells. Six cells were fabricated to test the reproducibility, and the average of the best three cells is used to report the cell performance in the present paper.

5.3.2.2 NICISS, XPS and UPS

Experimental details for neutral impact collision ion scattering spectroscopy (NICISS) [14], X-ray photoelectron spectroscopy (XPS), and ultraviolet photoelectron spectroscopy (UPS) can be found in chapter 3. Singular value decomposition (SVD) was used to analyze a series of UP spectra. The SVD procedure results in reference spectra, which are used to reproduce the UP spectra as a linear combination representing the sample surface with a specific composition and electronic structure. A summary is provided in chapter 3, and more details of the procedure can be found in references [15, 16]

5.4 Results and Discussion

Table 5.1 and 5.2 (see also Figure 5-1 and Figure 5-2) summarize the photovoltaic performance of the DSSCs using N719 and Z907 as the photosensitizers. The reference N719 cell without DPA shows an overall conversion efficiency (η) of 4.8 %, with J_{sc} of 10.8 mA/cm², V_{oc} of 0.75 V, and FF of 0.59. The respective reference Z907 cell shows an overall conversion efficiency (η) of 4.7 %, with J_{sc} of 9.4 mA/cm², V_{oc} of 0.73 V, and FF of 0.67.

Upon adding the phosphonic acid-based co-adsorbents DPA, the N719 based cells reach a maximum η of 5.9 % in N719: DPA of 4:1 ratio. Then it increases to 5.9 %, which is an increase of 23 % compared to the N719 reference cell (see Table 5.1). The η drops to 4.6 % on further increasing the DPA concentration to N719: DPA 1:1 ratio. The increase in efficiency is achieved through both an increase of the V_{oc} (0.80 V at the 4:1 N719: DPA ratio) and J_{sc} , (11.2 mA/cm² at the 4:1 N719: DPA ratio).

Adding DPA to the Z907 cells shows a little variation of the cell performance (see Table 5.2). The maximum η of 4.9 % is achieved at a Z907: DPA ratio of 10:1. However, both the V_{oc} and J_{sc} change only to a minor degree.

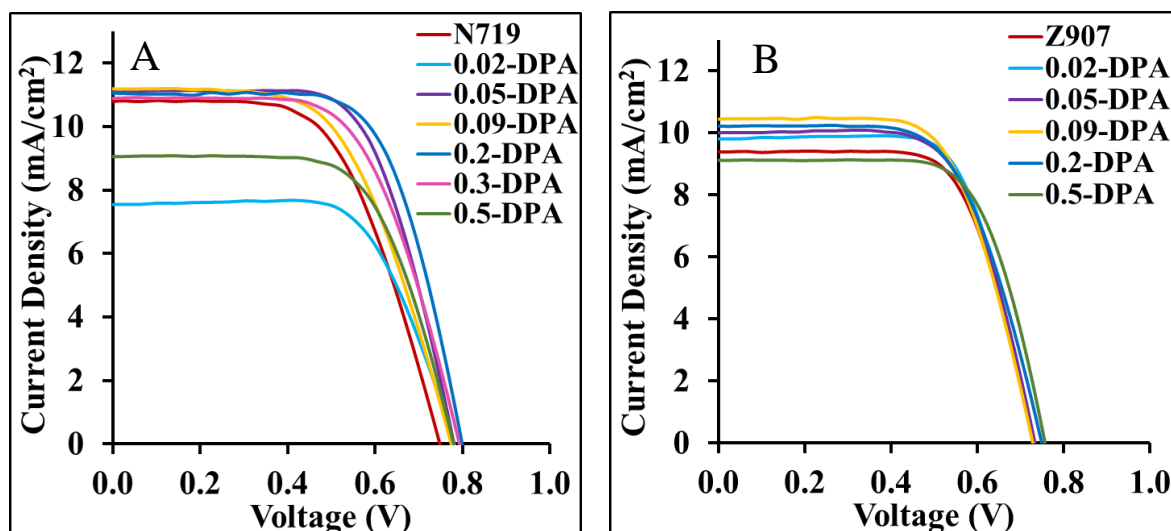


Figure 5-1: J-V characteristics for DSSCs fabricated with different concentration of DPA using two different dyes: N719 (A) and Z907 (B).

Table 5.1: The influence of various concentrations of DPA using the dye N719 on the cell performance. The N719: DPA ratio is shown in the first column and the respective DPA molar ratio in the second column.

N719:DPA conc. ratio	DPA molar ratio	Jsc (mA/cm ²)	Voc (V)	FF	η (%)
1:0	0	10.8 \pm 0.3	0.75 \pm 0.0	0.59 \pm 0.04	4.8 \pm 0.3
40:1	0.02	11.1 \pm 0.5	0.78 \pm 0.01	0.64 \pm 0.01	5.5 \pm 0.3
20:1	0.05	11.1 \pm 0.2	0.78 \pm 0.01	0.65 \pm 0.02	5.7 \pm 0.2
10:1	0.09	11.2 \pm 0.2	0.78 \pm 0.01	0.58 \pm 0.03	5.0 \pm 0.2
4:1	0.2	11.1 \pm 0.1	0.80 \pm 0.01	0.67 \pm 0.01	5.9 \pm 0.2
2:1	0.3	10.9 \pm 0.3	0.79 \pm 0.01	0.62 \pm 0.04	5.4 \pm 0.1
1:1	0.5	9.1 \pm 0.1	0.78 \pm 0.01	0.65 \pm 0.02	4.6 \pm 0.1

Table 5.2: The influence of various concentrations of DPA using the dye N719 on the cell performance. The Z907: DPA ratio is shown in the first column and the respective DPA molar ratio in the second column.

Z907:DPA conc. ratio	DPA molar ratio	Jsc (mA/cm ²)	Voc (V)	FF	η (%)
1:0	0	9.4±0.3	0.73±0.01	0.67±0.03	4.7±0.3
40:1	0.02	9.8±0.1	0.73±0.01	0.69±0.02	4.9±0.2
20:1	0.05	10.0±0.2	0.73±0.01	0.66±0.03	4.8±0.2
10:1	0.09	10.4±0.1	0.73±0.01	0.65±0.03	4.9±0.2
4:1	0.2	10.2±0.2	0.75±0.01	0.63±0.03	4.9±0.2
1:1	0.5	9.1±0.5	0.76±0.01	0.68±0.02	4.7±0.3

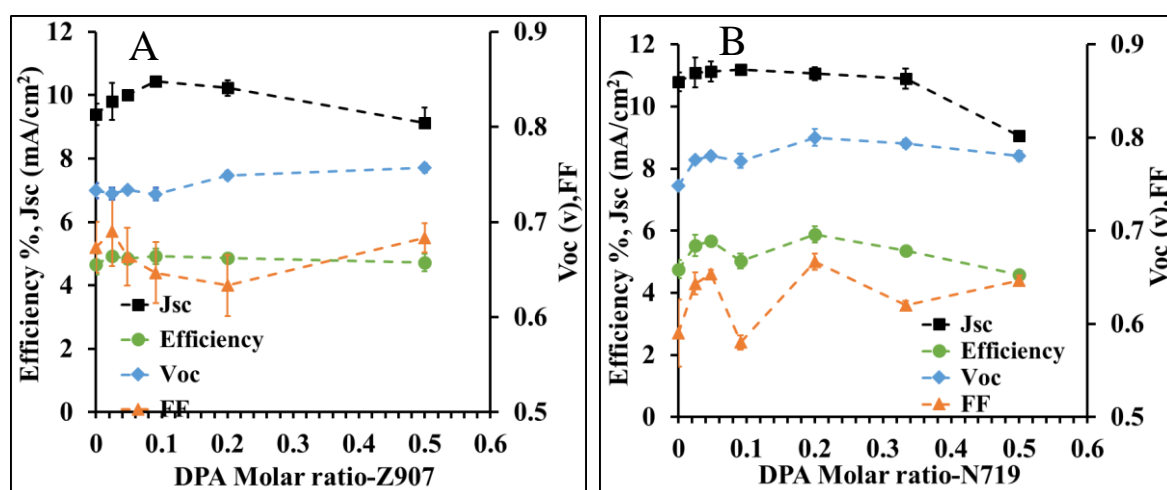


Figure 5-2: Efficiency, Jsc, Voc and FF for DSSCs based on different concentration of DPA using two different dyes: N719(A) and Z907(B). (The dashed line is used for guiding eyes).

The change of the cell performance upon adding DPA raises the question of how the structure of the dye layer is changing upon addition of DPA. It has been reported for various dye systems that the improvement in DSSCs efficiencies when adding co-adsorbents is caused by the formation of a more compact monolayer decreasing the dye aggregation [17, 18].

5.5 The influence of different concentrations of DPA on dye coverage and depth

The Ru concentration depth profiles for all samples measured with NICISS are shown in Figure 5-3. They have a maximum at a depth between a depth of 10 - 20 Å in samples sensitized with N719 and between 20 - 30 Å in samples sensitized with Z907. A measure for the coverage is shown in Figure 5-4. It should be noted that the concentration depth profiles have not been deconvoluted as it has been done in earlier work [19]. The reason is that we are here only interested in the relative changes of the dye coverage and the concentration depth profiles.

The Ru profiles of the N719 samples show a change in coverage represented by the integral of the profiles but only a minor change in shape when increasing the DPA content. The profiles become somewhat broader when adding DPA and also decrease in intensity. The shape of the Ru concentration depth profile in case of N719 can be interpreted as a mix of monolayers and multilayers as has been reported earlier in [19]. Upon changing the DPA concentration, the ratio between mono- and multilayers is not changing significantly. The Ru profiles of the Z907 samples show a significant change in shape with a decrease in concentration at the position of the maximum but minor changes at larger depth. The concentration depth profile of Z907 samples can be interpreted as a loss of the Ru coverage more within the monolayers than the multilayers.

The molecular coverage of Ru as a function of various concentrations of co-adsorbents is shown in Figure 5-4. P cannot be identified in the NICIS spectra because the Ti contribution dominates the P signal, and thus the P signal cannot be separated from the NICIS spectra. Maximum coverage of Z907-based sample is 11×10^{-11} mol/cm² and is higher than it found in N719-based sample 5.2×10^{-11} mol/cm². It can be seen that the surface coverage is changing considerably with the DPA concentration. The highest coverage for the N719/DPA samples is reached with 6.6×10^{-11} mol/cm² at DPA molar ratio of 0.02. The coverage is rather constant up to a DPA molar ratio of 0.09. The lowest coverage is reached at the highest DPA molar ratio of 0.5. At this DPA concentration, the coverage is only about 11 % of the highest coverage. The Ru intensity for this DPA concentration is quite low, and it is difficult to assess the shape of the Ru profile of this sample. For the Z907/DPA samples, the highest coverage is found for the Z907 sample only and then decreases to about 65 % of the maximum coverage and then stays approximately constant up to the highest DPA concentration. A similar observation was obtained by Chandiran et al. when they studied the effect of different functional of co-

adsorbents with Ru-based dye C106. Their revealed decrease in the dye loading of 57 % when DPA was co-grafted with the dye C106. Furthermore, their ATR-FTIR spectroscopy results showed the occurrence of the C-O vibration mode at 1047 cm^{-1} when DPA was used as co-adsorbent, and this vibration originating from the P-O-C group of the phosphonic acid function increasing with increased DPA concentration was increased [20].

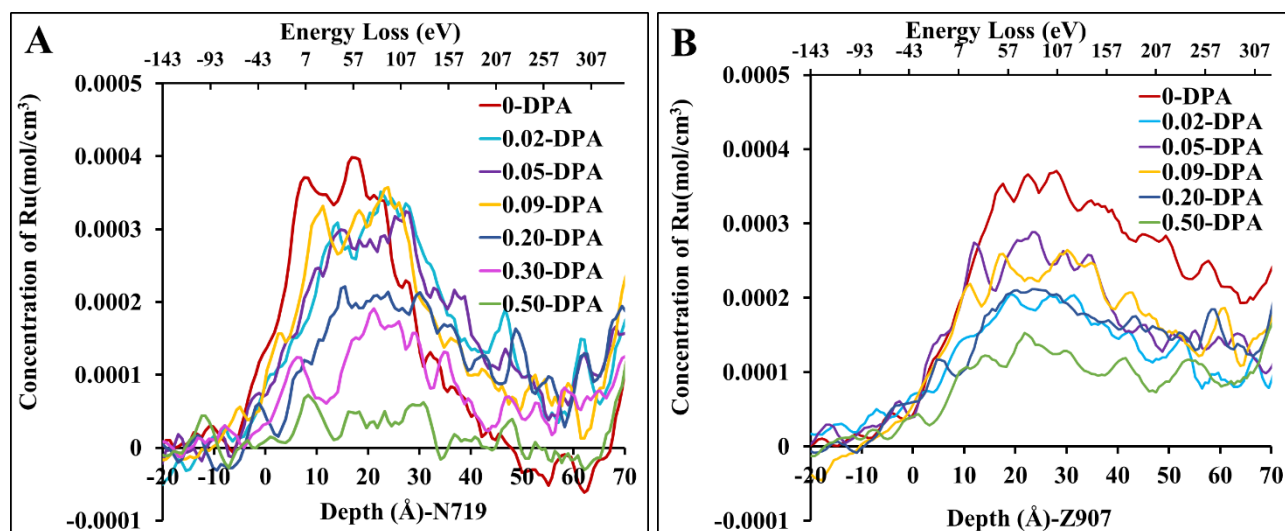


Figure 5-3: NCISS Concentration depth profile of Ru with varying concentrations of DPA using N719 (A) and Z907 (B) as sensitizer.

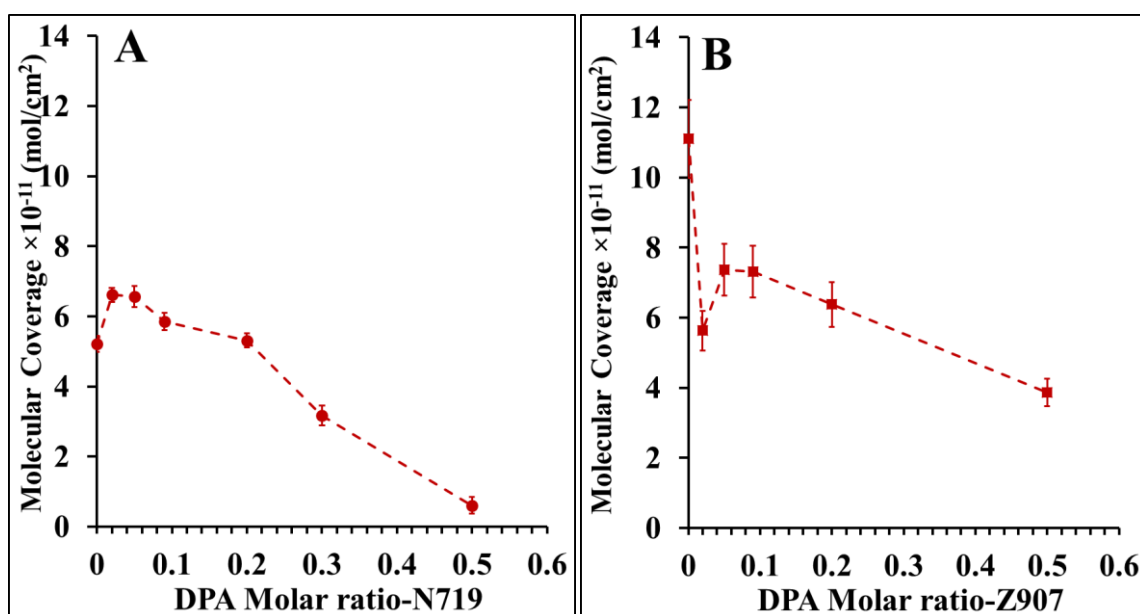


Figure 5-4: Molecular coverage of Ru with different concentration of DPA using N719 (A) and Z907 (B) as sensitizer. (The dashed line is used for guiding eyes)

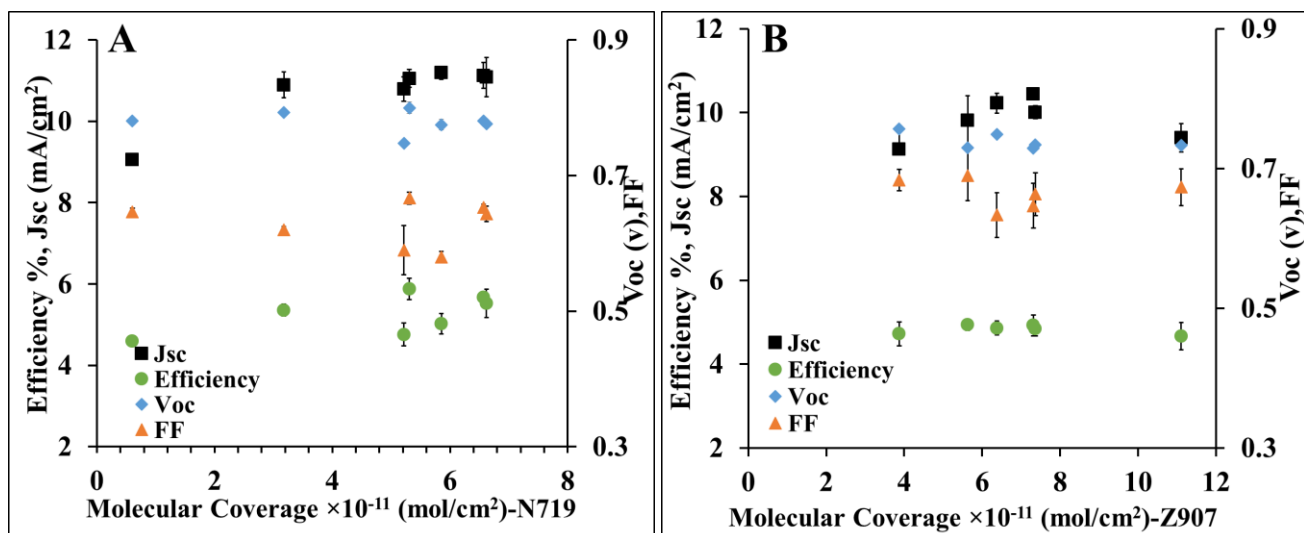


Figure 5-5: short-circuit current, efficiency, open-circuit voltage and fill factor with the coverage of the dye N719 (left) and Z907 (right).

Figure 5-5 shows the relation of the cell performance to the coverage with dye molecules. For N719, J_{sc} and η decrease slightly with decreasing coverage and V_{oc} , and FF stays almost constant. For Z907, there is no clear trend for either of the cell parameters. We will discuss these findings further below.

5.6 Changes in the chemical state

In XPS peaks from the elements C, O, Ru, N, S, Ti and P were found. The C 1s, O 1s, Ru 3d, N1s, and S 2p were used to analyse the adsorbed dye. The Ti 2p peak and also O 1s are related to the TiO₂ substrate. The P 2p peak was used to analyse the presence of the co-adsorbent DPA. The amount of dye adsorbed to the TiO₂ surface was quantified by determining the intensity ratio of Ru 3d to the Ti 2p peak. Fitted high-resolution spectra are shown in Figure 5-6, and the peak positions with the relative peak intensities are listed in Table 5.3 and Table 5.4

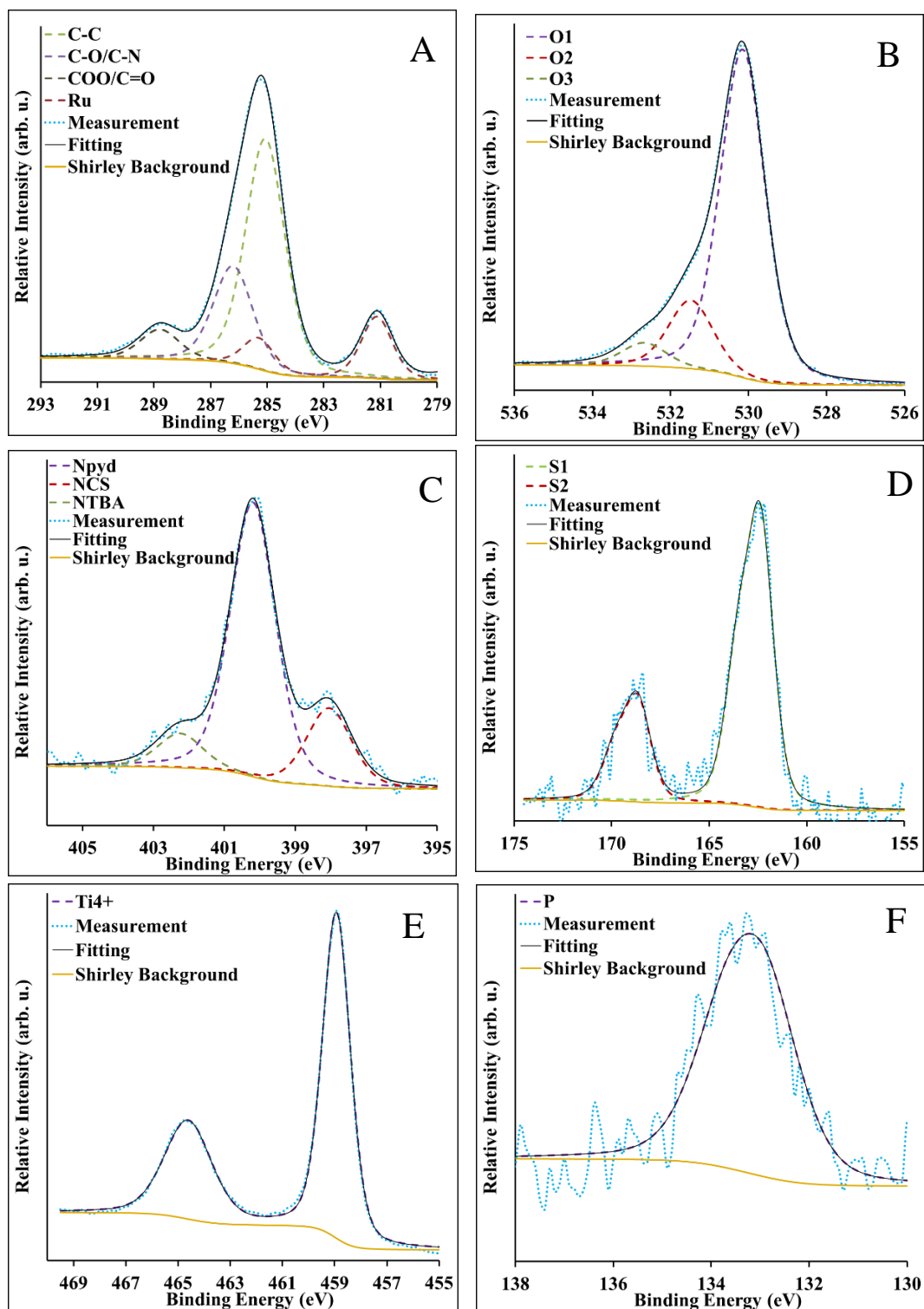


Figure 5-6: (A) Carbon 1s, (B) Oxygen 1s, (C) Nitrogen 1s, (D) Sulfur 2p, (E) Titanium 2p and (F) phosphorus 2p spectra.

Table 5.3: Peak positions (eV) with uncertainty of ± 0.2 and the relative peak intensities ± 0.3 for N719 based samples.

Peak	DPA molar Ratio	0	0.02	0.05	0.09	0.2	0.3	0.5
C1	Position	285.0	285.0	285.0	285.0	285.0	285.0	285.0
	Intensity %	17.4	19.6	18.2	22.8	21.8	22.8	24.5
C2	Position	286.1	286.1	286.0	286.1	286.2	286.2	286.1
	Intensity %	8.8	8.2	15.2	12.5	8.3	6.7	6.6
C3	Position	288.6	288.7	288.8	288.7	288.8	288.7	287.9
	Intensity %	2.4	2.5	3.3	1.9	2.1	1.6	1.5
O1	Position	530.0	530.1	530.2	530.0	530.2	530.1	530.2
	Intensity %	40.3	38.1	35.0	34.8	36.6	38.9	38.5
O2	Position	531.4	531.4	531.5	531.3	531.5	531.4	531.4
	Intensity %	7.6	7.9	7.0	6.7	8.7	8.4	8.8
O3	Position	532.8	532.6	532.7	532.3	532.7	532.6	532.5
	Intensity %	2.0	2.7	2.7	2.6	3.3	2.0	2.7
Ti	Position	458.8	458.9	459.0	458.8	459.0	458.9	459.0
	Intensity %	14.4	13.7	12.7	12.7	13.3	14.1	14.0
Ru	Position	281.0	281.1	281.2	281.0	281.2	281.2	281.2
	Intensity %	0.4	0.4	0.4	0.3	0.3	0.3	0.1
N1	Position	397.9	398.0	398.2	398.0	397.6	397.9	398.0
	Intensity %	1.1	0.8	0.8	0.8	0.6	0.5	0.2
N2	Position	400.1	400.1	400.3	400.1	400.2	400.2	400.1
	Intensity %	3.0	2.9	2.5	2.5	2.3	2.1	0.9
N3	Position	402.0	402.2	402.3	402.3	402.3	402.2	402.4
	Intensity %	0.5	0.4	0.3	0.3	0.2	0.2	0.1
P	Position	132.9	133.0	133.1	132.9	133.0	133.1	133.1
	Intensity %	0.0	0.2	0.3	0.3	0.6	0.8	1.5
S1	Position	162.2	162.3	162.4	162.2	162.4	162.3	162.0
	Intensity %	0.6	0.7	0.6	0.7	0.2	0.3	0.1
S2	Position	168.3	168.6	168.5	168.5	168.8	168.6	169.2
	Intensity %	0.1	0.2	0.1	0.1	0.5	0.3	0.1
F	Position	683.9	684.1	684.3	684.1	684.3	684.1	684.1
	Intensity %	1.0	1.3	0.9	0.8	1.0	0.8	0.5
Sn	Position	484.4	484.2	484.5	484.4	484.9	484.0	484.5
	Intensity %	0.2	0.2	0.2	0.2	0.2	0.2	0.1

Table 5.4: Peak positions (eV) with uncertainty of ± 0.2 and the relative peak intensities ± 0.3 for Z907 based samples.

Peak	DPA molar Ratio	0	0.02	0.05	0.09	0.2	0.5
C1	Position	285.0	285.0	285.0	285.0	285.0	285.0
	Intensity %	32.2	35.2	31.9	34.7	32.4	31.8
C2	Position	286.1	286.5	286.1	286.1	285.9	285.9
	Intensity %	9.5	7.7	10.4	7.6	9.0	10.6
C3	Position	288.3	288.2	288.4	288.4	287.1	287.2
	Intensity %	1.4	2.5	1.0	1.2	1.1	0.8
O1	Position	530.0	530.0	530.1	530.0	530.1	530.1
	Intensity %	31.0	27.5	30.2	29.5	31.6	30.2
O2	Position	531.2	531.5	531.4	531.4	531.4	531.4
	Intensity %	5.0	5.5	6.4	6.8	7.4	7.3
O3	Position	532.1	533.3	532.5	532.6	532.6	532.5
	Intensity %	1.9	4.4	2.3	2.2	2.7	3.0
Ti	Position	458.8	458.8	458.8	458.8	458.9	458.9
	Intensity %	11.4	9.8	10.8	10.7	11.5	11.0
Ru	Position	281.1	281.0	281.1	281.1	281.2	281.2
	Intensity %	0.5	0.3	0.4	0.4	0.4	0.2
N1	Position	398.1	397.7	398.1	397.9	397.8	397.8
	Intensity %	1.0	1.0	0.8	0.7	0.4	0.4
N2	Position	400.1	400.1	400.2	400.2	400.3	400.3
	Intensity %	3.4	2.9	2.7	2.8	1.5	1.5
P	Position	132.9	132.9	132.9	132.9	133.0	133.0
	Intensity %	0.0	0.3	0.4	0.7	0.5	1.5
S1	Position	162.2	162.2	162.3	162.3	162.5	162.4
	Intensity %	0.9	0.8	0.8	0.5	0.2	0.2
S2	Position	168.6	168.3	168.9	168.5	168.7	168.8
	Intensity %	0.2	0.4	0.2	0.2	0.1	0.3
F	Position	684.1	684.2	684.1	684.8	684.5	684.6
	Intensity %	0.8	0.8	0.9	1.2	0.6	0.6
Sn	Position	484.2	484.4	484.4	484.3	483.6	484.2
	Intensity %	0.9	1.0	0.9	0.6	0.6	0.6

The high-resolution C1s and Ru 3d spectrum were fitted with five peaks. Fitting the C1s spectra resulted in three peaks, the main C peak is located at 285.0 eV is attributed to C-C bonds, the peak at 286.7 ± 0.2 eV corresponds to C-O/C-N and peak at 289.3 ± 0.2 eV to C(=O)OH bonds. The Ru $3d_{5/2}$ located at 281.2 ± 0.2 eV and Ru $3d_{3/2}$ at 285.3 ± 0.2 eV, with the latter overlapping with the carbon C1s contribution in the spectrum [21, 22].

P 2p peak was fitted with one spin-orbit doublet at binding energy 133.0 ± 0.2 eV [10, 23]. The

P was observed in all co-adsorbed samples with DPA with similar binding energy indicating that the adsorption of DPA on the TiO₂ surface is the same in all samples.

A relative measure for the dye and DPA coverage on the TiO₂ surface was derived by determining the Ru/Ti and P/Ti intensity ratio and is shown in Figure 5-7. It can be seen that, with increasing DPA concentration the dye coverage decreases approximately linear and the DPA coverage linearly increases. The first result is in line with the NICISS findings.

The decrease of the Ru/Ti intensity ratio and increase of the P/Ti intensity ratio is reflecting the competition between DPA and the dyes for adsorption sites on TiO₂ surface.

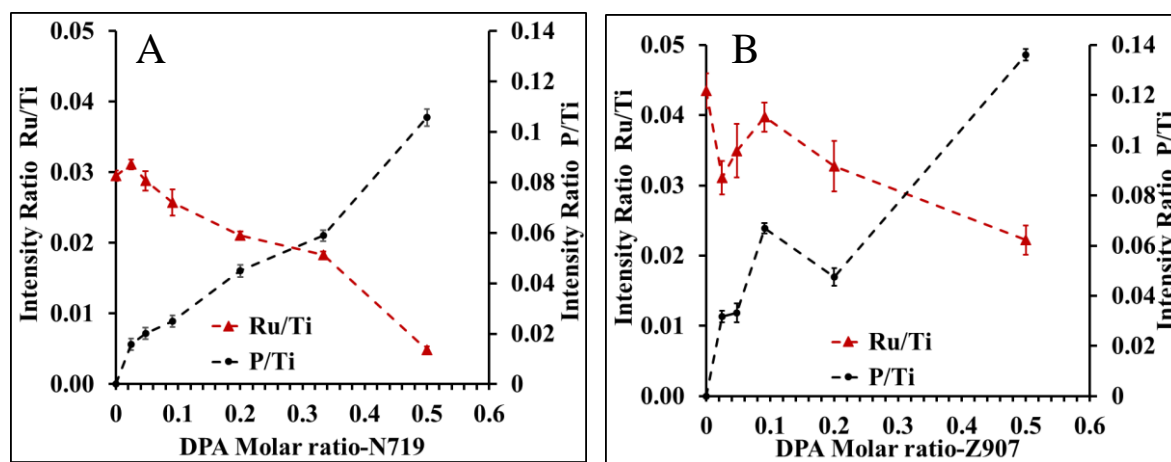


Figure 5-7: intensity ratio of Ru/Ti and P/Ti with different concentration of DPA using N719 (A) and Z907 (B) as sensitizer. (The dashed line is used for guiding eyes).

The high-resolution O1s XPS of oxygen show three peaks, a major peak at 530.1 ± 0.2 eV originating from the substrate, and 531.4 ± 0.2 eV, 532.6 ± 0.2 eV originating from oxygen in the dye molecules the carbonyl, and carboxylic groups, respectively [24].

The high-resolution scan of the N719 samples of the N region show three peaks located at 397.9 ± 0.2 eV, 400.2 ± 0.2 eV, and 402.2 ± 0.2 eV and are assigned to thiocyanate ligands (NNCS), bipyridine ligands (Npyd) and N_{TBA} respectively [25]. For the Z907 samples, the N1s region is composed of two peaks located at 397.9 ± 0.2 eV and 400.2 ± 0.2 eV assigned to NNCS and Npyd ligands, respectively [10].

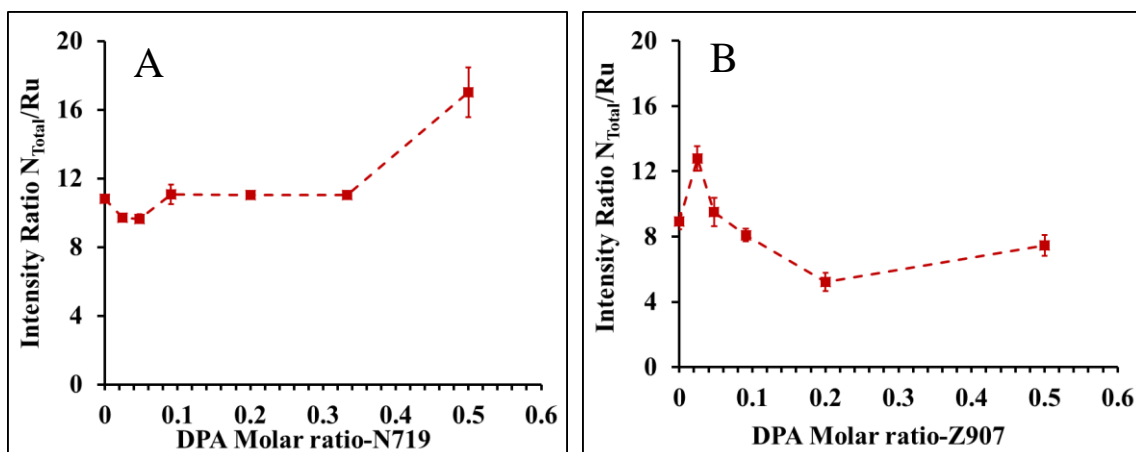


Figure 5-8: Intensity ratio of N_{Total}/Ru versus the molar ratio of DPA in the solution using N719 (A) and Z907 (B) as sensitizer. (The dashed line is used for guiding the eye).

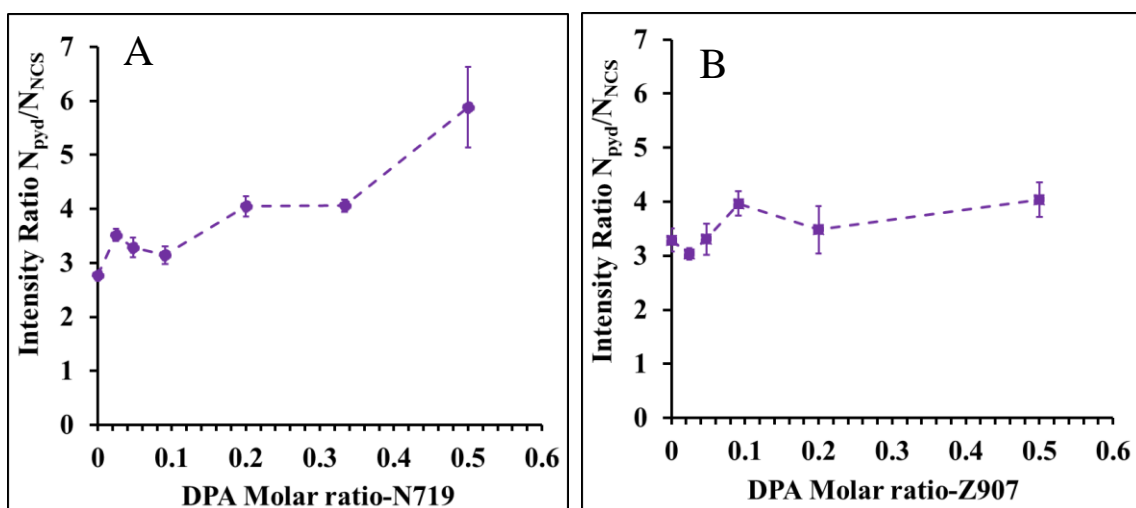


Figure 5-9: The intensity ratio between N_{pyd} and N_{NCS} with different concentration of DPA using N719 (A) and Z907 (B) as sensitizer. (The dashed line is used for guiding eyes).

The total intensity of N 1s of the N719 samples is constant with increasing DPA concentration apart from the highest DPA concentration as can be seen in Figure 5-8A but decreased for the Z907 samples, as shown in Figure 5-8B. The ratio N_{pyd}/N_{NCS} in both N719 and Z907 based on their chemical structure is 2:1. Figure 5-9 shows the experimental N_{pyd}/N_{NCS} ratio measured at various concentrations of DPA. It can be seen that the ratio is larger than 2:1, which can be attributed to the preferential orientation of the dye molecules. A ratio larger than 2 has to be interpreted such that the N_{pyd} moiety is pointing to the outermost layer (i.e., away from the TiO_2 surface) and that the N_{NCS} group is positioned closer to the TiO_2 surface in both dyes N719 and Z907. The N_{pyd}/N_{NCS} ratio increases for N719 with increasing DPA concentration and seems to indicate an orientation effect becoming stronger with increasing DPA and decreasing N719

loading. The change of the $N_{\text{Total}}/\text{Ru}$ ratio could potentially be interpreted as change in orientation of the dye molecules in the dye layer. However, the change is too subtle for being interpreted. Similar but stronger changes are observed for S and will be described below.

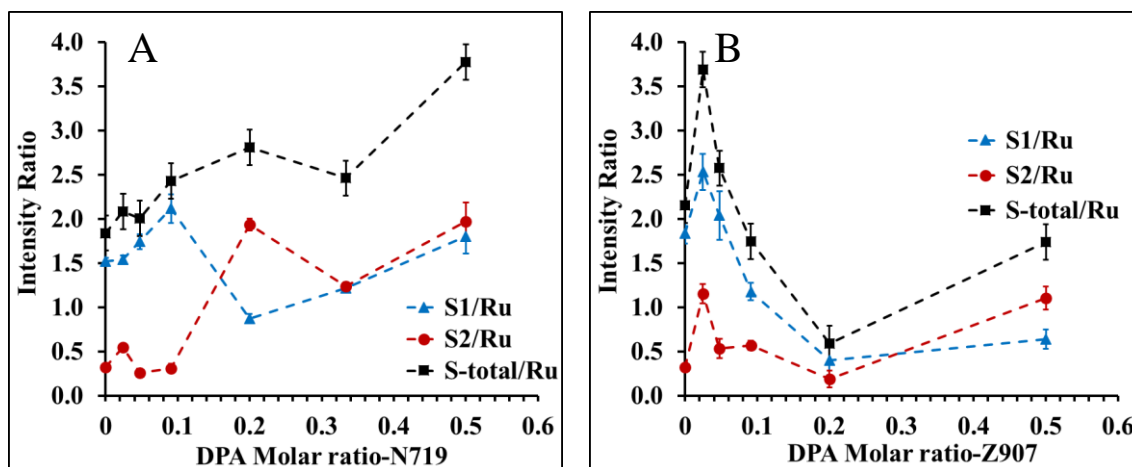


Figure 5-10: Intensity ratio of the total S and S components with Ru versus the molar ratio of DPA in the solution using N719 (A) and Z907 (B) as sensitizer. (The dashed line is used for guiding eyes).

Two S 2p peaks are observed with a binding energy of 162.4 ± 0.2 eV (S1) assigned to S atoms in the NCS group interacts with TiO_2 surface [26], and at a binding energy of 168.3 ± 0.2 eV (S2) attributed to highly oxidized sulfur (such as S^{6+} to S^{8+}) [27] and not involved in formation a bond to the substrate. The binding energies of the S1 component are the same for all samples. However, in S2, a shift to the higher binding energy of 0.5 eV, 0.9 eV for N719 samples with DPA molar ratio of 0.2 and 0.5, respectively. This shift in the binding energy indicates some changes in the oxidation state of sulfur.

The intensity ratio of $S_{\text{total}}/\text{Ru}$, $S1/\text{Ru}$, and $S2/\text{Ru}$ for both dyes are plotted versus the molar ratio of DPA in Figure 5-10. For the N719 samples, the total S/Ru ratio is increasing with increasing DPA concentration. The effect is strongest for the highest DPA concentrations. The intensity ratio of $S1/\text{Ru}$ tends to remain constant, which is in agreement with the unchanged shape of the Ru depth profile as measured with NCISS when changing the DPA concentration. For the Z907 samples, the total S/Ru ratio is decreasing with increasing DPA concentration as well as the intensity ratio of $S1/\text{Ru}$. This observation is also in agreement with NCISS results showing the loss in Ru coverage in regions with thinner layers. The $S2/\text{Ru}$ peak (oxidized sulfur) of the N719 samples is profoundly affected by the addition of DPA, where it's increased as DPA increased. The $S2/\text{Ru}$ ratio is not suitable for conclusions about the dye orientation because the S2 is not involved in the formation of a bond to the substrate.

5.7 Analysis of UP spectra

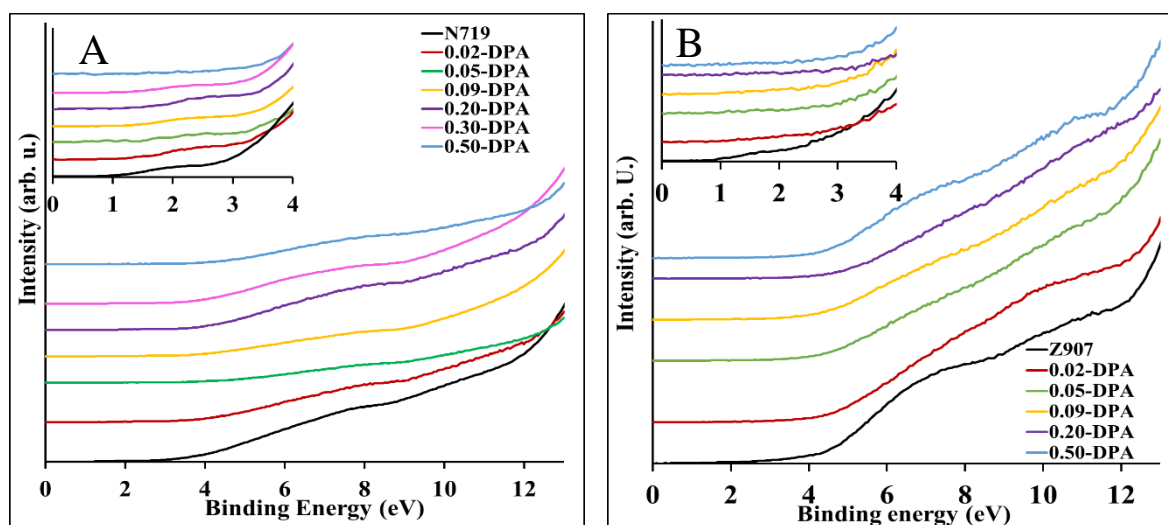


Figure 5-11: UP spectra comparison with different concentration of DPA using N719 (A) and Z907 (B) as sensitizer. (Inset shows the magnified region of the HOMO level).

UPS was used to measure the work-function and evaluate the position of the highest occupied molecular orbital (HOMO) level of the samples. Figure 5-11 shows the UP spectra, and the inset shows the HOMO level. In case on N719, a clear structure can be seen at binding energy of ~ 2 eV for the plain N719 sample. This feature gradually decreases with increasing DPA concentration and cannot be identified for the highest DPA concentration. This is in accordance with the finding from XPS and NICISS that the amount of N719 strongly decreases with increasing DPA concentration. In the plain Z907, a structure can be identified at ~ 1.5 eV, the HOMO level is hard to discern when DPA is added. It can be seen that the intensity of the peak with the lowest binding energy at 1.5 eV decreases in the Z907 samples stronger than the respective structure in the spectra of the N719 samples, even though the decrease in Z907 coverage is less strong than in the case of N719 samples. It is not clear why this is the case.

Table 5.5: Work Function ± 0.1 eV

dye:DPA Molar Ratio	WF (eV)	
	N719	Z907
0	4.1	4.0
0.02	3.7	3.7
0.05	3.6	3.3
0.09	3.9	3.3
0.2	3.7	3.8
0.3	3.9	-
0.5	3.5	3.5

The work-function was measured by determining the secondary electron cut-off as described and is listed in Table 5.5 Where the work function is defined as the difference between fermi level and the vacuum level. The work function of the samples with only N719 and Z907 is 4.1 eV and 4 eV, respectively. The work-function is decreasing for both dyes with increasing DPA concentration. The substantial decrease in the work function might be responsible for a relative change in the energy level between the co-adsorbent dye/TiO₂ interfaces and could influence the cell performance. For a more detailed analysis the energetic position of the dye in its excited state and the valence band edge of the titania would have to be known. We note that the best photovoltaic performance was obtained with the cells having low work function.

5.8 Singular Value Decomposition analysis (SVD)

Further analysis of the UP spectra was applied using the mathematical algorithm SVD. The SVD procedure is used here to fit a series of UP spectra as a linear combination of reference spectra. It was found that two reference spectra are required for the series of spectra for both the N719 and the Z907 samples, and resulted in two reference spectra in each of the N719 and Z907 samples, representing a surface with a specific composition and electronic structure. The reference spectra were compared with the pristine N719, Z907 and DPA spectra. In the SVD of the N719 samples, both the reference spectrum A and B have a very similar shape and features as the spectrum of the dye, and thus it is assumed that they both represent the dye on the sample Figure 5-12. Reference spectrum B is shifted slightly to higher binding energies in case of N719. The shift of reference B is probably subjected to a dipole as described in [28]. If that is the case, the dipole would be located at the interface between the dye and TiO₂. For the Z907 samples, reference spectrum A shown in Figure 5-13 is very similar to the spectrum of the pristine Z907. While the exact nature of reference B could not be clarified so for reference

B is not identical with any of Z907 or DPA spectra. It might be possible that it represents either of these two materials but with a different orientation at the surface.

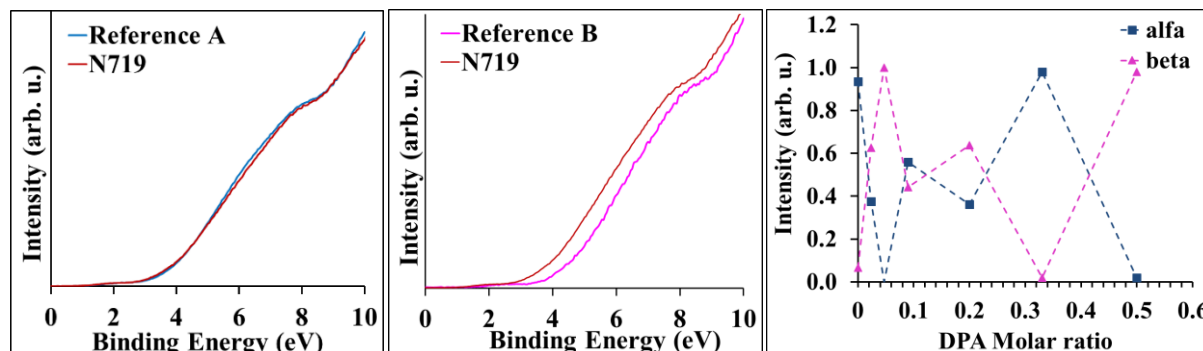


Figure 5-12: SVD reference spectra A, reference spectra B compared with pristine N719, and their respective weighting factors for samples sensitized with N719.

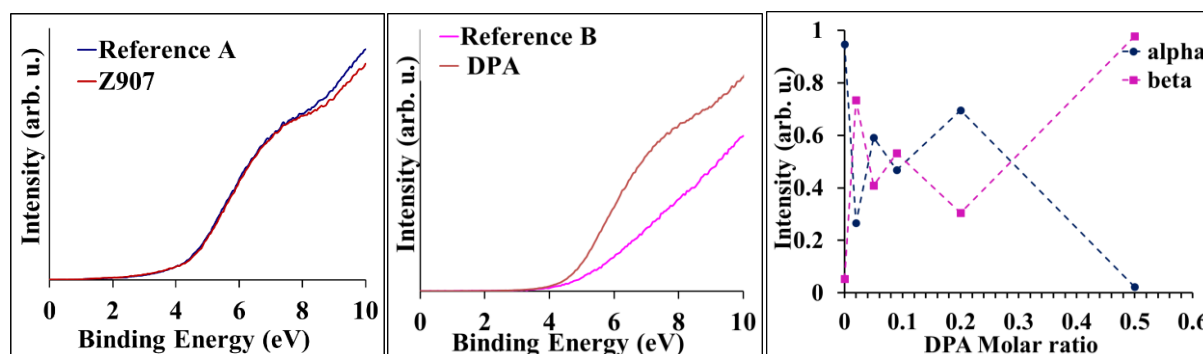


Figure 5-13: SVD reference spectra A compared with pristine Z907, reference spectra B compared with pristine DPA and their respective weighting factors (right) for samples sensitized with Z907.

5.9 The adsorption configuration of the dye molecules on TiO₂ surface and the cell performance

From XPS, the Ru/Ti ratio shows that the amount of dye adsorbed in N719 samples decreased by 83 %, and for Z907 decreased by 50 % at DPA molar ratio of 0.5. These results are in line with the dye coverage obtained from NICISS, where a decrease in the dye coverage \sim 87 % and 60 in N719 and Z907 samples, respectively. Within experimental uncertainty, the decrease in dye coverage measured with XPS and NICISS is the same. Through the shape of the Ru concentration depth profiles as measured with NICISS it was found that the structure of the dye layer in case of N719 is hardly changing while for Z907 a loss of the dye coverage at places with thinner dye coating was found. The information about the dye layer structure through the

S spectra in XPS allow for conclusions about the orientation of the molecules in the dye layer and the thickness of the dye layer which is in agreement with the NICISS results.

Despite the strong decrease in the dye coverage, the performance of the cells is hardly decreasing with decreasing dye coverage. The highest concentration of DPA in case of N719 shows some exemption. However, even in this case a reduction in dye coating by > 80 % results in a decrease in efficiency by only 15 % when averaging over the efficiencies of all other DPA concentration. This observation allows for the conclusion that the adsorption of DPA onto the titania results in inhibiting of the adsorption only of those dye molecules which would not contribute significantly to the cell performance.

Furthermore, it can be observed that both XPS and NICISS showed that the dye coverage in Z907 samples is larger than N719. However, the Z907 cell shows a lower J_{sc} , due to the remaining of some thicker dye layers, thus increasing the charge recombination.

XPS results show that the coverage of P on TiO_2 substrate in Z907 samples is higher than in N719 samples; the increase of DPA adsorption in Z907 samples can be related to the large size on N719 compared to Z907 allowing more DPA to be adsorbed on the TiO_2 surface, moreover, the dye adsorbed on TiO_2 surface by its carboxylic group, and N719 contains four carboxyl groups, whereas Z907 contains only two [29], allowing N719 to occupy more area on the substrata minimizing the dye/dye interaction and resulting in less DPA adsorption.

5.10 Conclusion

Different concentrations of DPA as co-adsorbent were studied by ion scattering and electron spectroscopy. Using DPA as co-adsorbent in the dye solution decreases the dye coverage in the sample and changes the dye's bonding to the titania substrate and dye layer formation for both of the dyes on the TiO_2 surface. XPS and NICISS analysis showed that DPA co-adsorbed with the dye strongly reduces the amount of adsorbed dye. It is assumed that the adsorbing DPA affects the weakly adsorbed dye molecules on TiO_2 and inhibits their adsorption onto the TiO_2 . In N719 samples, the substantial decrease in the dye coverage is accompanied by a slight increase in the efficiency. For the highest DPA concentration, the cell efficiency was stable compared to that large decrease in the dye coverage. For the Z907 sample, the dye decreases but not as strongly as for the N719 and does not affect the cell efficiency.

In conclusion, the main role of DPA replaces the weakly and undesirable dye on the TiO_2 surface and having efficient cell performance with the strongly bounded dye molecules.

5.11 Reference

1. O'Regan, B.; Grätzel, M., A Low-Cost, High-Efficiency Solar Cell Based on Dye-Sensitized Colloidal TiO₂ Films. *Nature* **1991**, *353*, 737–740.
2. Bella, F.; Gerbaldi, C.; Barolo, C.; Grätzel, M., Aqueous Dye-Sensitized Solar Cells. *Chem Soc Rev* **2015**, *44*, 3431-73.
3. Boschloo, G.; Hagfeldt, A., Characteristics of the Iodide/Triiodide Redox Mediator in Dye-Sensitized Solar Cells. *Acc Chem Res* **2009**, *42*, 1819-26.
4. Kakiage, K.; Aoyama, Y.; Yano, T.; Oya, K.; Fujisawa, J.; Hanaya, M., Highly-Efficient Dye-Sensitized Solar Cells with Collaborative Sensitization by Silyl-Anchor and Carboxy-Anchor Dyes. *Chem Commun (Camb)* **2015**, *51*, 15894-7.
5. Boschloo, G., Improving the Performance of Dye-Sensitized Solar Cells. *Front Chem* **2019**, *7*, 77.
6. Chen, H.; Cole, J. M.; Stenning, G. B.; Yanguas-Gil, A.; Elam, J. W.; Stan, L.; Gong, Y., Imaging Dye Aggregation in Mk-2, N3, N749, and Sq-2 Dye··· TiO₂ Interfaces That Represent Dye-Sensitized Solar Cell Working Electrodes. *ACS Applied Energy Materials* **2020**, *3*, 3230-3241.
7. Zhang, L.; Cole, J. M., Dye Aggregation in Dye-Sensitized Solar Cells. *Journal of Materials Chemistry A* **2017**, *5*, 19541-19559.
8. Krishna, N. V.; Krishna, J. V. S.; Mrinalini, M.; Prasanthkumar, S.; Giribabu, L., Role of Co-Sensitizers in Dye-Sensitized Solar Cells. *ChemSusChem* **2017**, *10*, 4668-4689.
9. Manthou, V. S.; Pefkianakis, E. K.; Falaras, P.; Vougioukalakis, G. C., Co-Adsorbents: A Key Component in Efficient and Robust Dye-Sensitized Solar Cells. *ChemSusChem* **2015**, *8*, 588-599.
10. Oscarsson, J.; Hahlin, M.; Johansson, E. M. J.; Eriksson, S. K.; Lindblad, R.; Eriksson, A. I. K.; Zia, A.; Siegbahn, H.; Rensmo, H., Coadsorption of Dye Molecules at TiO₂ Surfaces: A Photoelectron Spectroscopy Study. *Journal of Physical Chemistry C* **2016**, *120*, 12484-12494.
11. Honda, M.; Yanagida, M.; Han, L.; Miyano, K., Investigation of the Influence of Coadsorbent Dye Upon the Interfacial Structure of Dye-Sensitized Solar Cells. *J Chem Phys* **2014**, *141*, 174709.
12. Wang, P.; Zakeeruddin, S. M.; Humphry-Baker, R.; Moser, J. E.; Grätzel, M., Molecular-Scale Interface Engineering of TiO₂ Nanocrystals: Improve the Efficiency and Stability of Dye-Sensitized Solar Cells. *Advanced Materials* **2003**, *15*, 2101-2104.
13. Liu, Y.; Jennings, J. R.; Wang, X.; Wang, Q., Significant Performance Improvement in Dye-Sensitized Solar Cells Employing Cobalt(III/II) Tris-Bipyridyl Redox Mediators by Co-Grafting Alkyl Phosphonic Acids with a Ruthenium Sensitizer. *Phys Chem Chem Phys* **2013**, *15*, 6170-4.
14. Andersson, G.; Morgner, H., Determining the Stopping Power of Low Energy Helium in Alkanethiolates with Neutral Impact Collision Ion Scattering Spectroscopy (Nicciss). *Nuclear Instruments & Methods in Physics Research Section B-Beam Interactions with Materials and Atoms* **1999**, *155*, 357-368.
15. Oberbrodthage, J., Determination of a Solute Electron Energy Spectrum Not Accessible Experimentally by Means of Singular Value Decomposition. *Journal of Electron Spectroscopy and Related Phenomena* **2000**, *107*, 231-238.

16. Schmerl, N. M.; Quinton, J. S.; Andersson, G. G., On the Growth of Evaporated Lif on P3ht and Pcbm. *Journal of Physical Chemistry C* **2018**, *122*, 23420-23431.
17. Rodriguez-Perez, M.; Noh-Pat, F.; Romero-Contreras, A.; Reyes-Ramirez, E. J.; Krishnan, S. K.; Ortiz-Quinonez, J. L.; Alvarado, J.; Pal, U.; Olalde-Velasco, P.; Villanueva-Cab, J., Re-Evaluating the Role of Phosphinic Acid (Dinhop) Adsorption at the Photoanode Surface in the Performance of Dye-Sensitized Solar Cells. *Phys Chem Chem Phys* **2020**, *22*, 1756-1766.
18. Neale, N. R.; Kopidakis, N.; van de Lagemaat, J.; Grätzel, M.; Frank, A. J., Effect of a Coadsorbent on the Performance of Dye-Sensitized Tio₂ Solar Cells: Shielding Versus Band-Edge Movement. *J Phys Chem B* **2005**, *109*, 23183-9.
19. Ellis-Gibbins, L.; Johansson, V.; Walsh, R. B.; Kloo, L.; Quinton, J. S.; Andersson, G. G., Formation of N719 Dye Multilayers on Dye Sensitized Solar Cell Photoelectrode Surfaces Investigated by Direct Determination of Element Concentration Depth Profiles. *Langmuir* **2012**, *28*, 9431-9.
20. Chandiran, A. K.; Zakeeruddin, S. M.; Humphry-Baker, R.; Nazeeruddin, M. K.; Grätzel, M.; Sauvage, F., Investigation on the Interface Modification of Tio₂ Surfaces by Functional Co-Adsorbents for High-Efficiency Dye-Sensitized Solar Cells. *Chemphyschem* **2017**, *18*, 2724-2731.
21. Singh, J.; Gusain, A.; Saxena, V.; Chauhan, A.; Veerender, P.; Koiry, S.; Jha, P.; Jain, A.; Aswal, D.; Gupta, S., Xps, Uv-Vis, Ftir, and Exafs Studies to Investigate the Binding Mechanism of N719 Dye onto Oxalic Acid Treated Tio₂ and Its Implication on Photovoltaic Properties. *The Journal of Physical Chemistry C* **2013**, *117*, 21096-21104.
22. Zen, S.; Inoue, Y.; Ono, R., Low Temperature (150° C) Fabrication of High-Performance Tio₂ Films for Dye-Sensitized Solar Cells Using Ultraviolet Light and Plasma Treatments of Tio₂ Paste Containing Organic Binder. *Journal of Applied Physics* **2015**, *117*, 103302.
23. Van de Vondel, D.; Wuyts, L.; Van der Kelen, G.; Bevernage, L., X-Ray Pes of Some Manganese Carbonyl Compounds. *Journal of Electron Spectroscopy and Related Phenomena* **1977**, *10*, 389-392.
24. Ardhi, R. E. A.; Tran, X. M.; Wang, M.; Liu, G.; Lee, J. K., Chemically Tuned, Bi-Functional Polar Interlayer for Tio₂ Photoanodes in Fibre-Shaped Dye-Sensitized Solar Cells. *Journal of Materials Chemistry A* **2020**.
25. Hahlin, M.; Johansson, E. M. J.; Scholin, R.; Siegbahn, H.; Rensmo, H., Influence of Water on the Electronic and Molecular Surface Structures of Ru-Dyes at Nanostructured Tio₂. *Journal of Physical Chemistry C* **2011**, *115*, 11996-12004.
26. Oscarsson, J.; Fredin, K.; Ahmadi, S.; Eriksson, A. I.; Johansson, E. M.; Rensmo, H., Molecular Degradation of D35 and K77 Sensitizers When Exposed to Temperatures Exceeding 100° C Investigated by Photoelectron Spectroscopy. *Physical Chemistry Chemical Physics* **2016**, *18*, 8598-8607.
27. Siow, K. S.; Britcher, L.; Kumar, S.; Griesser, H. J., Xps Study of Sulfur and Phosphorus Compounds with Different Oxidation States. *Sains Malaysiana* **2018**, *47*, 1913-1922.
28. Yin, Y. T.; Sibley, A.; Quinton, J. S.; Lewis, D. A.; Andersson, G. G., Dipole Formation at the Moo₃/Conjugated Polymer Interface. *Advanced Functional Materials* **2018**, *28*, 1802825.
29. De Angelis, F.; Fantacci, S.; Selloni, A.; Nazeeruddin, M. K.; Grätzel, M., First-Principles Modeling of the Adsorption Geometry and Electronic Structure of Ru (Ii) Dyes on Extended Tio₂

Substrates for Dye-Sensitized Solar Cell Applications. *The Journal of Physical Chemistry C* **2010**, *114*, 6054-6061.

Chapter Six

6 The effect of the carboxylic chenodeoxycholic as a co-adsorbent on the dye formation on dye/TiO₂ interface

6.1 ABSTRACT:

Co-adsorbents are small organic amphiphilic molecules containing carboxylic or phosphonic groups on one end that is responsible for efficient anchoring of the co-adsorbent on to the mesoporous TiO₂, and long hydro-phonic alkyl groups on the other end, and they are mostly used as anti-aggregation in dye-sensitized solar cells (DSSCs). In this study, the carboxylic chenodeoxycholic (CDCA) co-adsorbent used to study the effect on the adsorption mode of the dyes N719 and Z907 in DSSCs and the correspondent photovoltaic performance. The co-adsorption interface structure of the ruthenium-based dyes with different concentrations of CDCA was investigated using a combination of electron spectroscopic techniques, X-ray photoelectron spectroscopy (XPS), ultraviolet photoelectron spectroscopy (UPS), and metastable induced electron spectroscopy (MIES). While neutral impact collision ion scattering spectroscopy (NICISS) was used to measure the concentration depth profile of the adsorbed dye.

NICISS results shows that the co-adsorption of CDCA with Z907 is more effective on the reduction of the dye coverage and can reduce the formation of dye multilayers. The dyes N719 and Z907 are expected to be adsorb to TiO₂ surface via the carboxylic acid groups. However, XPS shows that the dyes can adsorb in mixed configurations on TiO₂ substrate. XPS shows signs of interacting with TiO₂ surface via the sulfur atom from the thiocyanate group in the dye. The results show that CDCA with different concentration plays a role in restructuring dye layers on TiO₂ surface.

6.2 Introduction:

Since 1991, dye-sensitized solar cells (DSSCs) have been studied extensively in consequence of their simple synthesis, and moderate to high power conversion efficiencies. DSSCs represent promise for next-generation photovoltaic technology [1, 2]. They are composed of dye sensitized molecules chemisorbed on a mesoporous semiconductor with a wide bandgap (TiO_2) in contact with the counter electrode and redox mediator. When the cell is irradiated with light, photons absorbed by the dye result in the excitation of electrons which will be injected into the conduction band of TiO_2 while dye loses electrons thus oxidized. Subsequently, the oxidized dye is then reduced by the redox mediator iodide/triiodide (I^-/I_3^-) in the electrolyte. The electrons through the external circuit will recombine with the triiodide (I_3^-) ions regenerating the iodide (I^-). However, several drawbacks are limiting the conversion efficiency of DSSCs. One of them is charge recombination, where the electrons injected into the conduction band of TiO_2 recombine with the cations formed by the dye after the electron transfer to the titania and with the I_3^- reducing the cell performance.

Furthermore, the amount of adsorbed dye on the TiO_2 surface can affect the charge generation. A high dye loading can be beneficial increasing the charge generation; however, a too high loading can form dye multilayers causes dye aggregation on the TiO_2 . The distance between the top layer dyes and the TiO_2 surface will be increased due to the aggregation, leading to blocking some of the charge carriers' transport to the TiO_2 surface. Moreover, aggregation of dye molecules on the TiO_2 surface will decrease the interaction of the electrolyte with dye cations formed through the excitation process and thus slow down the regeneration of the oxidized dyes molecules after excitation [3, 4]. Therefore, to alleviate these drawbacks, small molecules such as co-adsorbents are used to adsorb simultaneously with the dye to decrease and prevent the dye aggregation. The addition of the co-adsorbents can help in suppressing the recombination between the injected electrons and the electrolyte [5, 6]. Co-adsorbent contains either carboxylic or phosphonic groups on one end and long hydrophobic alkyl groups on the other end. The co-adsorbent attach to the TiO_2 surface by its carboxylic or phosphonic groups. The alkyl group acts as a buffer between TiO_2 and the electrolyte, preventing charge recombination. Adding co-adsorbent simultaneously with the dye solution has been reported to prevent dye aggregation by occupying the uncovered sites on the TiO_2 surface [5, 7-9], and is known to improve the cell efficiency by reducing the charge recombination [10, 11]. Chenodeoxycholic Acid (CDCA) binds strongly to the TiO_2

substrate, CDCA is mostly used as deaggregating agent reducing the dye aggregation, and forming a tightly packed layer working as a barrier shielding the electron recombination from the conduction band in TiO₂ to the triiodide electrolyte [6, 12-14]. It has been shown that the usage of CDCA as co-adsorbent in DSSCs fabricated with organic-based dyes P1 and P2 [10], and in the Rhodamine and indoline dyes improved the cell performance [15].

A recent study by Trilaksana et al. [16] investigated the effect of CDCA on the N719 dye coverage of TiO₂ for various CDCA concentrations in the dye solution for preparing the DSSCs. Their results showed that by increasing the CDCA concentration to 10 mM resulted in the decrease of the dye coverage. At CDCA concentrations larger than 10 mM the dye coverage starts to increase and reached at 20 mM a coverage close to that for the samples without CDCA. Adding the CDCA also reduced the multilayer formation of the N719. The authors provide reasoning that the decrease in dye multilayer formation should increase cell performance [16].

In the present work, CDCA in a range of concentrations is used as co-adsorbent with ruthenium-based dyes, the hydrophilic N719 and the hydrophobic Z907. The co-adsorbent/dye/TiO₂ system is studied using neutral impact collision ion scattering spectroscopy (NICISS) to measure the concentration depth profile of ruthenium sensitized on the TiO₂ surface. The surface-sensitive photoelectron spectroscopy techniques XPS and UPS are used to determine the composition of the dye layer and its electronic properties.

6.3 Experimental

6.3.1 Sample preparation

Details of DSSCs fabrication can be found in chapter 3. The working electrodes with various concentrations of CDCA as co-adsorbents, manufactured for both the N719 and the Z907 dye and assembled into fully operating DSSCs. All cells were made identical with the same components and had the same compositions, apart from the difference in the dye used (N719 or Z907) and CDCA concentrations. Any changes in the cell performance attributed to the concentration of CDCA. Working electrodes of N719-based dye and Z907-based dye fabricated for comparison purpose. (Six cells were fabricated to test the reproducibility and the average of best three cells used in this work).

6.4 Methods

6.4.1 J-V characteristics

All J-V measurements were conducted using an Oriel solar simulator system fitted with 150 W Xenon lamp (Newport) filtered to give the irradiation of 100 mW/cm^2 , an equivalent of 1 sun at air mass (AM 1.5G). A Si reference cell was used to calibrate the light intensity before the I-V measurement. A Keithley 2400 source meter operated by LabVIEW software was used to determine the open-circuit voltage (V_{oc}), short-circuit current density (J_{sc}), the fill factor (FF) and the over conversion efficiency (η) of the cells.

6.4.2 NICISS, XPS, UPS and MIES

Experimental details for neutral impact collision ion scattering spectroscopy (NICISS) [17, 18], X-ray photoelectron spectroscopy (XPS), ultraviolet photoelectron spectroscopy (UPS), and metastable induced electron spectroscopy (MIES) can be found in chapter 3.

In NICISS, He ions were used as projectiles in with energy of 3 keV to bombard the sample with a beam diameter of 1 mm. While an X-ray emission with Mg $K\alpha$ was used as the source of photons in XPS and operating with excitation energy of 1253.6 eV and at 200W, using a medium magnification lens mode to analyze an area of 7 mm in diameter. UV photons from the HeI line having the energy ($h\nu=21.2 \text{ eV}$) was used in UPS, and a metastable helium atom ($\text{He}^* 2s1s$) with excitation energy of 19.8 eV was used in MIES.

6.1 Results and Discussion

6.1.1 Photovoltaic performance

Typical J-V curves of N719 and Z907 DSSCs are shown in Figure 6-1. and short circuit current (J_{sc}), open circuit voltage (V_{oc}), fill factor (FF) and efficiency η are tabulated in Table 6.1 and 2. An overall conversion efficiency of 4.8 % obtained from the reference N719 cell without CDCA, with J_{sc} of 10.8 mA/cm^2 , V_{oc} of 0.75 mV, and FF of 0.59. The respective reference Z907 cell shows an overall conversion efficiency of 4.7 % with J_{sc} of 9.4 mA/cm^2 , V_{oc} of 0.73 mV, and FF of 0.67.

The photovoltaic performance of the DSSCs upon adding CDCA as co-adsorbents are summarized

in Table 6.1 and 2 (see also Figure 6-1) using N719 and Z907 as the photosensitizers, respectively. The highest efficiency of 5.4% was found for the N719 cells at a CDCA concentration of 5mM. For Z907 a very moderate variation of the cell efficiency was found with a maximum of 4.8% at 15 mM CDCA.

Furthermore, increasing the CDCA concentration in the Z907 cells has resulted in an increase in the J_{sc} with more stabilized V_{oc} and FF, while in N719 cell a slight decrease in J_{sc} with small variations in V_{oc} and FF.

Table 6.1: The influence of various concentrations of CDCA on the performance of the N719 cells.

CDCA (mM)	J_{sc} (mA/cm²)	V_{oc} (V)	FF	η (%)
0	10.8±0.3	0.75±0.01	0.59±0.04	4.8±0.3
5	10.5±0.2	0.76±0.01	0.68±0.02	5.4±0.2
10	10.5±0.1	0.76±0.01	0.67±0.01	5.3±0.1
15	10.4±0.3	0.74±0.01	0.64±0.02	4.9±0.1
20	10.3±0.3	0.75±0.01	0.67±0.02	5.2±0.0

Table 6.2: The influence of various concentrations of CDCA on the performance of the Z907 cells.

CDCA (mM)	J_{sc} (mA/cm²)	V_{oc} (V)	FF	η (%)
0	9.4±0.3	0.73±0.01	0.67±0.03	4.7±0.3
5	9.7±0.6	0.73±0.01	0.68±0.03	4.7±0.1
10	9.6±0.2	0.73±0.01	0.67±0.03	4.7±0.2
15	9.9±0.1	0.73±0.00	0.66±0.01	4.8±0.1
20	9.2±0.3	0.73±0.02	0.67±0.02	4.5±0.1

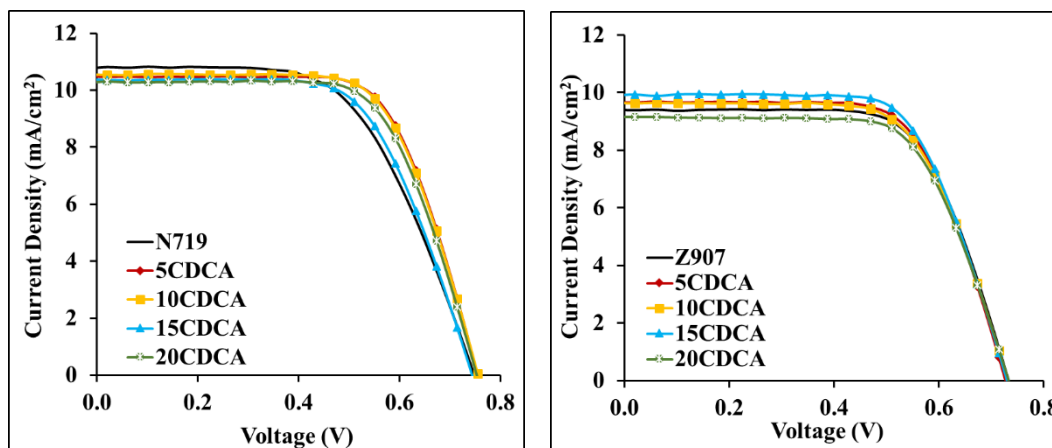


Figure 6-1: J-V measurements of DSSCs based on different concentration of CDCA using two different dyes: N719(A) and Z907(B).

6.1.2 Restructuring the dye layers

Figure 6-2 shows the Ru concentration depth profiles for all samples measured with NICISS. Upon the addition of CDCA, a noticeable shift in the Ru peak was observed in all co-adsorbed samples compared to the plain one which is probably related to restructuring of the dye layer. Furthermore, a change in peak width and depth, showing a maximum height between 10-20 Å in N719 samples, and 10 - 30 Å in Z907 samples. The concentration depth profile in the pure N719 in this study is in agreement with the previously published by Ellis-Gibbins et al. [19] and Johansson et al. [20]. However, a larger contribution of dye multilayers was observed by Trilaksana. This difference could be related to the pre and post treatment of the working-electrodes by TiCl₄ in this study, where TiCl₄ treatment is known to increase the surface roughness and forming about 1 nm shell of ultrapure TiO₂, increasing the dye adsorption [21-23]. The main finding in this study is to investigate the effect of CDCA as a co-adsorbent with different concentration on the dye formation on the TiO₂ surface. Thus the main finding is not affected by this difference.

It should be noted that the concentration depth profiles have been deconvoluted as it has been done in earlier work [19]. The measured coverage in this work is corrected for the spherical nature of the nonporous titania substrate.

The molecular coverage as a function of various concentrations of CDCA is shown in Figure 6-3. A maximum coverage of Z907-based sample is 11×10^{-11} mol/cm² and is higher than it found in

N719-based sample 5.2×10^{-11} mol/cm². The coverage is rather constant with a slight increase in the N719 samples, reaching a maximum of 6.4×10^{-11} mol/cm² at 15 mM CDCA.

For the Z907 samples, the highest coverage is found for the Z907 sample only and then decreases with increasing the CDCA concentration to about 65 % of the maximum coverage at 20 mM CDCA.

There is no noticeable change within the error bars in the dye coverage of the N719 samples, while a slight change in shape when increasing CDCA concentrations. The onset of Ru peak in N719 samples, shifted to higher depth, indicating that the formation of Ru on the TiO₂ surface is affected by the presence of CDCA, where CDCA tends to stay on the outermost layer driving the Ru deeper. The observed change in the intensity is different to what has been previously published by Trilaksana et al. [16], their results show a decrease in the dye coverage from 0 to 10 mM CDCA then an increase in the coverage again from 10 to 20 mM CDCA. In the present work, the coverage is almost steady with small variations as can be seen in Figure 6-3A. This difference could be due to the TiCl₄ treatments of the photoanode in this work which was not applied in the work of Trilaksana et al. [16]. The TiO₂ surface structure for both treatments could be different. The difference in surface structure for both treatments has not been investigated here. A significant change in Z907 samples was observed with a decrease in the dye coverage by ~ 50 % at 5 mM CDCA, followed by a small decrease in the dye coverage with further increase in CDCA concentrations. Figure 6-2B shows a significant decrease within the larger depth in the regions between 30--~50 Å, which is an indication that a lesser area is covered with thicker dye layers when CDCA is used as co-adsorbent.

CDCA consist mostly of C and O, the region of these elements is dominated by the backscattering projectiles from Ti, and thus NCISS is not suitable to determine the profiles of O and C in this case and thus the coverage with CDCA.

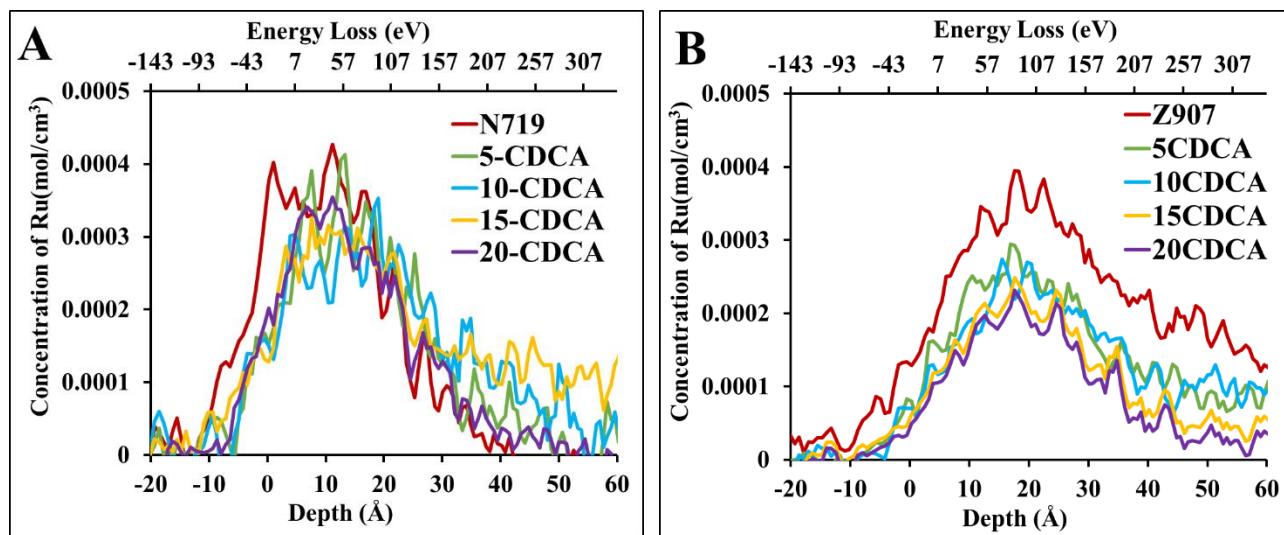


Figure 6-2: NISS Concentration depth profile of Ru with varying concentrations of CDCA using N719 (A) and Z907 (B) as sensitizer.. The concentration is plotted via two axis, the energy loss represent the measurement and the depth scale which is approximation due to the shape of porous titania.

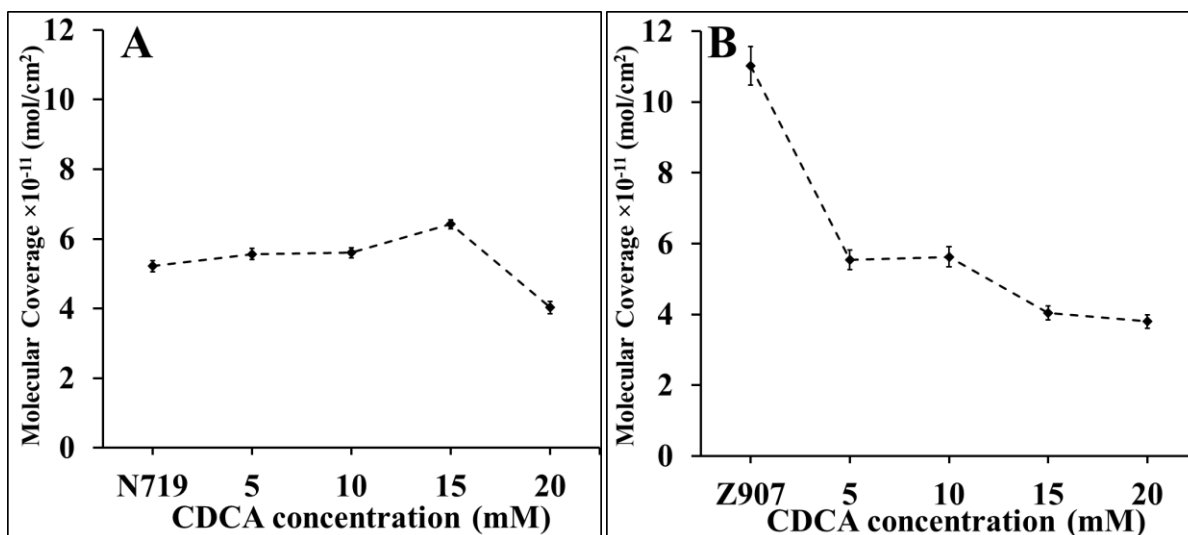


Figure 6-3: Molecular coverage of Ru with different concentration of DPA using N719 (A) and Z907 (B) as sensitizer.

Relevance of photovoltaic performance and the dye coverage from NICISS

Figure 6-4 shows the cell performance with respect to the dye coverage. A stabilized cell performance regardless the slight change in the dye coverage in N719 samples, while in Z907 samples, even though the Ru coverage reduced by about 60 %, the cell performance remains stable without compromising the cell performance.

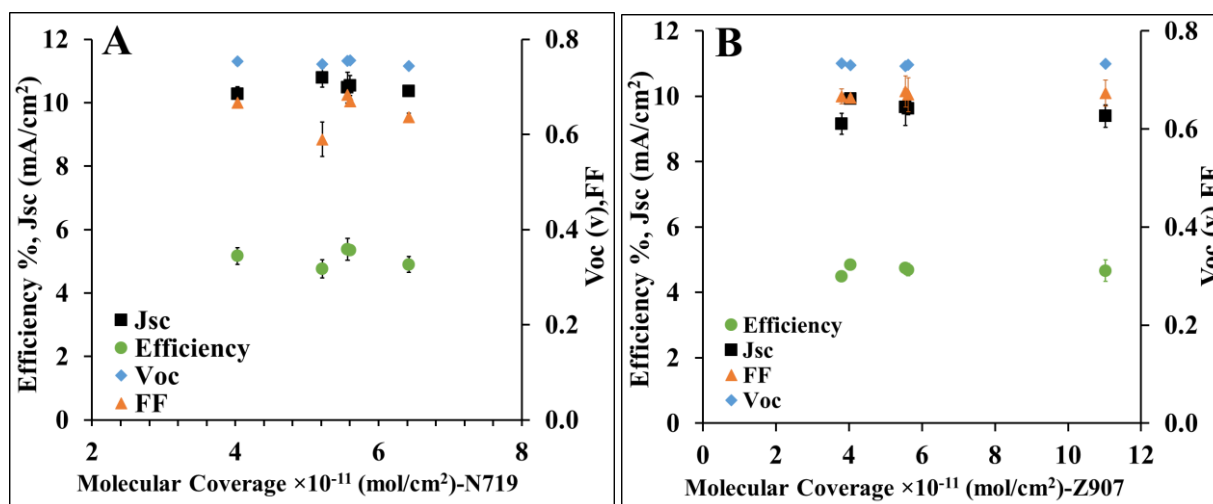


Figure 6-4: Short-circuit current and efficiency (left y-axis), open-circuit-voltage and fill factor (right y-axis) with the coverage of the dye N719(A) and Z907(B). The x-axis are different for better illustration of the data.

6.1.3 Chemical characteristics

XPS performed on all samples, to assess the changes in the elemental composition. The peaks C, O, Ru, N, S and Ti, were found. The C 1s, O 1s, Ru 3d, N 1s, and S 2p were used to analyze the adsorbed dye. The Ti 2p peak and O 1s are related to the TiO₂ substrate. Fitted high-resolution spectra are shown in Figure 6-5, and the peak positions with the relative peak intensities are listed in Table 6.3 and Table 6.4.

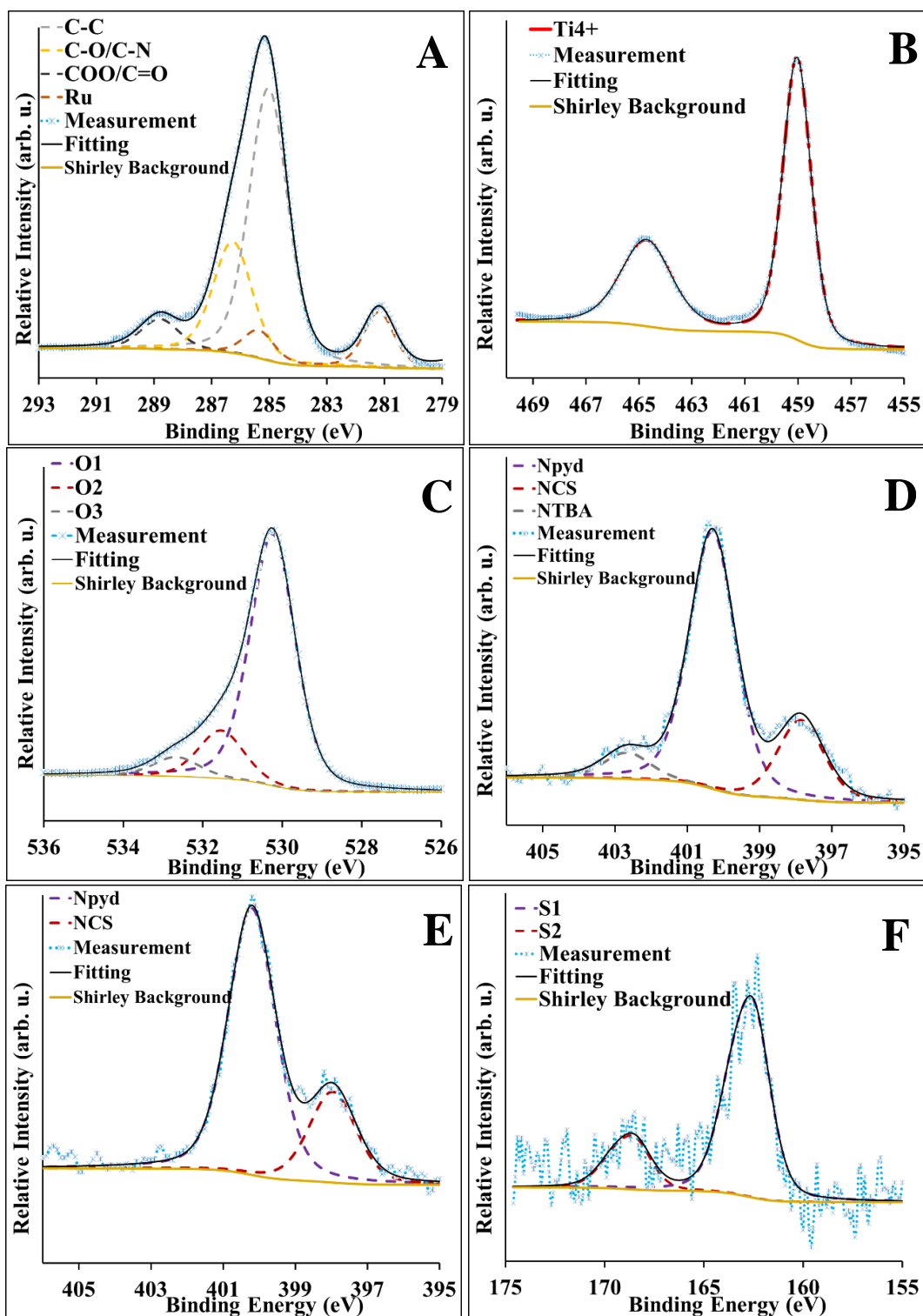


Figure 6-5: High resolution XPS spectra; (A) Carbon 1s, (B) Titanium 2p, (C) Oxygen 1s, (D) Nitrogen 1s in N719 dye, (E) Nitrogen 1s in Z907 dye, and (F) Sulfur 2p.

Table 6.3: Peak positions (eV) with uncertainty of ± 0.2 . Small peaks have relative intensities errors of ± 0.4 for (Ru, N3, S1, and S2) and an uncertainty of ± 0.3 for the other components in N719 based samples.

CDCA mM	0		5		10		15		20	
	Position	%Intensity								
C1	285.0	17.4	285.0	17.1	285.0	20.7	285.0	20.2	285.0	20.4
C2	286.1	8.8	286.2	8.3	286.1	14.4	286.2	10.3	286.2	8.4
C3	288.6	2.4	288.8	2.3	288.9	2.3	288.8	2.3	288.8	2.3
O1	530.0	40.3	530.2	39.7	530.2	33.4	530.2	36.3	530.2	37.9
O2	531.4	7.6	531.5	7.6	531.4	7.0	531.5	7.2	531.5	7.2
O3	532.8	2.0	532.6	2.9	532.6	3.2	532.7	2.7	532.6	2.9
Ti	458.8	14.4	459.0	14.3	459.0	12.5	459.0	13.0	459.0	13.7
Ru	281.0	0.4	281.2	0.3	281.1	0.3	281.1	0.3	281.2	0.3
N1	397.9	1.1	398.0	0.8	397.9	0.7	397.9	0.7	397.8	0.8
N2	400.1	3.0	400.3	2.6	400.2	2.2	400.3	2.5	400.3	2.6
N3	402.0	0.5	402.4	0.3	402.2	0.2	402.5	0.3	402.6	0.3
S1	162.2	0.6	162.4	0.7	162.4	0.5	162.4	0.4	162.4	0.4
S2	168.3	0.1	169.9	0.1	168.9	0.1	168.3	0.1	168.4	0.1
F	683.9	1.0	684.2	1.3	684.0	1.0	684.1	1.0	684.2	0.9
Sn	484.4	0.2	484.0	1.7	483.4	1.5	485.4	2.6	483.6	1.8

Table 6.4: Peak positions (eV) with uncertainty of ± 0.2 . Small peaks have relative intensities errors of ± 0.4 for (Ru, N3, S1, and S2) and an uncertainty of ± 0.3 for the other components in Z907 based samples.

CDCA mM	0		5		10		15		20	
	Position	%Intensity								
C1	285.0	32.1	285.0	30.2	285.0	32.2	285.0	31.8	285.0	31.3
C2	286.1	9.4	286.0	12.2	286.1	6.9	286.1	7.3	286.1	9.1
C3	288.3	1.4	288.4	1.3	288.5	1.6	288.5	1.4	288.6	1.1
O1	530.0	30.9	530.1	30.9	530.1	32.9	530.1	31.4	530.1	31.2
O2	531.2	5.0	531.3	5.4	531.2	5.6	531.0	6.1	531.1	6.0
O3	532.1	1.9	532.5	2.2	532.3	2.2	532.0	3.4	532.1	3.3
Ti	458.8	11.3	458.9	11.5	458.9	12.0	458.9	12.1	459.0	12.2
Ru	281.1	0.5	281.0	0.4	281.0	0.6	281.0	0.6	281.1	0.5
N1	398.1	1.0	397.7	0.9	397.8	0.9	397.9	0.9	398.0	0.9
N2	400.1	3.4	400.1	3.0	400.1	3.1	400.2	3.0	400.2	2.7
S1	162.2	0.9	162.2	0.5	162.3	0.6	162.3	0.7	162.2	0.7
S2	168.6	0.2	168.5	0.1	169.3	0.1	168.5	0.1	169.7	0.1
F	684.1	0.8	684.1	1.2	684.1	0.9	684.2	0.9	684.3	0.7
Sn	484.2	0.9	484.0	0.2	484.0	0.2	484.4	0.2	484.4	0.2

The high-resolution C1s and Ru 3d spectrum were fitted with five peaks are shown in Figure 6-5A. Three main components can be identified in the C1s spectra, the main C peak is located at 285.0 eV and is attributed to C-C bonds, the peak at 286.2 ± 0.2 eV corresponds to C-O/C-N, and the peak at 288.8 ± 0.2 eV to C(=O)OH species. The Ru 3d_{5/2} is located at 281.1 ± 0.2 eV and Ru 3d_{3/2} at 285.2 ± 0.2 eV, with the latter overlapping with the carbon C1s contribution in the spectrum [24, 25].

The amount of dye adsorbed to the TiO₂ surface was quantified by determining the intensity ratio of Ru 3d to the Ti 2p peak. The Ru intensity remains constant within the error bars in the N719 samples, while in the Z907 samples an increase in the intensity reaching its maximum at 10 mM of CDCA, then decrease in the intensity was observed with further CDCA addition. Within the experimental uncertainty, the dye coverage measured by NICISS and XPS is the same in N719 samples. In contrast, in the Z907 sample, there is a variation in NICISS and XPS results. NICISS shows a decrease in the dye coverage, and an increase was observed from XPS results. This variation in the dye coverage is probably related to some inhomogeneity in the surface coverage with the dye, and the difference of the area measured using NICISS is much smaller compared with area measured using XPS. Where in NICISS a 1 mm diameter of the area was measured while 7 mm diameter in XPS.

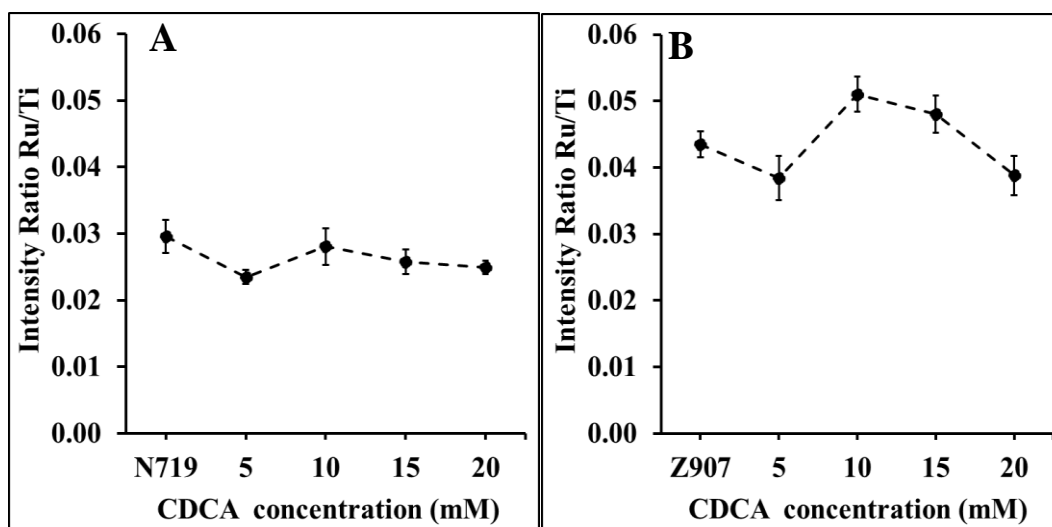


Figure 6-6: intensity ratio of Ru/Ti with different concentration of CDCA using N719 (A) and Z907 (B) as sensitizer.

The high-resolution O1s XPS of oxygen was fitted with three peaks as can be seen in Figure 6-5C, with peaks at 530.2 ± 0.2 eV and 531.5 ± 0.2 eV attributed to O^- and Ti-OH from TiO_2 surface. The peak at 531.5 ± 0.2 eV has also some contribution from the C=O groups of the dye [24]. The third peak at 532.7 ± 0.2 eV is attributed to oxygen in carboxylic groups of the dye [26].

A high-resolution scan of the N1s peaks measured, and N1s peak composed of three peaks as in Figure 6-5D. The peaks are located at 397.9 ± 0.2 eV, 400.3 ± 0.2 eV, and 402.3 ± 0.2 eV and are assigned to the thiocyanate ligands (N_{NCS}), bipyridine ligands (N_{pyd}) and N_{TBA} respectively, in N719 samples. While in Z907 samples, the N1s composed of two peaks as in Figure 6-5E. The peaks can be found at 397.9 ± 0.2 eV and 400.2 ± 0.2 eV and are assigned to N_{NCS} and N_{pyd} ligands, respectively [27, 28].

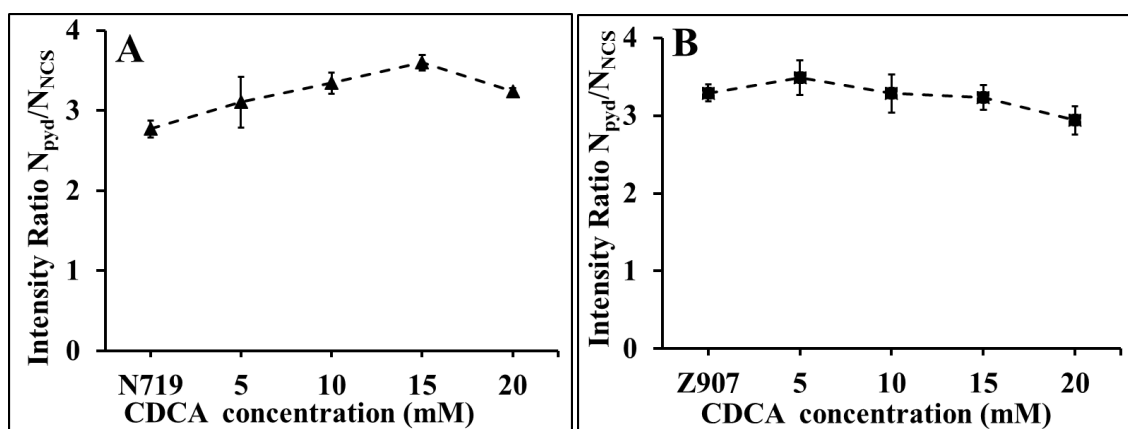


Figure 6-7: The intensity ratio between N_{pyd} and N_{NCS} with different concentration of CDCA using N719 (A) and Z907 (B) as sensitizer.

The ratio N_{pyd}/N_{NCS} in both N719 and Z907 dyes is 2:1 based on their chemical structure. Figure 6-7 shows that the measured N_{pyd}/N_{NCS} ratios for different concentration of CDCA. The intensity ratio of N_{pyd}/N_{NCS} is higher than the theoretical ratio, which can be attributed to a preferential orientation of the dye molecules. A ratio larger than 2 has to be interpreted such that the N_{pyd} moiety is pointing to the outermost layer (i.e., away from the TiO_2 surface) and that the N_{NCS} group is positioned closer to the TiO_2 surface. The N_{pyd}/N_{NCS} ratio in both of the N719 samples and the Z907 samples are rather constant and the same for both dyes. Thus, both dyes have a similar orientation where their N_{NCS} group is positioned closer to the TiO_2 surface.

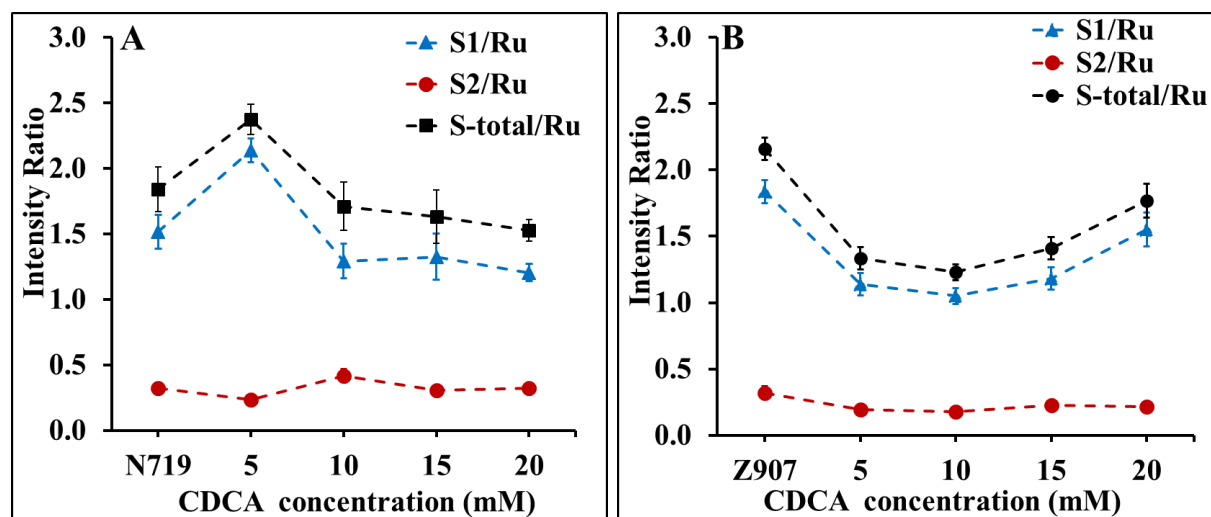


Figure 6-8: Intensity of S1/Ru and S2/Ru with different concentration of CDCA using N719 (left) and Z907 (B) as sensitizer.

Two species were found in the high resolution S 2p spectra shown in Figure 6-5F. The main peak is found at a binding energy of 162.4 ± 0.2 eV (S1) assigned to S atoms in the NCS group interacting with TiO₂ surface [29], and a second peak at a binding energy of 168.3 ± 0.2 eV (S2) attributed to highly oxidized sulfur (such as S⁶⁺ to S⁸⁺) [30]. The latter species cannot be involved in the formation of a bond to the substrate due to its high oxidation state. Figure 6-8 shows the intensity ratio of S_{Total}/Ru, S₁/Ru and S₂/Ru. The addition of 5 mM CDCA to the N719 dye causes a reorientation of the dye on TiO₂ surface, whereas further increments of CDCA did not effect on the dye orientation which also can be observed from the constant ratio between S₁/Ru and S₂/Ru, and it's in agreement with unchanged shape of Ru depth profile measured with NICISS. In the Z907 samples, the total ratio of S_{Total}/Ru is decreasing, which is showing the loss of coverage in Ru in the region within the thicker layers as measured with NICISS, with some orientation since the ratio between S₁/Ru and S₂/Ru is changing.

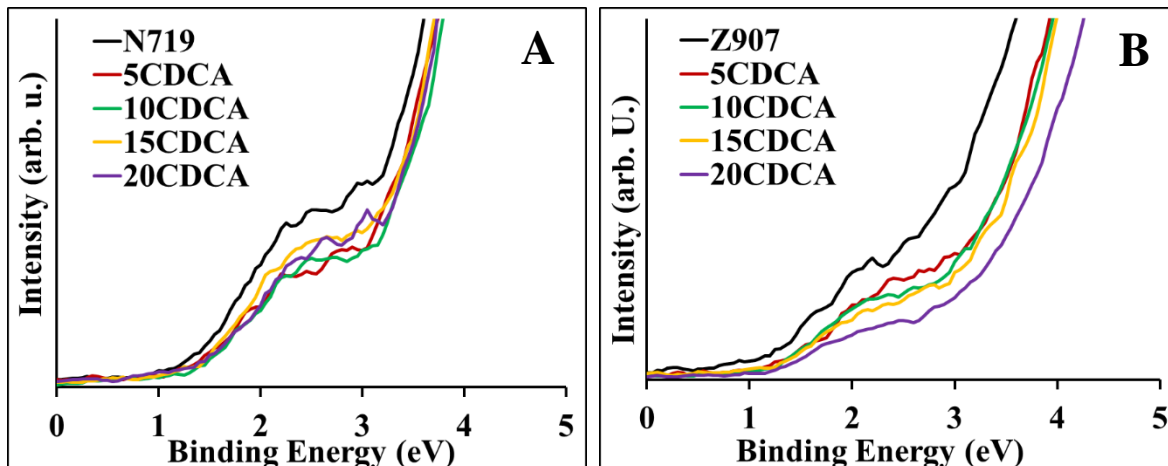
6.1.4 UPS analysis of TiO₂/dye interface with various CDCA concentrations

Figure 6-9: UP spectra of samples sensitized using N719 (A) and Z907 (B) with different concentration of CDCA showing the valence band level.

The UP spectra and the valence band (VB) level of all samples are shown in Figure 6-9. A feature presents in all the samples at ~2 eV representing the dye on the sample, and the intensity of this peak is lesser in Z907 samples than N719 samples and become slightly broader with a high concentration of CDCA. Which means that there are fewer electrons at the HOMO level, and it can be observed in cell performance, where a higher current was produced in the N719 cells than the Z907 cells.

Table 6.5: Work Function ± 0.1 (eV)

CDCA mM	N719	Z907
0	4.1	4.0
5	3.5	3.5
10	3.4	3.6
15	3.7	3.6
20	3.6	3.7

The work-function was measured by determining the secondary electron cut-off and is listed in Table 6.5, where the work function is defined as the difference between the fermi level and the vacuum level. The work function of the samples with only N719 and Z907 is 4.1 eV and 4 eV, respectively. The work-function is decreasing for both dyes with increasing CDCA concentration.

This difference in work-function suggests the formation of a dipole layer on the dye/TiO₂ interface. However, it is unclear what this would mean for the device performance.

6.1.5 The observation from MIES

The MIE spectra of all samples are presented in Figure 6-10. The spectra are almost identical, with more pronounced features in Z907 samples at 6 eV and 11 eV attributed to the presence of hydrocarbons [31]. The feature observed at ~2 eV in UPS was not observed in the outermost layer in MIES, illustrating that the changes are in deeper layers and not pronounced at the outermost layer.

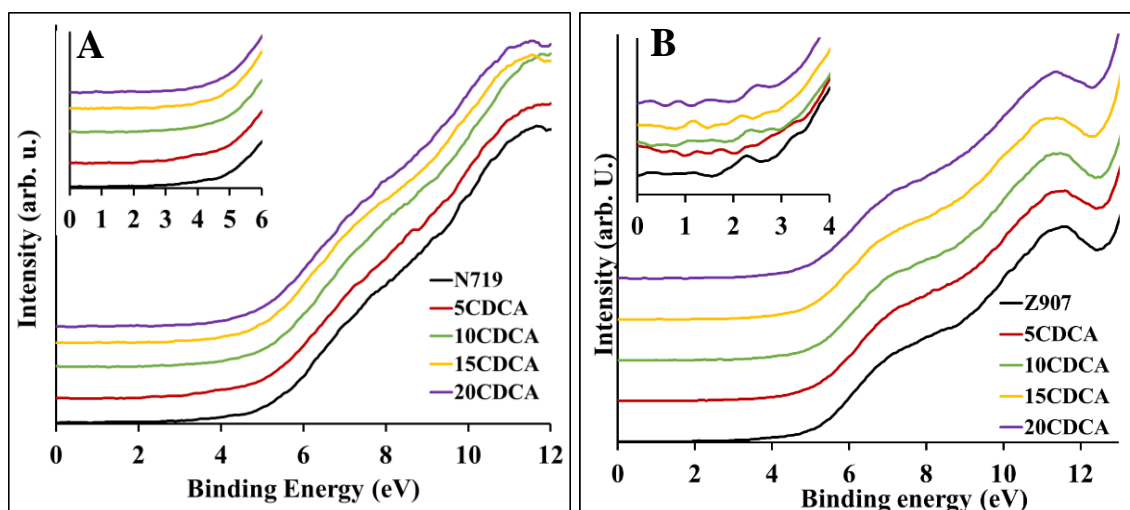


Figure 6-10: MIE spectra of samples sensitized using N719 (A) and Z907 (B) with different concentration of CDCA.

Measuring the samples with a combination of NICISS, XPS, UPS, and MIES illustrate the amount and how the dye molecules adsorbed on the TiO₂ surface with the addition of the co-adsorbent CDCA. NICISS results showed that the addition of CDCA remains on the surface and moves the dye deeper into TiO₂ surface, and this is consistent with UPS and MIES results, in UPS the feature that corresponded to the dye was observed. A reduction in the intensity was observed with increasing the CDCA concentration, while the outermost layer contains mostly hydrocarbons, and no significant change was observed.

The coverage remains constant in N719 samples, while in Z907 samples, a decrease in the dye coverage, as well as the change of the Ru concentration depth profiles, was observed by NICISS. A strong contribution of thicker dye layers was observed in Z907 sample at 0 mM of CDCA, upon

the addition of CDCA a significant decrease in the region of the thicker layers. CDCA reduces the dye/dye interaction and strengthens the dye/TiO₂ interactions. The difference of the CDCA behaviour when added to the dyes can be attributed the large molecule size of N719 compared to Z907, in the case of N719 samples CDCA push the dye deeper and mostly remain on top of the dye. The small size of Z907 allows more CDCA to be adsorbed on the TiO₂ surface and have the benefit to reduce the dye aggregation with some dye orientation. This can be observed from the increase in J_{sc} with the steadiness of the V_{oc} and FF in Z907 cells are more than N719 cells, illustrating that CDCA adsorbed on TiO₂ surface works as a buffer to reduce the charge recombination and improving J_{sc}.

Furthermore, the difference in the dye coverage of N719 samples in our results with the previously published by Trilaksana, could be related to the pre and post treatment of the working-electrodes by TiCl₄. In addition of reducing the dye multilayers, CDCA has the benefit to improve the cell performance when adsorbed on TiO₂ surface and work as buffer layer reducing the charge recombination.

In MIES measurements, which is sensitive to the outermost layer. The co-adsorbed and non-co-adsorbed samples spectra are similar, indicating that the changes related to the co-adsorbent CDCA are within the dye layers not on the outer surface.

6.2 Conclusion

The effect of CDCA as a co-adsorbent in the formation of the dye layer on the dye/TiO₂ interface was investigated using two different Ru-based dyes (N719 and Z907). The dye formation was investigated with the use of surface sensitive techniques. Co-adsorption of CDCA resulted in a shift of the Ru peak onset in both N719 and Z907 samples pushing the dye deeper into TiO₂ than on the surface. The addition of CDCA with different concentrations replaces the weakly and undesirable dye molecules in Z907 samples and maintaining the cell performance. By occupy the vacant spots on the TiO₂ surface, CDCA works as a buffer layer that prevents the charge recombination. A minor change was observed on the N719 structure and this is due to the large molecule size of N719 made it difficult for CDCA to be adsorbed on TiO₂ surface, resulted in a minor change in the cells current due to an increase in the charge recombination.

6.3 Reference

1. O'Regan, B.; Grätzel, M., A Low-Cost, High-Efficiency Solar Cell Based on Dye-Sensitized Colloidal TiO₂ Films. *Nature* **1991**, *353*, 737–740.
2. Grätzel, M., Photoelectrochemical Cells. *Nature* **2001**, *414*, 338-344.
3. Hestand, N. J.; Spano, F. C., Expanded Theory of H- and J-Molecular Aggregates: The Effects of Vibronic Coupling and Intermolecular Charge Transfer. *Chem Rev* **2018**, *118*, 7069-7163.
4. Buene, A. F.; Almenningen, D. M.; Hagfeldt, A.; Gautun, O. R.; Hoff, B. H., First Report of Chenodeoxycholic Acid-Substituted Dyes Improving the Dye Monolayer Quality in Dye-Sensitized Solar Cells. *Solar Rrl* **2020**.
5. Hara, K.; Dan-oh, Y.; Kasada, C.; Ohga, Y.; Shinpo, A.; Suga, S.; Sayama, K.; Arakawa, H., Effect of Additives on the Photovoltaic Performance of Coumarin-Dye-Sensitized Nanocrystalline TiO₂ Solar Cells. *Langmuir* **2004**, *20*, 4205-4210.
6. Wang, P.; Zakeeruddin, S. M.; Comte, P.; Charvet, R.; Humphry-Baker, R.; Grätzel, M., Enhance the Performance of Dye-Sensitized Solar Cells by Co-Grafting Amphiphilic Sensitizer and Hexadecylmalonic Acid on TiO₂ Nanocrystals. *The Journal of Physical Chemistry B* **2003**, *107*, 14336-14341.
7. Manthou, V. S.; Pefkianakis, E. K.; Falaras, P.; Vougioukalakis, G. C., Co-Adsorbents: A Key Component in Efficient and Robust Dye-Sensitized Solar Cells. *ChemSusChem* **2015**, *8*, 588-99.
8. Chandiran, A. K.; Zakeeruddin, S. M.; Humphry-Baker, R.; Nazeeruddin, M. K.; Grätzel, M.; Sauvage, F., Investigation on the Interface Modification of TiO₂ Surfaces by Functional Co-Adsorbents for High-Efficiency Dye-Sensitized Solar Cells. *Chemphyschem* **2017**, *18*, 2724-2731.
9. Saranya, G.; Yam, C.; Gao, S.; Chen, M., Roles of Chenodeoxycholic Acid Coadsorbent in Anthracene-Based Dye-Sensitized Solar Cells: A Density Functional Theory Study. *The Journal of Physical Chemistry C* **2018**, *122*, 23280-23287.
10. Li, J.; Wu, W.; Yang, J.; Tang, J.; Long, Y.; Hua, J., Effect of Chenodeoxycholic Acid (Cdca) Additive on Phenothiazine Dyes Sensitized Photovoltaic Performance. *Science China Chemistry* **2011**, *54*, 699.
11. Najm, A. S.; Ludin, N. A.; Abdullah, M. F.; Almessiere, M. A.; Ahmed, N. M.; Al-Alwani, M. A. M., Areca Catechu Extracted Natural New Sensitizer for Dye-Sensitized Solar Cell: Performance Evaluation. *Journal of Materials Science-Materials in Electronics* **2020**, *31*, 3564-3575.
12. Delcamp, J. H.; Shi, Y.; Yum, J. H.; Sajoto, T.; Dell'Orto, E.; Barlow, S.; Nazeeruddin, M. K.; Marder, S. R.; Grätzel, M., The Role of Pi Bridges in High-Efficiency Dscs Based on Unsymmetrical Squaraines. *Chemistry* **2013**, *19*, 1819-27.
13. Li, W.; Liu, Z.; Xu, X.; Cheng, Y.-B.; Zhao, Z.; He, H., Near-Infrared Absorbing Porphyrin Dyes with Perpendicularly Extended Π -Conjugation for Dye-Sensitized Solar Cells. *RSC Advances* **2014**, *4*, 50897-50905.

14. Neale, N. R.; Kopidakis, N.; Van De Lagemaat, J.; Grätzel, M.; Frank, A. J., Effect of a Coadsorbent on the Performance of Dye-Sensitized TiO₂ Solar Cells: Shielding Versus Band-Edge Movement. *The Journal of Physical Chemistry B* **2005**, *109*, 23183-23189.
15. Kumar, V.; Gupta, R.; Bansal, A., Role of Chenodeoxycholic Acid as Co-Additive in Improving the Efficiency of DSSCs. *Solar Energy* **2020**, *196*, 589-596.
16. Trilaksana, H.; Shearer, C.; Kloo, L.; Andersson, G. G., Restructuring of Dye Layers in Dye Sensitized Solar Cells: Cooperative Adsorption of N719 and Chenodeoxycholic Acid on Titania. *ACS Applied Energy Materials* **2018**, *2*, 124-130.
17. Andersson, G. a. H. M., Investigations on Solutions of Tetrabutylonium Salts in Formamide with Niciss and Iciss: Concentration Depth Profiles and Composition of the Outermost Layer. *Surface Science* **2000**, *445*, 89-99.
18. Andersson, G.; Morgner, H., Impact Collision Ion Scattering Spectroscopy (Iciss) and Neutral Impact Collision Ion Scattering Spectroscopy (Niciss) at Surfaces of Organic Liquids. *Surface Science* **1998**, *405*, 138-151.
19. Ellis-Gibbins, L.; Johansson, V.; Walsh, R. B.; Kloo, L.; Quinton, J. S.; Andersson, G. G., Formation of N719 Dye Multilayers on Dye Sensitized Solar Cell Photoelectrode Surfaces Investigated by Direct Determination of Element Concentration Depth Profiles. *Langmuir* **2012**, *28*, 9431-9.
20. Johansson, V.; Ellis-Gibbins, L.; Clarke, T.; Gorlov, M.; Andersson, G. G.; Kloo, L., On the Correlation between Dye Coverage and Photoelectrochemical Performance in Dye-Sensitized Solar Cells. *Phys Chem Chem Phys* **2014**, *16*, 711-8.
21. Barbe, C. J.; Arendse, F.; Comte, P.; Jirousek, M.; Lenzmann, F.; Shklover, V.; Grätzel, M., Nanocrystalline Titanium Oxide Electrodes for Photovoltaic Applications. *Journal of the American Ceramic Society* **1997**, *80*, 3157-3171.
22. Lee, S. W.; Ahn, K. S.; Zhu, K.; Neale, N. R.; Frank, A. J., Effects of TiCl₄ Treatment of Nanoporous TiO₂ Films on Morphology, Light Harvesting, and Charge-Carrier Dynamics in Dye-Sensitized Solar Cells. *Journal of Physical Chemistry C* **2012**, *116*, 21285-21290.
23. Adhikari, S. G.; Shamsaldeen, A.; Andersson, G. G., The Effect of TiCl₄ Treatment on the Performance of Dye-Sensitized Solar Cells. *J Chem Phys* **2019**, *151*, 164704.
24. Singh, J.; Gusain, A.; Saxena, V.; Chauhan, A.; Veerender, P.; Koiry, S.; Jha, P.; Jain, A.; Aswal, D.; Gupta, S., Xps, Uv-Vis, Ftir, and Exafs Studies to Investigate the Binding Mechanism of N719 Dye onto Oxalic Acid Treated TiO₂ and Its Implication on Photovoltaic Properties. *The Journal of Physical Chemistry C* **2013**, *117*, 21096-21104.
25. Zen, S.; Inoue, Y.; Ono, R., Low Temperature (150° C) Fabrication of High-Performance TiO₂ Films for Dye-Sensitized Solar Cells Using Ultraviolet Light and Plasma Treatments of TiO₂ Paste Containing Organic Binder. *Journal of Applied Physics* **2015**, *117*, 103302.
26. Ardhi, R. E. A.; Tran, X. M.; Wang, M.; Liu, G.; Lee, J. K., Chemically Tuned, Bi-Functional Polar Interlayer for TiO₂ Photoanodes in Fibre-Shaped Dye-Sensitized Solar Cells. *Journal of Materials Chemistry A* **2020**.

27. Oscarsson, J.; Hahlin, M.; Johansson, E. M. J.; Eriksson, S. K.; Lindblad, R.; Eriksson, A. I. K.; Zia, A.; Siegbahn, H.; Rensmo, H., Coadsorption of Dye Molecules at Tio₂ Surfaces: A Photoelectron Spectroscopy Study. *Journal of Physical Chemistry C* **2016**, *120*, 12484-12494.
28. Hahlin, M.; Johansson, E. M. J.; Scholin, R.; Siegbahn, H.; Rensmo, H., Influence of Water on the Electronic: And Molecular Surface Structures of Ru-Dyes at Nanostructured Tio₂. *Journal of Physical Chemistry C* **2011**, *115*, 11996-12004.
29. Oscarsson, J.; Fredin, K.; Ahmadi, S.; Eriksson, A. I.; Johansson, E. M.; Rensmo, H., Molecular Degradation of D35 and K77 Sensitizers When Exposed to Temperatures Exceeding 100° C Investigated by Photoelectron Spectroscopy. *Physical Chemistry Chemical Physics* **2016**, *18*, 8598-8607.
30. Siow, K. S.; Britcher, L.; Kumar, S.; Griesser, H. J., Xps Study of Sulfur and Phosphorus Compounds with Different Oxidation States. *Sains Malaysiana* **2018**, *47*, 1913-1922.
31. Alharbi, T. M. D.; Andersson, G. G., Ordering in Surfactant Foam Films Transferred onto Hydrophilic and Hydrophobic Substrates. *The Journal of Physical Chemistry C* **2017**, *121*, 25967-25977.

Chapter Seven

7. Interfacial study of aged semiconductor/dye/electrolyte in Dye Sensitized Solar Cells

7.1 ABSTRACT:

For cell commercialization, long-term stability is an essential factor. The electronic structure of the TiO₂/dye/electrolyte interface was investigated using ion spectroscopy and photoemission spectroscopy as the cell aging prolong, and compared with cell performance. Dye-sensitized solar cells (DSSCs) were fabricated with and without co-adsorbents, where the N719 dye was used as sensitizer and decylphosphonic acid (DPA) was used as the co-adsorbent. A study of a 1000 h stability-test of DSSCs working under different conditions was conducted to provide explanation of the degradation mechanics in the cell.

The thick dye layer in the N719 DSSCs performed as a buffer layer, slowing down the electrolyte penetration. In N719/DPA DSSCs, dye desorption was observed resulting from the competition between the cell components to be adsorbed on the TiO₂ surface. XPS results showed that small changes in electrolyte components with an increase in the oxidized sulfur are the main reasons for the cell to be degraded.

7.2 Introduction:

The increase in the environmental pollution along with the increased demand for energy makes it extremely important to find an energy sources and reducing emissions that impacting the climate. Photovoltaic cells of different types have been intensively investigated as a solution for this situation [1]. Dye-sensitized solar cells (DSSCs) were discovered in 1991 by Graetzel with an efficiency of ~7 %. DSSCs are representing the most cost-effective cells from the third generation of solar cells reaching an efficiency of ~13 % using porphyrin as sensitizer [2]. Although this efficiency is not impressive compared to an efficiency of 38 % in perovskite solar cells [3], DSSCs still represent a perfect model for the fundamental study of charge-transfer dynamics in electrochemical based solar cells, which can provide insights into structural and material engineering [4]. Designing a flexible colourful and transperence solar cell that can perform under diffuse light conditions and at high temperature made DSSC the most promising candidate solar cells. The main goal in the field of DSSCs is currently to focus on designing and developing new dyes and electrolytes to increase the cell performance and the stability, where the long-term stability is still challenging for commercialization this technology. With the tendency for establishing a stable DSSCs, the need for further understanding of DSSCs degradation mechanisms is essential for their commercialization. The TiO_2 /dye/electrolyte interfaces in DSSCs play a crucial role in cell performance as well as stability, where the main processes in DSSCs such as charge generation, collection, and recombination occurs at the interface. Studying these interfaces during the aging process with photoelectron spectroscopy techniques and comparing it with the cell performance will provide a better understanding of the changes of the chemical mechanism as the cell ages.

The weakly bounded dye molecules on TiO_2 is one of the reasons for DSSC instability [5]. Different types of co-adsorbents have been added to the dye solution to enhance cell performance by orienting and reducing the weakly bonded dye molecules on TiO_2 surface. Sharma et al. [6], found that the addition of deoxycholic acid (DCA) as co-adsorbent to DSSCs sensitized with perylene monoamide derivatives, enhances the cell performance by improving the short-circuit current. This enhancement was attributed to the increase in the electron injection efficiency, where the role of DCA as co-adsorbent was suppressing the charge recombination [6]. Furthermore, malonic acid derivatives (phenylmalonic acid-PMA) and acetic acid derivatives (cyclopentylacetic

acid-CPEAA) were used by Matsuyoshi et al., as co-adsorbents in DSSC sensitized with the dye D908 to investigate their effect on the cell performance. The ATR-FTIR spectroscopy results revealed that both the co-adsorbents increased the amount of dye anchored to TiO₂ surface increasing the short-current circuit [7]. In addition, using additives in the electrolyte such as 4-tert-butylpyridine (4TBP) can influence the TiO₂/dye/electrolyte interfaces by shifting the conduction band of TiO₂ [8].

Many studies were conducted to study the stability of DSSC. Wang and collaborators [9], showed long-term stability with more than 7 % power conversion efficiency for the first time. Nano-crystalline TiO₂ was covered with a mixture of self-assembled monolayers containing phosphonate as co-adsorbents and Z907 Ru dye to enhance the efficiency and stability of the DSSC. A significant improvement in the DSSC efficiency was achieved by stabilization of the voltage output after the co-adsorption of (decylphosphonic acid) DPA. This was attributed to long chain phosphonate excluding the water molecules from the interface [9]. A stability-test that took 2.5 years was successfully obtained in an outdoor stability-test using a series interconnected DSSC, without specification about module efficiency [10]. With a continuous light soaking at 0.8 sun, a stability test of 2280 h at 25 °C was achieved by Leonardi et al. [11]. A year later, Dyesol Ltd. achieved a stability test of 25600 h at 55 °C - 60 °C. With a minor degradation with the open circuit voltage corresponds to the positive shift of the conduction band [12].

Despite the plethora of the efforts in the stability tests, there is a lack of direct observation of the TiO₂/dye/electrolyte interfaces during the aging process that need to be investigated. The aim of this study is to investigate the TiO₂/dye/electrolyte interfaces for further understanding of the chemical reactions at the interfaces during the aging process using surface sensitive techniques. Ion and photoelectron spectroscopy are essential for monitoring the chemical changes in DSSCs periodically during their accelerating aging test, and correlate these changes with the cell performance. Understanding these changes will provide some information towards fabricating stabilized DSSCs.

In chapter 5, the co-adsorbent DPA was used with N719, showing an improvement in the cell performance even though the dye coverage was decreased ~80 %. The main role of co-adsorbents is to reduce the weakly bonded dye and filling the vacancy on TiO₂ surface thus reducing the recombination current. In this chapter, the cell stability was tested using the N719 dye with DPA

as co-adsorbent, and by using DPA concentration resulted of the best cell performance from chapter 5. Using ion and photoelectron spectroscopy to understand the interaction of the cell components at the TiO₂/dye/electrolyte interfaces and associate these changes with the photovoltaic parameters upon the aging test. DSSCs were assembled using the dye N719 only and were used as a reference cells. The reference cells were fabricated with the same procedures used in N719/DPA DSSCs, then subjected to same stability tests. The findings of the reference and the co-adsorbed sets will be compared and displayed in conjunction.

7.3 Experimental

Details of DSSCs fabrication can be found in chapter 3. After the final sintering of the TiO₂-electrodes as described in chapter 3, a batch of 40 TiO₂-electrodes were soaked in a dye solution of (0.3 mM) of N719 dye and named the N719 DSSCs, and another batch of 40 TiO₂-electrodes were soaked in a solution of (N719 : DPA) with 0.2 molar ratio. The cell were then assembled as described in chapter 3.

In order to understand deeply how DSSCs behave, the accelerated test was performed under three different conditions, 1) DSSCs were exposed to continuous irradiation (100 mW cm⁻²) in Atlas Suntest CPS, and the temperature was constantly maintained at 60 °C, these cells named light-set. 2) DSSCs were exposed to temperature at 60 °C without exposing to irradiation, named heat-set. 3) In the third conditions DSSCs were kept at in dark at room temperature, dark-set. The photovoltaic characteristics of the cells were recorded during the aging test at selected intervals. After that, DSSCs were disassembled and gently washed with ethanol to remove the residual electrolyte on the surface. Each cell measured at once only, where after disassembling the cell and measuring the interface no further aging done on that cell.

7.4 Results and Discussion

7.4.1 JV- Curve (Stability test)

The cell's parameters such as short circuit current density (J_{sc}), open circuit voltage (V_{oc}), efficiency (η) and fill factor (FF) were measured periodically during the aging test and their parameters are summarized in Table 7.1 and Table 7. 2. Figure 7-1 shows the photovoltaic parameters during the aging test for DSSCs sensitized with N719 and N719/DPA.

Table 7.1: Photovoltaic parameters of N719 DSSCs during the three conditions of aging test

Aging-Time (h)	Sun				Heat				Dark			
	J_{sc} (mA/cm ²)	V_{oc} (V)	FF	η	J_{sc} (mA/cm ²)	V_{oc} (V)	FF	η	J_{sc} (mA/cm ²)	V_{oc} (V)	FF	η
24	11.0	0.78	0.61	5.2	9.8	0.82	0.65	5.0	10.2	0.81	0.66	5.4
48	10.5	0.77	0.61	4.9	9.9	0.82	0.64	5.2	10.5	0.81	0.65	5.5
100	9.5	0.78	0.68	5.0	6.5	0.72	0.66	5.1	9.8	0.80	0.62	4.8
200	10.4	0.74	0.63	4.8	8.9	0.80	0.65	3.1	9.8	0.82	0.68	5.5
400	3.0	0.62	0.69	1.3	2.4	0.71	0.65	4.6	9.3	0.81	0.49	3.7
600	6.6	0.60	0.50	2.0	7.5	0.77	0.7	1.1	9.1	0.78	0.65	4.6
800	5.6	0.60	0.44	1.5	4.1	0.70	0.63	4.1	9.3	0.81	0.66	4.9
1000	-	-	-	-	2.4	0.69	0.63	1.0	6.7	0.77	0.66	3.4

Table 7. 2: Photovoltaic parameters of N719/DPA DSSCs during the three conditions of aging test.

Aging-Time (h)	Sun				Heat				Dark			
	J_{sc} (mA/cm ²)	V_{oc} (V)	FF	η	J_{sc} (mA/cm ²)	V_{oc} (V)	FF	η	J_{sc} (mA/cm ²)	V_{oc} (V)	FF	η
24	10.2	0.75	0.56	4.3	9.2	0.82	0.52	3.9	9.5	0.82	0.57	4.5
48	10.8	0.75	0.58	4.7	9.6	0.83	0.53	4.2	9.3	0.81	0.63	4.8
100	9.5	0.73	0.62	4.3	8.2	0.81	0.66	4.4	8.2	0.82	0.67	4.5
200	10.0	0.72	0.57	4.2	9.0	0.82	0.67	5.0	9.0	0.82	0.65	4.8
400	9.5	0.70	0.58	3.9	6.6	0.82	0.63	3.4	8.5	0.81	0.67	4.6
600	1.9	0.56	0.68	0.7	5.0	0.74	0.70	2.6	8.2	0.83	0.68	4.7
800	4.7	0.56	0.53	1.4	4.3	0.79	0.69	2.4	2.8	0.74	0.60	1.3
1000	2.7	0.54	0.57	0.8	2.8	0.70	0.54	1.1	3.2	0.69	0.58	1.3

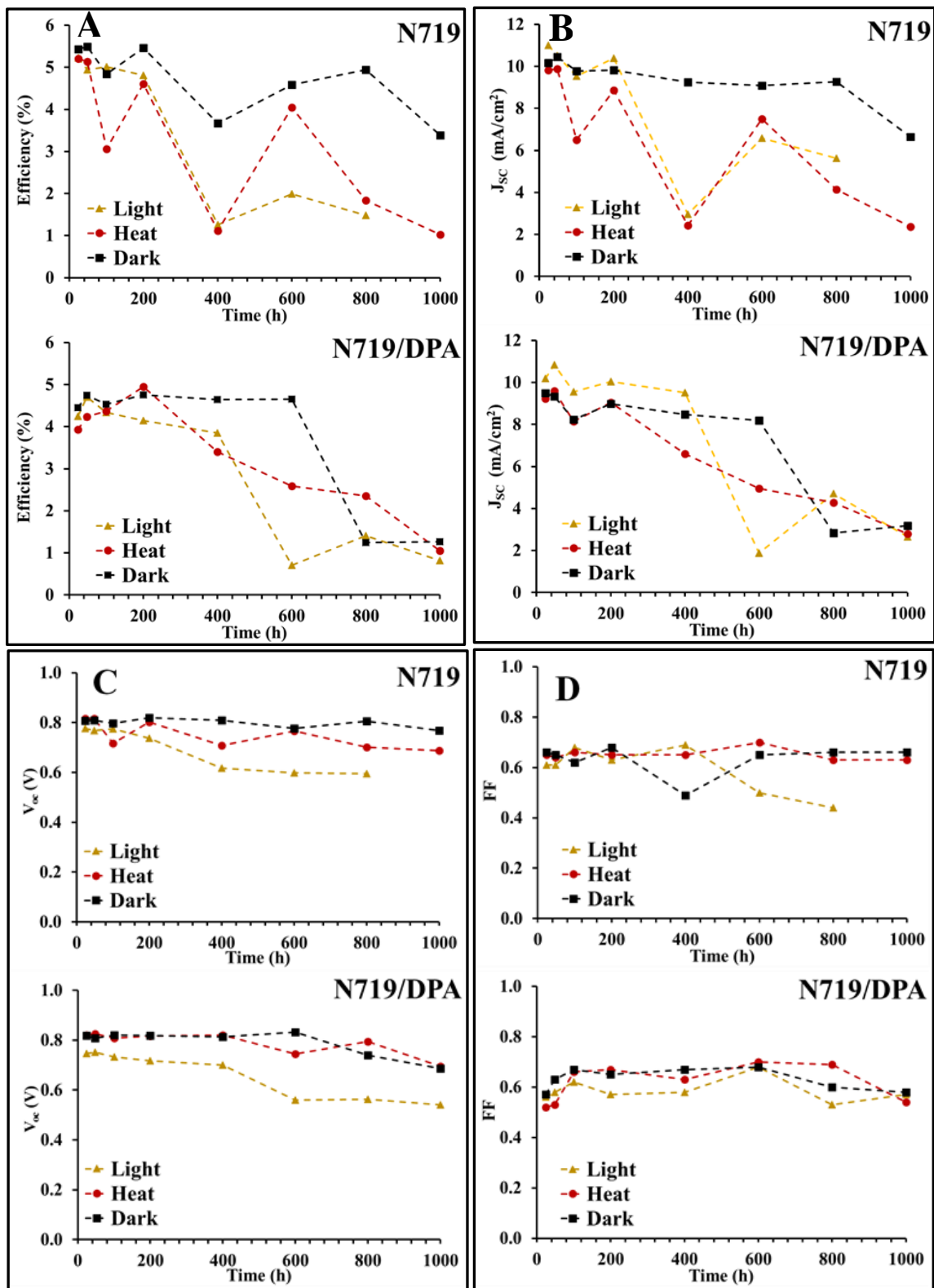


Figure 7-1: Photovoltaic parameters of DSSCs sensitized with N719 and N719/DPA in three different conditions during the aging test.

In Figure 7-1A, an initial increase in the cell performance was observed in all test conditions in the co-adsorbed cells during the first 48 hours, while steadiness with a slight decrease in N719 cells. Upon aging, the efficiency of the co-adsorbed cells exhibits stabilized and an increase in its efficiency up to 400 h in light-set, 200 h in heat-set, and 600 h in dark-set. While the N719 cells fluctuates in efficiency as the cell ages.

The efficiency in N719/DPA cells in the light-set increased to maximum then a drastic drop in the efficiency by 80 % at 600 h. While in the heat-set a boost in the efficiency was observed up to 200 h, then it's systematically decreased as the cell ages. In the dark-set steepest efficiency decreased at 800 h.

The maximum efficiency was obtained with the N719 cells in all conditions compared to the co-adsorbed cells. However, a variation in the efficiency as the cell aged in the three conditions.

From Figure 7-1B, similar behavior was observed for the J_{sc} comparing with the efficiency, where the highest J_{sc} was obtained from the light-set in both N719 /DPA and N719 DSSCs, indicating more injection of electrons due to the photoexcitation of the dye in the light condition. A systematical decrease in N719/DPA cell, while a variation in N719 cell in the heat-set. A stabilized J_{sc} in the dark-set in both N719/DPA and N719 DSSCs with a drop at 800 h in N719/DPA DSSC.

A total drop of 28 % and 27 % in V_{oc} observed in the light-set of N719/DPA and N719 DSSCs respectively, while no major changes in the heat-set and dark-set maintaining ~85 % after 1000 h of aging. Indicating that exposing the cell to heat without light exposure worked in favor with V_{oc} Figure 7-1D shows the fill factor in the three conditions. A stabilized fill factor in the N719 DSSCs while a slight improvement observed in N719/DPA DSSCs.

There are two types of resistance need to be considered when reviewing the cell efficiency. The series resistance (R_s) which results from the contact between the interfaces of DSSC and the shunt resistance (R_{sh}) which is attributed to the current leakage generated from the electrons that do not reach the electrode due to charge recombination [13]. Figure 7-2 shows both of R_s and R_{sh} as the cells ages. It can be seen from Figure 7-2A that R_s in N719 DSSCs constant within the first 200 h, in the three conditions, then an increase in the resistance at 400 h in the light and heat sets while R_s in the dark-set remains almost constant. In Figure 7-2B, the R_s of N719/DPS DSSCs are more

stabilized up to 400 h in light-set, 800 h in heat-set and 600 h in the dark-set. The sudden increase in R_s is attributed to the electrolyte consumption.

Figure 7-2C show R_{sh} in N719 DSSCs, in the light-set an increases in the resistance reaching a maximum at 400 h then drops down and remain increasing in the light-set, while a very low resistance was observed in the dark-set. Figure 7-2D shows stabilized R_{sh} in N719/DPA DSSCs as the cell ages. However, a sudden increase at 600 h in the light and heat sets.

Both resistances R_s and R_{sh} have contribution on the cell performance, the effect of the R_s is more dominant on the cell performance, where a small variation of R_s effect the cell performance.

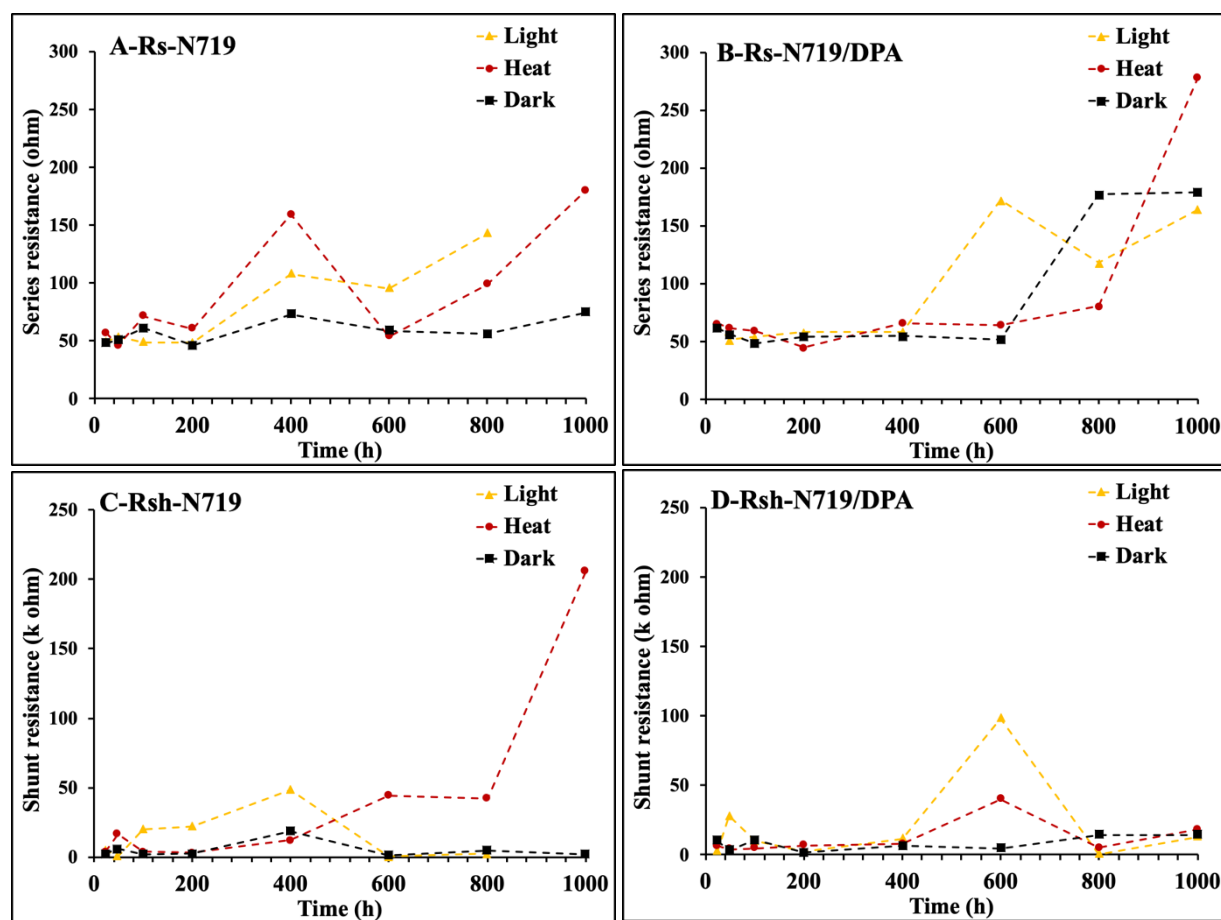


Figure 7-2: Series and Shunt resistance of DSSCs sensitized with N719 and N719/DPA in three different conditions during the aging test.

7.4.2 Elemental depth profiles

Figure 7-3 shows the concentration depth profiles for all aged samples under the three different conditions, and Figure 7-4 shows their respective molecular coverage. Ruthenium and iodide onset are quite close to each other; that is why their depth profiles appeared close to each other and made it difficult to differentiate between the contribution of how the depth of each of I and Ru peaks infiltrating into the TiO_2 . Figure 7-4A shows an increase in the coverage in the three conditions in N719 sample. In N719 cells, an increase in the coverage with cells subjected to light, while fluctuating in coverage was observed for cells subjected to heat and dark.

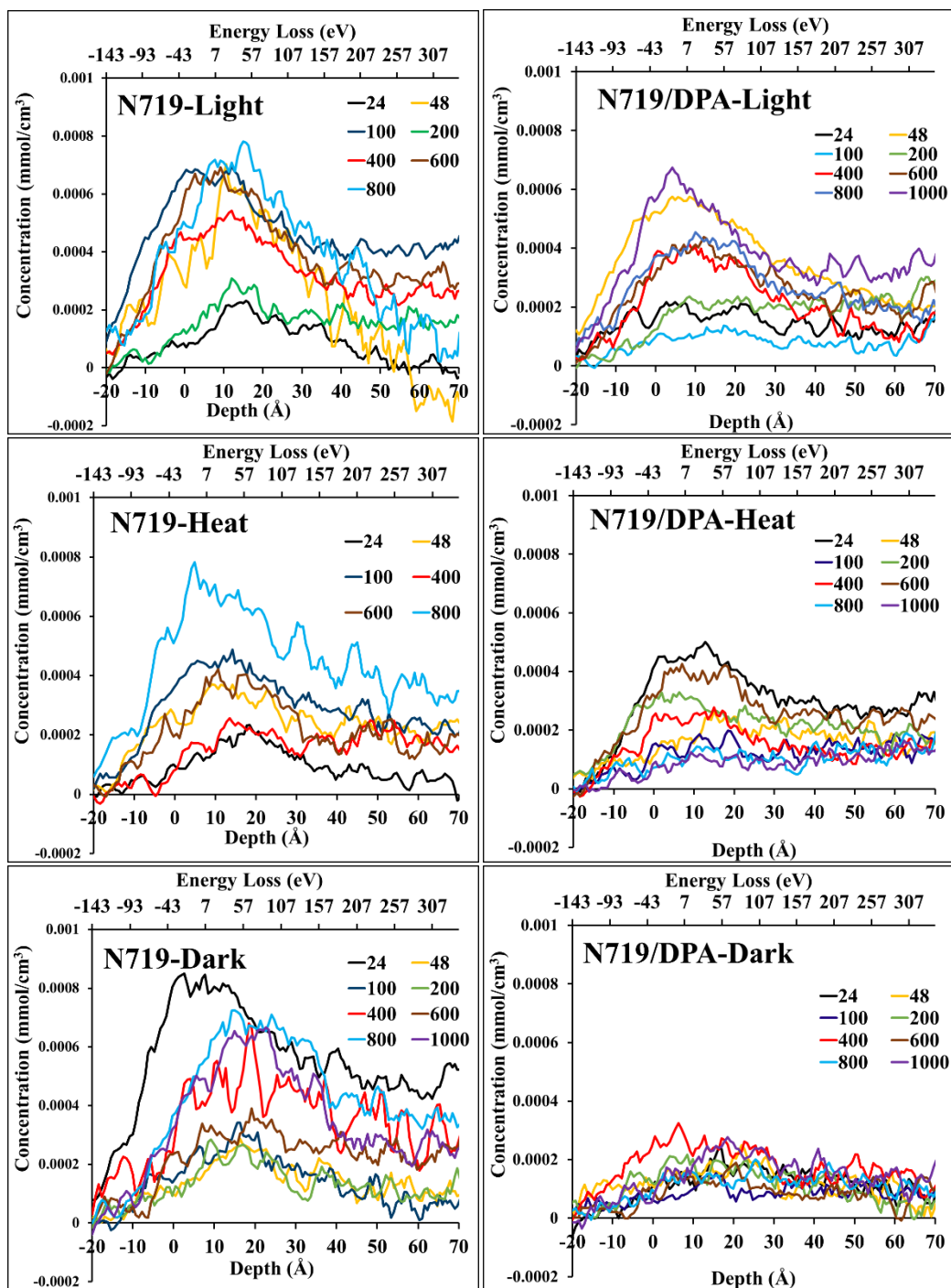


Figure 7-3: Concentration depth profile of N719 (left) and N719/DPA (right) aged sample in three different conditions. (With respect to iodine depth scale).

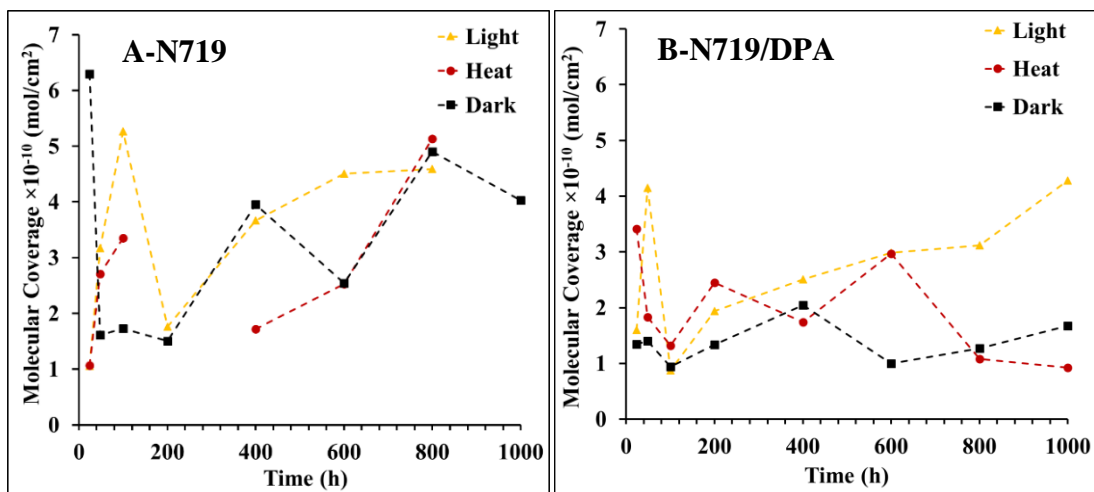


Figure 7-4: Molecular coverage of N719 (A) and N719/DPA (B) aged sample in three different conditions.

7.4.3 XPS

XPS was used in this study to analyze the surface composition and the changes in the chemical state, providing a complementary data to monitor these changes and the interactions between the TiO₂/dye/electrolyte interfaces as the cell ages. DSSCs were disassembled and analyzed by XPS, comparing with unexposed photoanode to the electrolyte, all the aged samples showed a new doublet peak at 619 eV arising from I 3d due to the electrolyte penetration into the substrate. Moreover, there was no trace of Pt immigrating from the counter electrode, where the iodide/triiodide redox is known as highly corrosive and attacks most metals. The thermally platinized counter electrode was used to prepare the counter electrode for fabricating DSSCs in this study, and this method is more favorable for long-term stability avoiding the redox attack [14]. Table 7.3- 7.8 shows the peak position and the relative intensities of each element as DSSCs aged.

The first part of the results will give an introduction presenting the total intensities of the main elements (Ti, O, C, Ru, N, S, I, and P) as the cell ages. The second part will deal with the changes in ratio between the elements such as Ru, N, S, and I, where they represent the dye, additives and electrolyte in the cell.

In the last part the XPS results will be linked with the cell performance to investigate the how the changes in intensities can affect the cell performance as the cell ages.

Chapter Seven

Table 7.3: Peak positions (eV) ± 0.2 and the relative intensities with errors of ± 0.4 for (Ru, N3, S1, S2, I1 and I2) and ± 0.3 for the other components in N719 samples in the light-set. Remaining percentage is F and Sn.

Time (h)	24		48		100		200		400		600		800	
Element	Position	Intensity %												
C1	285.0	12.9	285.0	9.6	285.0	10.5	285.0	21.7	285.0	10.3	285.0	10.8	285.0	23.9
C2	286.0	15.0	285.9	17.9	286.0	21.6	285.9	20.0	286.0	18.9	285.9	19.3	286.2	14.2
C3	288.3	2.8	288.2	2.6	288.0	2.8	288.1	2.1	288.2	2.9	288.3	3.1	288.2	2.1
O1	530.0	35.3	530.0	35.2	529.9	30.7	529.7	25.4	530.0	32.5	530.0	34.6	529.9	27.5
O2	531.3	6.4	531.0	5.6	531.2	5.4	531.1	5.4	531.3	5.3	531.3	6.1	531.3	5.4
O3	532.6	1.9	531.9	3.3	532.2	1.9	532.3	2.7	532.2	1.5	532.4	2.3	532.5	2.1
Ti	458.7	12.5	458.8	13.5	458.7	11.4	458.5	9.1	458.8	11.4	458.8	12.5	458.7	9.9
Ru	281.0	0.4	281.1	0.4	281.1	0.4	280.9	0.3	281.0	0.3	281.1	0.4	280.9	0.2
N1	401.8	1.9	401.9	1.9	401.9	3.7	401.7	2.4	401.8	2.9	401.9	1.8	401.7	3.4
N2	400.1	2.8	400.2	2.9	400.2	2.5	400.0	2.4	400.1	2.8	400.2	2.9	400.0	2.3
N3	398.1	1.1	398.3	1.1	398.3	1.0	398.1	0.6	398.4	0.9	398.3	0.8	398.1	0.7
S1	162.3	0.8	162.3	1.0	162.4	0.9	162.1	0.5	162.4	0.5	162.3	0.8	162.2	0.5
S2	168.5	0.16	168.2	0.1	167.7	0.1	168.3	0.2	168.5	0.3	168.5	0.2	168.1	0.3
I1	618.6	1.0	618.7	1.2	618.6	3.8	618.4	2.1	618.7	4.7	618.7	2.0	618.5	3.8
I2	620.3	0.1	620.9	0.1	620.4	0.4	619.9	0.1	620.8	0.3	620.9	0.1	620.2	0.2

Table 7.4: Peak positions (eV) ± 0.2 and the relative intensities with errors of ± 0.4 for (Ru, N3, S1, S2, I1 and I2) and ± 0.3 for the other components in N719/DPA samples in the light-set. Remaining percentage is F and Sn.

Time (h)	24		48		100		200		400		600		800		1000	
Element	Position	Intensity %														
C1	285.0	19.6	285.0	21.1	285.0	24.8	285.0	25.2	285.0	22.5	285.0	21.1	285.0	16.9	285.0	21.2
C2	286.0	13.4	286.1	12.3	286.0	8.7	286.1	13.0	286.1	11.1	286.1	12.1	286.0	15.6	286.1	8.9
C3	288.1	1.5	287.3	3.3	287.1	2.9	288.1	3.5	287.3	3.1	288.2	2.0	288.4	1.6	288.4	2.4
O1	530.0	31.9	530.1	30.7	530.0	34.0	530.1	27.7	530.1	30.4	529.9	33.0	530.0	34.5	530.0	37.4
O2	530.8	8.2	531.3	6.1	531.2	7.2	531.3	7.6	531.0	6.0	530.9	6.9	531.0	6.4	531.2	7.1
O3	531.8	4.2	532.3	1.7	532.3	2.2	532.4	2.0	531.9	2.5	531.8	2.9	531.9	2.8	532.2	2.4
Ti	458.9	12.6	458.9	11.3	458.8	12.7	458.8	10.0	458.9	11.7	458.7	12.4	458.8	12.7	458.8	13.2
Ru	281.1	0.2	281.1	0.3	281.0	0.2	281.0	0.4	281.1	0.2	281.0	0.16	281.0	0.2	280.9	0.2
N1	401.9	1.8	401.9	3.7	401.9	1.8	401.9	2.1	401.9	3.4	401.8	2.4	401.9	2.1	401.8	1.0
N2	400.2	1.6	400.1	2.0	400.1	1.4	400.2	3.5	400.2	1.6	400.2	1.7	400.1	2.0	400.1	2.2
N3	398.3	0.5	398.3	0.7	398.1	0.3	398.3	1.0	398.4	0.3	398.8	0.6	398.3	0.5	398.0	0.5
S1	162.4	0.4	162.4	0.6	162.4	0.3	162.3	0.9	162.5	0.4	162.4	0.2	162.3	0.4	162.4	0.3
S2	168.1	0.04	168.3	0.1	168.3	0.0	168.7	0.1	169.1	0.1	168.5	0.1	169.1	0.1	168.8	0.1
P	132.9	1.0	133.0	0.8	132.9	1.1	133.0	0.8	132.9	1.0	132.7	1.2	132.9	0.8	132.9	1.0
I1	618.7	2.0	618.6	4.4	618.7	2.0	618.7	1.9	618.6	5.0	618.6	2.8	618.6	2.8	618.7	1.2
I2	620.6	0.2	620.5	0.4	620.7	0.2	620.7	0.1	620.6	0.5	620.5	0.4	620.8	0.3	620.8	0.1

Table 7.5: Peak positions (eV) ± 0.2 and the relative intensities with errors of ± 0.4 for (Ru, N3, S1, S2, I1 and I2) and ± 0.3 for the other components in N719 samples in the heat-set. Remaining percentage is F and Sn.

Time (h)	24		48		100		200		400		600		800		1000	
Element	Position	Intensity %														
C1	285.0	5.5	285.0	11.3	285.0	10.3	285.0	11.1	285.0	8.4	285.0	10.7	285.0	20.3	285.0	12.0
C2	286.1	38.5	286.1	16.5	286.0	17.2	286.1	19.3	286.0	18.1	286.1	16.9	286.1	15.6	286.1	15.4
C3	288.5	3.5	288.5	3.1	288.2	2.9	288.5	2.6	288.6	3.3	288.2	3.1	288.1	2.4	288.3	3.4
O1	530.2	23.5	530.0	34.6	529.9	32.4	530.0	30.6	530.1	36.5	530.0	33.8	529.8	29.9	529.9	35.9
O2	531.8	4.7	531.3	6.6	530.8	6.2	531.0	5.7	531.4	6.6	531.0	5.5	531.2	5.1	531.2	6.2
O3	533.2	2.6	532.5	2.0	531.8	3.1	532.0	3.2	532.5	1.9	531.9	3.5	532.1	1.8	532.1	2.7
Ti	459.0	8.1	458.8	12.3	458.7	12.8	458.8	11.5	458.9	13.0	458.8	12.6	458.5	10.4	458.7	13.2
Ru	281.3	0.3	281.0	0.4	281.0	0.4	281.1	0.4	281.1	0.4	281.1	0.4	280.9	0.3	281.0	0.4
N1	401.8	3.4	401.9	2.2	401.8	3.1	401.9	2.8	402.1	1.6	401.9	2.5	401.6	4.2	401.9	2.6
N2	400.2	1.1	400.1	2.4	400.1	2.7	400.1	2.3	400.2	2.9	400.2	2.4	400.0	1.8	400.1	2.5
N3	398.5	0.8	398.1	1.3	398.2	1.0	398.0	1.1	397.7	1.0	398.3	1.1	398.1	1.0	398.2	1.1
S1	162.6	0.6	162.4	0.7	162.3	0.9	162.4	0.5	162.3	0.4	162.4	0.9	162.2	0.6	162.3	0.9
S2	168.7	0.1	168.3	0.2	168.7	0.1	-0.5	0.0	168.5	0.2	168.5	0.1	168.3	0.2	168.2	0.2
I1	618.7	1.6	618.8	1.8	618.6	2.7	618.8	3.4	619.1	0.9	619.0	1.3	618.4	3.8	618.6	0.5
I2	620.1	0.9	620.9	0.1	620.5	0.2	621.3	0.2	621.8	0.07	621.7	0.1	620.6	0.27	619.5	0.16

Table 7.6: Peak positions (eV) ± 0.2 and the relative intensities with errors of ± 0.4 for (Ru, N3, S1, S2, I1 and I2) and ± 0.3 for the other components in N719/DPA samples in the heat-set. Remaining percentage is F and Sn.

Time (h)	24		48		100		200		400		600		800		1000	
Element	Position	Intensity %														
C1	285.0	30.3	285.0	24.0	285.0	16.5	285.0	23.2	285.0	26.3	285.0	24.3	285.0	20.3	285.0	22.1
C2	286.2	18.7	286.2	13.5	285.8	26.2	286.2	9.8	286.2	8.3	286.0	13.7	286.1	10.1	286.3	6.9
C3	288.5	1.2	288.2	2.4	288.4	1.4	288.1	1.8	288.2	1.8	288.5	1.7	288.6	1.9	288.3	1.8
O1	530.1	17.9	530.0	29.5	530.0	27.2	529.8	19.7	529.8	29.5	529.9	31.4	529.9	37.7	529.9	37.6
O2	531.1	7.8	531.3	7.1	531.3	6.3	530.3	11.6	530.4	9.7	531.1	6.5	531.0	7.5	531.3	8.8
O3	532.6	4.8	532.3	1.5	532.5	1.8	531.1	11.0	531.5	4.7	532.3	2.0	531.9	2.6	532.5	3.7
Ti	458.9	7.4	458.8	10.2	458.8	9.7	458.8	13.0	458.6	12.9	458.7	11.1	458.7	13.8	458.6	11.8
Ru	281.2	0.2	281.1	0.3	281.1	0.3	281.1	0.1	281.0	0.1	281.0	0.2	281.1	0.2	281.0	0.1
N1	401.9	3.0	401.9	2.9	401.8	3.0	401.8	2.3	401.8	1.7	401.8	2.2	401.9	1.3	401.8	1.0
N2	400.2	1.2	400.2	2.3	400.1	1.6	400.1	1.6	400.0	1.6	400.1	1.4	400.1	1.4	400.0	1.3
N3	398.3	0.4	398.2	0.8	398.2	0.5	398.2	0.5	398.0	0.5	398.2	0.6	398.1	0.4	397.9	0.3
S1	162.5	0.3	162.4	0.7	162.4	0.5	162.3	0.3	162.1	0.3	162.3	0.5	162.2	0.3	162.4	0.1
S2	168.8	0.1	169.0	0.0	168.5	0.1	-0.5	0.0	168.5	0.1	168.6	0.1	168.5	0.1	168.8	0.1
P	133.0	0.8	132.8	0.9	132.7	0.8	132.7	1.0	132.6	1.2	132.5	1.2	132.7	1.0	132.7	1.1
I1	618.6	3.7	618.7	2.8	618.6	3.3	618.7	3.1	618.8	0.8	618.7	2.1	619.0	0.3	618.9	0.4
I2	620.6	0.4	620.9	0.2	620.2	0.3	620.8	0.3	621.8	0.03	620.9	0.1	621.4	0.02	621.4	0.05

Chapter Seven

Table 7.7: Peak positions (eV) ± 0.2 and the relative intensities with errors of ± 0.4 for (Ru, N3, S1, S2, I1 and I2) and ± 0.3 for the other components in N719 samples in the dark-set. Remaining percentage is F and Sn.

Time (h)	24		48		100		200		400		600		800		1000	
Element	Position	Intensity %														
C1	285.0	6.2	285.0	10.6	285.0	8.0	285.0	10.1	285.0	10.9	285.0	13.0	285.0	28.7	285.0	11.2
C2	286.5	51.0	286.0	16.2	285.9	26.4	286.0	17.5	286.1	16.5	286.1	15.9	286.3	8.3	286.0	17.2
C3	288.7	3.3	288.3	3.0	288.4	2.9	288.4	2.8	288.4	3.1	288.2	3.4	287.9	3.1	288.3	3.0
O1	530.2	11.3	530.0	36.1	530.0	32.1	530.0	35.5	530.0	33.3	529.9	30.2	529.7	26.0	529.9	35.1
O2	531.3	4.0	531.2	6.3	531.3	5.8	531.4	6.3	531.3	6.5	530.7	6.3	531.2	7.3	531.1	5.1
O3	533.5	6.3	532.2	2.6	532.5	2.2	532.6	1.5	532.3	2.4	531.7	3.9	532.4	3.3	531.9	2.9
Ti	459.0	5.0	458.8	12.9	458.7	11.3	458.8	12.5	458.8	12.0	458.7	12.0	458.5	8.7	458.7	12.5
Ru	281.3	0.2	281.0	0.4	281.1	0.4	281.0	0.4	281.0	0.4	281.1	0.3	280.9	0.6	281.0	0.4
N1	403.8	0.9	401.9	2.2	401.9	2.7	401.9	1.9	401.9	2.0	401.9	2.7	401.6	1.7	401.9	2.8
N2	401.8	2.5	400.1	2.6	400.2	2.3	400.1	2.7	400.2	2.8	400.2	2.5	399.9	3.6	400.1	2.1
N3	400.3	0.9	398.2	1.4	398.3	1.0	398.1	0.9	398.0	1.1	398.3	1.0	397.9	0.8	398.2	0.9
S1	162.5	0.2	162.3	0.8	162.3	1.0	162.3	0.9	162.4	0.5	162.3	1.0	162.6	0.3	162.3	0.7
S2	169.1	0.1	169.2	0.1	168.3	0.2	168.9	0.3	168.6	0.2	168.8	0.2	168.1	0.2	168.4	0.2
I1	618.6	2.5	618.7	1.1	618.6	1.8	618.7	1.2	618.7	1.0	618.7	1.4	618.7	1.5	618.7	1.0
I2	620.5	1.34	621.8	0.09	620.5	0.13	621.1	0.06	620.8	0.11	620.9	0.08	620.7	0.09	621.0	0.08

Table 7.8: Peak positions (eV) ± 0.2 and the relative intensities with errors of ± 0.4 for (Ru, N3, S1, S2, I1 and I2) and ± 0.3 for the other components in N719/DPA samples in the dark-set. Remaining percentage is F and Sn.

Time (h)	24		48		100		200		400		600		800		1000	
Element	Position	Intensity %														
C1	285.0	21.5	285.0	23.1	285.0	25.9	285.0	21.3	285.0	17.1	285.0	20.1	285.0	27.6	285.0	19.8
C2	286.0	15.0	285.9	15.1	286.1	6.7	285.9	13.4	285.8	16.4	286.1	8.6	286.2	9.0	286.2	10.1
C3	288.5	2.4	288.5	1.4	288.4	1.0	288.3	1.3	288.5	0.8	287.9	1.6	288.2	1.6	288.2	2.7
O1	530.0	31.6	529.9	32.2	529.9	35.2	530.0	35.7	529.9	33.0	529.9	31.2	529.9	32.7	529.9	36.4
O2	531.3	7.7	531.2	6.1	530.9	8.0	531.2	6.7	530.7	8.2	530.5	11.1	531.1	7.4	531.1	6.7
O3	532.4	2.6	532.5	2.7	531.8	3.9	532.3	1.9	531.7	3.6	531.5	5.7	532.3	2.9	531.9	2.6
Ti	458.8	11.1	458.6	11.6	458.7	13.6	458.7	12.7	458.7	13.1	458.8	14.2	458.7	11.5	458.7	13.1
Ru	281.1	0.3	280.9	0.2	281.0	0.1	281.0	0.2	280.9	0.2	281.0	0.2	281.0	0.1	281.0	0.3
N1	401.9	1.5	401.7	1.4	401.9	1.0	401.8	1.2	401.8	2.1	401.8	1.5	401.8	1.7	401.9	2.0
N2	400.1	2.3	399.9	1.6	400.1	1.2	400.0	1.4	400.1	1.3	400.1	1.4	400.1	1.3	400.1	2.2
N3	398.1	0.8	397.8	0.5	397.9	0.3	397.7	0.4	397.6	0.4	398.0	0.5	398.1	0.5	398.1	0.9
S1	162.2	0.5	162.1	0.4	162.3	0.2	162.0	0.1	162.5	0.2	162.3	0.3	162.3	0.4	162.3	0.6
S2	168.5	0.1	168.4	0.2	168.7	0.1	168.9	0.1	168.0	0.1	168.6	0.1	168.4	0.1	167.9	0.1
P	132.8	0.9	132.7	0.9	132.8	1.4	132.9	1.0	132.7	1.0	132.8	1.3	132.7	1.1	132.7	0.8
I1	618.8	0.6	618.5	0.8	619.2	0.1	618.8	1.0	618.4	1.1	618.7	0.5	618.6	0.8	618.8	0.3
I2	620.4	0.02	620.3	0.07	619.9	0.01	621.1	0.10	620.7	0.14	620.3	0.06	620.4	0.0	620.7	0.0

7.4.3.1 Elements intensities as the cell ages

Ti 2p

A high-resolution scan of the Ti 2p spectra is shown in Figure 7-5A. The splitting is due to the spin-orbital coupling, where the peaks position at 458.8 ± 0.2 eV and 464.5 ± 0.2 eV attributed to $\text{Ti}^{4+} 2p_{3/2}$ and $\text{Ti}^{4+} 2p_{1/2}$ states respectively. In all aged samples, the Ti 2p peaks show that the surface consists of Ti^{4+} and there were no traces of other oxidation states such as Ti^{1+} , Ti^{2+} and Ti^{3+} . An increase in the intensity was observed in the heat and dark sets in both N719 and N719/DPA samples within the first 48h. The intensity remains constant with small variations as the cell aged as illustrated in Figure 7-5B and C.

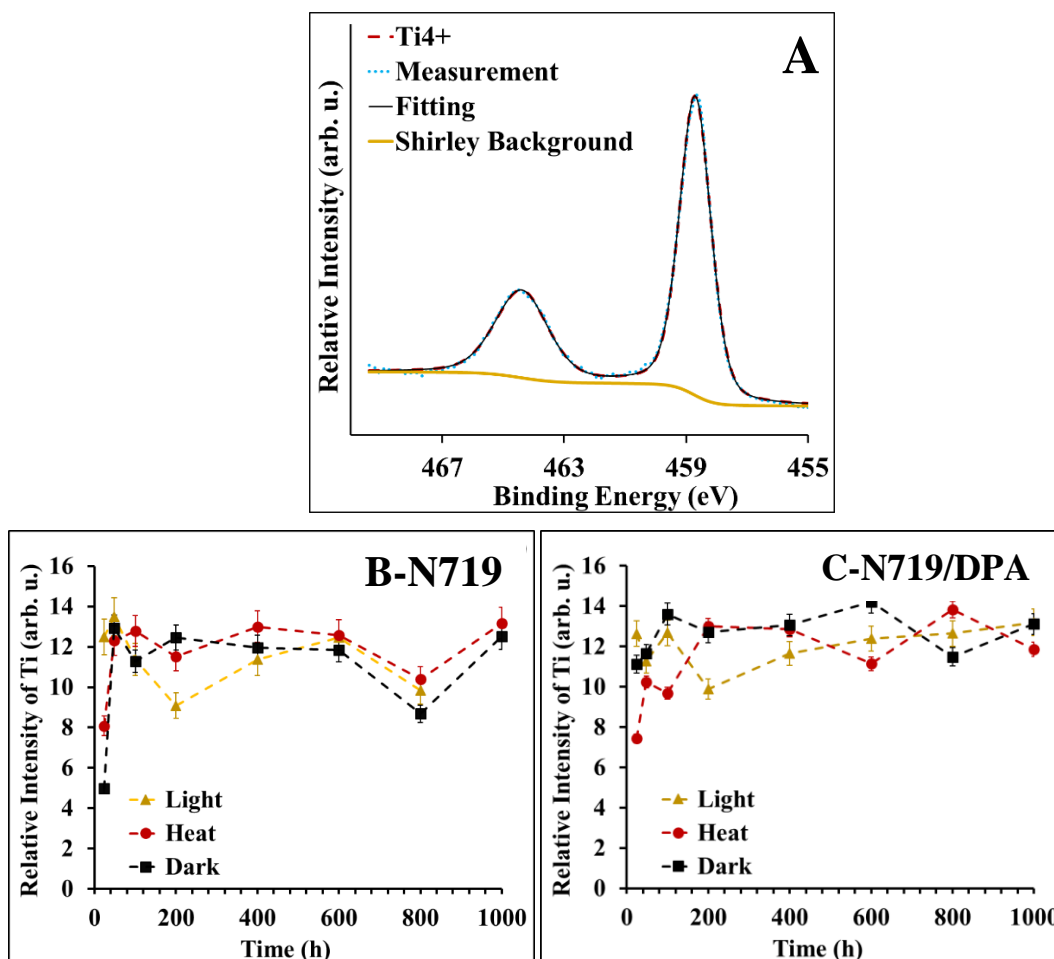


Figure 7-5: A) High resolution scan of Titania and Ti intensity in three different conditions in B) N719 and C) N719/DPA samples.

O 1s

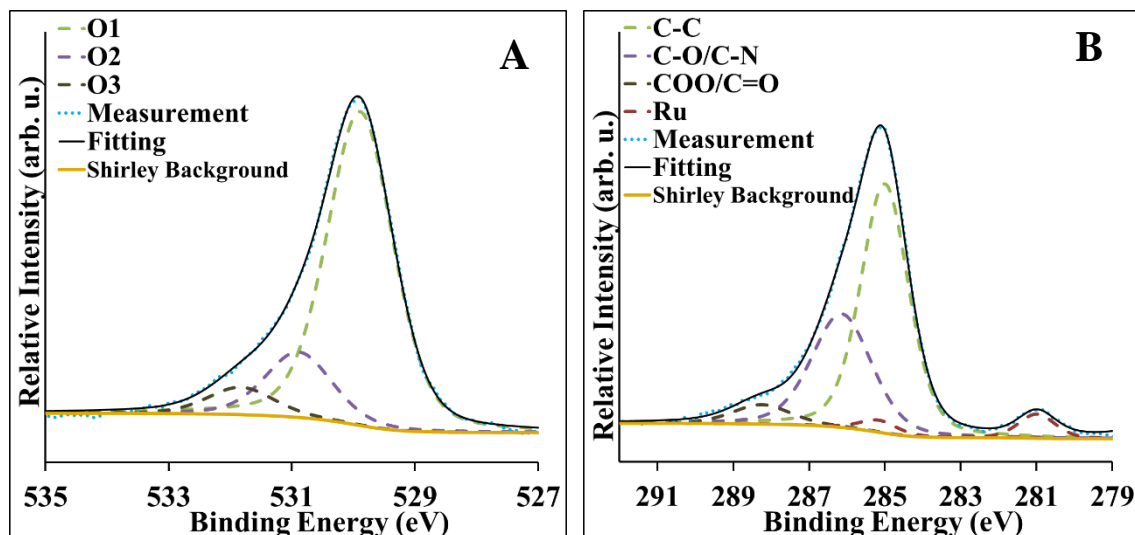


Figure 7-6: High-resolution scan of A) Oxygen and B) Carbon.

The O 1s was deconvoluted into three peaks as in Figure 7-6A. The peaks with lowest binding energy at 529.9 ± 0.2 eV and 531.1 ± 0.2 eV are attributed to O^- and Ti-OH from TiO_2 surface, in addition the peak at 531.5 ± 0.2 eV has some contribution from the double bonded oxygen ($O=C$), oxygen in the carboxylate attached with the counter-ions ($-COO^-TBA^+$), and carboxylate groups bonded to TiO_2 substrate ($COO-Ti$) [15]. The peak located at 532.1 ± 0.2 eV originating from oxygen in carboxylic groups of the dye [16-18]. A similar observation to Ti was observed with O.

C 1s

A high-resolution scan of the C reveals three peaks at 285.0, 286.2 ± 0.2 , and 288.3 ± 0.2 eV. It is worth to be noted that the Ru $3d_{3/2}$ peak is hidden under the main C 1s peak at 285 eV. This peak contains a contribution from the TBA^+ and NCS groups of the dye as well [15]. Therefore, the main peak of C 1s at 285.0 eV is contributed to C=C, C-C, C=N, TBA^+ and Ru $3d_{3/2}$, the peak at 286.2 ± 0.2 is attributed to C-O/C-N, and the peak at 288.3 ± 0.2 eV correspond to C (=O) OH [15, 19, 20] Figure 7-6B.

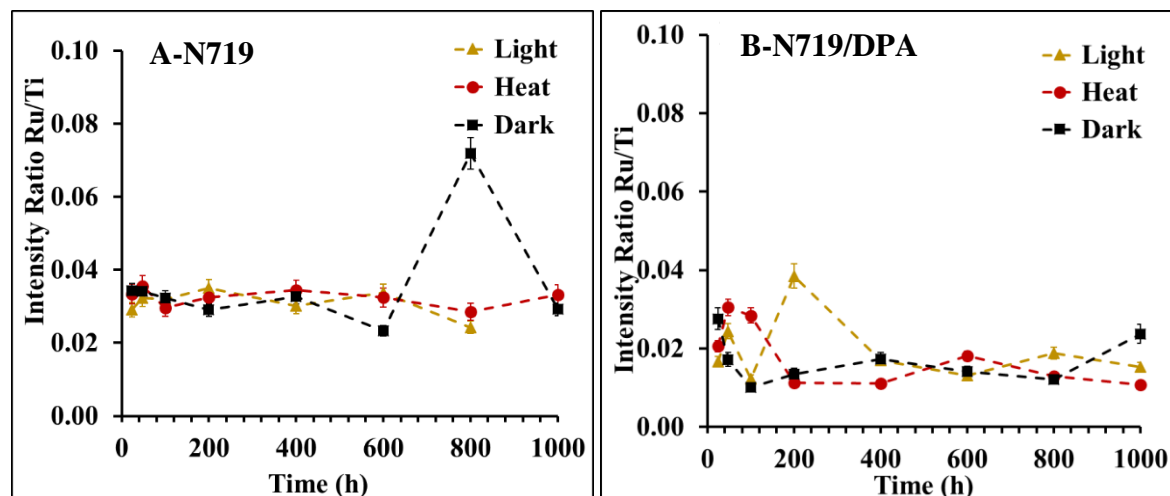
Ru 3d

Figure 7-7: Ru/Ti ratio intensity of N719 (A) and N719/DPA (B) aged samples in three different conditions.

Figure 7-6B shows the spectrum of Ru 3d adsorbed on TiO₂ at a binding energy of 281.0 ± 0.2 eV, the splitting due to spin-orbital coupling corresponds to Ru 3d_{3/2} and Ru 3d_{5/2} with the former overlap with C 1s peak as mentioned above. The Ru 3d_{3/2} peak is shifted 4.2 eV from Ru 3d_{5/2}. The dye coverage of the aged cells was measured by a comparison between the intensity ratio of Ru and Ti in each sample, as illustrated in Figure 7-7. The intensity ratio of Ru/Ti is nearly constant in N719 samples, despite the 800 h in the dark where the obtained FWHM for this sample increased from 1 to 1.5 indicating substantial changes in the Ru and its interaction with TiO₂ surface. In the N719/DPA samples, a slight increase in the intensity in the light and heat sets, while the intensity decreases in the dark set during the first 48 h. Upon aging the intensity of Ru/Ti is decreased and remain stable as the cell aged. It is worth noticing that the Ru/Ti intensity in the N719/DPA samples is almost 50 % less than the N719 samples, due to the presence and effect of the co-adsorbent DPA.

N1s

The nitrogen can be found in the following components of the cell, the dye N719, which contains eight nitrogen atoms, including its cations. In the electrolyte additives 4-TBP and BMII. XPS reference measurements were performed on four of the TiO₂ working electrode were immersed in

the following separately, the dye N719, 4-TBP, BMII, and the full components of the electrolyte. The high-resolution scan of the N region of each electrode is shown in Figure 7-8.

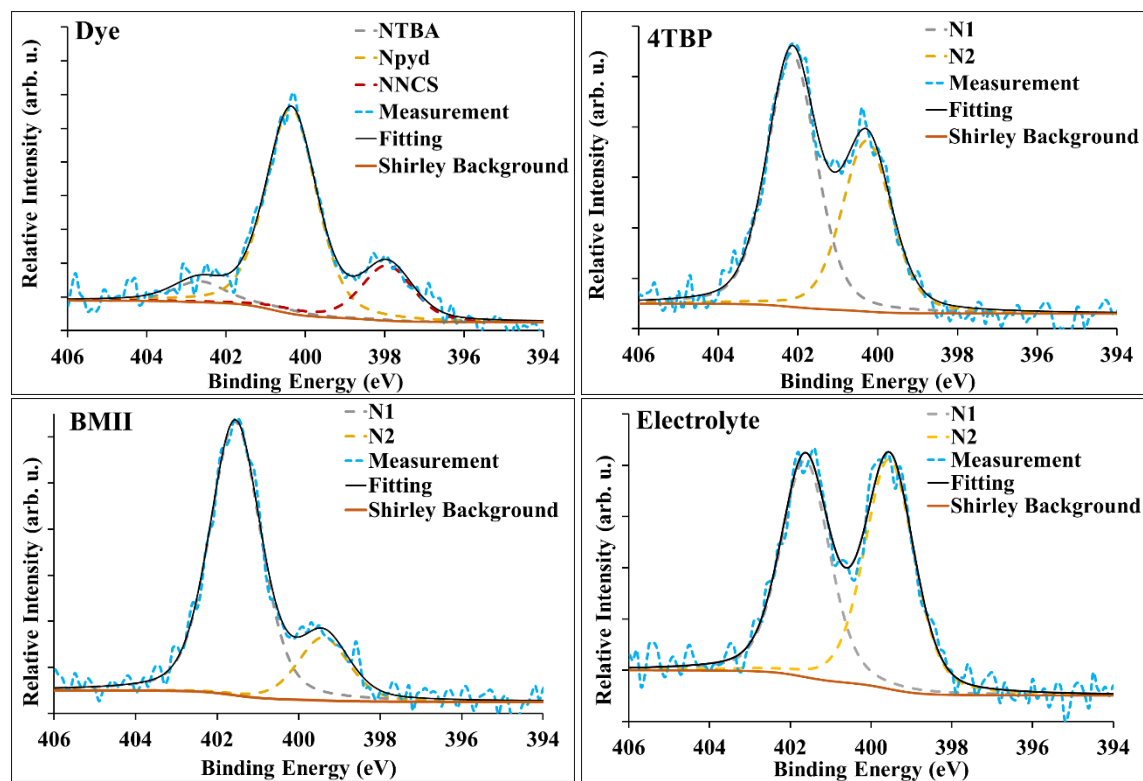


Figure 7-8: A) High resolution scan of Nitrogen in A) Dye, B) 4TBP, C) BMII and D) electrolyte.

In the N719/ TiO₂ electrode, three peaks were observed, and they are located at 398.2 ± 0.2 eV, 400.1 ± 0.2 eV, and 401.8 ± 0.2 eV. The peaks are assigned to thiocyanate ligands (N_{NCS}), bipyridine ligands (N_{Npyd}) and nitrogen in tetra butyl ammonium cations (N_{NTBA}) respectively [17, 21] Figure 7-8-Dye. Both of the electrolyte additives exhibit two peaks, at 402.1 ± 0.2 eV and 400.3 ± 0.2 eV in 4-TBP/ TiO₂ electrode as in Figure 7-8-4TBP, and at 401.6 ± 0.2 eV and 399.4 ± 0.2 eV in BMII/ TiO₂ electrode as can be seen in Figure 7-8-BMII, with different intensities between the peaks in each electrode. The peaks with the higher binding energies at 402-401 eV are attributed to the O-Ti-N or Ti-N-O linkage, while the peaks with lower binding energies at 399-400 eV originating from N-O, as reported by Phan *et. al.* [22].

S 2p

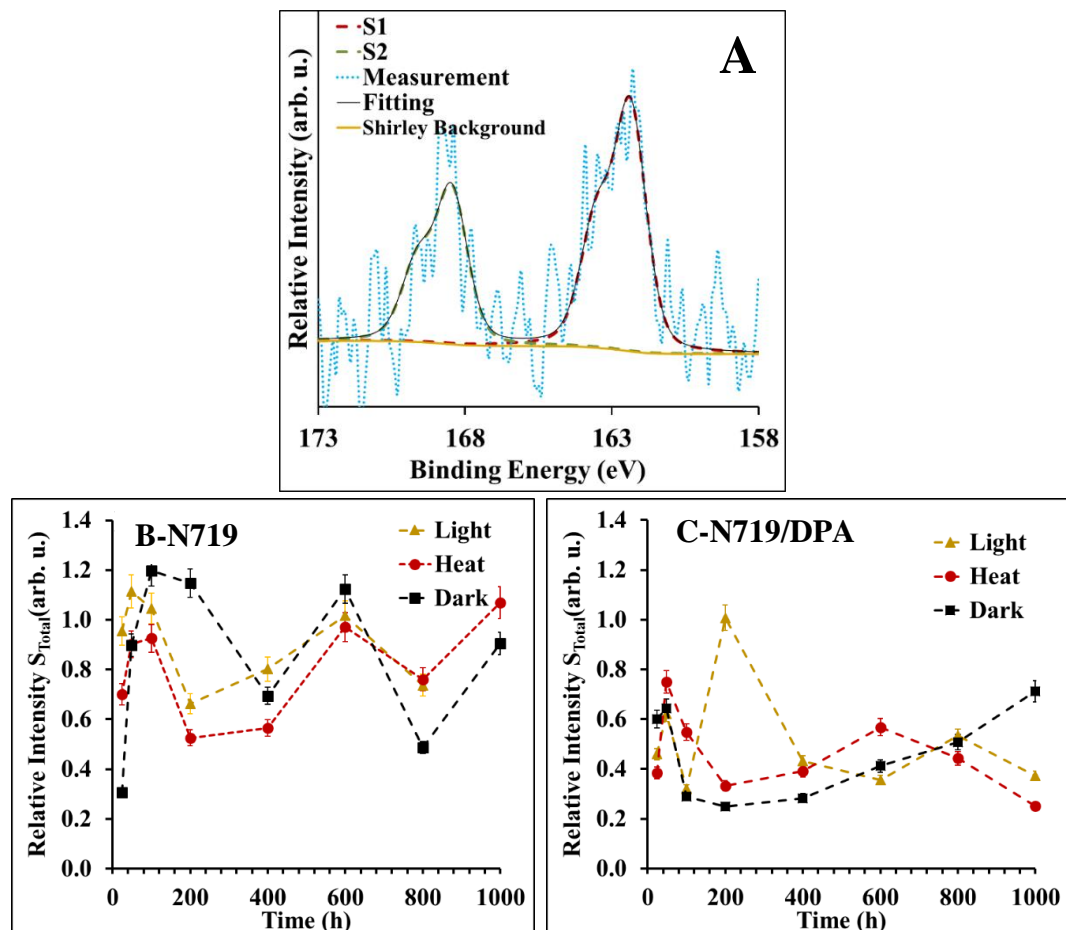


Figure 7-9: High resolution scan of S, S_{Total} intensity of N719 (B) and N719/DPA (C) aged samples in three different conditions.

The high-resolution S 2p spectrum was fitted with two components as shown in Figure 7-9A, one at $(162.4 \pm 0.2 \text{ eV})$ corresponding to C-S/C=S bond, the second component at high binding energy $(168.5 \pm 0.2 \text{ eV})$ attributed to highly oxidized sulfur (such as S^{6+} to S^{8+}) [23].

The S_{Total} intensities as the cell ages at the three conditions are shown in Figure 7-9B and Figure 7-9C. An increase in the intensity within the first 100 h in the three sets of N719 samples was observed and variations in the intensities as the cell ages Figure 7-9B. Furthermore, the stabilized Ru/Ti intensity in N719 samples as shown in Figure 7-7A, with the change in S_{Total} indicate different dye configuration as the cell ages. From Figure 7-9C, and despite the high intensity of S_{Total} at 200 h in the light-set, a notable decrease in the S_{Total} intensity after 48 h in N719/DPA samples was observed in all sets and returning to increase after 600 h in the dark-set.

13d

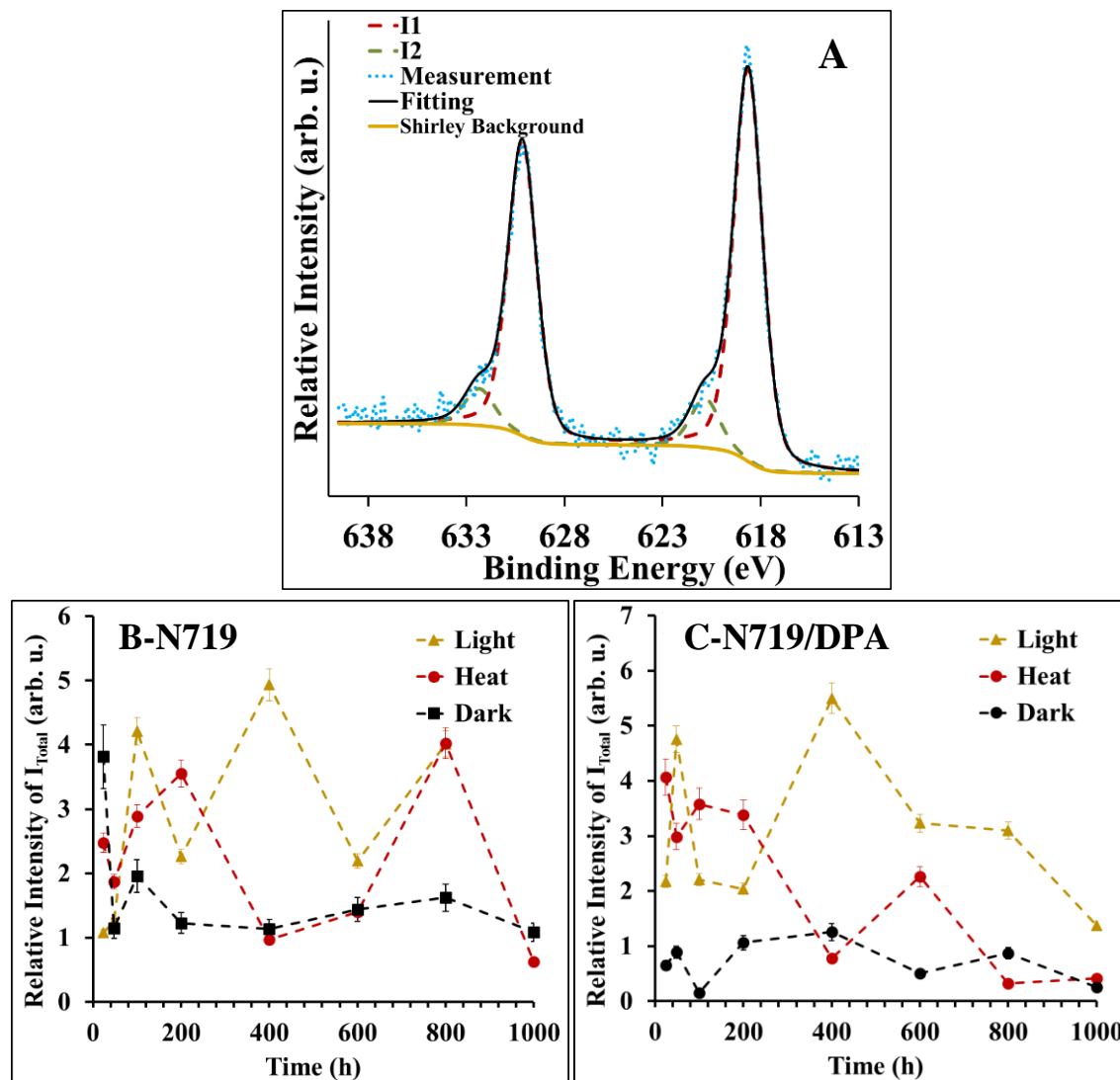


Figure 7-10: A) High resolution scan of I, and the I_{Total} intensity of N719 (B) and N719/DPA (C) aged samples in three different conditions.

To observe the electrolyte behavior, the high-resolution scan of iodine (I) was measured. The XP spectra of I 3d exhibits a doublet with peaks close to 618.0 ± 0.2 eV and 630.0 ± 0.2 eV attributed to I $3d_{5/2}$ and I $3d_{3/2}$ states respectively [24]. As shown in Figure 7-10A the high-resolution scan of I 3d was deconvoluted to two doublets at $(618.8 \pm 0.2$ eV, 620.5 ± 0.2 eV and 630.0 ± 0.2 eV, 632.1 ± 0.2 eV). The peak found at the lower binding energy 618.8 ± 0.2 eV is attributed to triiodide I_3^- denoted as I1, while the peak at higher binding energy assigned to iodide I^- [14, 25,

26] denoted as I₂. Inconsistent pattern in the I_{Total} intensity in the light-set in both N719 and N719/DPA samples.

Figure 7-10B and C shows the intensity of I_{Total} in the three conditions of all samples. The highest intensity of I_{Total} was observed in the light-set, while the lowest was observed in the dark-set in both of N719 and N719/DPA samples. In the heat-set, a variation with a decrease trend was observed in N719 samples while a systemically decreased in N719/DPA samples.

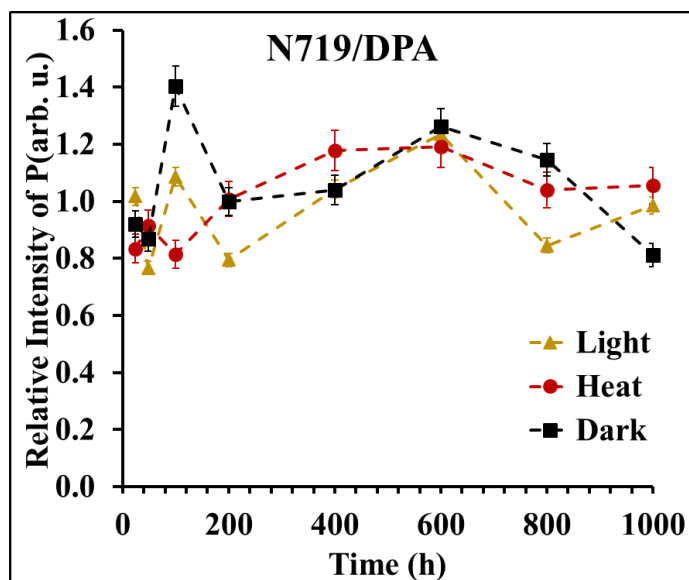


Figure 7-11: P intensity of N719/DPA aged samples in three different conditions.

The P was observed in all co-adsorbed samples with DPA with similar binding energy indicating that the adsorption of DPA on the TiO₂ surface is the same as the cell aged. P 2p peak was fitted with one spin-orbit doublet at binding energy 133.0 ± 0.2 eV attributed to (PO₄³⁻) [21, 27]. Figure 7-11 show P intensity in all three conditions having the tendency to increase.

In order to investigate the aging behavior of the cells, the atomic ratio between the relevant elements was determined to understand the changes during the aging process. Through this step, XPS can provide some of the mechanisms that possibly ruling the interactions between the cell components within the TiO₂/dye/electrolyte interfaces.

7.4.3.2 Intensity ratios as the cell ages

N ratio

Based on the results in the previous chapters 4, 5, and 6, the intensity of N_{TBA} is distinctively reduced after dye adsorption, and this observation agrees with Johansson *et al.*, and Lee *et al.* [16, 28]. Therefore, it is reasonable to conclude that the increase in the N 1s intensity at 401.9 ± 0.2 eV as the cell ages is due to additives (4TBP and BMII) adsorbing on the TiO_2 surface.

The intensities of the N1s relative to Ru for N719 and N719/DPA aged samples are summarized in Table 7.9 and 7.10 respectively, where N_1 is the peak located at 401.9 ± 0.2 eV (4TBP, BMII and TBA), N_2 is the peak located at 400.2 ± 0.2 eV (4TBP, BMII, bipyridine ligands) and the NCS ligand located at 398.3 ± 0.2 eV.

Table 7.9: N1s intensity ratio in N719 sample

Time(h)	Light			Heat			Dark		
	N_1/Ru	N_2/Ru	NCS/Ru	N_1/Ru	N_2/Ru	NCS/Ru	N_1/Ru	N_2/Ru	NCS/Ru
24	5.3	7.6	3.1	12.4	4.2	3.0	5.3	14.9	5.4
48	4.3	6.7	2.5	5.1	5.6	3.0	4.9	6.0	3.1
100	10.2	6.8	2.7	8.1	7.2	2.6	7.4	6.2	2.8
200	7.6	7.5	2.0	7.4	6.3	2.8	5.2	7.3	2.6
400	8.6	8.3	2.6	3.7	6.6	2.2	5.0	7.1	2.8
600	4.3	7.0	2.0	6.2	5.8	2.8	9.6	8.8	3.7
800	14.0	9.6	3.1	14.2	6.1	3.4	2.7	5.7	1.2
1000	-	-	-	6.0	5.7	2.6	7.6	5.8	2.4

Table 7.10: N1s intensity ratio in N719/DPA sample

Time(h)	Light			Heat			Dark		
	N ₁ /Ru	N ₂ /Ru	NCS/Ru	N ₁ /Ru	N ₂ /Ru	NCS/Ru	N ₁ /Ru	N ₂ /Ru	NCS/Ru
24	8.6	7.6	2.6	19.8	7.7	2.7	5.0	7.4	2.5
48	13.5	7.3	2.6	9.3	7.3	2.6	6.9	8.0	2.6
100	11.8	9.2	2.0	11.1	5.9	2.0	7.0	8.6	2.3
200	4.3	7.3	2.1	15.8	10.8	3.7	6.8	8.2	2.4
400	17.2	8.0	2.2	11.9	11.5	3.2	9.3	5.9	1.7
600	14.6	10.5	2.9	10.7	6.9	2.8	7.3	7.0	2.7
800	9.0	8.3	2.2	7.3	8.0	2.3	12.4	9.3	3.4
1000	5.2	11.2	2.3	7.9	10.5	2.3	6.5	7.0	2.8

Looking closely to the N/Ru intensities and starting with the N719 samples, a stabilized N/Ru intensity in the light, heat and dark sets is found with a slight increase in the N₁/Ru intensity in both light and heat sets. The steadiness in N/Ru as the cell ages could be due to the thicker dye layer make it difficult for the additives to be adsorbed on TiO₂ surface.

The highest nitrogen intensities were observed in the N719/DPA samples, especially in the heat-set the N₁/Ru presence in abundance and decreasing as the cell ages, followed by fluctuating in the light-set reaching a maximum at 400 h then decreased and stabilized in the dark-set. N₂/Ru and NCS/Ru, both had a stabilized performance in the light-set, NCS/Ru had the trend to decrease in the heat-set and increase in the dark-set.

7.4.3.3 Competition for adsorption on TiO₂ surface

Comparing the intensities for P, R/Ti and N₁/Ru (which is attributed mostly to the additive TBP adsorbed on TiO₂ surface) in N719/DPA samples, the following conclusions can be made. The intensity ratio of Ru/Ti in N719 samples is almost constant despite the high intensity in the dark-set at 800 h. In N719/DPA samples, the intensity ratio of Ru/Ti has the tendency to increase within the first 200 h in both light and heat sets, while an apparent decrease was observed in the dark-set as can be seen from Figure 7-7. Since not all the aggregated dye molecules are removed by DPA as previously observed in chapter 5. The variation in the intensity ratio of Ru/Ti can be attributed

to additives competing with the dye molecules to be adsorbed on the TiO_2 surface, resulting in weakening some of the dye/ TiO_2 and dye/dye interaction as the cell ages [29]. From Table 7.10, an increase in N1/Ru intensity was observed after dye desorption is an indication of more additives were adsorbed on the TiO_2 surface. This phenomenon was observed more in the light and heat set in N719/DPA samples. While in the dark-set, it was observed later after 600 h.

Furthermore, the opposite trend was observed between Ru/Ti and P intensities. Where the sample that contains high P intensity, lower R/Ti intensity was observed. There is no clear information that can be drawn from this observation. Since Ru and N ratios almost stable in the N719 samples, there was no such observation can be concluded from their intensities.

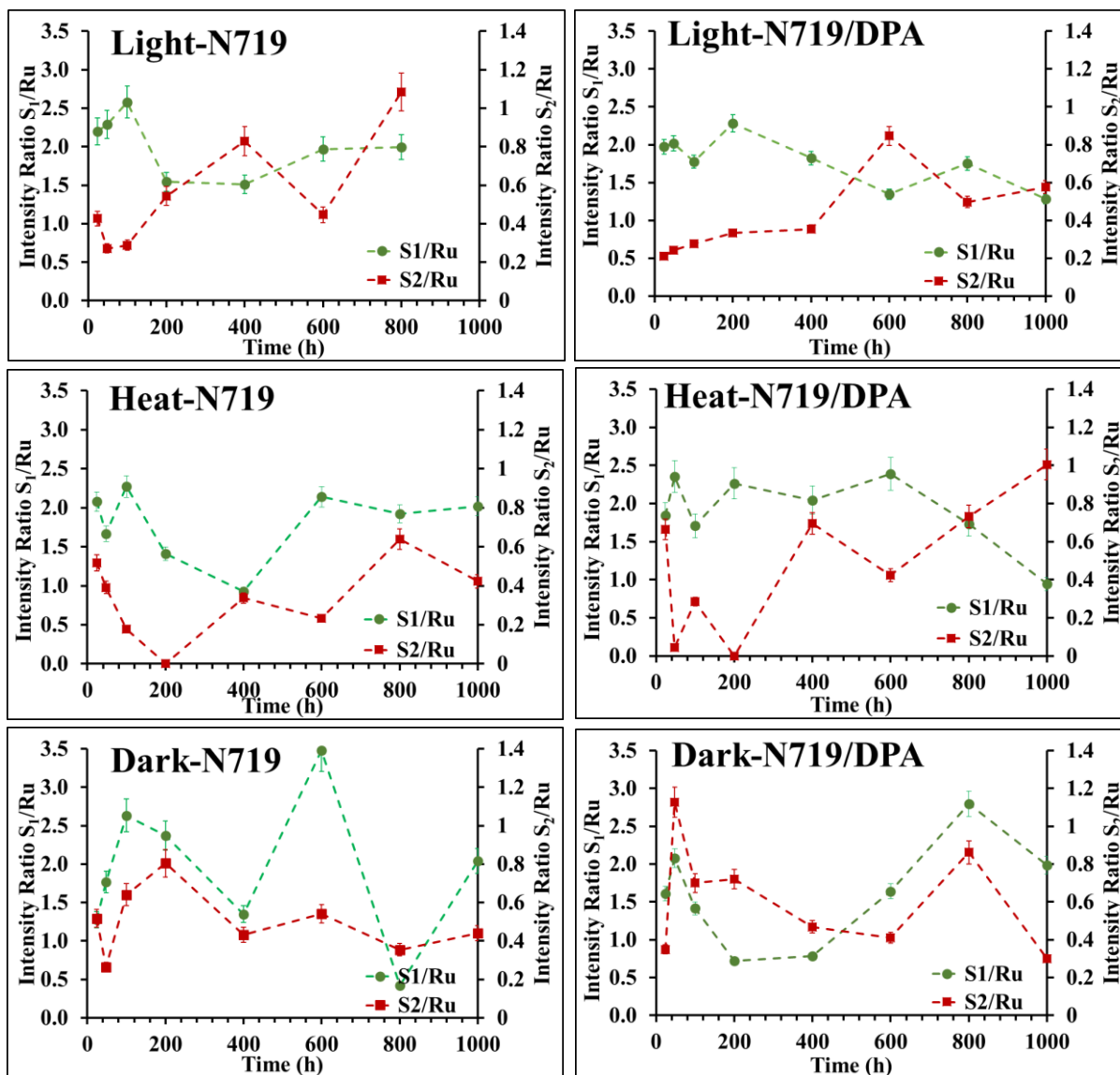
S and *I* ratios

Figure 7-12: Intensity ratio of S_1/Ru representing (NCS) and S_2/Ru representing (oxidized sulfur) of N719 (left) and N719/DPA (right) aged samples in three different conditions.

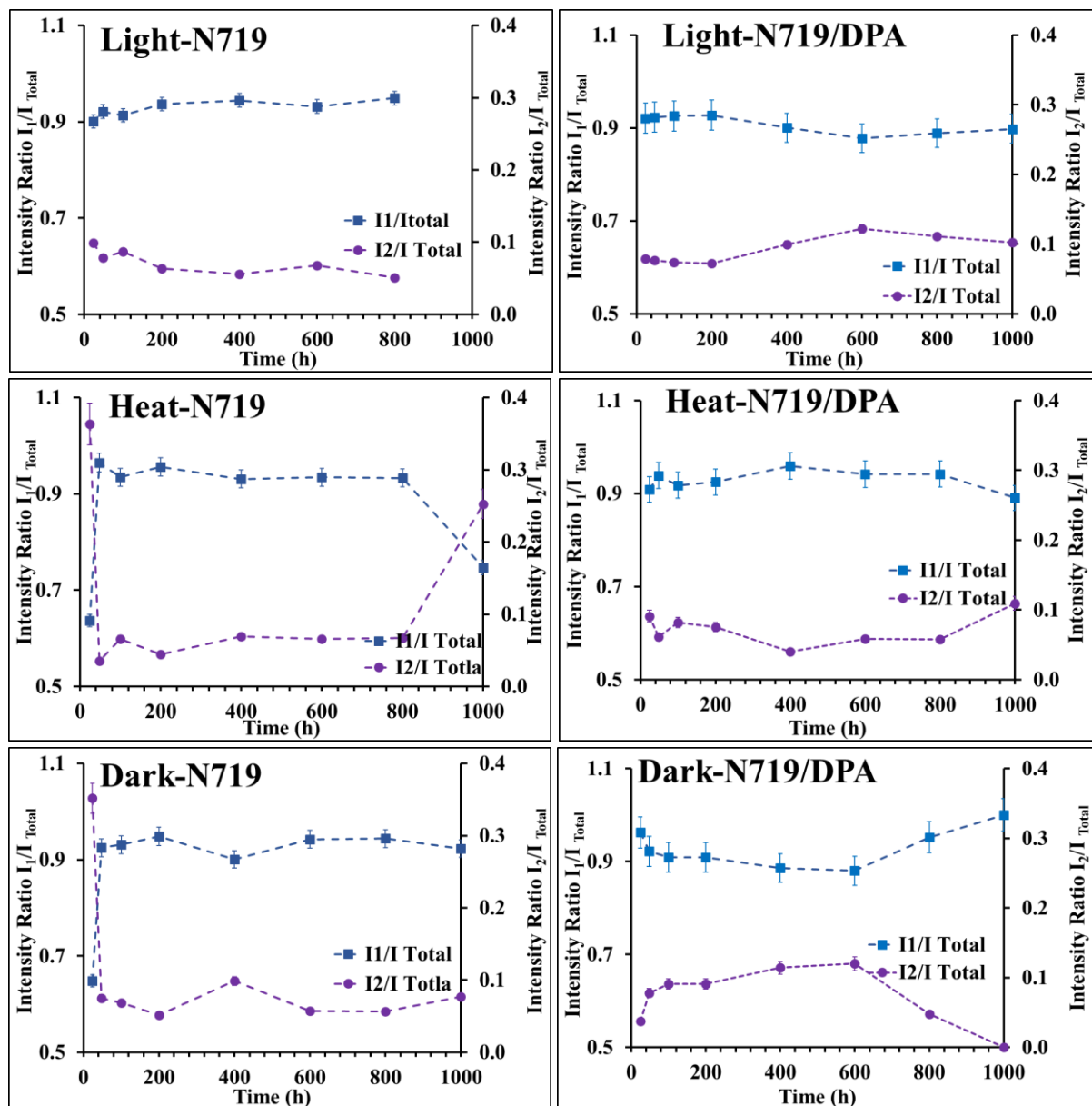


Figure 7-13: Intensity ratio of I_1/I_{Total} representing (I_3^-) and I_2/I_{Total} representing (I^-) of N719 (left) and N719/DPA (right) aged samples in three different conditions.

Figure 7-12 shows the intensity ratio of S1/Ru and S2/Ru, representing the NCS ligand and the oxidized sulfur, and Figure 7-13 shows I_1/I_{Total} and I_2/I_{Total} representing the triiodide (I_3^-) and iodide (I^-) as the samples aged. In the light-set a clear decrease in S1/Ru in N719 samples with increasing in oxidized sulfur S2/Ru. Similar results were obtained from N719/DPA. In the heat-set, a stabilized ratio of S1/Ru with a drop at 400 h in the N719 samples, while S2/Ru start to

increase after 200 h. in N719/DPA sample, S1/Ru remain almost stable the start decreasing after 600 h, while S2/Ru increased.

In the dark-set, S1/Ru is fluctuating, and S2/Ru stabilized after 400 h in N719 sample. Both of S1/Ru and S2/Ru follows the trend in N719/DPA sample.

In order to maintain a well-operating cell, an optimum and stable concentration of I^-/I_3^- is required to sustain the electrolyte conductive as the cell ages. A small change in I^-/I_3^- concentration will affective on the cell performance. From Figure 7-13, a decrease in the intensity of I^- in N719 samples, while an increase in the intensity in N719/DPA samples was observed in the light-set. In the heat-set almost a stabilized I^- , despite the high values at 24 h and 1000 h in N719 samples. While in N719/DPA samples, stabilized I^- with a small increase as the cell ages. In the dark-set, I^- was stable in N719 samples with an increase at 400 h. For N719/DPA, I^- increases then. A sudden decrease after 600 h.

7.4.4 Analysis of MIE spectra

The MIE spectra were measured for all aged samples at the three conditions. Figure 7-14 shows a magnified valance electron spectrum reveals the HOMO level of the dye/electrolyte adsorbed on TiO_2 surface. Two clear features were observed in N719 samples, at ~ 3.5 eV with high intensity and a peak at ~ 2 eV. A broader feature at ~ 3.5 eV in N719/DPA samples in the three conditions. The peak located at ~ 3.5 eV is attributed to the presence of the iodine at the outermost layer of the sample [30]. While the broad peak shows that the outermost layer contains both electrolyte and dye in N719/DPA samples, it cannot be distinguished to what extent the dye or the electrolyte covers the surface, where dye and electrolyte have contribution as shown in Figure 7-15.

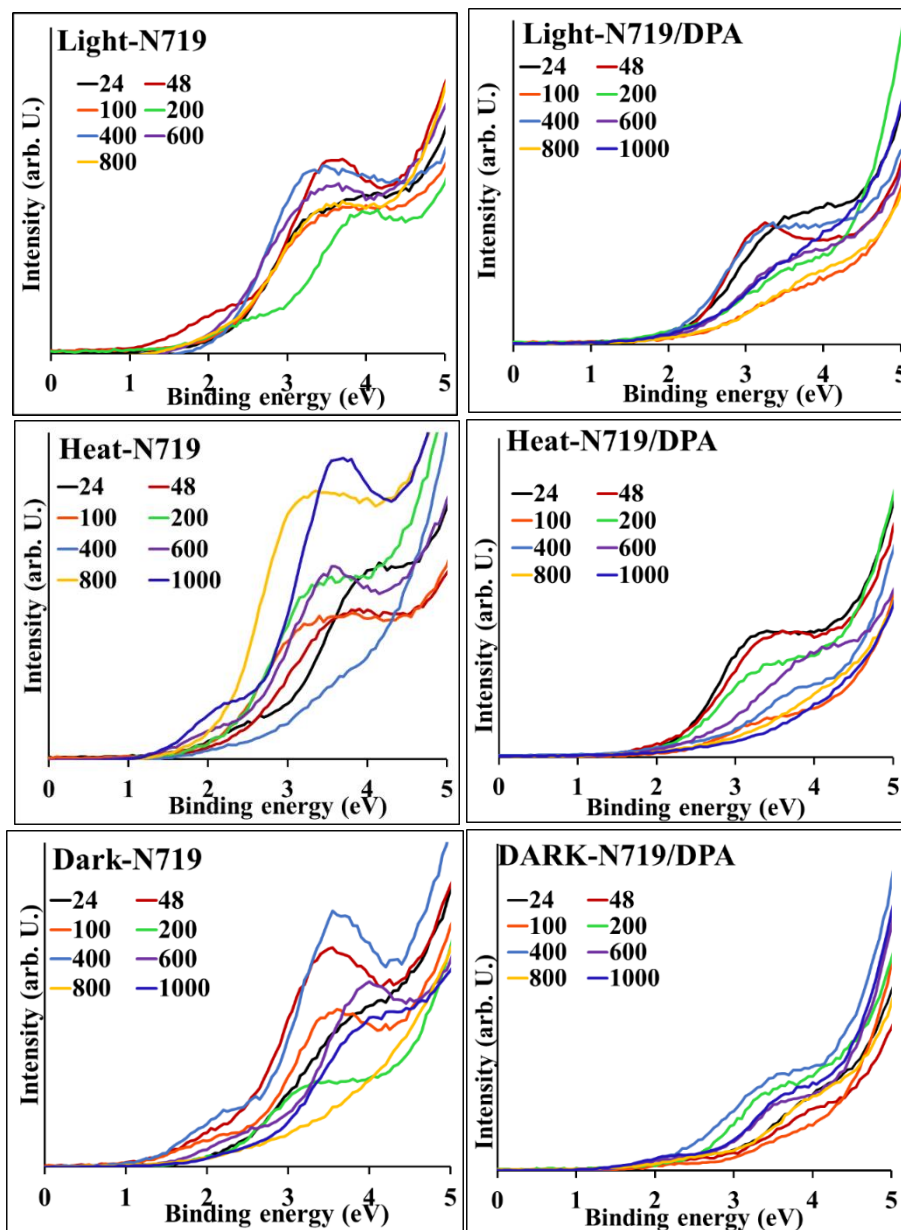


Figure 7-14: MIES spectra of aged samples (showin the HOMO level).

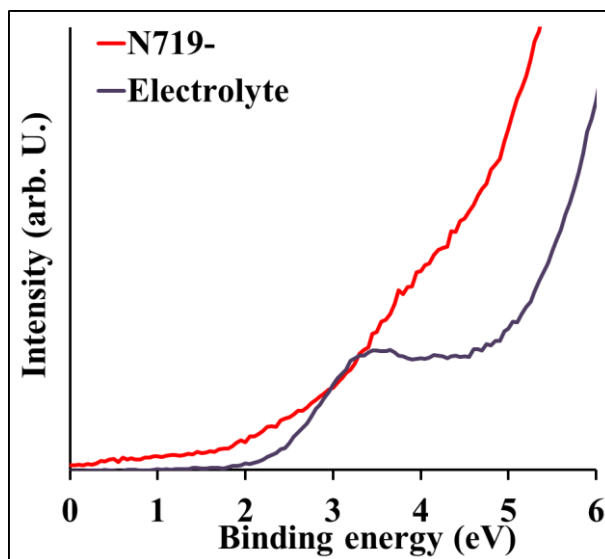


Figure 7-15: MIE spectra of reference samples N719 and electrolyte

In order to find a physical explanation for the cell performance as the cell ages, the results obtained from the photovoltaic parameters are linked with the results obtained from XPS.

7.5 Light-set aging cells

Cell performance (48h)

The results obtained from the cells exposed to light at $\sim 60^\circ\text{C}$ shows some differences in the performance when the co-adsorbent DPA was used. In the N719 cells, a small decrease in the cell performance in the light-set during the first 48 h. A similar result was observed by Xue et al. [31]. While an increase in the cell performance was observed in the co-adsorbed cells during the first 48 h. This increase attributed to the final equilibrium between the electrolyte components and the dye system on TiO_2 surface was reached during the first 48 h, also due to electrolyte penetration into the mesoporous TiO_2 substrate improving the dye regeneration and reducing the recombination [32-34]. A similar observation was also previously reported by Hara et al., using the organic dye MK-2 [35], Lee et al., by fabricating plastic DSSC [36], and Han et al., using ionic liquid electrolyte [37].

7.5.1 Identifying the mechanisms behind changes in the cell performance.

From Figure 7-1B a fluctuating behavior in the current was observed in the N719 cells, with an increase in R_s in the N719 samples as shown in Figure 7-2. The increase in the resistances indicates less electrolyte penetration as can be seen from the low FF obtained within the first 48 h as shown in Figure 7-1D, the low contact between the electrolyte and the thick dye layer resulted in slowing down the dye regeneration which results in decrease in the current within the first 48 h [38].

From Figure 7-7, the amount of dye on N719/DPA samples is almost 40 % lesser than what was observed in the N719 samples, and this is due to the presence of DPA decreasing the weakly bonded dye and occupying the vacant spots on TiO_2 surface, Having the advantages of removing the weakly bonded dye on TiO_2 surface allows better infiltration of the electrolyte in to the mesoporous TiO_2 for faster dye regeneration and decreasing the charge recombination [34]. Furthermore, a stabilized R_s and R_{sh} was observed in the N719/DPA samples as shown in Figure 7-2 resulting in J_{sc} almost close to N719 samples even though the N719/DPA samples containing 40 % lesser dye adsorbed on TiO_2 surface.

Cell performance after (48h)

N719-sample

Sample N719 experiences some fluctuations in its efficiency after 48 hours with maximums at 200 h followed by a continuous decrease after 600 h. The decrease in the cell performance in N719 cell resulted from the high resistance was obtained from the cell. Where an increase in R_s is an indication of some changes occurred at the interface of TiO_2 /dye/electrolyte. The FF increases after 48 h and remains stable indicating better electrolyte penetration. A decrease in the FF was observed after 400 h due to some changes occurring which affect the FF. However, a big drop in J_{sc} was observed at 400 h, attributed to the increase in R_s which is resulted from the increase in the oxidized sulfur at this aging time. Suggesting some of the dye molecules losing their S from NCS ligands resulting in an increase in oxidized sulfur. A notable change in S_{Total} intensity was observed as in Figure 7-9. In Figure 7-12 a clear increase in S_2/Ru ratio indicating more oxidized S with less S_1/Ru , and comparing with R_s in Figure 7-2, a parallel behavior between the increase in the oxidized S and increase in R_s in the cell. A similar behavior of an increase in oxidized sulfur and R_s combined with decrease in J_{sc} was observed at 800 h as well.

The decrease in FF is due some changes in the electrolyte penetration into the TiO₂ surface. From Figure 7-12, I⁻ was decreased after 400 h which indicates non-regenerative reduction of I⁻ in the cell. The thick dye layer makes it difficult for the electrolyte to penetrate the TiO₂, thus a competition between the oxidized dyes within the thick dye layer to be regenerated resulting in an increase in I⁻ consumption. The decrease in I⁻ influencing the I⁻/I₃⁻ ratio as the cell ages changing the electrolyte ingredients. A low I⁻/I₃⁻ concentration will result in difficulties in maintaining the required conductivity [39]. From Figure 7-17 a comparison between J_{sc} and V_{oc} performance with respect to the changes in I₂/I_{Total} (I⁻). A clear increased in both of J_{sc} and V_{oc} with increasing in I₂/I_{Total} ratio.

N719/DPA-sample

In the N719/DPA samples, the cell's efficiency and J_{sc} were stabilized then dropped at 600 h, while a drop in the FF was observed after 600 h. A notable increase in the R_s at 600 h was observed, indicating some changes at the interface. From the XPS results, and despite the aged sample at 200 h in light-set, a certain amount of dye was desorbed in the electrolyte in the three chosen conditions caused by the presence of the additives and electrolyte on TiO₂ surface [4]. This desorbed dye becomes oxidized and starts competing to be regenerated with the bonded oxidized dye on TiO₂ surface, slowing down the regeneration of the oxidized dye on TiO₂ surface which led to the decrease in the current in the cell as has been noticed. Furthermore, a clear increase in I₂/I_{Total} intensity which is corresponded to (I⁻) in the electrolyte solution attributed to deeper penetration of the electrolyte into the mesoporous TiO₂ getting closer such that the excited electrons will be more easily captured by the I₃⁻, causing charge recombination, therefore lowering the cells efficiency. This phenomenon is affecting on the electrolyte structure as the cell ages by changing the ratio between the redox couple and can be observed in drop of the cell efficiency.

An increase in the oxidized sulfur having a maximum at 600 h in parallel was found with the increase in R_s at 600 h. However, an increase in the FF was observed which is an indication of the good contacts between the dye and electrolyte on TiO₂ surface as illustrated above.

7.6 Heat and dark sets aging cells

N719-sample

In N719 cells, both efficiency and J_{sc} in the heat-set follows the same trend in the light-set. From XPS results, despite the drop at 400 h, a stabilized S1/Ru ratio was observed with a slight increase in the oxidized sulfur compared to the light-set with a stabilized I^-/I_3^- ratio as the cell ages. The fluctuating in cell performance is due to R_s increases resulting from the increase in the oxidized sulfur as described above.

In the dark-set, stabilized cell performance, however a decrease in the FF at 400 h. This decrease can be verified from XPS results from the changes in the electrolyte concentration, as shown in Figure 7-13.

N719/DPA-sample

In N719/DPA, cell efficiency and J_{sc} systematically decreased with stabilized FF. The FF decreased at 1000 h due to the change in the electrolyte concentration and the high increase in the oxidized sulfur as in Figure 7-12, resulted in R_s increasing in the cell. In the dark-set, stabilized cell performance dropping mainly due to the drop in the I^- .

Influence of the additives on cell ageing.

More additives were observed in N719/DPA samples than N719 samples, and this is due to the presence of DPA as co-adsorbent reducing the thick dye layer, thus allowing more of additives to be adsorbed on TiO_2 in N719/DPA sample.

Furthermore, a clear competition between the dye and additives to be adsorbed on TiO_2 surface causing some dye desorption from the TiO_2 surface. A change of the photoanode colors was observed in the N719/DPA samples getting brighter as the cell ages, could be resulted from the dye desorption as can be seen from Figure 7-16 showing the heat-set as an example where in those cells the N1/Ru intensity (representing TBP adsorbed on TiO_2 surface) was more observed as can be seen from Table 7.10.

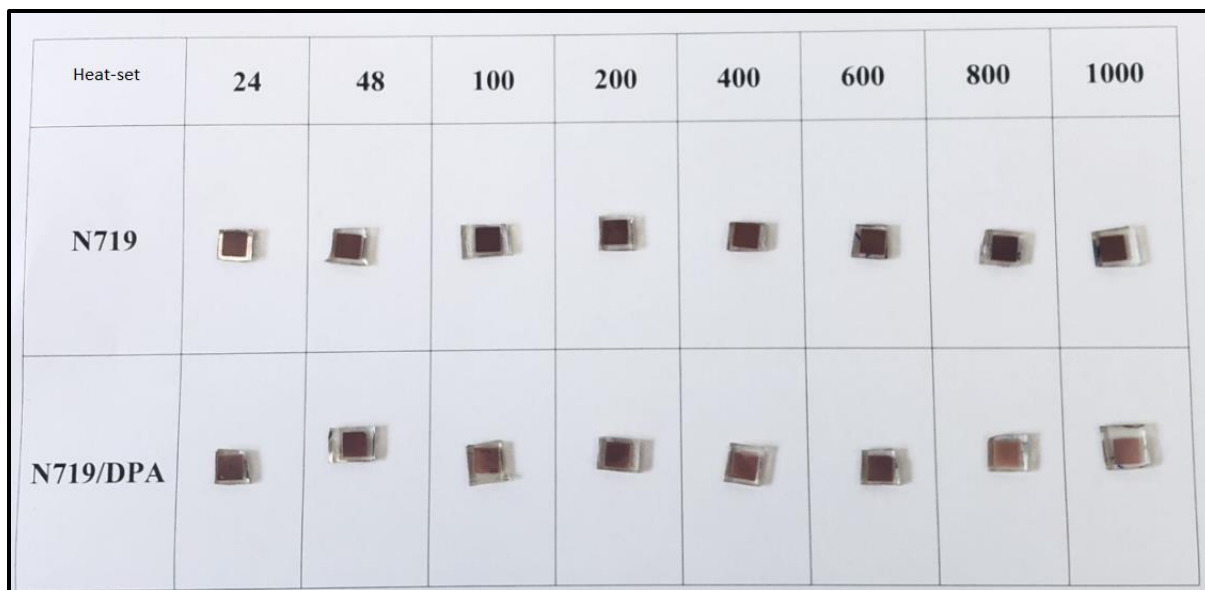


Figure 7-16: N719 and N719/DPA disassembled aged cell in the heat-set

An additional explanation to the change in the samples color could be due to some degradation in the dye molecules by exchanging one of its NCS ligands with nitrogen additives like TBP as previously shown by Nguyen et al. [40, 41]. Therefore, the systematically decrease of J_{sc} in the heat-set could be resulted from the dye degradation.

However, the V_{oc} was observed mostly being stabilized in the N719/DPA cells, resulting from the more additives were adsorbed on TiO_2 where the additive TBP is well known to increase the open circuit voltage in the cell by suppressing the back reaction and shifting the conduction band of TiO_2 to more negative potential [8, 42, 43]. The presence of the co-adsorbent, with the remaining of the thicker dye layers on the TiO_2 surface made it over time possible for dye molecules to rearrange on the substrate. Restructuring and desorption of some of the dye molecules allows more of electrolyte additives to be adsorbed on the TiO_2 surface forming Ti-N bonds [44].

Effect of desorbed dye as the cell ages

Desorption of the dye was initiated by the electrolyte additives; these desorbed dye molecules dissolved in the electrolyte solvent and are expected to be less photo-stable inducing a higher viscosity in the electrolyte and hinder the diffusion of I_3^- slowing down the electrolyte regeneration at the counter electrode [45].

Adsorption of the dye and the additives on TiO₂ surface cause shift in the Fermi level, where the adsorbed protons from the dye molecules on TiO₂ surface will lead to a positive shift, while adsorbing additives from the electrolyte onto TiO₂ surface will cause a negative shift of the Fermi level [46].

Diagnosing the cell performance

The competition between DSSC components to be adsorbed on the TiO₂ surface causing different alignments in the levelling of the TiO₂/dye/electrolyte interface affecting the cell performance. In this regard, a comparison has been made between the cell performance and XPS results. Figure 7-17, Figure 7-18, and Figure 7-19 illustrate the correlation drawn from the comparison between both J_{sc} and V_{oc} and the intensity ratios of N1/Ru, I₂/I_{Total} (I⁻), and S₂/Ru (oxidized sulfur). A gradient observation can describe a correlation occurs due to changes in the cell performance attributed to the changes in the intensity.

The N1/Ru intensity showed a scattering pattern in the light-set, thus no correlation can be concluded of such a pattern. While a strong correlation was observed due the changes in I₂/I_{Total} and S₂/Ru intensities with the cell performance in both N719 and N719/DPA samples in the light set.

The correlation between those elements can clearly be observed in Figure 7-17. From Figure 7-17 in the light-set, a scattering pattern in both of J_{sc} and V_{oc} was observed in N719 and N719/DPA samples with respect to N1/Ru. The increase in J_{sc} is more correlated to the I⁻/I₃⁻ ratio, where a small changes effect on J_{sc} values, as shown previously in the N719 samples, where a decrease in the I⁻ causes the decrease in J_{sc}. The increase in I⁻ in N719/DPA samples causes the decrease in J_{sc}. In addition, the increase of S₂/Ru (oxidized sulfur) decreases J_{sc} in both of N719 and N719/DPA samples. The same was observed with V_{oc} in both N719 and N719/DPA.

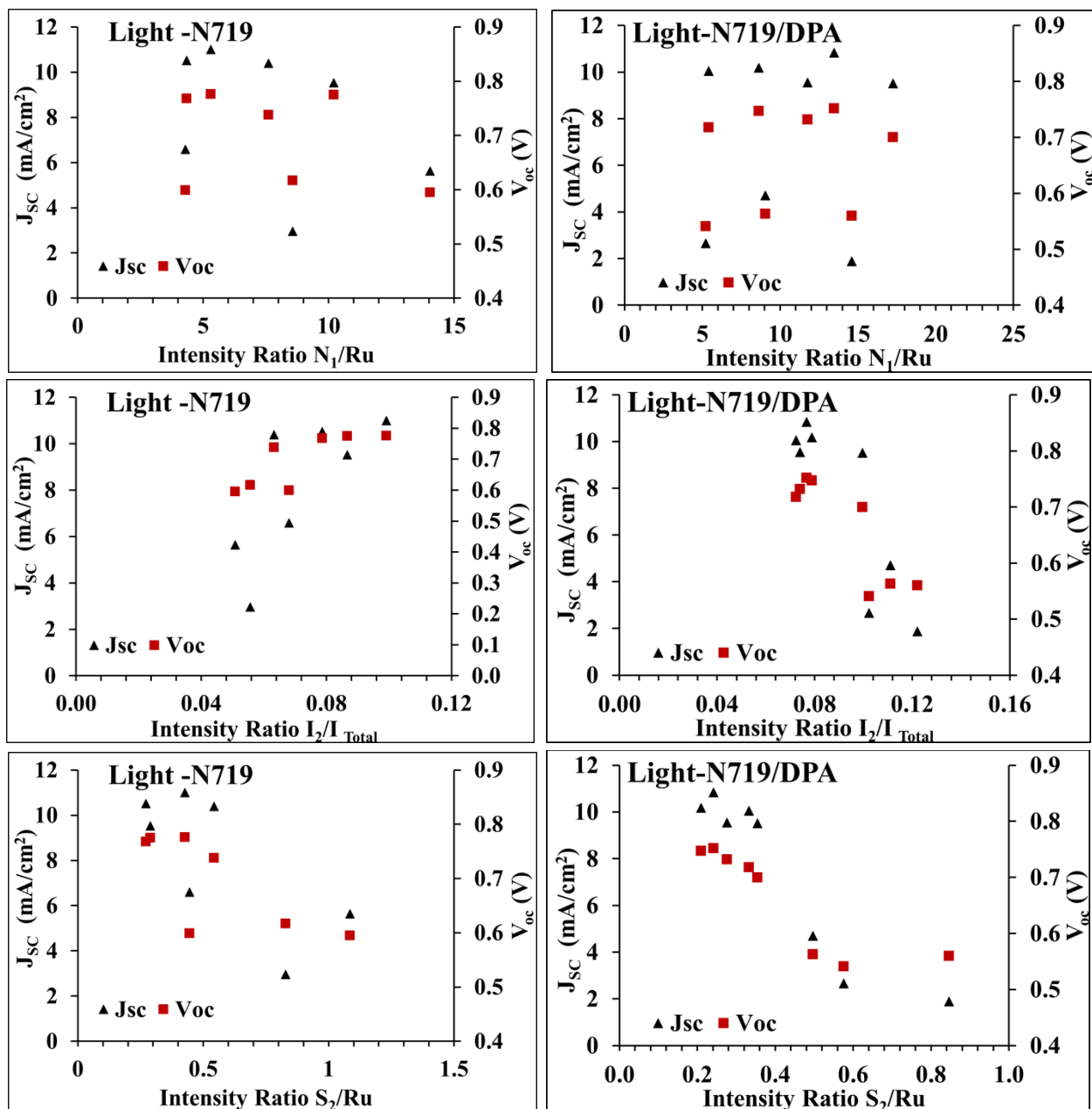


Figure 7-17: J_{sc} and V_{oc} performance with XPS intensity ratio of N_1/Ru , I_2/I_{Total} , and D) S_2/Ru of aged samples in the light-set.

From Figure 7-18 in the heat-set, J_{sc} and V_{oc} have a scattering pattern in N719 samples, while J_{sc} is increasing and V_{oc} has the tendency to be constant in N719/DPA samples. There is no clear correlation with I^- . While a clear decrease in J_{sc} as S_2/Ru increases in N719/DPA samples.

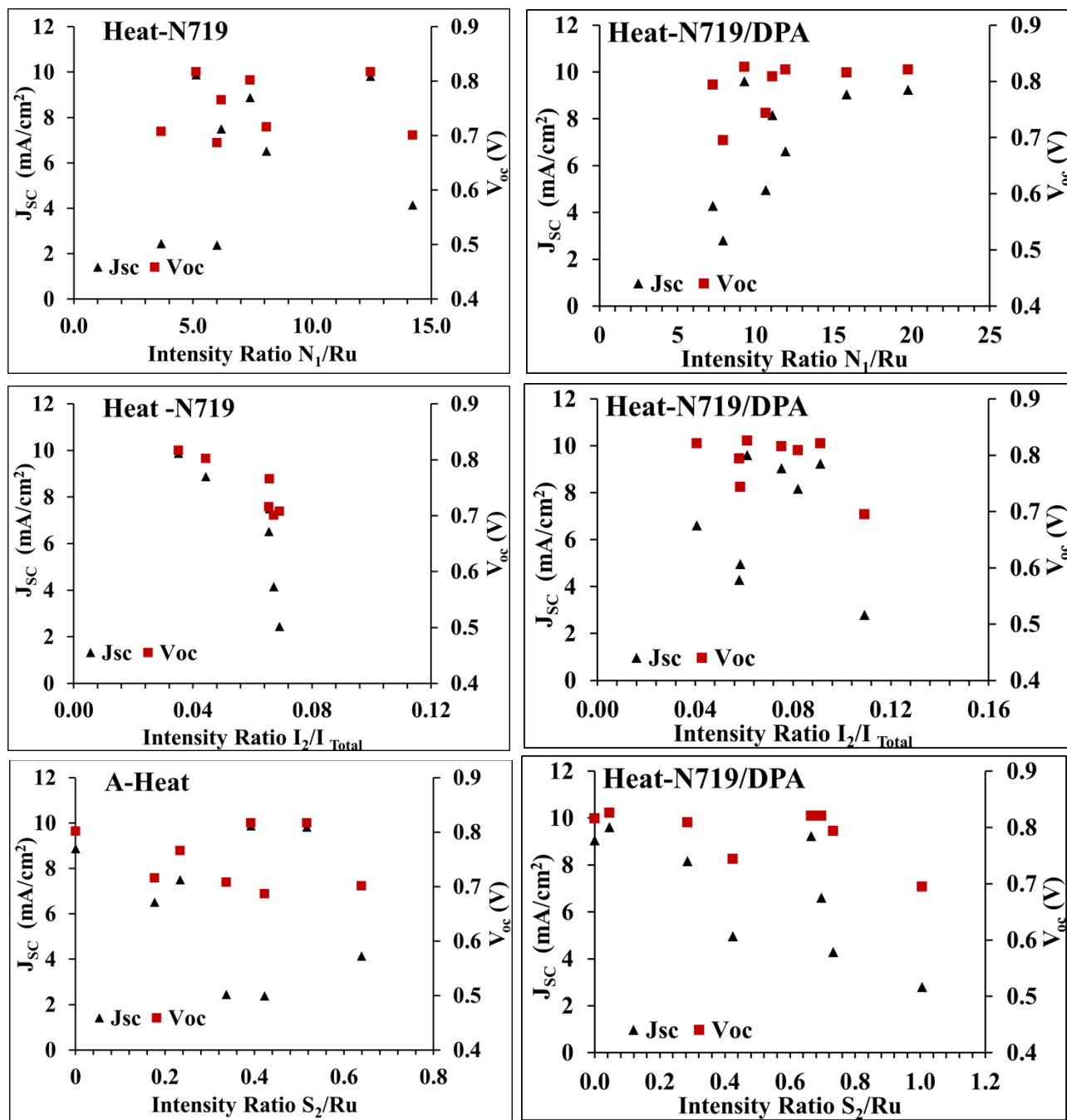


Figure 7-18: J_{sc} and V_{oc} performance with XPS intensity ratio of $N1/Ru$, I_2/I_{Total} , and D) S_2/Ru of aged samples in the heat-set.

In the dark-set Figure 7-19, there is no clear correlation between the cell performance and the results obtained from XPS, showing constant pattern.

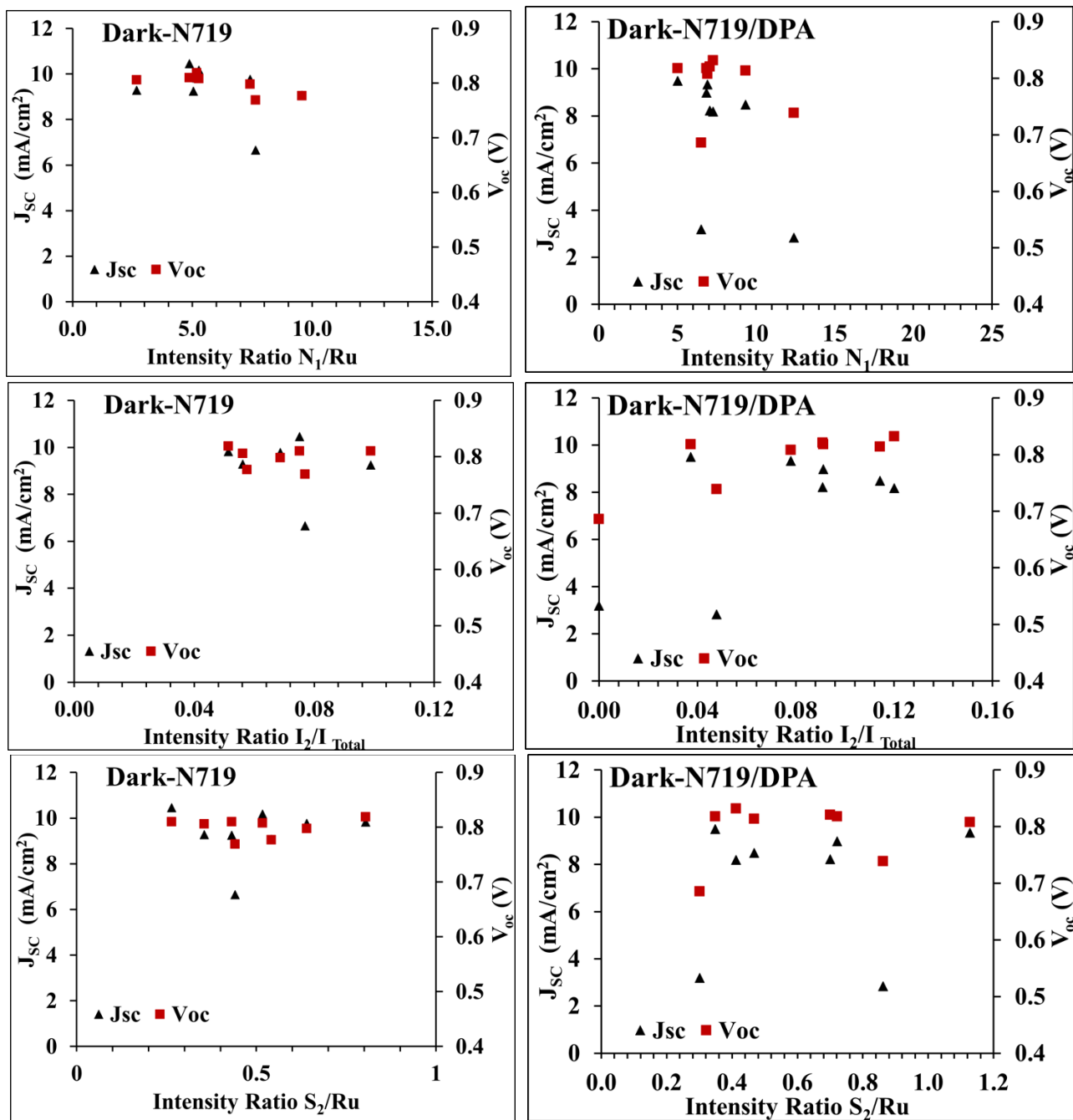


Figure 7-19: J_{sc} and V_{oc} performance with XPS intensity ratio of A) I_1/I_{Total} , B) $N1/Ru$, C) $N2/Ru$ and D) S_2/Ru of aged samples in the dark-set.

7.7 Summary

The thick dye layer in the N719 samples acts as a buffer layer preventing I_3^- penetrating, thus slowing down the regeneration of the dye molecules bonded to the TiO_2 surface.

The main reason for N719/DPA DSSCs degradation in this study could be due to the following. The resulted thin dye layer due to the presence of the co-adsorbent made it possible for more electrolyte penetration. The ease of electrolyte penetration resulted in a competition between the dye, electrolyte, and its additives to be adsorbed on the TiO_2 surface resulting in dye desorption dissolving in the electrolyte solvent. The desorbed dye oxidized and compete with the oxidized dye bonded on the TiO_2 surface to be regenerated, resulting in some changes in the redox ratio.

The increase in the oxidized sulfur was observed in both N719 and N719/DPA samples, and it was the main role in increasing R_s , this in turn results in a decrease in cell performance. DSSCs degradation was mainly caused by the change in the redox ratio with the increase in the oxidized sulfur in both N719 and N719/DPA samples.

7.8 Conclusion

XPS revealed that it's a powerful technique that can be used to reveal some of the degradation mechanism on the TiO_2 /dye/electrolyte interface and correlate them with the cell performance as the cell ages. DSSC consist of many components, studying each component individually does not necessarily enhance the understanding of the cell performance. From this work it has been shown that the performance of DSSCs is strongly affected by the interaction between each component and the degradation mechanisms are localized at the TiO_2 /dye/electrolyte interface. A clear correlation was found between the cell's degradation mechanism and the XPS results.

Furthermore, exposing the cell to light is not the dominant factor that effect on the long-term stability of the cell. In the heat condition the cells showed a similar degradation where thermal stress has contribution in reducing J_{sc} , however V_{oc} was almost stable in N719/DPA samples. In addition, exposing the cells to thermal stress can affect strongly on the chemical compositions on TiO_2 surface (dye, additives and the electrolyte). A competition between the dye and electrolyte was observed in the co-adsorbed samples due to the thinner dye layer causing some dye desorption.

The thin dye layer allowed for a better penetration to electrolyte and its additives resulting in more stabilized Voc.

Finally, DSSCs sensitized with Ru-based dyes can offer stabilized cell to temperatures up to 60°C by choosing the ideal concentration of each component that is compatible with each other plus maintaining the proportion of those concentrations as the cell ages with proper sealing methods.

7.9 References:

1. Asghar, M. I.; Miettunen, K.; Halme, J.; Vahermaa, P.; Toivola, M.; Aitola, K.; Lund, P., Review of Stability for Advanced Dye Solar Cells. *Energy & Environmental Science* **2010**, *3*, 418-426.
2. Mathew, S.; Yella, A.; Gao, P.; Humphry-Baker, R.; Curchod, B. F.; Ashari-Astani, N.; Tavernelli, I.; Rothlisberger, U.; Nazeeruddin, M. K.; Grätzel, M., Dye-Sensitized Solar Cells with 13% Efficiency Achieved through the Molecular Engineering of Porphyrin Sensitizers. *Nature chemistry* **2014**, *6*, 242-247.
3. Nishigaki, Y.; Nagai, T.; Nishiwaki, M.; Aizawa, T.; Kozawa, M.; Hanzawa, K.; Kato, Y.; Sai, H.; Hiramatsu, H.; Hosono, H., Extraordinary Strong Band-Edge Absorption in Distorted Chalcogenide Perovskites. *Solar RRL* **2020**, *4*, 1900555.
4. Gao, J., et al., Light-Induced Interfacial Dynamics Dramatically Improve the Photocurrent in Dye-Sensitized Solar Cells: An Electrolyte Effect. *ACS Appl Mater Interfaces* **2018**, *10*, 26241-26247.
5. Heo, N.; Jun, Y.; Park, J. H., Dye Molecules in Electrolytes: New Approach for Suppression of Dye-Desorption in Dye-Sensitized Solar Cells. *Scientific reports* **2013**, *3*, 1-6.
6. Sharma, G. D.; Kurchania, R.; Ball, R. J.; Roy, M. S.; Mikroyannidis, J. A., Effect of Deoxycholic Acid on the Performance of Liquid Electrolyte Dye-Sensitized Solar Cells Using a Perylene Monoimide Derivative. *International Journal of Photoenergy* **2012**, *2012*, 983081.
7. Matsuyoshi, H.; Tomita, H.; Nishino, H.; Sakamoto, H.; Manabe, K., The Effects of Malonic Acid Derivatives and Acetic Acid Derivatives as Coadsorbents on the Photovoltaic Performance of Dye-Sensitized Solar Cells. *International Journal of Photoenergy* **2013**, *2013*.
8. Boschloo, G.; Häggman, L.; Hagfeldt, A., Quantification of the Effect of 4-Tert-Butylpyridine Addition to I-/I³-Redox Electrolytes in Dye-Sensitized Nanostructured TiO₂ Solar Cells. *The Journal of Physical Chemistry B* **2006**, *110*, 13144-13150.
9. Wang, P.; Zakeeruddin, S. M.; Humphry-Baker, R.; Moser, J. E.; Grätzel, M., Molecular-Scale Interface Engineering of TiO₂ Nanocrystals: Improving the Efficiency and Stability of Dye-Sensitized Solar Cells. *Adv. Mater.* **2003**, *15*, 2101-+.
10. Kato, N.; Takeda, Y.; Higuchi, K.; Takeichi, A.; Sudo, E.; Tanaka, H.; Motohiro, T.; Sano, T.; Toyoda, T., Degradation Analysis of Dye-Sensitized Solar Cell Module after Long-Term Stability Test under Outdoor Working Condition. *Solar Energy Materials and Solar Cells* **2009**, *93*, 893-897.
11. Leonardi, E.; Penna, S.; Brown, T. M.; Di Carlo, A.; Reale, A., Stability of Dye-Sensitized Solar Cells under Light Soaking Test. *Journal of Non-Crystalline Solids* **2010**, *356*, 2049-2052.
12. Harikisun, R.; Desilvestro, H., Long-Term Stability of Dye Solar Cells. *Solar Energy* **2011**, *85*, 1179-1188.
13. Tripathi, B.; Yadav, P.; Kumar, M., Effect of Varying Illumination and Temperature on Steady-State and Dynamic Parameters of Dye-Sensitized Solar Cell Using Ac Impedance Modeling. *International Journal of Photoenergy* **2013**, *2013*.
14. Boschloo, G.; Hagfeldt, A., Characteristics of the Iodide/Triiodide Redox Mediator in Dye-Sensitized Solar Cells. *Acc Chem Res* **2009**, *42*, 1819-26.

15. Singh, J.; Gusain, A.; Saxena, V.; Chauhan, A.; Veerender, P.; Koiry, S.; Jha, P.; Jain, A.; Aswal, D.; Gupta, S., Xps, Uv–Vis, Ftir, and Exafs Studies to Investigate the Binding Mechanism of N719 Dye onto Oxalic Acid Treated Tio₂ and Its Implication on Photovoltaic Properties. *The Journal of Physical Chemistry C* **2013**, *117*, 21096-21104.
16. Johansson, E. M.; Hedlund, M.; Siegbahn, H.; Rensmo, H., Electronic and Molecular Surface Structure of Ru(Tcterpy)(Ncs)₃ and Ru(Dcbpy)₂(Ncs)₂ Adsorbed from Solution onto Nanostructured Tio₂: A Photoelectron Spectroscopy Study. *J Phys Chem B* **2005**, *109*, 22256-63.
17. Lee, K. E.; Gomez, M. A.; Regier, T.; Hu, Y.; Demopoulos, G. P., Further Understanding of the Electronic Interactions between N719 Sensitizer and Anatase Tio₂ Films: A Combined X-Ray Absorption and X-Ray Photoelectron Spectroscopic Study. *The Journal of Physical Chemistry C* **2011**, *115*, 5692-5707.
18. Ardhi, R. E. A.; Tran, X. M.; Wang, M.; Liu, G.; Lee, J. K., Chemically Tuned, Bi-Functional Polar Interlayer for Tio₂ Photoanodes in Fibre-Shaped Dye-Sensitized Solar Cells. *Journal of Materials Chemistry A* **2020**.
19. Singh, J.; Gusain, A.; Saxena, V.; Chauhan, A. K.; Veerender, P.; Koiry, S. P.; Jha, P.; Jain, A.; Aswal, D. K.; Gupta, S. K., Xps, Uv–Vis, Ftir, and Exafs Studies to Investigate the Binding Mechanism of N719 Dye onto Oxalic Acid Treated Tio₂ and Its Implication on Photovoltaic Properties. *The Journal of Physical Chemistry C* **2013**, *117*, 21096-21104.
20. Chambers, B. A.; Notarianni, M.; Liu, J. Z.; Motta, N.; Andersson, G. G., Examining the Electrical and Chemical Properties of Reduced Graphene Oxide with Varying Annealing Temperatures in Argon Atmosphere. *Applied Surface Science* **2015**, *356*, 719-725.
21. Zen, S.; Inoue, Y.; Ono, R., Low Temperature (150° C) Fabrication of High-Performance Tio₂ Films for Dye-Sensitized Solar Cells Using Ultraviolet Light and Plasma Treatments of Tio₂ Paste Containing Organic Binder. *Journal of Applied Physics* **2015**, *117*, 103302.
22. Lee, K. E.; Gomez, M. A.; Regier, T.; Hu, Y. F.; Demopoulos, G. P., Further Understanding of the Electronic Interactions between N719 Sensitizer and Anatase Tio₂ Films: A Combined X-Ray Absorption and X-Ray Photoelectron Spectroscopic Study. *Journal of Physical Chemistry C* **2011**, *115*, 5692-5707.
23. Oscarsson, J.; Hahlin, M.; Johansson, E. M. J.; Eriksson, S. K.; Lindblad, R.; Eriksson, A. I. K.; Zia, A.; Siegbahn, H.; Rensmo, H., Coadsorption of Dye Molecules at Tio₂ Surfaces: A Photoelectron Spectroscopy Study. *Journal of Physical Chemistry C* **2016**, *120*, 12484-12494.
24. Phan, T. A. P.; Nguyen, N. P.; Nguyen, P. H.; Le, T. K.; Van Huynh, T.; Lund, T.; Tsai, D.-H.; Wei, T.-C.; Nguyen, P. T., Direct Experimental Evidence for the Adsorption of 4-Tert-Butylpyridine and 2, 2'-Bipyridine on Tio₂ Surface and Their Influence on Dye-Sensitized Solar Cells' Performance. *Applied Surface Science* **2020**, *509*, 144878.
25. Siow, K. S.; Britcher, L.; Kumar, S.; Griesser, H. J., Xps Study of Sulfur and Phosphorus Compounds with Different Oxidation States. *Sains Malaysiana* **2018**, *47*, 1913-1922.
26. Ai, Z. H.; Wang, M.; Zheng, Z.; Zhang, L. Z., Doping Iodine in Cds for Pure Hexagonal Phase, Narrower Band Gap, and Enhanced Photocatalytic Activity. *Journal of Materials Research* **2011**, *26*, 710-719.

27. Liu, I. P.; Wang, L. W.; Chen, Y. Y.; Cho, Y. S.; Teng, H. S.; Lee, Y. L., Performance Enhancement of Dye-Sensitized Solar Cells by Utilizing Carbon Nanotubes as an Electrolyte-Treating Agent. *Acc Sustainable Chemistry & Engineering* **2020**, *8*, 1102-1111.
28. Yao, Z.; Nie, H.; Yang, Z.; Zhou, X.; Liu, Z.; Huang, S., Catalyst-Free Synthesis of Iodine-Doped Graphene Via a Facile Thermal Annealing Process and Its Use for Electrocatalytic Oxygen Reduction in an Alkaline Medium. *Chem Commun (Camb)* **2012**, *48*, 1027-9.
29. Van de Vondel, D.; Wuyts, L.; Van der Kelen, G.; Bevernage, L., X-Ray Pes of Some Manganese Carbonyl Compounds. *Journal of Electron Spectroscopy and Related Phenomena* **1977**, *10*, 389-392.
30. Lee, K. E.; Gomez, M. A.; Elouatik, S.; Demopoulos, G. P., Further Understanding of the Adsorption Mechanism of N719 Sensitizer on Anatase Tio₂ Films for Dssc Applications Using Vibrational Spectroscopy and Confocal Raman Imaging. *Langmuir* **2010**, *26*, 9575-83.
31. Gao, R.; Wang, L.; Geng, Y.; Ma, B.; Zhu, Y.; Dong, H.; Qiu, Y., Interface Modification Effects of 4-Tertbutylpyridine Interacting with N3 Molecules in Quasi-Solid Dye-Sensitized Solar Cells. *Phys Chem Chem Phys* **2011**, *13*, 10635-40.
32. Pulm, S.; Hitzke, A.; Gunster, J.; Mausfriedrichs, W.; Kempter, V., Iodine Adsorption on Clean and Cesiated W(110) Studied with Ups and Metastable Impact Electron-Spectroscopy (Mies). *Surface Science* **1995**, *325*, 75-84.
33. Xue, G. G.; Guo, Y.; Yu, T.; Guan, J.; Yu, X. R.; Zhang, J. Y.; Liu, J. G.; Zou, Z. G., Degradation Mechanisms Investigation for Long-Term Thermal Stability of Dye-Sensitized Solar Cells. *International Journal of Electrochemical Science* **2012**, *7*, 1496-1511.
34. Toivola, M.; Halme, J.; Peltokorpi, L.; Lund, P., Investigation of Temperature and Aging Effects in Nanostructured Dye Solar Cells Studied by Electrochemical Impedance Spectroscopy. *International Journal of Photoenergy* **2009**, *2009*.
35. Zhang, Z.; Ito, S.; Moser, J. E.; Zakeeruddin, S. M.; Grätzel, M., Influence of Iodide Concentration on the Efficiency and Stability of Dye-Sensitized Solar Cell Containing Non-Volatile Electrolyte. *Chemphyschem* **2009**, *10*, 1834-8.
36. Lee, K. M.; Chen, C. Y.; Wu, S. J.; Chen, S. C.; Wu, C. G., Surface Passivation: The Effects of Cdca Co-Adsorbent and Dye Bath Solvent on the Durability of Dye-Sensitized Solar Cells. *Solar Energy Materials and Solar Cells* **2013**, *108*, 70-77.
37. Hara, K.; Wang, Z.-S.; Cui, Y.; Furube, A.; Koumura, N., Long-Term Stability of Organic–Dye-Sensitized Solar Cells Based on an Alkyl-Functionalized Carbazole Dye. *Energy & Environmental Science* **2009**, *2*, 1109-1114.
38. Lee, K. M.; Chiu, W. H.; Lu, M. D.; Hsieh, W. F., Improvement on the Long-Term Stability of Flexible Plastic Dye-Sensitized Solar Cells. *Journal of Power Sources* **2011**, *196*, 8897-8903.
39. Han, Y.; Pringle, J. M.; Cheng, Y. B., Improved Efficiency and Stability of Flexible Dye Sensitized Solar Cells on Ito/Pen Substrates Using an Ionic Liquid Electrolyte. *Photochem Photobiol* **2015**, *91*, 315-22.

40. Yang, R. Y.; Chen, H. Y.; Lai, F. D., Performance Degradation of Dye-Sensitized Solar Cells Induced by Electrolytes. *Advances in Materials Science and Engineering* **2012**, 2012.
41. Mehmood, U.; Rahman, S. U.; Harrabi, K.; Hussein, I. A.; Reddy, B. V. S., Recent Advances in Dye Sensitized Solar Cells. *Advances in Materials Science and Engineering* **2014**, 2014.
42. Gao, J.; El-Zohry, A. M.; Trilaksana, H.; Gabrielsson, E.; Leandri, V.; Ellis, H.; D'Amario, L.; Safdari, M.; Gardner, J. M.; Andersson, G., Light-Induced Interfacial Dynamics Dramatically Improve the Photocurrent in Dye-Sensitized Solar Cells: An Electrolyte Effect. *ACS applied materials & interfaces* **2018**, 10, 26241-26247.
43. Nguyen, H. T.; Ta, H. M.; Lund, T., Thermal Thiocyanate Ligand Substitution Kinetics of the Solar Cell Dye N719 by Acetonitrile, 3-Methoxypropionitrile, and 4-Tert-Butylpyridine. *Solar Energy Materials and Solar Cells* **2007**, 91, 1934-1942.
44. Nguyen, P. T.; Andersen, A. R.; Skou, E. M.; Lund, T., Dye Stability and Performances of Dye-Sensitized Solar Cells with Different Nitrogen Additives at Elevated Temperatures—Can Sterically Hindered Pyridines Prevent Dye Degradation? *Solar energy materials and solar cells* **2010**, 94, 1582-1590.
45. Nguyen, T. D.; Lin, C. H.; Mai, C. L.; Wu, C. G., Function of Tetrabutylammonium on High-Efficiency Ruthenium Sensitizers for Both Outdoor and Indoor Dsc Application. *ACS Omega* **2019**, 4, 11414-11423.
46. Hoshikawa, T.; Ikebe, T.; Kikuchi, R.; Eguchi, K., Effects of Electrolyte in Dye-Sensitized Solar Cells and Evaluation by Impedance Spectroscopy. *Electrochimica Acta* **2006**, 51, 5286-5294.
47. Shi, C. W.; Dai, S. Y.; Wang, K. J.; Pan, X.; Kong, F. T.; Hu, L. H., The Adsorption of 4-Tert-Butylpyridine on the Nanocrystalline TiO₂ and Raman Spectra of Dye-Sensitized Solar Cells in Situ. *Vibrational Spectroscopy* **2005**, 39, 99-105.
48. Lai, S. C.; Connor, K. N. P.; Ke, L., Degradation Mechanisms and Electron Kinetics Analysis in Aging Dye Sensitized Solar Cell Using Electrochemical Impedance Spectroscopy. *Journal of the Electrochemical Society* **2011**, 158, H1193-H1200.
49. Nazeeruddin, M. K.; Humphry-Baker, R.; Liska, P.; Grätzel, M., Investigation of Sensitizer Adsorption and the Influence of Protons on Current and Voltage of a Dye-Sensitized Nanocrystalline TiO₂ Solar Cell. *Journal of Physical Chemistry B* **2003**, 107, 8981-8987.

Chapter Eight

8. Conclusion and future work

DSSCs are the promising technology to convert the sun's energy into electricity that might be applied in the near future. This thesis presents the results of using photoelectron and ion spectroscopy techniques to study the geometrical and electronic surface structure at the TiO₂ surface in DSSC.

For further understanding, in chapter 4, two different surface treatments were performed on the TiO₂ substrate. The treatments were heating with four ascending temperatures and heating-sputtering with different doses using Ar⁺. The heating treatment was effective in removing surface contamination, while surface defects (Ti³⁺) were created using the heating-sputtering treatment.

An increase in the dye adsorption was obtained upon removing the surface contamination in heat treatment, while a decrease in the dye adsorption was observed as the Ti³⁺ increases, thus generating surface defects reduces the ability of the dye to be adsorbed on the TiO₂ samples. Furthermore, the dye configuration was different in both of the treatments. Removing the adventitious hydrocarbons on TiO₂ surface in the heating treatment did not affect the dye orientation. In contrast, in the heating-sputtering treatment, a second sulfur peak was observed at higher binding energy, indicating that S atoms in NCS ligands of the dye interact strongly with TiO₂ surface.

Expanding the work, in chapters 5 and 6, DSSCs were sensitized with two different Ru-based dyes: the hydrophilic dye N719 and the hydrophobic dye Z907. Then the process of co-adsorption with co-adsorbents was further investigated. Two different functional groups of co-adsorbents DPA and CDCA with various concentrations were used to investigate how the presence of co-adsorbent (type-concentration) in the dye solution influenced the formation of the dye layer on TiO₂, and how these changes are effecting on the cell performance.

In chapter 5, co-adsorbing DPA with both of N719 and Z907 induces changes on the dye coverage and formation. A significant decrease of the dye loading upon increasing DPA concentration in the sensitization solution. Despite this robust decrease in the dye coverage, the performance of

DSSCs with the lowest dye loading is hardly affected. Where a small decrease in the efficiency of DSSCs sensitized with the dye N719, and almost stabilized performance in DSSCs sensitized with the dye Z907 was observed. That is because DPA reduces the formation of the thicker dye layers on TiO₂ surface, reducing the dye molecules that not actively participate in the charge generation. The effect of DPA was found to be dependent on the type of dye. The Z907 dye tends to form a thicker layer than the N719, even with the presence of DPA in high concentration. The size of the dye molecule influences the amount of DPA adsorbed on the TiO₂ surface. The smaller molecule size of the Z907 dye than the N719 dye, allowed more of DPA molecules to be adsorbed on Z907 samples, resulting in competing and reducing more of the thinner layers of Z907.

When CDCA was used as co-adsorbents, a shift of the Ru peak was observed in the co-adsorbed sample, with a small change in the dye coverage in the N719 samples and a notable decrease in the dye coverage in the Z907 samples when the lowest concentration of CDCA was used. With further increments in CDCA concentration, the dye coverage remains almost stable in the N719 samples as well as the cells' Voc and FF with a minor decrease in Jsc. While in the Z907 samples, the dye coverage was decreasing with further increases in CDCA concentrations, with a prominent decrease in the depth regions indicating that CDCA reduces the formation of the thicker layers of the dye leading with more stabilized Voc and FF and a slight increase in Jsc.

Different effects of CDCA was obtained when it was used with the dyes N719 and Z907. The small size of the Z907 molecule compared to N719 molecule allows CDCA to penetrate to be more adsorbed on the TiO₂ surface, decreasing the formation of thicker dye layers and suppressing the charge recombination.

A closely look between the two co-adsorbent DPA and CDCA with the N719 dye the following can be concluded. Better cell performance was obtained with samples co-adsorbed with DPA than CDCA, where an increase in the efficiency with an increase in current was observed despite the significant decrease in the dye coverage, and maintaining the cell performance when the highest concentration of DPA was used. In the cells co-adsorbed with CDCA, the performance cell was almost stabilized, with a slight increase in efficiency and a decrease in the current was observed. The decrease in the current is an indication of the occurrence of the charge recombination due to thicker layers dye formation.

Although the concentration of DPA was much lower than the concentration of CDCA used in the dye solution, a higher effect on the dye loading was observed with DPA. Both DPA and the CDCA molecules have a similar size. However, DPA effect was more potent than CDCA, and this is due to the presence of P atom in DPA, where P is strongly bonded to the TiO₂ surface and made it a strong competitor with N719 to be adsorbed on TiO₂ surface. While CDCA mostly pushes the dye more in depth into the sample where a shift in the Ru peak was observed.

The decrease in the dye coverage was observed using both DPA and CDCA as co-adsorbents in Z907 samples. However, DPA strongly effects on the dye coverage, decreasing the thinner layers, while CDCA was more effective in reducing the thicker layers. More current was obtained with the cells co-adsorbed with DPA than CDCA, attributed to the strongly P binding on TiO₂ surface occupying the uncovered areas on TiO₂ reorienting the dye molecules and suppression the charge recombination.

The results showed that co-adsorbents have different functions when co-adsorbed with the dye. They replace the weakly interacting and undesirable dye that is not contributing to the photoexcitation, where they are used as anti-aggregation but not removing all aggregated dyes. In addition, competing with the other dye molecules to be adsorbed on TiO₂ surface and influence to some extent the anchoring configuration of dye molecules on TiO₂ substrate, subsequently reducing the charge recombination that enhances the cell performance.

The aging test of DSSCs sensitized with and without the co-adsorbent DPA was investigated under three different conditions, continuous light irradiation, thermal stress and dark. In chapter 7, DSSCs were disassembled to study their components as the cell ages. Focusing on how the interactions within the TiO₂/dye/electrolyte interface is changing as the cell ages.

The co-adsorbed DSSCs showed an initial improvement in the cell performance related to the inner equilibrium of the cell components was during the first 100 h of aging, followed by a variable decreasing in the efficiency according to each condition. The results obtained from the photovoltaic parameters were linked with the some of the chemical changes from XPS results. A clear correlation was found in the compositional changes on the TiO₂/dye/electrolyte interface using XPS with the cell performance.

In the co-adsorbed cell, an apparent decrease in the dye intensity was observed from XPS results. The competition between the dye, electrolyte and additives to be adsorbed on the TiO_2 , resulted in desorbing some of the dye molecules. Consequently, better penetration of the electrolyte and its additives was observed with the co-adsorbed cells, resulting in a stabilized V_{oc} .

The reason for the dramatic drop of the cell efficiency is mostly due to a combination of factors, mainly the changes in the redox ratio and the increase in the oxidized sulfur.

NICISS is an ideal technique for measuring the concentration depth profiles of the elements. However, due to the close masses of iodine and ruthenium, their onsets have appeared close to each other cause's difficulties in evaluating their depth profiles. Thus, further investigation using heavier gasses (such as Ne) is needed to study the depth profiles of the iodine and ruthenium at the interface during aging.

To ensure long-term stability and avoid any extrinsic contamination penetrating the cell, hermetic sealing is required in DSSC. Since the electrolyte is in contact with the polymer sealants which cause some damaging in the sealant that hold the cell substrates as the cell ages, where this issue was observed in this work, a modification on DSSC design is needed to prevent this connection. An example of such design is illustrated in Figure 8-1, where the dyed adsorbed photoanode (red) in contact with the electrolyte (yellow) are separated from the sealant (dark grey) each in a different layer.

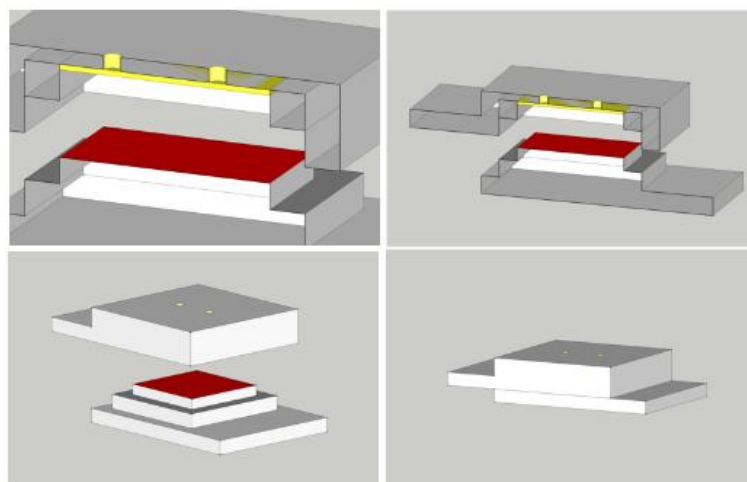


Figure 8-1: Modified DSSC

Further studies can be carried out using a selection of different dyes with different chemical structure and electrolyte to obtain the best conformity of materials with a controllable method maintaining a stabilized interface, where a slight change on the interface had influenced the cell performance. Refilling the cell with dye or/and electrolyte as time prolong and investigate their influences on cell stability will lead to a deeper dimension to test the cell's quality. Finding a system that allows refilling the cell while maintaining its skeleton (photoanode and counter electrode), will accelerate DSSCs commercialization.